

Ministry of Education and Science of Ukraine
Sumy State University



JOURNAL OF ENGINEERING SCIENCES

Scientific Journal

Volume 8, Issue 1 (2021)

ISSN 2312-2498 (print)
ISSN 2414-9381 (online)

Founded in 2014

Journal of Engineering Sciences is an open-access peer-reviewed scientific journal. It covers urgent issues of up-to-date high-tech production in the development of new engineering trends and future technologies. The general topics of the journal include manufacturing, mechanical, and chemical engineering. The publication language is English. The editorial board is represented by scientists from different international research institutions that cover the journal's topics and evaluate all the submitted articles. The system of double-blinded review provides a high-quality presentation of articles. The editorial policy, including submission, review, acceptance, and publication of articles, is entirely transparent.

The journal was founded in 2014. It is published by Sumy State University of Ministry of Education and Science of Ukraine with the support of the International Association for Technological Development and Innovations.

ISSN 2312-2498 (print)
ISSN 2414-9381 (online)

The journal is intended for a wide range of scientists, researchers, practitioners, and others interested in manufacturing, mechanical, and chemical engineering. All the publications in the journal are free of articles processing charges (APCs) and articles submission charges.

*Recommended for publication
by the Academic Council of Sumy State University,
(minutes No. 16 of 24.06.2021)*

The journal is the scientific professional edition of Ukraine (Category “B”) in Engineering Sciences ordered by the Ministry of Education and Science of Ukraine, November 7, 2018, No. 1218.

Partners:

- International Association for Technological Development and Innovations, <http://iatdi.org>;
- Ministry of Education and Science of Ukraine, <https://mon.gov.ua>;
- Faculty of Mechanical Engineering and Management, Poznan University of Technology (Poland), <https://www.put.poznan.pl>;
- Faculty of Manufacturing Technologies with a seat in Prešov, Technical University of Košice (Slovakia), <http://www.fvt.tuke.sk>;
- Faculty of Mechanical Engineering of University of West Bohemia (Czech Republic), <http://www.fst.zcu.cz>.

Editorial Board: 2, Rymskogo-Korsakova St., 40007 Sumy, Ukraine; Apt. M-211
Contact Phone: +380-993-845-740
E-mail: jes@teset.sumdu.edu.ua
Website: <http://jes.sumdu.edu.ua>

State registration certificate of the print mass-media No. 20499-10299 PR.



TOPICS

Manufacturing Engineering:

- Machines and Tools;
- Technical Regulations and Metrological Support;
- Materials Science.

Mechanical Engineering:

- Dynamics and Strength of Machines;
- Computational Mechanics.

Chemical Engineering:

- Processes in Machines and Devices;
- Energy Efficient Technologies;
- Environmental Protection.

STATISTICS

- **Publication frequency:** biannually (2 issues per year)
- **Papers per issue:** 20
- **Acceptance rate:** 26 %
- **Timeline:**
 - days from submission of the manuscript to first decision: 30
 - days from acceptance at the publisher to published online: 14
- **Editorial Board:**
 - members: 66
 - institutions: 46
 - countries: 25

EDITOR-IN-CHIEF

Ivan PAVLENKO, DSc., Professor, Sumy State University, Sumy, Ukraine

DEPUTY EDITOR-IN-CHIEF

Vitalii IVANOV, DSc., Professor, Sumy State University, Sumy, Ukraine

BOARD OF CO-EDITORS

Manufacturing Engineering

Erwin RAUCH, Ph.D., Professor, Free University of Bozen-Bolzano, Bolzano, Italy

Jose MACHADO, Ph.D., Professor, University of Minho, Braga, Portugal

Mechanical Engineering

Jan PITEL, Ph.D., Professor, Technical University of Kosice, Presov, Slovakia

Noel BRUNETIERE, Ph.D., Senior Researcher, University of Poitiers, Poitiers, France

Chemical Engineering

Alex-Enrich PRAST, Ph.D., Professor, Linkoping University, Linkoping, Sweden

Mathieu GAUTIER, Ph.D., Professor, University of Lyon, Lyon, France

INTERNATIONAL EDITORIAL BOARD

Praveen AGARWAL, Ph.D., Professor, Anand International College of Engineering, Jaipur, India

Katarzyna ANTOSZ, DSc., Associate Professor, Rzeszow University of Technology, Rzeszow, Poland

Peter ARRAS, DSc., Professor, KU Leuven, Leuven, Belgium

Viktor ASTAKHOV, DSc., Professor, Production Service Management Inc., Ann Arbor, USA

Volodymyr ATAMANYUK, DSc., Professor, Lviv Polytechnic National University, Lviv, Ukraine

Eddy BAJIC, Ph.D., Professor, University of Lorraine, Nancy, France

Marian BARTOSZUK, Ph.D., Professor, Opole University of Technology, Opole, Poland

Jean BOUYER, Ph.D., Associate Professor, University of Poitiers, Poitiers, France

Robert CEP, Ph.D., Professor, Technical University of Ostrava, Ostrava, Czech Republic

Olaf CISAK, Ph.D., Associate Professor, Poznan University of Technology, Poznan, Poland

Predrag DASIC, DSc., Professor, VTMS Trstenik, Trstenik, Serbia

Kostiantyn DYADYURA, DSc., Professor, Odessa Polytechnic State University, Odessa, Ukraine

Milan EDL, Ph.D., Associate Professor, University of West Bohemia, Pilsen, Czech Republic

Domenico GUIDA, Ph.D., Professor, University of Salerno, Salerno, Italy

Oleksandr GUSAK, Ph.D., Professor, Sumy State University, Sumy, Ukraine

Michal HATALA, Ph.D., Professor, Technical University of Kosice, Presov, Slovakia

Koichi HASEGAWA, Ph.D., Associate Professor, Chubu University, Kasugai, Japan

Siamak HOSEINZADEH, Ph.D., Post Doc., University of Pretoria, Pretoria, South Africa

Jozef HUSAR, Ph.D., Assistant Professor, Technical University of Kosice, Presov, Slovakia

Yury IVANOV, Ph.D., Associate Professor, Chubu University, Kasugai, Japan

Fuat KARA, Ph.D., Assistant Professor, Duzce University, Istanbul, Turkey

Isak KARABEGOVIC, DSc., Professor, University of Bihac, Bihac, Bosnia and Herzegovina

Jakub KASCAK, Ph.D., Assistant Professor, Technical University of Kosice, Presov, Slovakia

Serhii KLIMENKO, DSc., Professor, Bakul Institute for Superhard Materials, National Academy of Sciences of Ukraine, Kyiv, Ukraine

Dmytro KRYVORUCHKO, DSc., Associate Professor, Sumy State University, Sumy, Ukraine
Czeslaw KUNDERA, DSc., Professor, Kielce University of Technology, Kielce, Poland
Ivan KURIC, Ph.D., Professor, University of Zilina, Zilina, Slovakia
Milovan LAZAREVIC, Ph.D., Associate Professor, University of Novi Sad, Novi Sad, Serbia
Stanislaw LEGUTKO, DSc., Professor, Poznan University of Technology, Poznan, Poland
Oleksandr LIAPOSHCHENKO, DSc., Professor, Sumy State University, Sumy, Ukraine
Athanasios MAMALIS, DSc., Professor, Demokritos National Centre for Scientific Research, Athens, Greece
Arun MATHEW, Ph.D., Associate Professor, Vellore Institute of Technology, Vellore, India
Thomas MATHIA, Ph.D., Professor, Ecole Centrale de Lyon, Lyon, France
Yurii MATSEVITYI, DSc., Professor, Podgorny Institute for Mechanical Engineering Problems, National Academy of Sciences of Ukraine, Kharkiv, Ukraine
Ronald MERSEY, Ph.D., Associate Professor, Widener University, Chester, USA
Arun NAGARAJAH, DSc., Professor, University of Duisburg-Essen, Duisburg, Germany
Eduard Laurentiu NITU, Ph.D., Professor, University of Pitesti, Pitesti, Romania
Dragan PERAKOVIC, Ph.D., Professor, University of Zagreb, Zagreb, Croatia
Alejandro PEREIRA, Ph.D., Professor, University of Vigo, Vigo, Spain
Yurii PETRAKOV, DSc., Professor, National Technical University of Ukraine “Kyiv Polytechnic Institute”, Kyiv, Ukraine
Roman PETRUS, DSc., Professor, Rzeszow University of Technology, Rzeszow, Poland
Leonid PLYATSUK, DSc., Professor, Sumy State University, Sumy, Ukraine
Frantisek POCHYLÝ, Ph.D., Professor, Brno University of Technology, Brno, Czech Republic
Yimin RONG, DSc., Professor, South University of Science and Technology, Shenzhen, China
Vitalii SIMONOVSKIY, DSc., Professor, Sumy State University, Sumy, Ukraine
Vsevolod SKLABINSKYI, DSc., Professor, Sumy State University, Sumy, Ukraine
Michael STORCHAK, DSc., Professor, Institute for Machine Tools of Stuttgart University, Stuttgart, Germany
Fabio TEIXEIRA, DSc., Professor, Federal University of Rio Grande do Sul, Porto Alegre, Brazil
Justyna TROJANOWSKA, Ph.D., Assistant Professor, Poznan University of Technology, Poznan, Poland
Kaname TSUTSUMIUCHI, DSc., Professor, Chubu University, Kasugai, Japan
Raul TURMANIDZE, DSc., Professor, Georgian Technical University, Tbilisi, Georgia
Michal VARCHOLA, Ph.D., Professor, Slovak University of Technology in Bratislava, Bratislava, Slovakia
George-Christopher VOSNIAKOS, Ph.D., Professor, National Technical University of Athens, Athens, Greece
Jozef ZAJAC, DSc., Professor, Technical University of Kosice, Presov, Slovakia
Viliam ZALOGA, DSc., Professor, Sumy State University, Sumy, Ukraine
Lianyu ZHENG, Ph.D., Professor, Beihang University, Beijing, China

PUBLISHING MANAGER

Kristina BERLADIR, Ph.D., Senior Lecturer, Sumy State University, Sumy, Ukraine

MARKETING AND COMMUNICATION MANAGER

Vladyslav KONDUS, Ph.D., Senior Lecturer, Sumy State University, Ukraine



CONTENTS

MANUFACTURING ENGINEERING

Materials Science

- Taku J. K., Amartey Y. D., Ejeh S. P., Lawan A.
Durability Evaluation of Calcined Clay and Limestone Powder
Blended Ternary Self-Compacting Concrete C1–C10
DOI: [10.21272/jes.2021.8\(1\).c1](https://doi.org/10.21272/jes.2021.8(1).c1)
- Novokhat O. A., Vozniuk V. T., Hritsiuk H. I., Lysii V.
Determination of Kinetic Regularities of the Process of Drying Perlite by Radiation Method C11–C17
DOI: [10.21272/jes.2021.8\(1\).c2](https://doi.org/10.21272/jes.2021.8(1).c2)
- Chernobrovchenko V. S., Dyadyura K. O., Balynskiy M., Panda A.
Influence of Technological Manufacturing Conditions on the Porosity of Calcium-Phosphate Scaffolds C18–C28
DOI: [10.21272/jes.2021.8\(1\).c3](https://doi.org/10.21272/jes.2021.8(1).c3)
- Javanbakht T., Laurent S., Stanicki D., Salzmänn I.
Rheological Properties of Superparamagnetic Iron Oxide Nanoparticles C29–C37
DOI: [10.21272/jes.2021.8\(1\).c4](https://doi.org/10.21272/jes.2021.8(1).c4)
- Hurey I., Gurey V., Bartoszyk M., Hurey T.
Formation of Residual Stresses during Discontinuous Friction Treatment C38–C44
DOI: [10.21272/jes.2021.8\(1\).c5](https://doi.org/10.21272/jes.2021.8(1).c5)
- Povstyanoy O., MacMillan A.
Mechatronic System's Permeable Materials with Controlled Porosity C45–C49
DOI: [10.21272/jes.2021.8\(1\).c6](https://doi.org/10.21272/jes.2021.8(1).c6)

MECHANICAL ENGINEERING

Dynamics and Strength of Machines

- Demianenko M., Volf M., Pavlenko I., Liaposhchenko O.
Experimental Studies on Oscillation Modes of Vibration Separation Devices D1–D9
DOI: [10.21272/jes.2021.8\(1\).d1](https://doi.org/10.21272/jes.2021.8(1).d1)

Computational Mechanics

- Kanagasabai L.
Heat Transfer and Simulated Coronary Circulation System Optimization Algorithms
for Real Power Loss Reduction E1–E8
DOI: [10.21272/jes.2021.8\(1\).e1](https://doi.org/10.21272/jes.2021.8(1).e1)
- Eze P. C., Ugoh C. A., Inaibo D. S.
Positioning Control of DC Servomotor-Based Antenna Using PID Tuned Compensator E9–E16
DOI: [10.21272/jes.2021.8\(1\).e2](https://doi.org/10.21272/jes.2021.8(1).e2)
- Janigová S., Schürger B.
Design Optimization of the Modified Planetary Carrier E17–E22
DOI: [10.21272/jes.2021.8\(1\).e3](https://doi.org/10.21272/jes.2021.8(1).e3)

Prydalnyi B. I., Sulym H. T.
Mathematical Model of the Tensioning in the Collet Clamping Mechanism
with the Rotary Movable Input Link on Spindle Units E23–E28
DOI: [10.21272/jes.2021.8\(1\).e4](https://doi.org/10.21272/jes.2021.8(1).e4)

Kanagasabai L.
FCC Algorithm for Power Loss Diminution E29–E38
DOI: [10.21272/jes.2021.8\(1\).e5](https://doi.org/10.21272/jes.2021.8(1).e5)

Pawar R. S., Patil J.
Improvement in Seismic Performance of Building with BRBs E39–E49
DOI: [10.21272/jes.2021.8\(1\).e6](https://doi.org/10.21272/jes.2021.8(1).e6)

CHEMICAL ENGINEERING

Processes in Machines and Devices

Nogueira E.
Applying the Concepts of Efficiency and Effectiveness to Analyze the Influence of the Number
of Passes in the Shell and Tubes Condenser Thermal Performance F1–F10
DOI: [10.21272/jes.2021.8\(1\).f1](https://doi.org/10.21272/jes.2021.8(1).f1)

Vaneev S. M., Martynkovskyy V. S., Kulikov A., Miroshnichenko D. V.,
Bilyk Ya. I., Smolenko D. V., Lazarenko A. D.
Investigation of a Turbogenerator Based on the Vortex Expansion Machine
with a Peripheral Side Channel F11–F18
DOI: [10.21272/jes.2021.8\(1\).f2](https://doi.org/10.21272/jes.2021.8(1).f2)

Hu W. J., Tan K., Markovych S., Liu X. L.
Study of a Cold Spray Nozzle Throat on Acceleration Characteristics via CFD F19–F24
DOI: [10.21272/jes.2021.8\(1\).f3](https://doi.org/10.21272/jes.2021.8(1).f3)

Babalola F. U., Akanji I. O., Oyegoke T.
Comparative Analysis of the Performance of Mixing Rules
for Density Prediction of Simple Chemical Mixtures F25–F31
DOI: [10.21272/jes.2021.8\(1\).f4](https://doi.org/10.21272/jes.2021.8(1).f4)

Environmental Protection

Gundu M., Abhaysinha S.
Experimental Study on the Performance of Concrete Mix with Paper Waste,
Waste Plastic, Quarry Dust, and Fly Ash H1–H7
DOI: [10.21272/jes.2021.8\(1\).h1](https://doi.org/10.21272/jes.2021.8(1).h1)

Shtepa V. N., Chernysh Ye. Yu., Danilov D. V.
Preventive Improvement of Wastewater Treatment Efficiency H8–H15
DOI: [10.21272/jes.2021.8\(1\).h2](https://doi.org/10.21272/jes.2021.8(1).h2)

Kiran A. V. N. S., Ramanjaneyulu B., Lokanath M., Nagendra S., Balachander G. E.
Control of Exhaust Emissions Using Piston Coating on Two-Stroke
SI Engines with Gasoline Blends H16–H20
DOI: [10.21272/jes.2021.8\(1\).h3](https://doi.org/10.21272/jes.2021.8(1).h3)



5th International Conference on
**Design, Simulation, Manufacturing:
The Innovation Exchange**
June 7-10, 2022 | Sumy, Ukraine



Together we can do more for science, technology, engineering, and education. © DSMIE Team



Together we can do more for science, technology, engineering, and education. © DSMIE Team



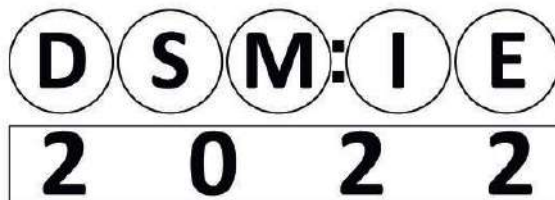
DSMIE-2022 focuses on research challenges in the fields of **Manufacturing Engineering, Materials Engineering, Mechanical Engineering, and Chemical Engineering**, addressing current and future trends in design approaches, simulation techniques, manufacturing technologies, computer-aided systems and ICT tools and Industry 4.0 strategy implementation for engineering tasks solving.

Full research papers will be published as Conference Proceedings in **Lecture Notes in Mechanical Engineering** (ISSN 2195-4356, Springer Nature), indexed by **Scopus** and submitted to **Web of Science Core Collection** databases.

Paper submission is supported by EasyChair Conference Management System. The deadline is **October 15, 2021**.



5th Anniversary



5th International Conference on
**Design, Simulation,
Manufacturing:
The Innovation Exchange**

June 7-10, 2022 | Sumy, Ukraine

<http://dsmie.sumdu.edu.ua>

Organized by
Sumy State University and
International Association for Technological Development and Innovations,
in partnership with Technical University of Kosice,
Kielce University of Technology, University of West Bohemia,
Poznan University of Technology, Association for Promoting Innovative
Technologies - InnovativeFET, Society for Robotics of Bosnia and Herzegovina

Agenda

- June 7 | Registration
- June 8 | Keynote Sessions & Round Table
- June 9 | Technical Sessions & Industry Tour
- June 10 | Technical Sessions & Awards

Contacts

- ✉ dsmie@teset.sumdu.edu.ua
- 📘 DSMIEConferenceSeries
- 🌐 DSMIEConferenceSeries



DSMIE-2022

Where science, industry, and education meet

5th International Conference on
**Design, Simulation, Manufacturing:
The Innovation Exchange**



Taku J. K., Amartey Y. D., Ejeh S. P., Lawan A. (2021). Durability evaluation of calcined clay and limestone powder blended ternary self-compacting concrete. *Journal of Engineering Sciences*, Vol. 8(1), pp. C1–C10, doi: 10.21272/jes.2021.8(1).c1

Durability Evaluation of Calcined Clay and Limestone Powder Blended Ternary Self-Compacting Concrete

Taku J. K.^{1*}, Amartey Y. D.², Ejeh S. P.², Lawan A.²

¹ Department of Civil Engineering, Joseph Saawuan Tarka University, P. M. B. 2373 Makurdi, 970101 Makurdi, Nigeria;

² Department of Civil Engineering, Ahmadu Bello University, P. M.B. 1013 Zaria, 810001 Zaria, Nigeria

Article info:

Received: March 3, 2021
The final version received: June 16, 2021
Accepted for publication: June 21, 2021

*Corresponding email:

kumataku@yahoo.com

Abstract. This research investigates the durability-based properties of a ternary calcined clay and limestone powder blended Self Compacting Concrete by measuring the short- and long-term permeation properties using water absorption and sorptivity properties testing. Also, the variation of compressive strength with age was evaluated at 7, 14, 28, and 56 days, while the split tensile strength was determined at 7 and 28 days curing. The ternary SCC's mineralogy and morphology were evaluated using FT IR Spectroscopy, SEM imaging, and EDS. The results obtained show that the ternary SCC showed improved durability and strength properties with dense and improved microstructure.

Keywords: ternary concrete, self-compacting concrete, durability properties, calcined clay, limestone powder.

1 Introduction

Sustainable construction requires the use of durable and economical construction materials locally available and can perform optimally throughout the design life of the structure for which they are used. One measure of the durability of concrete is the permeation property, which is a function of the pore structure of the concrete and controls the ingress or otherwise of water and other substances into the concrete. Durable concrete should have minimal amounts of water and other minerals ingress as it ages.

Due to its non-vibrated nature, self-compacting concrete (SCC) could be quite porous, especially if the mix does not have adequate workability. This workability can be enhanced using Supplementary Cementitious Materials (SCM) and fillers [1]. This work investigates the properties of a ternary SCC comprising Calcined Clay (CC) and Limestone Powder (LP) as Supplementary Cementitious Material (SCM) and filler, respectively.

2 Literature Review

The past decade has witnessed rapid breakthroughs in the development and application of SCC in the construction industry [2]. A lot of research has been put into the design and production of SCC with very positive

results. However, there is no limit to improving this very viable construction material further to improve further its properties in the fresh and hardened states [3].

Different research works have been carried out on self-compacting concrete to either characterize this essential construction material and improve it. [4] presented an overview of various research works on SCC to investigate the new properties, strength, permeability, diffusivity, tribological behavior and thixotropy of SCC incorporating different CRMs and the effects on the interfacial Transition Zone (ITZ). He also reported on different mix design methods and the performance of SCC for different applications. [5] investigated the flow of SCC with and without steel fibers and carried out a 3D modelling of the flow of SCC in slump and L-box tests using a Lagrangian particle-based method known as the Smooth Particle Hydrodynamics (SPH). [6] investigated and modelled the bond strength between SCC and reinforcement using the RILEM pull out method, developing a model for evaluating the bond stress and ultimate slip for SCC. [7] reported on recent updates and developments on SCC as presented at the 2016 RILEM conference on SCC in the areas of mix design methods, materials, test methods, durability, and sustainability. It is interesting that the report contains novel research on the production of eco-

efficient SCC (eco-SCC) produced by optimizing aggregate gradation with good results by [8].

One way of improving SCC is the incorporation of SCMs and fillers into the concrete. The absorption of cement composites is principally controlled by the connectivity, pore size, and total porosity, which provides the moisture pathways. This is expected because Concretes with blended binder systems exhibit a more refined pore structure than OPC systems because of the additional/prolonged hydraulic and pozzolanic reactions [9]. Other properties that may be improved include strength [10], durability [11], and microstructural properties [12] of SCC.

Incorporating different mineral admixtures to replace cement or as fillers improve the workability of concrete; thus, helping to improve the concrete microstructure and durability [11]. [13] reports that ternary blends in concrete help reduce/ eliminate the drawbacks of a particular SCM or filler. [14] also investigated ternary blended SCCs with good results. In a similar vein, [15] used different mineral powders in a ternary blend of SCC and reported improved durability. Simoes et al. (2012) reported improved workability in the paper "Ternary mixes of self-compacting concrete with fly ash and municipal solid waste incinerator bottom ash". Thus, the use of Ternary blends in SCC helps to improve the durability of SCC. This work investigates the durability of a ternary SCC using locally available materials (calcined clay and Limestone powder) as supplementary cementitious material and filler, respectively.

3 Research Methodology

3.1 Materials testing

The fine aggregate- river sand, and the coarse aggregate – crushed granite rock of maximum size 20mm, both obtained locally in Zaria, Nigeria, and the CC was characterized for their gradation using sieve analysis. At the same time, the chemical, mineralogical and morphological properties of the cement, CC and LP were determined using SEM, XRF, FTIR and XRD analysis.

3.2 Testing of fresh state properties of SCC

The flowability/ deformability properties of SCC were investigated by carrying out slump flow and V-Funnel tests. The slump flow tests were carried out to determine the flow time, time taken to reach a diameter of 500 mm, and the flow diameter under the procedure set out in [16, 17] while the V-Funnel test was carried out to determine the time taken for the SCC to flow out of the funnel and is carried out under the provisions of [18]. According to the European guidelines for SCC (EGSCC 2005), the slump flow value gives the flowability of a fresh SCC, and SCC class SF2 is suitable for most standard applications.

The passing and filling ability of fresh SCC was evaluated using the L-Box and the J-Ring to determine the ability of the SCC to pass through reinforcements and fill the formwork without segregation. The J-ring was used to determine the flow spread and the blocking step in line with the provisions of [19], while the L-box

tests were carried out under the procedure set out in [22]. Both the J-ring and L-box tests were used to determine how well a specific batch of SCC will flow through restricted spaces without blocking. The filling ability, determined using the L-box, gives an idea of how well an SCC mix batch can flow into and fill formwork under the action of gravity alone [20].

3.3 Permeation and strength properties

3.3.1 Water absorption and sorptivity tests

The durability of the SCC in this research was measured using the rate at which water and other substances can ingress into the SCC, which is a function of the pore structure of the concrete. While water sorptivity measured the rate of water ingress through interconnected pore spaces, the water absorption that measures the general water ingress through all kinds of pore spaces. The Sorptivity test was carried out using the procedure outlined in [21] to determine the susceptibility of the unsaturated concrete to the penetration of water through capillarity by determining the increase in the mass of the specimen resulting from absorption of water as a function of time when only one surface is exposed to water. The initial rate of water absorption (or sorptivity, $\text{mm/s}^{1/2}$) is defined as the slope of the line that is the best fit of absorption, I plotted against the square root of time [21]. The value of the initial rate of absorption for each sample is the slope of the plot of the least squares, linear regression analysis of I vs. the square root of time in seconds. The test was carried out at 28 and 56 days for each mix to evaluate the short and long-term effects of the SCM and filler materials on water absorption rate through interconnected capillary pores as a measure of the concrete durability. Three numbers diameter 100 by 50 discs, cut from 100 by 200 concrete cylinder specimens, were used for each test and the average result calculated, while the water absorption test was carried out to determine, in line with the provisions of [24,28], the change in water absorption capacity of the specimens with age after being submerged for 24 hours. The test was carried out at 7, 14, 21, 28, and 56 days to monitor the change in water absorption capacity of the SCC with age. For each test, three 50x50x50 cubes were used and the average value was taken.

3.3.2 Strength tests

The compressive strength test was carried out to measure the effect of CC and LP on the long-term strength development of the ternary SCC and was determined using 100 cubic millimeters concrete cubes cured at 7, 14, 28, and 56 days in accordance with the provisions of [27].

Granted that although concrete is not typically designed to resist direct tension, the knowledge of tensile strength is used to estimate the load under which cracking will develop. This is due to its influence on the formation of cracks and its propagation to the tension side of the reinforced concrete flexural members [25, 26], hence the importance of tensile strength testing. This test was carried out using diameter 100 by 200 cylinders at 7 and 28 days using the split tensile strength test by crushing the cylinders longitudinally on

a compressive strength test machine in line with the provisions of [27]. Three specimens were used for each test, and the average value was taken.

3.4 Microstructural analysis

The micromechanical properties of the SCC produced were investigated to determine the morphological and mineralogical properties of the ternary SCC after curing for 56 days and then kept outside the water for 90 days. This was to evaluate the effect of the pozzolanic reaction and the filler effect on the microstructural properties of the ternary. This characterization was carried out using SEM, EDS, and FTIR analysis. While the SEM was used to study the morphological properties of the SCC, EDX gave the quantitative and qualitative mineralogical properties thereof, and the FTIR gave the qualitative mineralogical properties of the SCC.

4 Results and Discussion

4.1 Materials characterization

Figure 1 gives the gradation curves for coarse and fine aggregates and calcined clay, respectively.

The fine and coarse aggregates are well graded, with the coarse aggregates having a maximum aggregate size of less than 20mm as specified in [16] for aggregates and are thus suited for SCC application. It can also be seen that more than 50 % of the clay is finer than 75 μm , and over 99 % of the clay particles are finer than 300 μm . That shows that the clay particles have a large surface area for reactivity and can also fill the pore spaces in the concrete. All the LP particles passed through the 75 μm sieve and thus should be well filled for filling the pore spaces in concrete.

The result of XRF analysis is presented in Table 1, and it shows that Calcined clay contains more than 70 % $\text{SiO}_2 + \text{Al}_2\text{O}_3 + \text{Fe}_2\text{O}_3$ stipulated by ASTM C618 for class F pozzolana and so have pozzolanic potential. Also, limestone powder contains more than 50 % CaO and less than 50 % $\text{SiO}_2 + \text{Al}_2\text{O}_3 + \text{Fe}_2\text{O}_3$, which means even though it is not pozzolanic, it has the potential of being a good filler in concrete and has been used severally in SCC and NVC with positive results [29–31]. The high loss on ignition content (LOI) was assumed to be due to the water chemically combined in kaolinite (11.0 % wt.), which would be lost during the calcination process [32].

The results of XRD analysis on the calcined clay and Limestone powder are presented in Figures 2–3 for the qualitative and quantitative analysis respectively of the CC and LP minerals, respectively. It can be seen from the result of the XRD analysis of Calcined clay as presented in Figure 2 a that the CC is made up principally of quartz which is basically SiO_2 , and thus shows that the material is pozzolanic in nature and can be used as supplementary cementitious material. It is evident that LP comprises calcite principally with quartz, Dolomite, Lime, and Garnet making up the other peaks, as seen in Figure 2 b. The quantitative analysis (Figure 3 a) shows that the calcite makes up the bulk of

the LP (77 % of the total composition) with quartz (10 %), dolomite (7.5 %), Lime (5.2 %), and Garnet (0.5 %) taking up the rest of the composition. This result agrees with [33, 34].

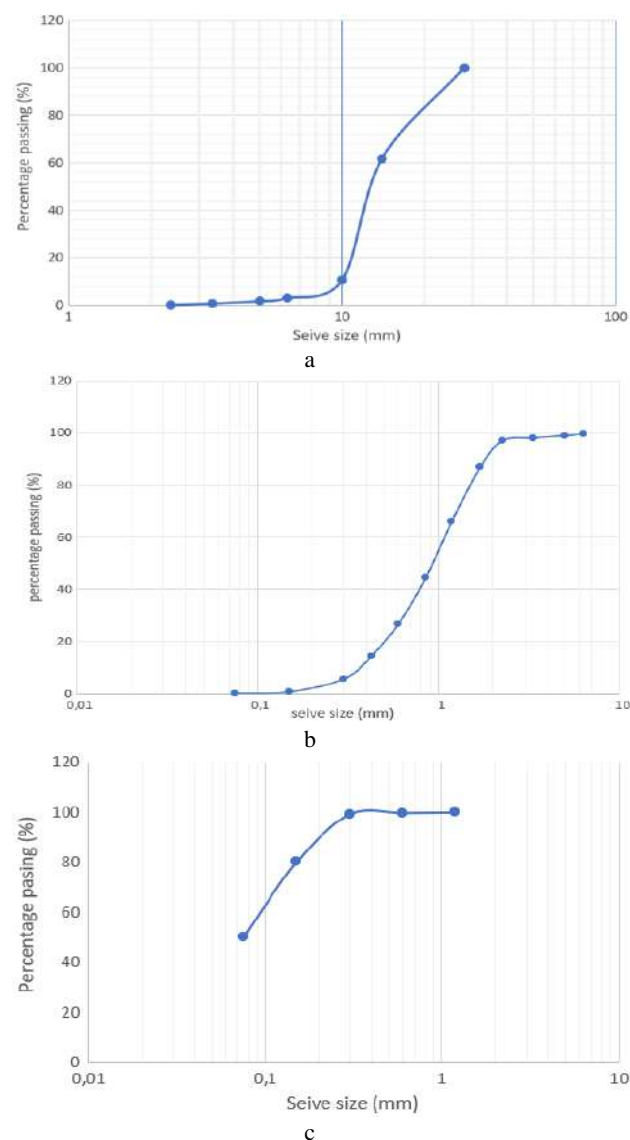
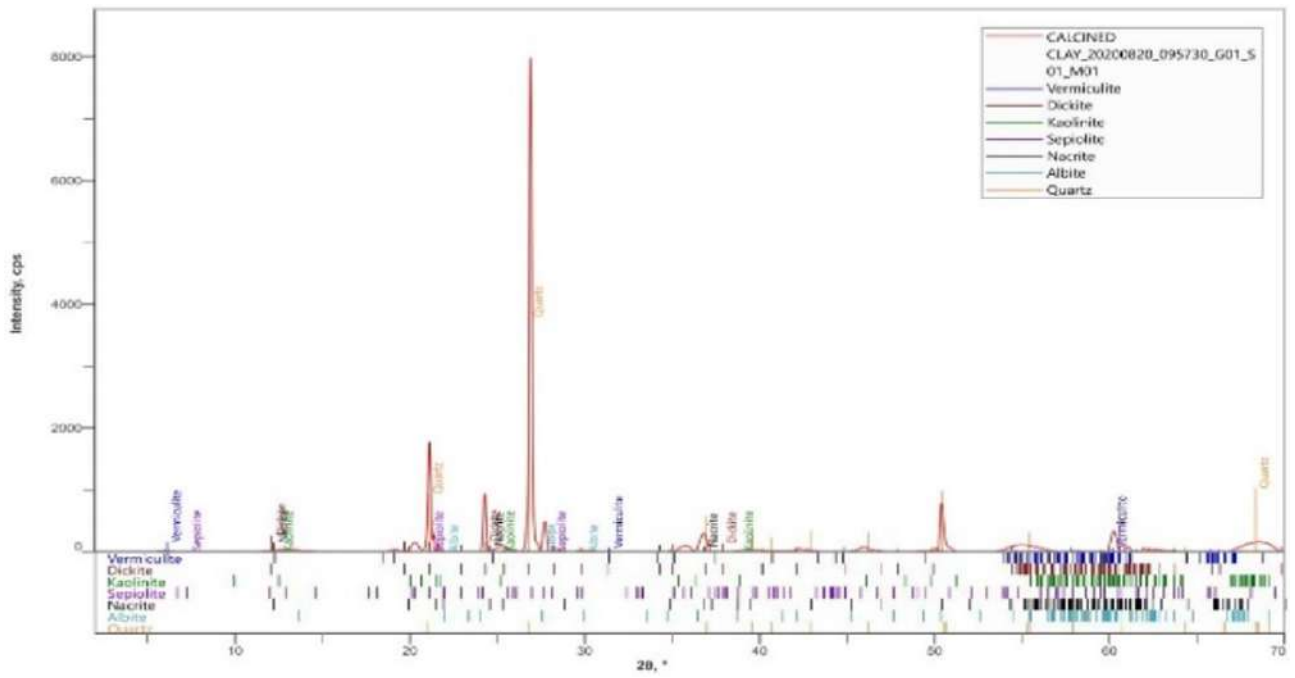


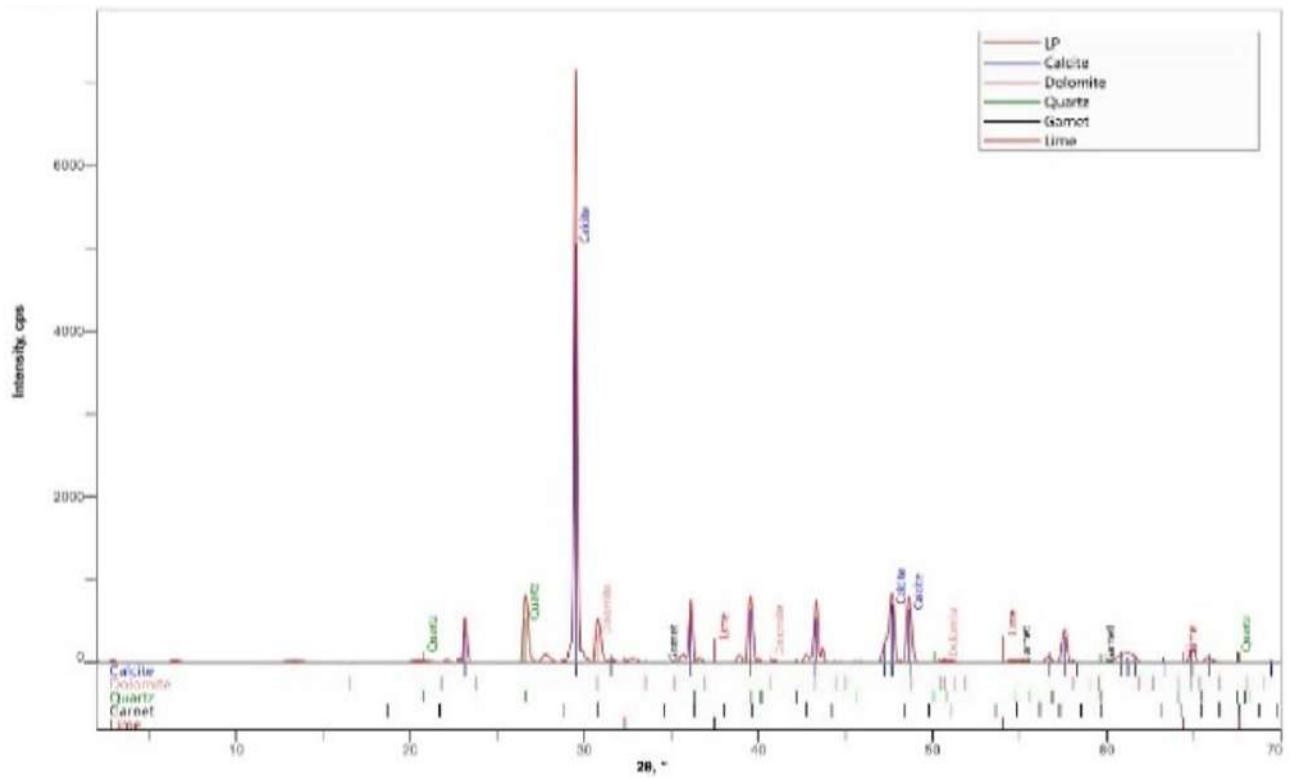
Figure 1 – Gradation curve for coarse (a) and fine (b) aggregates, and calcined clay (c)

Table 1 – Oxide composition of PLC, limestone (L), and calcined clay (CC) using XRF analysis

Oxide	CC	Cement	LP
CaO	1.50	66.5	53.2
Fe ₂ O ₃	0.90	6.83	1.4
Al ₂ O ₃	25.1	5.60	2.13
SiO ₂	59.2	16.2	3.96
TiO	–	0.20	–
K ₂ O	1.80	0.48	0.46
Na ₂ O	0.03	0.78	0.05
SO ₂	0.20	2.51	0.08
BaO	0.11	0.12	–
V ₂ O ₃	0.10	–	–
Cr ₂ O ₅	0.03	–	–
MnO	0.04	–	–
LOI	11.0	1.71	37.7



a



b

Figure 2 – XRD result (qualitative) of calcined clay(a) and limestone powder (b)

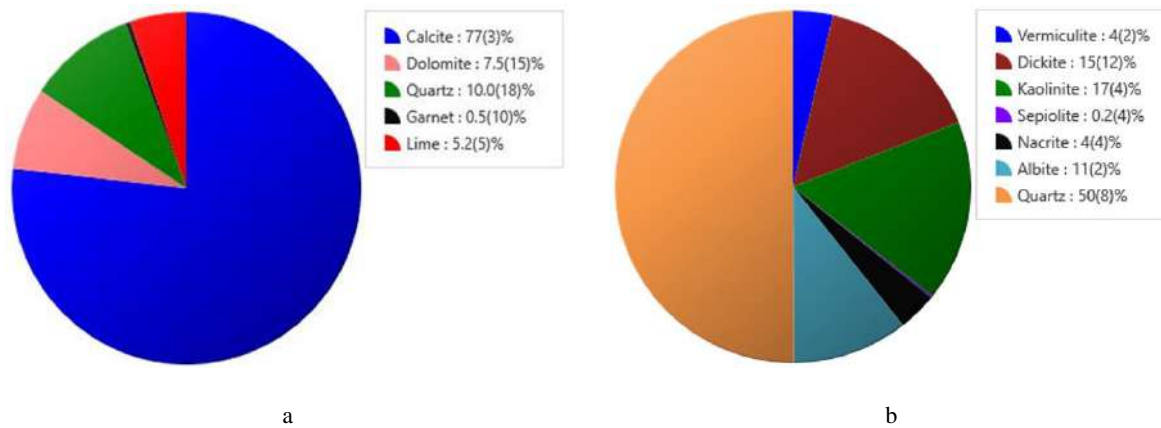


Figure 3 – Quantitative analysis of limestone powder (a) and calcined clay (b) minerals

It can also be seen from the result of XRF and XRD analysis of LP that it is not pozzolanic. Limestone powder has no pozzolanic activity and is still unhydrated at the age of 28 days. However, its filling effect can make the paste matrix and the interfacial transition zone between matrix and aggregate denser, which will improve the performance of concrete. Thus, using LP combined with CC in ternary concrete will significantly improve the overall concrete properties.

The result of the XRD analysis (quantitative) analysis report for CC presented in Figure 3 b shows that calcined clay comprises up to 50 % quartz and other clay

minerals of the kaolinite group, making 36 % of the calcined clay. Kaolinite, dickite, and nacrite are clays belonging to the kaolin group, which are 1:1 clay made up of Si-O tetrahedral and Al-O(OH) octahedral sheets. Together they form a “composite kaolin layer” with distorted Si-O and Al-O distances.

Figure 4 gives the results of FTIR spectroscopic analysis for Calcined clay and Limestone powder, respectively, using transmission spectroscopy. Major assignments of the bands as compared to literature are Si-O-Si, Si-O Stretching, and H-O-H.

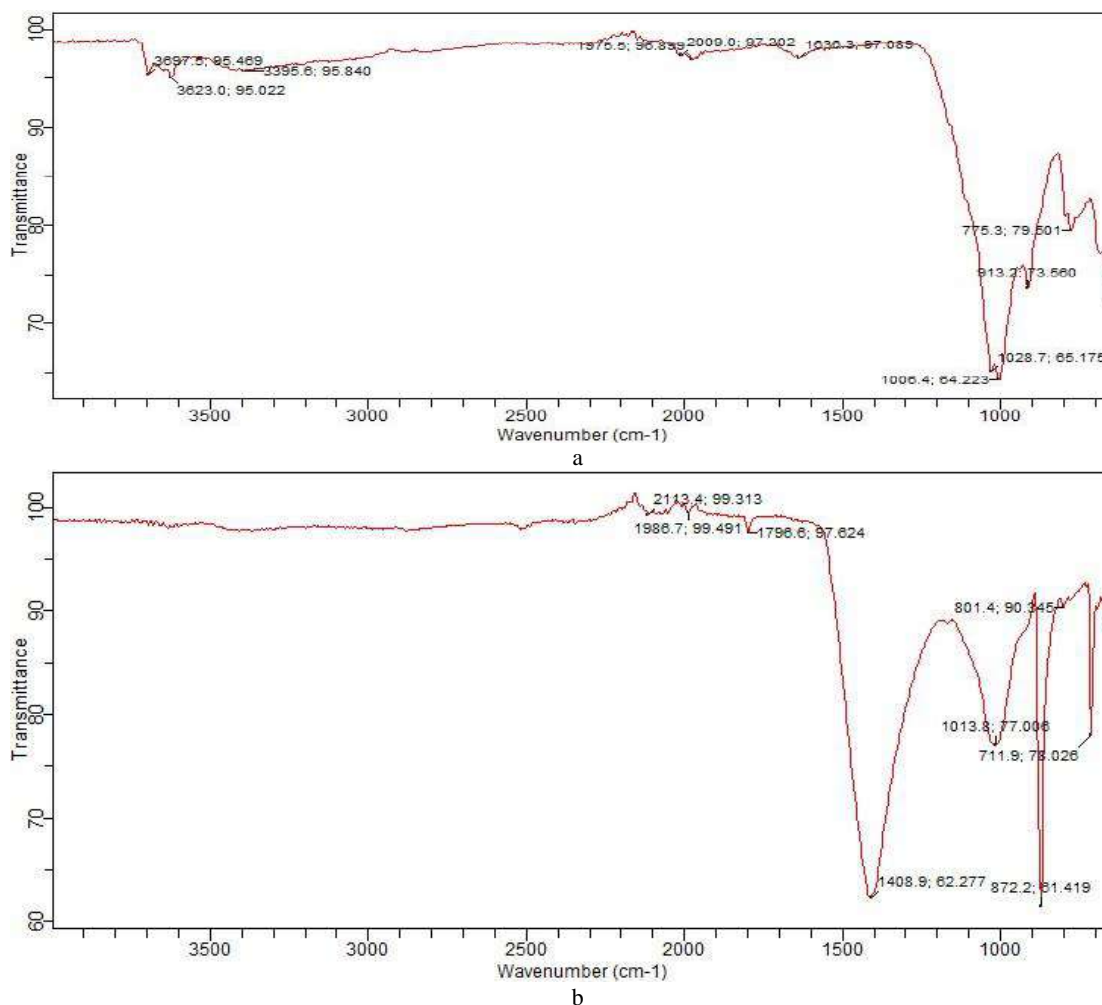


Figure 4 – FT IR Spectroscopic analysis for calcined clay (a) and limestone powder (b)

In the IR studies of the clays, Si-O stretching vibrations were observed at 773.3 cm^{-1} (775.3 cm^{-1}); 909.5 cm^{-1} (913.2 cm^{-1}), 998.9 cm^{-1} (1028.7 cm^{-1}), for clay (and calcined clay), showing the presence of quartz [35]. A strong band at $3,693.3\text{ cm}^{-1}$ ($3,697.5\text{ cm}^{-1}$) and $3,649.1\text{ cm}^{-1}$ ($3,623.0\text{ cm}^{-1}$) indicate the possibility of the hydroxyl linkage (Messaoud et al, 2018), while the interlayer hydrogen bonding is assigned by the characteristic band of $3,620.0\text{ cm}^{-1}$ [36]. Most of the bands present in the clays show the presence of the Kaolinites [35].

A study of the FTIR spectroscopic analysis presented in Figure 4 b shows a dissimilar pattern from the clays, with the characteristic bands of calcite near $1,408.9$, 872.2 , and 711.9 cm^{-1} . The IR peaks appearing at $1,793$ and $2,508\text{--}2,512\text{ cm}^{-1}$ are also an indication of the presence of calcite [37]. Other vibrations at $1,164.8$ and $1,035.6\text{ cm}^{-1}$ appearing as shoulders are also characteristic of quartz. quartz also gives two other characteristic bands at 800.3 and 781.0 cm^{-1} . The result agrees with [38] and correlates with the result of XRF and XRD analyses.

4.2 Fresh state SCC properties

The flowability of the SCC is measured using the slump flow and V-funnel tests, while the filling/ passing ability of the SCC was measured using the L-Box and J-ring tests, respectively. The results are presented in Table 2.

Table 2 – Flowability and filling/passing ability testing

Slump test/ V-funnel test		L-Box/ J-Ring	
T ₅₀₀ (s)	0.33	H ₁	8.4
Viscosity class	VS1/VF1	H ₂	7.81
T _{flow} (s)	4.20	H ₂ /H ₁	0.93
d ₁ (mm)	730	T ₂₀₀ (s)	0.36
d ₂ (mm)	730	T ₄₀₀ (s)	1.07
Slump flow (mm)	730	d _{Jx} (mm)	715
SCC class	SF2	d _{Jy} (mm)	715
V _{funnel} time (s)	5.84	SF J-Ring (mm)	715

The result of the flowability test indicates that the mix belongs to viscosity class VS1/ VF1 based on the result of the T₅₀₀ and V_{funnel} time tests, respectively, and the flowability characteristics are like [16] specification for SF2. [16] stipulates that, for proper filling ability $0.8 \leq H_2/H_1 \leq 1.0$; and this ratio holds for the ternary SCC. The mix also met the passing ability criterion and showed no signs of segregation or blockage. Compared with the provisions of [16], the sample shows no visible blockage due to the high workability. This result agrees with [29, 39, 40].

4.3 Durability characterization

4.3.1 Permeation properties (water absorption and sorptivity)

Figures 5, 6 gives the result of water absorption and sorptivity testing, respectively. The 24 hours water absorption after curing for 7, 14, 28, and 56 days given in Figure 5 show that the water absorption decreases with the age of the concrete because of the microstructural evolution related to the continuous cement hydration as well as the filling of the pore spaces by the very fine CC and LP filler.

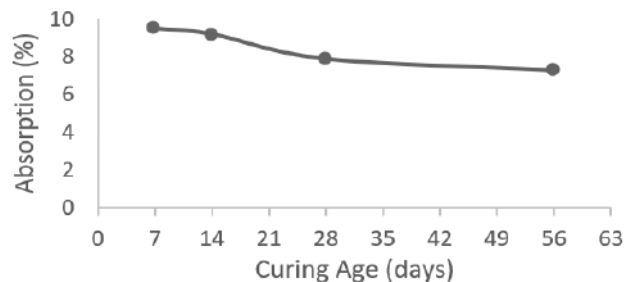


Figure 5 – Variation of water absorption with age

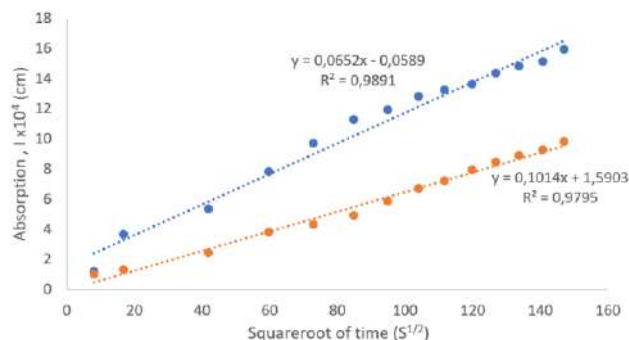


Figure 6 – Initial absorption rate vs square root of time

The incorporation of mixed LS and CC can make more dense interfacial transition zones between cement matrix and aggregates and refine the pore structures of the bulk [41]. Also, the rate at which water is absorbed by the discontinuous pore spaces in the concrete decreases with age. This is due to the pozzolanic reaction, which increases with age as the hydration of cement releases the CH for the pozzolanic reaction, the products thereof filling the pore spaces in the concrete [42, 13]. The primary reason for the better performance was attributed to the more compact and denser microstructure of the system, and the result agrees with [9, 13, 43].

The water sorptivity decreases with age, with the concrete showing better resistivity to capillary absorption at 58 days than at 28 days. What this means is that the concrete gets less porous as it ages. This is due to the filling of the pores by the products of cement hydration and the products of the pozzolanic reaction, and the additional filling up of the pore spaces by the filler effect of the LP [42]. Thus, the ternary blended SCC gets more durable as it ages. The pattern of the result agrees with [43, 46].

4.3.2 Strength Development

The compressive strength 7, 14, 28, and 56 days and the tensile strength at 7 and 28 days are plotted in Figure 7. Both the compressive and tensile strengths increased due to the pozzolanic reaction that starts after lime (CH) is released from cement hydration and the effect of the LP. In addition to its filler effect, LP also has a chemical effect; the calcium carbonate of the limestone powder can interact with the aluminate hydrates formed by the hydration reactions of Portland cement, leading to the stabilization of the ettringite and could increase the total volume of the hydration products, decrease the porosity of the concrete, and consequently increase its strength.

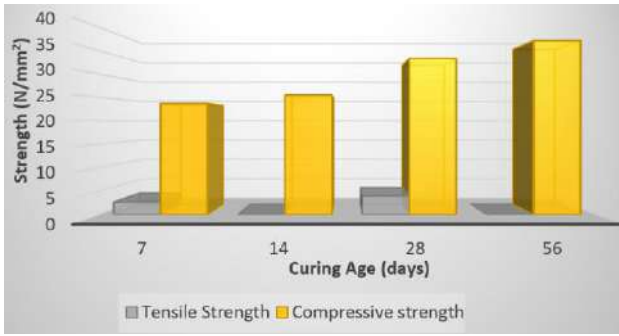


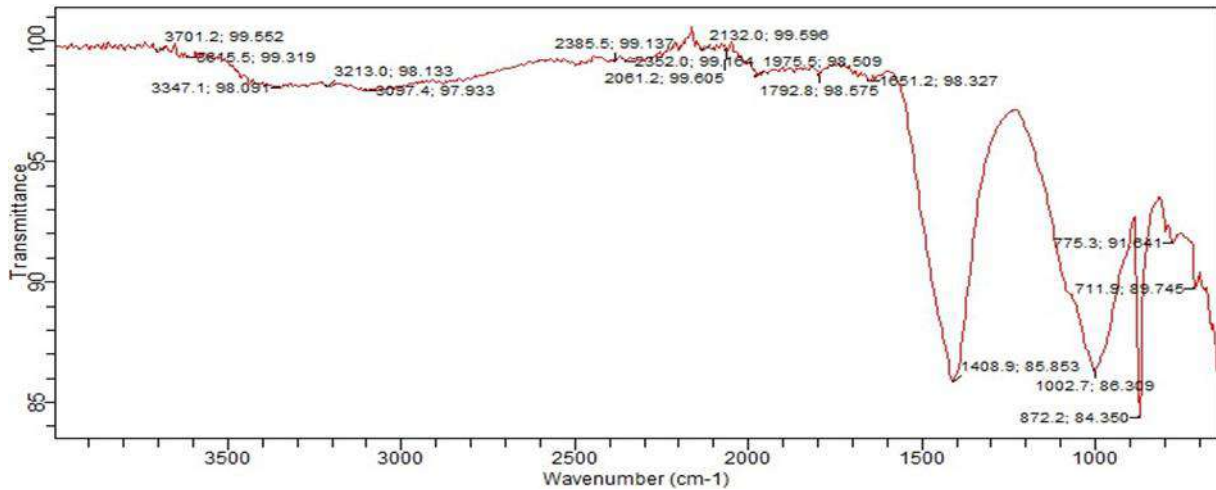
Figure 7 – Strength development of Ternary SCC

Limestone powder could also interact with the AFm and AFt hydration phases, leading to the formation of

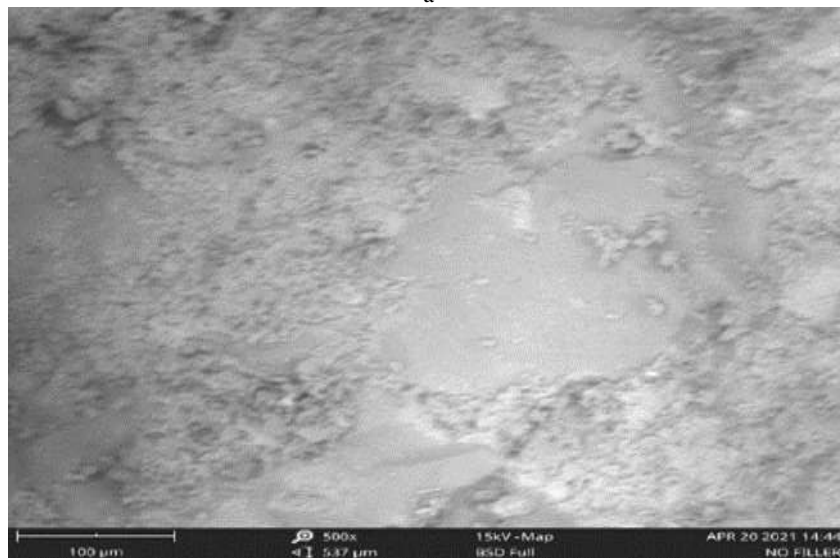
carboaluminates at the expense of monosulfate, thereby stabilizing the ettringite [39] reported that a ternary cementitious system containing 20 % LS filler and 30 % natural pozzolans exhibited improved early and long-term compressive and flexural strengths and enhanced durability against sulfate, acid, and chloride ion ingress. The trend in this result agrees with findings by [47, 48]. Thus, the pozzolanic properties of calcined clay and the filler effect of LP are combined to more significant advantage, aiding in the durability of SCC measured in terms of long-term strength development.

4.3.3 Microstructural Properties

The result of the microstructural investigation using FTIR Spectroscopy and SEM imaging of the ternary SCC is given in Figure 8.



a



b

Figure 8 – Microstructural analysis of SCC using FTIR (a) and SEM imaging (b)

It can be seen from Figure 8 that the microstructure of the ternary SCC has a dense microstructure, which is due to the combination of the pozzolanic reaction from the CC and the filler effect from the LP, hence the denser, more compact, and overall improved microstructure containing CSH, crystalline CH, and fewer voids than the other samples. The result of the

microstructural analysis is like research works by [49, 50].

The result of the mineralogical analysis from the SEM micrographs using EDS (Energy Distribution Spectroscopy), at x320 magnification is presented in Figure 9 and summarized in Table 3.

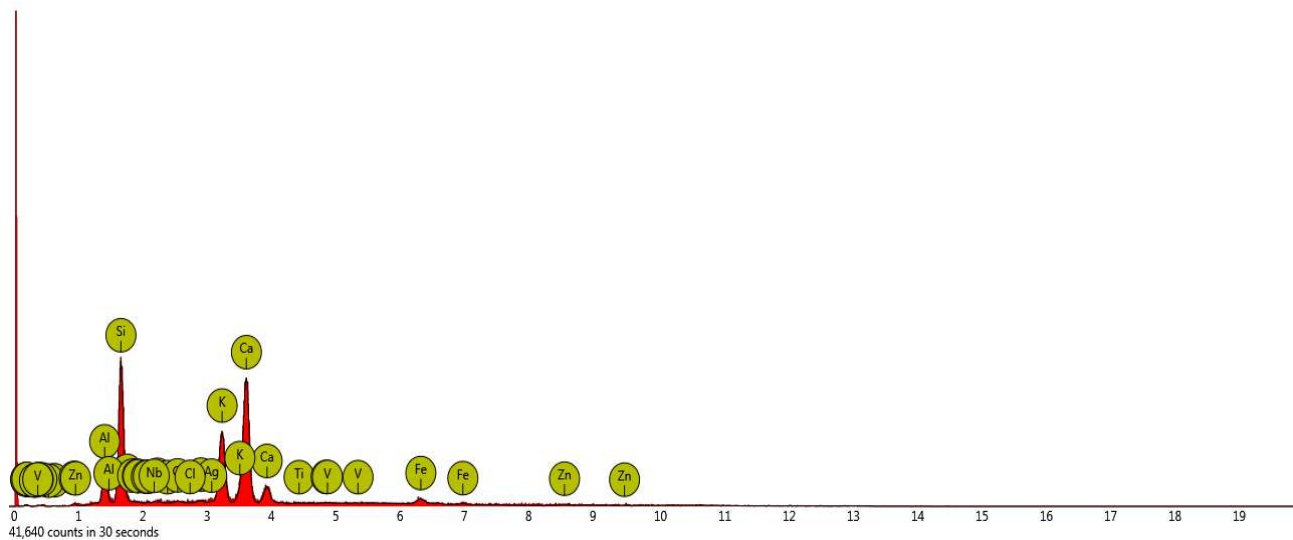


Figure 9 – Mineralogical analysis from SEM Micrographs

Table 3 – Resulting data of mineralogical analysis

Element Number	Element Symbol	Element Name	Atomic Conc.	Weight Conc.
20	Ca	Calcium	38.23	41.58
14	Si	Silicon	26.93	20.52
19	K	Potassium	18.93	20.08
13	Al	Aluminium	8.38	6.14
26	Fe	Iron	3.18	4.82
30	Zn	Zinc	1.53	2.72
47	Ag	Silver	0.47	1.37
39	Y	Yttrium	0.32	0.76
41	Nb	Niobium	0.18	0.46
16	S	Sulfur	0.51	0.44
17	Cl	Chlorine	0.39	0.38
23	V	Vanadium	0.18	0.24
22	Ti	Titanium	0.18	0.23
6	C	Carbon	0.48	0.16
15	P	Phosphorus	0.13	0.11

The ternary concrete has an even distribution of calcite, silicate, aluminate, and ferrite-based content due to the pozzolanic reaction and CC and LP filler effect, respectively.

5 Conclusions

In terms of recovery of permeation properties such as Sorptivity and water absorption, the durability performance of the ternary SCC is enhanced with the age of concrete. Also, the strength increased as the concrete ages due to the hydration of cement, the pozzolanic reaction, and the improved permeability because of the combined effect of the pozzolanic reaction and the filler effect, with a dense microstructure as well as better mineralogical distribution. Overall, the use of Calcined clay and Limestone powder blend in self-compacting concrete produces durable concrete.

References

- Promsawal, P., Chatveera, B., Sua-Iam, G., Makur, N. (2020). Properties of self-compacting prepared with ternary portland cement-high volume fly ash-calcium carbonate blends. *Case Studies in Construction Materials*, Vol. 13, pp. E1–E5, <https://doi.org/10.1016/j.cscm.2020.e00426>.
- Vahabi, A., Akbari Noghabi, K., Ramezani-pour, A. A. (2012). Application of biotechnology-based method for enhancing concrete properties. *Journal of Medical and Bioengineering*, Vol. 1(1), pp. 36–38, <https://doi.org/10.12720/jomb.1.1.36-38>.
- Gonsalves, G. M. (2011). *Bio-Concrete – A Sustainable Substitute for Concrete*. M.Sc Thesis, Polytechnic University of Catalonia, Spain.
- Aggarwal, P., Siddique, R., Aggarwal, Y., Gupta, M. S. (2008). Self compacting concrete - Procedure for mix design. *Leonardo Electronic Journal of Practices and Technology*, Vol. 7(1), pp 15–24.
- Deeb, R., Kulasegaram, S., Karihaloo, B. I. (2014). 3D modelling of the flow of self-compacting concrete with or without steel fibres, Part 1: Slump flow test, *Computational Particle Mechanics*, Vol. 1(4) pp 391–408, <https://doi.org/10.1007/s40571-014-0003-x>.
- Sabau, M., Onet, T., Pop, I. (2016). Experimental study on local bond stress-slip relationship in self-compacting concrete. *Materials and Structures*, Vol.49, pp. 3693–3711, <https://doi.org/10.1617/s11527-015-0749-5>.
- El Mir, A., Nehme, S. G., Nehme, K. (2016). Latest updates and developments on self-compacting concrete. *Journal of Silica Based and Composite Materials*, Vol. 68(3), pp. 80–84.
- Hu, J., Ledsinger, B., Kim, Y. (2016). Development of eco-efficient self consolidating concrete (Eco-SCC) with recycled concrete aggregates. *8th International RILEM Symposium on Self Compacting Concrete, Washington, USA, 15–18 May, 2016*, pp. 1033–1042.

9. Gruyaert, E., Van Tittelboom, K., Rahier, H., De Belie, N. (2015). Activation of Pozzolanic and latent-hydraulic reactions by alkalis in order to repair concrete cracks. *Journal of Materials in Civil Engineering*, Vol. 27(7), [http://dx.doi.org/10.1061/\(ASCE\)MT.1943-5533.0001162](http://dx.doi.org/10.1061/(ASCE)MT.1943-5533.0001162).
10. Xie, T. Y., Elchalakana, M., Mohamed Ali, M. S., Dong, M. H., Karrech, A., Li, G. (2018). Mechanical and durability properties of self-compacting concrete with blended binders. *Computers and Concrete*, Vol. 22(4), pp. 407–417, <https://doi.org/10.12989/cac.2018.22.4.407>.
11. Da-Silva, P. R., De-Britto, J. (2016). Durability performance of self-compacting concrete with binary and ternary mixes of fly ash and limestone filler. *Materials and Structures*, Vol. 49, pp. 2749–2766, <https://doi.org/10.1617/511527-015-0683-6>.
12. Simoes, B., Da Silva, P. R., Silva, R. V., Avila, Y., Forero, J. A. (2021). Ternary mixes of self-compacting concrete with fly ash and municipal solid waste incinerator bottom ash. *Applied Science*, Vol. 11(107), <https://doi.org/10.3390/app11010107>.
13. Kannan, V., Ganessan, K. (2014). Mechanical properties of self-compacting concrete with binary and ternary cementitious blends of metakaolin and fly ash. *Journal of the South African Institution of Civil Engineering*, Vol. 56(2), pp. 97–105.
14. Benli, A. (2019). Mechanical and durability properties of self-compacting mortars containing binary and ternary mixes of fly ash and silica fumes. *Structural Concrete*, Vol. 20(3), pp. 1096–1108, <https://doi.org/10.1002/suco.201800302>.
15. Danish, P., Ganesh, M. (2020). Durability properties of self-compacting concrete using different mineral powder additions in ternary blends. *Romanian Journal of Materials*, Vol 50(3), pp. 369–378.
16. EFNARC, The European Guidelines for Self-Compacting Concrete Specification, Production and Use, 2005. Retrieved from: www.efnarc.org.
17. BS EN 12390-8. Testing of Hardened Concrete. Self-Compacting Concrete; Slump Flow Test. *British Standards Institute, London, United Kingdom, 2010*.
18. BS EN 12390-9. Testing of Hardened Concrete. Self-Compacting Concrete; V-Funnel Test. *British Standards Institute, London, United Kingdom, 2010*.
19. BS EN 12390-12. Testing of Hardened Concrete. Self-Compacting Concrete; J-Ring Test. *British Standards Institute, London, United Kingdom, 2010*.
20. Rai, B., Kumar, S. and Satish, K. (2016).. Effect of quarry waste on self-compacting concrete containing binary cementitious blends of fly ash and cement. *Advances in Materials Science and Engineering*, Vol. 2016(7), <http://dx.doi.org/10.1155/2016/1326960>.
21. BS EN 206-9. Testing of Hardened Concrete. Self-Compacting Concrete, Additional Rules for SCC. *British Standards Institute, London, United Kingdom, 2010*.
22. BS EN 12390-10. Testing of Hardened Concrete. Self-Compacting Concrete; L-Box Test. *British Standards Institute, London, United Kingdom, 2010*.
23. ASTM C1585-13. Standard Test Method for Measurement of Rate of Absorption of Water by Hydraulic-Cement Concretes. *ASTM International, West Conshohocken, PA, 2013*. Retrieved from: www.astm.org.
24. BS 1881-122. Testing concrete. Method of Determination of Water Absorption, *British Standards Institute, London, United Kingdom, 2011*.
25. Davi, K., Aggarwal, P. Saini, B. (2020). Admixtures used in self-compacting concrete: A review. *Iran Journal of Science and Technology, Transactions of Civil Engineering*, Vol. 44, pp. 377–403, <https://doi.org/10.1007/s40996-019-00244-4>.
26. Xie, F., Zhang, C., Cai, D., Ruan, J. (2020). Comparative study on the mechanical strength of SAP internally cured concrete. *Frontiers in Materials*, Vol. 2020, <https://doi.org/10.3389/fmats.2020.588130>.
27. BS EN 12390-6. Testing of Hardened Concrete. Tensile Splitting Strength Test of Specimens. *British Standards Institute, London, United Kingdom, 2010*.
28. ASTM C 618. Standard Specification for Coal, Fly Ash and Raw or Calcined Natural Pozzolan. *ASTM International, West Conshohocken, PA, 2013*. Retrieved from: www.astm.org.
29. Grzeszczyk, S., Podkowa, P. (2009). The effects of limestone filler on the properties of self compacting concrete. *Annual Transactions of the Nordic Rheology Society*, Vol. 17, pp 1–7.
30. Michel, F., Courard, L. (2012). Natural limestone filler: Physical and Chemical properties with regard to cement based materials properties. *International Congress on Durability of Concrete, Belgium*, pp. 1–12. Retrieved from: https://orbi.uliege.be/bitstream/2268/116540/1/ICDC2012-D-11-00206_ULg_fillers.pdf.
31. Leeuwen, R. V., Kim, Y., Sriraman, V. (2016). The effect of limestone powder particle size on the mechanical properties and the lifecycle assessment of concrete. *Journal of Civil Engineering Research*, Vol. 6(4), pp. 104–113, <https://doi.org/10.5923/j.jce.20160604.03>.
32. Ryu, H., Kim, S., Kim, W., Lim, S., Park, W. (2019). Properties of cement mortar using limestone sludge powder modified with recycled acetic acid. *Sustainability*, Vol. 11(3), <https://doi.org/10.3390/su11030879>.
33. Liu, S., Yan, P. (2010). Effect of limestone powder on microstructure of concrete. *Journal of Wuhan University of Technology, Material Science Edition*, Vol. 25(2), pp 328–331, <https://doi.org/10.1007/s11595-010-2328-5>.
34. Kepniak, M., Woyciechowski, P., Franus, W. (2017). Chemical and physical properties of limestone powder as a partial micro-filler of polymer composites. *Achieves of Civil Engineering*, Vol. 43(2), <https://doi.org/10.1515/ace-2017-0017>.
35. Witkowski, H., Koniorczyk, M. (2018). New sampling method to improve the reliability of FTIR analysis for self-compacting concrete. *Construction and Building Materials*, Vol. 172, pp. 196–203, <https://doi.org/10.1016/j.conbuildmat.2018.03.216>.

36. Messaoud, I. B., Hamdi, N., Srasra, E. (2018). Physicochemical characterization of geopolymer binders and foams made from Tunisian clay, *Advances in Material Science and Engineering*, Vol. 2018, pp. 1–8, <https://doi.org/10.1155/2018/9392743>.
37. Gunasekaran, S., Anbalagan, G. (2007). Spectroscopic characterization of natural calcite minerals. *Spectrochimica Acta Part A: Molecular and Biomolecular Spectroscopy*, Vol. 68(3), pp. 656–664, <https://doi.org/10.1016/j.saa.2006.12.043>.
38. Sdiri, A.; Higashi; T., Hatta, T., Jamoussi, F., Tase, N. (2010). Mineralogical and spectroscopic characterization, and potential environmental use of limestone from the Abiod formation, Tunisia. *Environmental Earth Sciences*, Vol. 61(6), pp. 1275–1287, <https://doi.org/10.1007/s12665-010-0450-5>.
39. Gudisa, H., Dinku, K. (2010). The use of limestone powder as an alternative cement replacement material; An experimental study, *Journal of EAA*, Vol. 27, pp. 33–43.
40. Ryu, H., Kim, S., Kim, W., Lim, S., Park, W. (2019). Properties of cement mortar using limestone sludge powder modified with recycled acetic acid. *Sustainability*, Vol. 11(3), <https://doi.org/10.3390/su11030879>.
41. Guo, Z., Zhang, J., Jiang, T., Chen, C., Bo, R., Sun, Y. (2020). Development of sustainable self-compacting concrete using recycled concrete aggregate and fly ash, slag, silica fume. *European Journal of Environmental and Civil Engineering*, Vol. 2020, <https://doi.org/10.1080/19648189.2020.1715847>.
42. Jin, H. (2017). Late-age properties of concrete with different binders cured under 45°C, at early age. *Advances in Materials Science and Engineering*, Vol. 1, <https://doi.org/10.1155/2017/8425718>.
43. Dhandapani, Y., Vignish, K., Raja, T., Santhana, M. (2018). Development of the microstructure in LC³ systems and its effects on cement properties. *Martirena, et al (Eds): Calcined Clays for Sustainable Concrete, RILEM Bookseries 16*, https://doi.org/10.1007/978-94-024-1207-9_21.
44. Santhanam, M., Dhandapani, Y., Gettu, R., Pillai, R. (2020). Perspectives on durability of blended systems with calcined clay and limestone. *Bishnoi S. (eds) Calcined Clays for Sustainable Concrete. Springer, RILEM Book Series*, Vol 25, https://doi.org/10.1007/978-981-15-2806-4_65.
45. Pillai, R. G., Gettu, R., Santhanam, M. (2020). Use of supplementary cementitious materials (SCMs) in reinforced concrete systems – Benefits and limitations, *Revista ALCONPAT*, Vol. 10(2), pp. 147–164, <https://doi.org/10.21041/ra.v10i2.477>.
46. Pereira de Oliveira, L. A., Gomes, J. P., Pereira, C. N. A. (2006). Study of sorptivity of self-compacting concrete with mineral additives. *Journal of Civil Engineering and Management*, Vol. 12(3), pp. 215–220, <https://doi.org/10.1080/13923730.2006.9636395>.
47. Khan, M. S. H., Nguyen, Q. D., Castel, A. (2019). Performance of limestone calcined clay blended cement-based concrete against carbonation. *Advances in Cement Research*, Vol. 6, pp. 1–36, <https://doi.org/10.1680/jadcr.18.00172>.
48. Yu, J., Wu, H., Mishra, D. K., Li, G., Leung, C. Ky. (2021). Compressive strength and environmental impact of sustainable blended cement with high dosage limestone and calcined clay (LC²). *Journal of Cleaner Production*, Vol. 278, pp. 1–11, <https://doi.org/10.1016/j.jdepro.2020.123616>.
49. Jo, B. W., Sikandar, M. A., Chakraborty, S., Zafar Baloch, Z. (2017). Strength and durability assessment of portland cement mortars formulated from hydrogen-rich water. *Hindawi Advances in Materials Science and Engineering*, Vol. 2017, <https://doi.org/10.1155/2017/2526130>.
50. Tiwari, A. K., Chowdhury, S. (2016). Relative evaluation of performance of limestone calcined clay cement compared with Portland Pozzolana cement. *Journal of Asian Concrete Federation*, Vol. 2(2), pp. 110–116, <https://doi.org/10.187.04/act/2016.12.2.2.110>.



Novokhat O. A., Vozniuk V. T., Hritsiuk H. I., Lysii V. (2021). Determination of kinetic regularities of the process of drying perlite by radiation method. *Journal of Engineering Sciences*, Vol. 8(1), pp. C11–C17, doi: 10.21272/jes.2021.8(1).c2

Determination of Kinetic Regularities of the Process of Drying Perlite by Radiation Method

Novokhat O. A.^{1*}[0000-0002-1198-6675], Vozniuk V. T.², Hritsiuk H. I.¹, Lysii V.¹

¹ National Technical University of Ukraine “Igor Sikorsky Kyiv Polytechnic Institute”, 37, Peremohy ave., 03056, Kyiv, Ukraine;

² Archer-Daniels-Midland Company, Spycck GmbH – Werk Straubing, 23, Europaring, 94315, Straubing, Germany

Article info:

Received: April 2, 2021
 The final version received: June 17, 2021
 Accepted for publication: June 22, 2021

*Corresponding email:

novokhatoleh@gmail.com

Abstract. The actual methods of perlite drying are established. The radiation method of perlite drying is offered. A description of an experimental installation for drying perlite by the radiation method is given. The kinetic regularities of this method are established. Graphical dependences of moisture content on drying time, perlite surface temperature on drying time, and drying speed of perlite on drying time are described. The influence of the initial moisture content of perlite, the value of the heat flux density from the infrared emitter, the thickness of the perlite layer, and the value of the perlite fraction were determined. The analysis on the resulted graphic dependences is made. A drying installation with a combined drying method is proposed. The general conclusions concerning the expediency of a radiation method of drying perlite are made.

Keywords: perlite drying, drying time, radiation drying method, infrared radiation, drying curves.

1 Introduction

Perlite is a rock of volcanic origin used in agriculture, metallurgy, medicine, energy, construction, and other industries.

Perlite by chemical composition is a natural structure of oxides [1]. Depending on the grain size, expanded perlite is divided into the following fractions: fine sand, coarse sand, fine gravel, and coarse gravel.

Bulk materials, including perlite, are dried in drum dryers, in dryers with fluidized beds, vibrating, radiation dryers, and others. However, the most common methods of drying perlite are drying in drum dryers and fluidized bed machines. However, with such drying, there is a large percentage of dusty perlite. Moreover, dust formation can degrade the quality of the final product and complicate cleaning gaseous emissions. Therefore, there is a need to modernize the existing equipment and search for new methods and techniques of drying, which will consume less energy and preserve the granular structure of perlite.

Expanded perlite has found the greatest application. It is obtained by holding in furnaces at certain temperatures [2]. The unique microstructure of expanded perlite has a positive effect on its properties. Expanded perlite is lightweight and is an extremely low bulk density material. Also, expanded perlite has a low thermal conductivity [3]. It has high heat and sound insulation properties and fire

resistance, it is inorganic, chemically inert, and its properties are unchanged over time [4].

A promising method of drying bulk materials is the radiation method. After all, this method does not require active movement of the material and reduces the likelihood of abrasion of the material into dust. Because for intensification of radiation drying a slight blowing and mixing of the bulk material is enough.

It is obvious that the expediency of drying the material by radiation method depends primarily on the ability of the material to absorb infrared radiation and the lack of resistance on the surface of the material for the diffusion of moisture into the environment.

Since there is no data in the literature on the drying of perlite by radiation method, it is advisable to conduct appropriate experimental studies.

Therefore, the aim of the study is to determine the kinetic patterns and basic parameters of the process of drying perlite by radiation method.

The object of research is the process of drying perlite by radiation method.

The subject of the research is the kinetic regularities of the process of drying perlite by radiation method and determination of the main process parameters necessary for intensification of the drying process.

2 Literature Review

To achieve the required final dryness of perlite, it must be dried. One of the most common methods of drying perlite is drying with a hot gaseous coolant, in particular in a fluidized bed. Therefore, in the literature, there is usually information on the drying of perlite by this method [5].

Scientists have also considered less common methods of drying perlite, for example, using microwaves [6]. However, the kinetic patterns of perlite by the radiation method were not detected.

The radiation method of drying the material is quite common and in some cases is highly effective. Thus, in particular, the radiation drying method is suitable for drying such fibrous materials as paper [7], as well as granular bulk materials, such as zeolite [8]. Therefore, it is expedient to study the kinetic regularities of drying perlite by the radiation method to determine the effectiveness of this method.

The preliminary mathematical modeling of the perlite drying process by the radiation method was described by the authors in the article [9].

3 Research Methodology

3.1 Experimental installation

To study the process of drying perlite by radiation method, an experimental installation was used, shown in Figure 1. This installation allows obtaining sufficient accuracy the results of drying materials by radiation method [10].

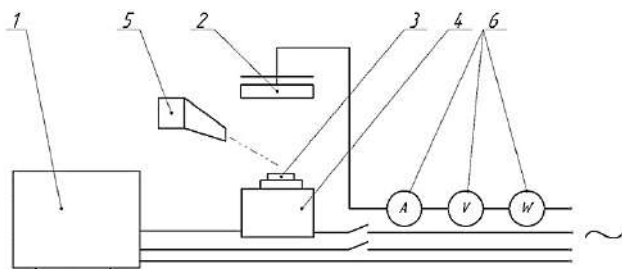


Figure 1 – Scheme of the experimental installation for drying perlite by radiation method: 1 – personal computer (PC); 2 – infrared emitter; 3 – platforms for placing perlite; 4 – electronic scales; 5 – pyrometer; 6 – wattmeter, ammeter, voltmeter

The experimental installation consists of scales that can measure the current weight of the perlite test specimens at a resolution of 1 mg. Mass values with a frequency of 3 times per second are sent to the computer with the ability to record them. Subsequently, the data were processed using Excel software.

The surface temperature of perlite was measured non-contact with a pyrometer. The measurement accuracy – 1 °C.

An electric ceramic infrared emitter was used as a heater. The rated electric power of the heater is 1 kW.

An ammeter and a voltmeter were used to determine the current and voltage. With the help of the obtained values,

the actual value of the electric power of the infrared emitter was obtained.

A reflector is installed on the reverse side to reduce heat loss from the infrared emitter to the environment.

Experimental samples of perlite during the experiment were placed on the vapor-permeable surface of the platforms, which was located on the scales.

3.2 The method of the experiment

Perlite of Ukrainian origin of three different factions was used as experimental samples. The average particle sizes of perlite by fractions were 0.4 mm, 0.7 mm, and 1.3 mm.

Before the experiment, perlite was kept for some time in desiccators. This made it possible to saturate the perlite with moisture to obtain a constant value of moisture content.

Perlite was placed on the vapor-permeable surface evenly without additional sealing.

Before drying, the infrared emitter was kept on until it was fully heated. The final surface temperature of the emitter became constant. Due to this, the heat flow from the surface of the radiator was stabilized.

The change in the magnitude of the heat flux from the infrared emitter to the surface of perlite occurred due to the change in the distance between them. In all cases, the area of the emitter significantly exceeded the area of the prototypes. The values of the heat flux density from the radiator to the perlite surface were about 4 kW/m², 7 kW/m², and 14 kW/m².

The main parameters of the environment were determined using a thermometer and hygrometer.

Before the experiment, the following values were recorded: ambient temperature and humidity, the temperature of the working surface of the infrared emitter, current, and voltage of the electrical network to which the emitter is connected.

During the experiment, the following current values were recorded: perlite mass, perlite surface temperature, time.

The experiments were performed before the onset of a constant value of the perlite mass for some time.

To determine the effect of a particular parameter on perlite's drying kinetics, all other process parameters remained constant.

4 Results

4.1 Experimental kinetic regularities of perlite drying by radiation method

The generalized results of the experimental researches are presented in the form of graphic dependences of moisture content of perlite on drying time $u = f(\tau)$ (drying curves), the surface temperature of perlite from drying time $t = f(\tau)$, and drying speed on moisture content $du/d\tau = f(u)$.

The kinetic regularities of the process of drying perlite by radiation method at different heat flux densities are obtained. The corresponding drying curves are shown in Figure 2.

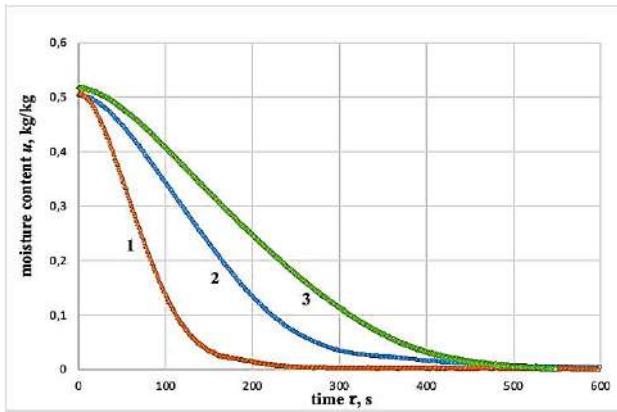


Figure 2 – Graphic dependence of the moisture content of perlite on the drying time at different heat flux densities: 1 – 14 kW/m²; 2 – 7 kW/m²; 3 – 4 kW/m²

The obtained perlite drying curves are similar to the typical drying curves of capillary-porous bodies.

It is established that with increasing the heat flux density, the drying rate of perlite increases, in particular in the heating period and the first period (constant speed period). As a result, the drying time of perlite is reduced. This is due to the increase in the amount of heat released in the volume of perlite. However, the decrease in the time the material reaches equilibrium is not proportional to the increase in heat flux density. In the second period of perlite drying, the intensity of heat supply does not limit the drying rate. This confirms the statement about the inexpediency of overdrying the material. Also, at the end of drying the perlite, it may be advisable to reduce the heat flux or conduct a periodic supply of heat energy.

According to the obtained experimental data, a graphical dependence of the drying rate on the moisture content is constructed (Figure 3).

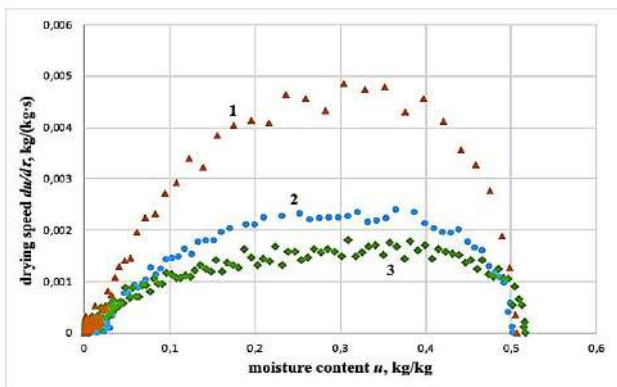


Figure 3 – Graphic dependence of the drying rate of perlite on the moisture content of perlite at different heat flux densities: 1 – 14 kW/m²; 2 – 7 kW/m²; 3 – 4 kW/m²

According to Figure 3, the acceleration of drying during the heating period is more intense at a higher heat flux density. This is due to the faster heating of the material to the temperature of a wet-bulb thermometer.

Also, this graphical dependence confirms the above conclusions on the drying curves.

Graphical dependences of perlite surface temperature at the heat flux density change are constructed (Figure 4).

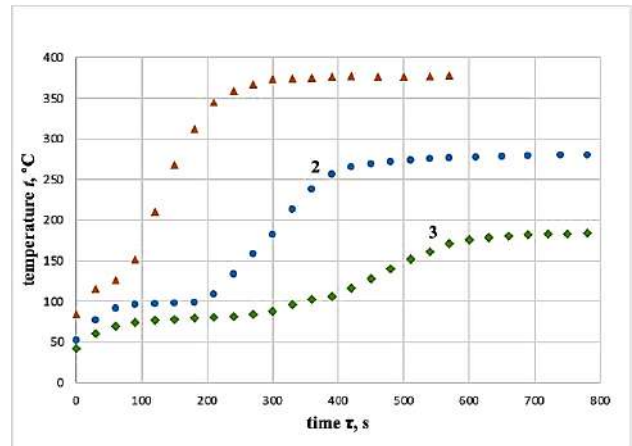


Figure 4 – Graphic dependence of the surface temperature of perlite on the drying time of perlite at different heat flux densities: 1 – 14 kW/m²; 2 – 7 kW/m²; 3 – 4 kW/m²

According to the obtained data with increasing heat flux, the intensity of temperature increase increases during the heating period, the first drying period. In the second period of perlite drying, the intensity of temperature rise occurs until the moisture content of perlite approaches the equilibrium value.

Also, with increasing the heat flux density, the temperature of the first drying period and the equilibrium temperature of perlite increase.

At small values of heat density (4 kW/m² and 8 kW/m²) flow, the surface temperature of perlite in the first drying period is close to constant. However, when the heat flux density increases to 14 kW/m², an increase in temperature can be observed in the first period of perlite drying. This indicates that under such conditions, the drying rate is not limited by the rate of supply of heat to the perlite.

The influence of the initial moisture content of perlite on the drying kinetics was also established.

Figure 5 shows the graphical dependence of the moisture content of perlite on the drying time.

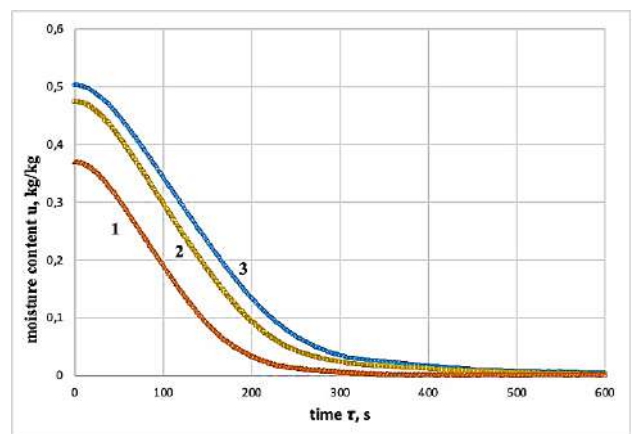


Figure 5 – Graphical dependence of the moisture content of perlite on the drying time at different initial moisture content: 1 – 0,37 kg/kg; 2 – 0,47 kg/kg; 3 – 0,5 kg/kg

The drying curves of perlite in the heating period and the first drying period are parallel. This indicates that the

drying rate of perlite does not depend on the initial moisture content.

With the increasing value of the initial moisture content, the amount of moisture in the material increases. This increases the drying time of perlite. However, in the second period of drying perlite, a phenomenon is observed when for perlite with lower moisture content, the drying time decreases disproportionately. This is due to the removal of adsorption-bound moisture.

Graphical dependences of the drying rate on the moisture content with changes in the initial moisture content are shown in Figure 6.

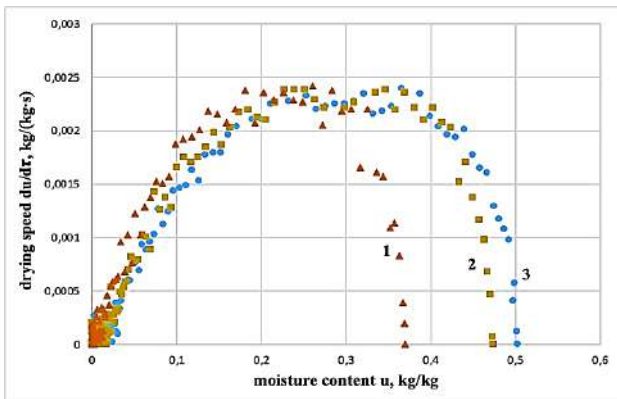


Figure 6 – Graphic dependence of the drying rate of perlite on the moisture content of perlite at different initial moisture content: 1 – 0.37 kg/kg; 2 – 0.47 kg/kg; 3 – 0.50 kg/kg

The obtained graphical dependencies (Figure 6) are parallel between the heating and the first drying periods. This indicates the exact nature of the drying process in these periods.

Graphical dependences of perlite surface temperature on drying time at different initial moisture content are constructed (Figure 7).

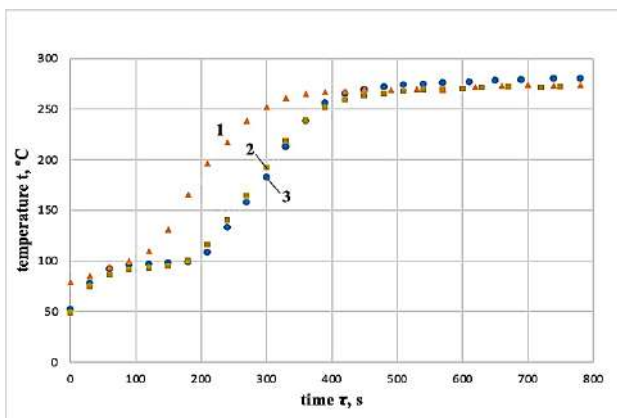


Figure 7 – Graphical dependence of the drying rate of perlite on the moisture content of perlite at different initial moisture content: 1 – 0.37 kg/kg; 2 – 0.47 kg/kg; 3 – 0.50 kg/kg

The influence of the initial moisture content on the temperature by drying periods and the intensity of temperature rise was not detected. Thus, the temperature of the first drying period and the equilibrium temperature

of perlite are the same for different initial moisture content. And the graphical dependences at the beginning of the second period of perlite drying are parallel.

The influence of the thickness of the perlite layer on the kinetic regularities of its drying was also established.

Graphical dependences of the moisture content of perlite on the drying time for different thicknesses of the perlite layer are shown in Figure 8.

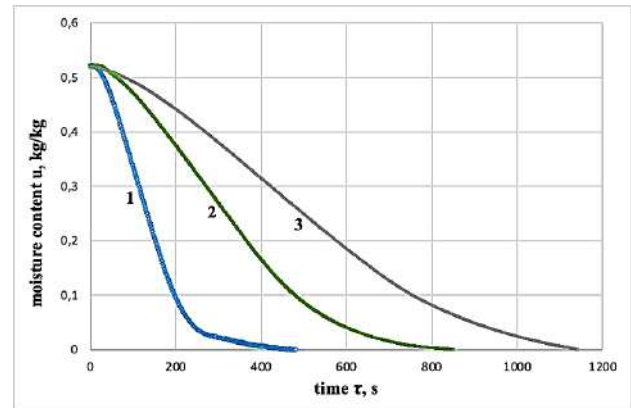


Figure 8 – Graphical dependence of the moisture content of perlite on the drying time at different thicknesses of the perlite layer: 1 – 1.5 mm; 2 – 3.0 mm; 3 – 5.5 mm

As the thickness of the perlite layer increases, the amount of moisture in it increases. The distance for the passage of moisture from the lower layers of perlite to the surface and hydraulic resistance also increases. And at the same heat flux density, its share concerning the total mass of perlite decreases. All this leads to a decrease in the intensity of moisture removal from perlite (drying rate) and, accordingly, increases perlite's heating and drying time.

The drying curves confirm this in Figure 8 and the dependence of the drying rate on the moisture content (Figure 9). Obviously, with increasing the layer of perlite, the drying rate decreases, particularly in the heating periods and the first period. Accordingly, as the thickness of the perlite layer increases, the total drying time increases.

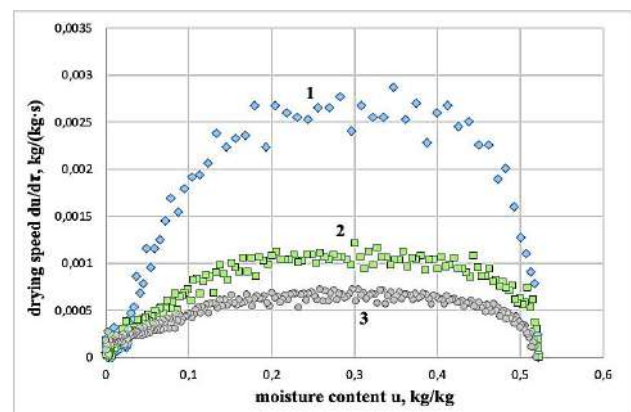


Figure 9 – Graphical dependence of the drying rate of perlite on the moisture content at different thicknesses of the perlite layer: 1 – 1.5 mm; 2 – 3.0 mm; 3 – 5.5 mm

As the thickness of the perlite layer increases, a slight increase in the temperature of the first drying period can be observed (Figure 10).

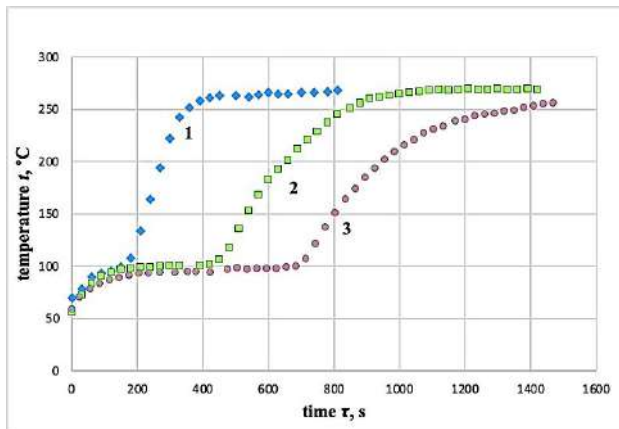


Figure 10 – Graphic dependence of the temperature of the perlite surface on the drying time for different thicknesses of the perlite layer: 1 – 1.5 mm; 2 – 3.0 mm; 3 – 5.5 mm

Also, an increase in the thickness of the perlite layer leads to a lower intensity of temperature rise at the beginning of the second drying period. This can be caused by faster heating of the inner layers of perlite at its insignificant thickness. This leads to a decrease in the thermal gradient and, accordingly, the amount of heat transferred into the material by thermal conductivity.

Experiments were also conducted to determine the effect of perlite particle size (fraction size) on the drying intensity. During the experiment, the perlite layer was made as minimal as possible.

Drying curves for different fractions are shown in Figure 11.

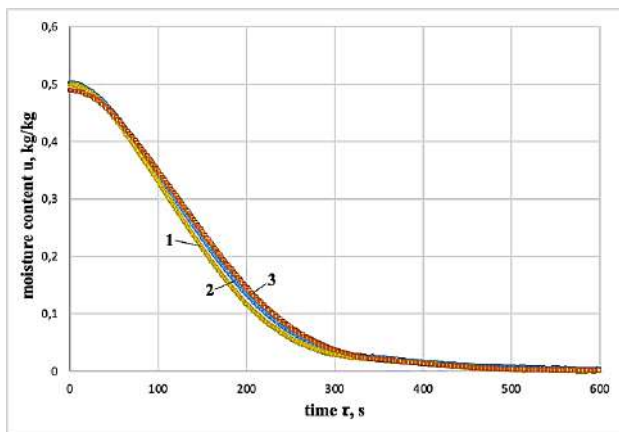


Figure 11 – Graphic dependence of the moisture content of perlite on the drying time for different fractions (particle size) and the minimum layer: 1 – fraction No. 2 (0.4 mm); 2 – fraction No. 1 (0.7 mm); 3 – fraction No. 3 (1.3 mm)

Since the fractions have different particle sizes of perlite, and the experiment was performed with the minimum possible layer of perlite, the size is effective. The layer of perlite was also different. As the perlite layer increases, as previously found, the drying rate decreases.

However, as the particle size increases, the porosity will be greater. In this case, the hydraulic resistance for the passage of surface moisture from particles and vapor to the surface decreases. There is a counteraction of various factors that simultaneously affect the intensity of drying in different ways.

Figure 11 shows that the drying curves almost overlap. A slight discrepancy can be caused by both the error of the experiment and various influences of factors.

Due to the dependence of the drying rate on the moisture content, no trend was found (Figure 12).

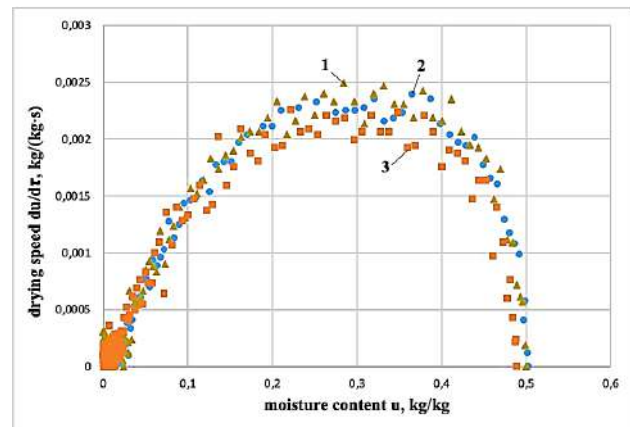


Figure 12 – Graphic dependence of the drying rate of perlite on the moisture content for different fractions (particle size) and the minimum layer: 1 – fraction No. 2 (0.4 mm); 2 – fraction No. 1 (0.7 mm); 3 – fraction No. 3 (1.3 mm)

As can be seen from Figure 13, the average speeds have almost no difference.

A similar situation is observed with the dependence of the surface temperature of perlite on the drying time (Figure 13).

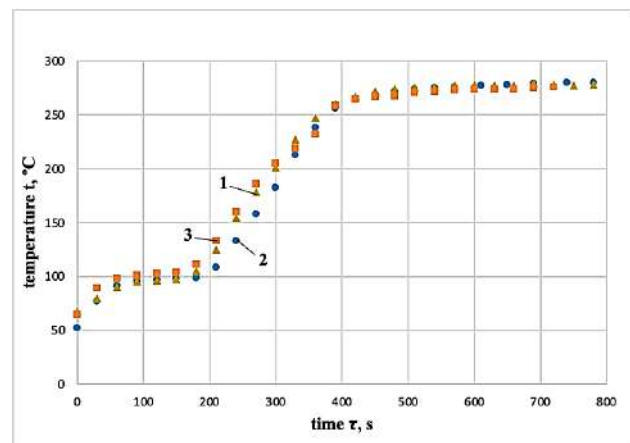


Figure 13 – Graphic dependence of the temperature of the perlite surface on the drying time for different fractions (particle size) and the minimum layer: 1 – fraction No. 2 (0.4 mm); 2 – fraction No. 1 (0.7 mm); 3 – fraction No. 3 (1.3 mm)

4.2 Design development

Based on the analysis of experimental data, the design scheme of a dryer for drying perlite was proposed (Figure 14).

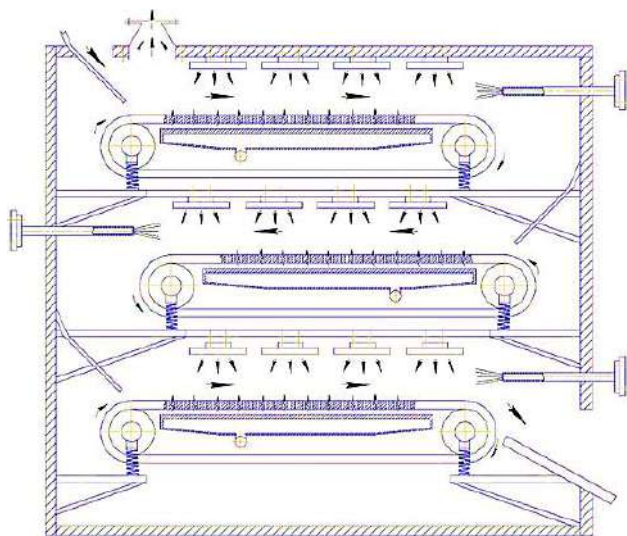


Figure 14 – The design scheme of the developed dryer

This dryer combines radiation, filtration, and convective drying methods. For additional intensification of drying due to active renewal of the drying surface, perlite vibrates during pouring and spills from belt to belt.

The dryer works as follows. Perlite enters the belt dryer with the perforated belt. Above the belt are infrared emitters aimed at it (radiation component of drying).

At the bottom of the perforated belt with perlite is fed hot gaseous coolant passing through them. Thus, filtration drying of perlite is realized.

Above the surface of the perlite, the countercurrent is blowing hot gaseous coolant. This increases the heat load on the perlite and helps to remove moist air from the drying area. This makes it possible to implement the convective component of drying.

This dryer may have a system of partial recirculation of a hot gaseous coolant to reduce heat loss.

To intensify drying, the belt dryer is mounted with a vibratory drive, which increases the oscillations of perlite and its mixing. Perlite is also mixed during pouring from one belt to another. In addition, it reduces the overall length of the dryer.

5 Conclusions

The kinetic regularities of the process of drying perlite by the radiation method are similar to the regularities of drying of capillary-porous bodies.

During the heating period, the drying rate and the temperature of the perlite surface increase. In the first period, the drying rate is constant and maximum. The temperature is also constant at low heat flux. However, with a significant increase in the heat flux, the drying process ceases to be limited by the speed of heat supply to perlite. Therefore, the excess heat is absorbed by perlite, and its temperature begins to rise.

In the second drying period, the drying rate of perlite begins to decrease sharply, and then the intensity of the decrease in moisture content decreases. At the beginning of the second period of perlite drying, the surface temperature begins to increase sharply, and then the intensity of temperature increase decreases.

At equilibrium, the value of the final moisture content and the surface temperature remains unchanged. And during the experiment, while drying, the values of temperature and moisture content can fluctuate amplitude within the error of the experiment.

The analysis of experimental data showed that in the period of heating and the first period of perlite drying, it is expedient to increase the value of heat flux to the surface of perlite. This will increase the intensity of moisture removal and reduce the drying time. However, in the second period of drying perlite, the increase in heat flux to a lesser extent affects the intensity of moisture removal. Therefore, it may be appropriate in the second drying period of perlite to reduce the heat flux or use intermittent drying.

Also, with increasing the heat flux, the temperature of perlite can increase significantly, particularly in the second drying period. This can degrade the qualitative indicators of perlite.

The obtained kinetic regularities of the process of drying perlite by radiation method make it possible to assess the nature of the process, which is necessary when choosing the method of drying and design of the drying installation.

In general, the study of drying perlite by radiation method has shown that it is effective. It has been suggested that this method of drying perlite can be intensified by combining it with active mixing of perlite and blowing hot coolant over its surface. Also promising is the study of perlite drying combining radiation and filtration drying methods.

References

1. Demirçivi, P., Gülhayat N. S. (2018). Comparative study of modified expanded perlite with hexadecyltrimethylammonium-bromide and gallic acid for boron adsorption. *Journal of Molecular Liquids*, Vol. 254, pp. 383–390, doi: 10.1016/j.molliq.2018.01.116.
2. Alekseeva, L. V. (2014). Features of energy-saving technology to produce expanded perlite for complex application in construction. *Building Materials and Products*, Vol. 4, pp. 52–55. Available online: http://nbuv.gov.ua/UJRN/smii_2014_4_24.

3. Ağbulut, Ü. (2018). Mathematical calculation and experimental investigation of expanded perlite based heat insulation materials' thermal conductivity values. *Journal of Thermal Engineering*, Vol. 4(5), pp. 2274-2286, doi:10.18186/thermal.438482.
4. Angelopoulos, P. M., Maliachova, C., Papakonstantinou, K. K., Taxiarchou, M., Diplas, S. (2016). Structural and physical characteristics of fine perlite expanded with a novel method in a vertical electric furnace. *Mineral Processing and Extractive Metallurgy*, Vol. 125(2), pp. 71–80, doi: 10.1080/03719553.2016.1156244.
5. Stepanyuk, A. R., Donets, O. Ye., Griffen, Yu. O., Malyuga, A. S. (2010). Modeling of the process of obtaining expanded perlite. *ONAFTs' Scientific Journals*, Vol. 37, pp. 143–145.
6. Skubic, B., Lakner, M., Plazl, I. (2015). Microwave drying of expanded perlite insulation board. *Industrial and Engineering Chemistry Research*, Vol. 51(8), pp. 3314–3321, doi: 10.1021/ie201790w.
7. Marchevsky, V., Novokhat, O. (2015). Kinetics of corrugated board flute drying with the use of infrared radiation. *The Advanced Science Journal*, Vol. 6, pp. 69–72.
8. Marchevsky, V., Novokhat, O., & Margarian, A. (2018). Analysis of the research results of the zeolite drying process. *Technology Audit and Production Reserves*, Vol. 1(3(45)), pp. 21–23, doi:10.15587/2312-8372.2019.163361.
9. Novokhat O., Hrytsyuk G. (2019). Modeling of the perlite drying process by radiation method. *Scientific Letters of Academic Society of Michal Baludansky*, Vol. 7(6B), pp. 28–31.
10. Karvatskii A., Marchevsky V., Novokhat O. (2017). Numerical modelling of physical fields in the process of drying of paper for corrugating by the infrared radiation. *Eastern-Europen Journal of Enterprise Technologies*, Vol. 2/5(86), pp. 14–22.



Chernobrovchenko V. S., Dyadyura K. O., Balynskyi M., Panda A. (2021). Influence of technological manufacturing conditions on the porosity of calcium-phosphate scaffolds. *Journal of Engineering Sciences*, Vol. 8(1), pp. C18–C28, doi: 10.21272/jes.2021.8(1).c3

Influence of Technological Manufacturing Conditions on the Porosity of Calcium-Phosphate Scaffolds

Chernobrovchenko V. S.^{1*}, Dyadyura K. O.¹, Balynskyi M.¹, Panda A.²

¹ Sumy State University, 2, Rymyskogo-Korsakova St., 40007, Sumy, Ukraine;

² Faculty of Manufacturing Technologies with a seat in Prešov, Technical University of Košice, 080 01, Prešov, Slovakia

Article info:

Received: April 15, 2021
 The final version received: June 17, 2021
 Accepted for publication: June 22, 2021

***Corresponding email:**

dyadyura@pmtkm.sumdu.edu.ua

Abstract. The implantation of bone substitutes depends on the material's osteoconductive potential and the structure's porosity. Porosity is a characteristic feature of most materials. The porosity of materials has a strong influence on some of their properties, both structural and functional. An essential requirement for bone scaffolds is porosity, which guides cells into their physical structure and supports vascularization. The macroporosity should be large enough and interdependent for bone ingrowth to occur throughout the entire volume of the implant. The pore size for cell colonization in bioceramics is approximately 100 μm. Pores larger than this value promote bone growth through the material. This pore size allows the flow of growth factors and cell adhesion and proliferation, allowing the formation of new bone and developing the capillary system associated with the ceramic implant. Porosity also affects the rate of resorption of ceramics: the larger the number of micropores, the higher the dissolution rate. The investigated properties were elastic moduli, ultimate strength, compressive strength, and average apparent density. The results obtained in this work are consistent with previous studies, proving the positive role of microporosity in osseointegration and bone formation.

Keywords: porosity, porosity influence, hydroxyapatite, bone substitute, relationship, osseointegration.

1 Introduction

Bone substitute materials differ in chemical composition, mechanical strength, and biological mechanism of action. Each of them has its advantages and disadvantages. Unfortunately, bone substitutes have not yet achieved optimal mechanical and biological characteristics. Synthetic bone substitutes based on hydroxyapatite and β-tricalcium phosphate are considered today as an adequate alternative to autografts and allografts [1]. Today, when using synthetic materials, a compromise is needed between mechanical and biological characteristics. Since scaffolds are not permanent implants, their primary role is to promote extracellular matrix formation. The relationship between scaffold structure and tissue compatibility has been widely discussed over the past decade. Material properties such as porosity, chemical composition, and geometry alter the relationship between mechanical and biological characteristics, determine interactions with body fluids, and affect the behavior of bone cells.

An essential requirement for bone scaffolds is porosity, which guides cells into their physical structure and supports vascularization [2]. Porosity also affects the rate of the resorption: the larger the number of micropores, the higher the rate of dissolution [3]. As is known, a typical porosity of 90 % and a pore diameter of at least 100 μm are necessary for cell penetration and proper vascularization of the ingrown tissue [4]. The pore size for cell colonization in bioceramics is about 100 μm. Pores larger than 100 microns promote bone growth through the material. This pore size allows the flow of growth factors and cell adhesion and proliferation, allowing for the formation of new bone and developing the capillary system associated with the ceramic implant.

Scaffolds for bone regeneration are synthesized by various methods using a wide range of biomaterials. Research into the integration of biological implants with host tissues is constantly increasing, which leads to the most modern technologies for the manufacture of scaffolds. The superior technology allows the fabrication of complex-shaped frameworks with controlled pore size, shape, and orientation reliably and cost-effectively.

However, natural bone has a unique structure that cannot be reproduced with conventional synthesis methods. The role of micropores in improving the characteristics of bone substitutes has not been studied enough [4]. Not all bone substitutes are equally effective when used as directed. In this regard, biocompatibility risks when using scaffolds from different biomaterials for their intended purpose. Assessing the best options among new technologies (e.g., new chemicals, nanotechnology) is complicated by trade-offs between benefits and risks that are difficult to quantify given the limited and fragmented information available. The introduction of innovations in medical technology should not jeopardize the safety of patients [5]. Risk management and performance assessment processes should be interdependent and regularly updated.

Therefore, the choice of optimal bone substitutes is not always straightforward and largely depends on the clinical application and associated biological and mechanical needs. Research efforts to determine the optimal design of bone substitutes have not led to well-defined solutions [3].

The purpose of this work is to investigate the properties of porous calcium-phosphate bone substitutes depending on the technological conditions of manufacture when changing the process parameters, such as pH, concentration, and calcination temperature, as well as the effect of porosity on physical and mechanical characteristics.

2 Literature Review

Pores in calcium phosphate materials are essential for bone formation as they allow the migration and proliferation of osteoblasts and mesenchymal cells and vascularization. Porous biomaterials are becoming essential in terms of their applications. Pore sizes can range from microscale to macroscale.

In the literature [6], there are independent reviews of theoretical developments of porous materials and their use. For example, in [7], synthetic bone graft substitutes (BGS) have been developed in different pore shapes and sizes using different fabrication technologies.

For almost entirely dense materials with only low residual porosity, it can be assumed with reasonable accuracy that the relationship between properties and porosity is linear. However, for higher porosity, the research results show non-linear correlations. It is expected that the presence of porosity leads to complex laws (not simple direct or inverse linear proportionality). Since the existing references in the literature are somewhat ambiguous in terms of porosity or density, an attempt was made in work to systematize the porosity characteristics of calcium phosphate materials.

Equation (1) [8] is a universal generalization that describes the dependence of the porosity of the investigated properties:

$$p = p_0 \left(1 - \frac{\theta}{\theta_M}\right)^n, \quad (1)$$

where p is the property of the material with porosity θ ; p_0 is the property for the pore-free material; θ_M is the

maximum porosity of the powder mass, and n is a fitting parameter (positive or negative).

Considering a positive value for n , Equation (1) satisfies the common boundary conditions: $p \rightarrow p_0$ as $\theta \rightarrow 0$, and $p \rightarrow 0$ as $\theta \rightarrow \theta_M$, since, in this last situation, interparticle contacts are points. This is the case with most properties analyzed in this paper, including Young's modulus, the electrical and thermal conductivities. If n is negative, $p \rightarrow p_0$ as $\theta \rightarrow 0$, and $p \rightarrow \infty$ as $\theta \rightarrow \theta_M$, the typical situation for properties such as the electrical or thermal resistivities or the magnetic coercivity.

Many studies have shown a greater degree and faster rate of ingrowth or attachment of bones with a percentage of porosity; however, there is still some debate about the optimal "type" of porosity. The rate and quality of bone integration are related to pore size, volume fraction of porosity, and the relationship as a function of structural permeability and mechanics.

Gibson and Ashby's paper [9] is the first attempt to revise the properties of porous materials from aspects of their mechanical properties. Ashby calls these materials "cellular" or "lattice" materials, discussing their plastic and brittle mechanical properties in a comprehensive text on the topic, including processing, properties, and uses. Typically, these materials are used as catalyst carriers, filters, and membranes in the chemical, transportation, and energy industries. This use takes advantage of their properties, such as strength-to-weight ratio [6].

Knowledge of elastic properties is critical in the design of intended structural applications:

$$E = E_0 f(\theta, \{c_i\}), \quad (2)$$

Where E is Young's modulus of the porous material; E_0 is Young's modulus of the solid (pore-free) material; f is a function of θ and $\{c_i\}$, a set of empirical or fitting parameters sensitive to the microstructural details of the material.

To model the dependence of the shear modulus G on porosity, expressions like expressions for Young's modulus were usually proposed, with the corresponding values of the parameter involved. Parameter θ_M (maximum porosity) should be the same (since it can be interpreted as the percolation threshold). But the characteristic indicators of Young's modulus and shear modulus do not have to be identical. So, if we assume that Young's modulus is described as follows:

$$E = E_0 \left[1 - \left(\frac{\theta}{\theta_M}\right)\right]^{nE} \quad (3)$$

and shear modulus by:

$$G = G_0 \left[1 - \left(\frac{\theta}{\theta_M}\right)\right]^{nG} \quad (4)$$

and considering that for homogeneous isotropic materials, Poisson's ratio ν can be determined from the moduli E and G as follows:

$$\nu = \frac{E}{2G} - 1 \quad (5)$$

substituting equation (3) and (4) into equation (5), we get:

$$\nu + 1 = (\nu_0 + 1) \left[1 - \left(\frac{\theta}{\theta_M} \right) \right]^{nE - nG}. \quad (6)$$

In the specific case, when $nE = nG$ or $nE \approx nG$, then $\nu = \nu_0$ or $\nu \approx \nu_0$. This justifies the experimental results, which indicate a certain insensitivity of Poisson's ratio in porosity for insignificant values of porosity. In practice, there is a difference $nE - nG = 0.09$ for baked iron, which is studied in the porosity range from 0 to 0.22. The model can describe negative values of Poisson's ratio of porous materials when approaching the maximum value of porosity, θ_M (seepage threshold).

In works [10–14], hydroxyapatite frameworks showed higher flexural and compressive strength in the presence of small micropores with an average size of 5 μm compared to 16 μm . Composite frameworks can provide greater rigidity by providing a mechanism to inhibit crack propagation. In the study, the mechanical behavior of porous HA and frameworks with multiscale porosity was evaluated to study the effect of the average micropore size on strength and reliability. The results showed that hydroxyapatite scaffolds with multiscale porosity showed strength (8 MPa) close to the cancellous bone (1–7 MPa). But these figures are lower than the 140–200 MPa range indicated for the cortical bone. The microporous hydroxyapatite framework had better elastic properties than cortical or cancellous bone. The moduli of elasticity of the microporous scaffold with GA from this study (28–30 GPa) were more significant than trabecular (11.4–18.1 GPa) and cortical (15.8–25.9 GPa). For a more accurate correspondence of the modulus of the cortical or trabecular bone, the content of microporosity must be increased by reducing the temperature and sintering time.

Low porosity scaffolds have a large surface area, which is more favorable for initial cell attachment, while high porosity scaffolds may have a lower density, which slows cell proliferation. On the one hand, a higher porosity correlates with an increase in the nutrient diffusion coefficient and a higher hydraulic permeability, but on the other hand, the loss of Young's modulus reduces the mechanical properties of the framework. In addition, the decrease in Young's modulus is higher for biodegradable materials as they lose their integrity upon degradation.

However, this effect may be partially counterbalanced by the newly synthesized extracellular matrix formed within the scaffold, which enhances the overall mechanical strength of the scaffold. Therefore, the porosity value affects both the available surface area and the fluid transfer properties, which must be carefully balanced to obtain an optimized framework [15].

Montazeryan et al. [16] showed that triple periodic minimal structures (that is, a structure whose principal curvature sum is zero at each point [17]) look like promising candidates for frameworks with a high porosity index and transport properties while retaining the corresponding mechanical properties.

Moreover, complex geometries can be achieved, leading to hierarchically organized structures, as shown in Figure 1 [15]. Since the advent of additive manufacturing technologies, triple periodic minimal surfaces (TPMS) have served as a promising tool for designing microstructures due to their superior intrinsic characteristics such as interconnection, tortuosity, and high surface-to-volume ratio. The design space is divided into two or more phases, applying the TPMS equation, resulting in open, periodic porous structures with smooth joints and curvatures. This architecture provided scaffolds with a high degree of fluidity and low modulus of elasticity in the trabecular bone range [16].



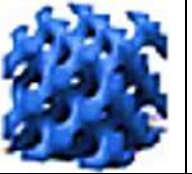




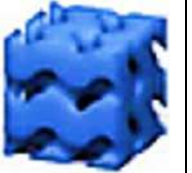


The hydraulic permeability can be calculated using Darcy's law, which relates the velocity V_D of the fluid flowing through the sample, represented in the pressure gradient, to provide the driving force of the flow [15]:

$$V_D = -k \frac{\rho g \Delta h}{\eta H}, \quad (7)$$

where k is the hydraulic permeability (cm^2); η is the dynamic viscosity of the fluid ($\text{Pa}\cdot\text{s}$); H is the sample thickness (cm); ρ is the density of the fluid (g/cm^3); $g = 9.81 \text{ m/s}^2$ is the gravitational acceleration; Δh is the height difference corresponding to a pressure drop $\Delta P = \rho g \Delta h$.

Table 1 presents examples of triple periodic minimal surfaces (TPMS) unit cell designs with different relative densities as potential scaffolds for tissue engineering.

Table 1 – Examples of TPMS unit cell designs with different relative densities as potential scaffolds for tissue engineering

Porous architecture					
Relative density, %	29	29	33	34	38
Porous architecture					
Relative density, %	51	63	66	66	68

There are various technologies for the manufacture of porous biomaterials. The introduction of new technologies for processing frames made it possible to manufacture individual porous structures with improved mechanical properties (Tables 2–3). A combination of techniques can improve the relationship between processing parameters, the resulting porous microstructures, and the physical, mechanical, and in vitro/in vivo behavior of materials.

Table 2 – Advantages and disadvantages of methods for the manufacture of materials based on hydroxyapatite

Technological method	Characteristics (properties) of porosity	Research results
Partial sintering	Graduated porosity, low interconnection, isotropic structure. As an example, the porosity size is 65 %	[6, 18]
Electro-spinning	When combined with RP, it can create a complex structure, larger pores, oriented fibers; smaller pore size in conventional technologies, low cell infiltration, uneven fiber distribution	[6, 19, 20]
Use of liquid hydrogen/hydrolysis	High interconnection, directional porosity, fully open porosity, use of organic solvent associated with small pore sizes sometimes show poor homogeneity of the pore structure. Porosity sizes – 47, 56, 45–55 %; pore sizes – 1–10, 90–110 μm	[6, 21]
The method of bubble formation	High porosity, low mechanical strength. Porosity size – 90 %; pore sizes: 1–10, 100, 800 μm	[6, 22, 23]
Gel casting	Almost reticulate, high uniformity, good cohesion combined with foaming. Porosity – 90 %; pore size: 20–1000 μm	[6, 24–26]
Rapid Prototyping (RP) methods	With the possibility of complex shape, the porous structure can be customized according to the host tissue, organic solvents, random microporosity. Porosity – 50–65 %; pore sizes – 700–900, 200–500 μm	[6, 27–31]
Polymer sponge replication	It is possible to create open and interdependent cells, anisotropic pore structure with elongated pores, homogeneity of the suspension. Porosity – 82, 76 %; pore sizes – 700–950 μm , 750–1100 μm	[32, 33]

Table 3 – Manufacturing methods and porosity indices for materials made by various methods

Material	Manufacturing method	Characteristics of porosity	Research results
Polyamide 12/HA	Laser sintering	200–400 μm	[34]
Nanofiber Scaffold (NFS)	Electrospinning	1.5–7.8 μm ; 68–93 %	[35]
HA/bioactive glass	Gel casting	100–400 mm; 78 %	[36]
B-TCP	Replication	200–750 mm; approx. 94 %	[37]
HA	3D gel printing	350x350 μm ; 52 %	[38]

Rapid prototyping methods allow precise control of porosity characteristics. It is interesting to fabricate hierarchically porous frameworks using methods for fabricating solids of arbitrary shape. The production of scaffolds with a stepped pore size distribution was mainly performed by this method. Polymers are the most studied biomaterials using free-form solid technology. The combination of electrospinning with such technologies has created nanopores next to macropores.

In the technique of partial sintering, the mechanisms of surface diffusion or evaporation-condensation under high-temperature exposure can be predominantly triggered in the composition of particles. This leads to coarsening of the grain/pore without compaction

The size of the original powders can change the porous structure or pore size and morphology, the level of initial compaction, and the following sintering parameters, including pressure, sintering temperature, and time. Microwave sintering and microwave heating can be used to process bioceramic powders. Microwave radiation saves time, energy, and associated processing costs [6, 18].

Electrospinning. In this method, a polymer solution is injected from an electrically conductive needle until it reaches the manifold. High voltage is applied from the end of the die to the manifold, which is fixed away from the die. The electric potential applied to the polymer solution overcomes the surface tension, and drops (Taylor cone) are formed. Polymer jets are ejected from the needle and collected on the manifold. This is how a non-woven and randomly oriented fibrous polymer network with different fiber diameters from 100 nm to several micrometers is obtained, depending on the specific polymer solution and electrospinning parameters. This method cannot control the size of the pores and their location concerning the internal channels [6, 19, 20].

Porosity using a liquid blowing agent. Here, the porogen can be a soluble or insoluble liquid. The resulting structure showed well-defined pore connectivity and directional and fully open porosity, such as lamellar morphology after sintering.

The size of the porosity can be controlled by changing the freezing rate and concentration of the suspensions. The change in the porosity content of lyophilized scaffolds was also studied by changes in parameters such as particle

concentration, the nature of the solvent, and the temperature gradient. The study showed that the thickness of the HA lamella decreased, and the pore width increased with decreasing particle concentration. A decrease in the base temperature from $-20\text{ }^{\circ}\text{C}$ to $-196\text{ }^{\circ}\text{C}$ created a thinner lamellar microstructure [6, 21].

The bubbling technique is based on mixing the desired components and allows the release of gas bubbles. Gel casting and foaming techniques have been used to create highly porous hydroxyapatite with up to 90% porosity. First, a homogeneous suspension of ceramic powder, water, and monomer solution (i.e., acrylate monomers and methylenebis (acrylamide) monomers) is foamed by adding surfactants. Foaming of suspensions occurs in the in-situ polymerization of organic monomers. Polymerization promoters can be added before shaping. Finally, organic additives are removed at temperatures above $300\text{ }^{\circ}\text{C}$, and sintering is carried out to consolidate the ceramic frameworks. Porous hydroxyapatite showed spherical interconnected cells ranging in size from 20 to $1000\text{ }\mu\text{m}$ [6, 22, 23].

Gel casting - a method of almost pure form, provides high homogeneity and strength of raw bodies. Powders, organic monomers such as a mixture of methacrylamide and N, N'-methylenebis (acrylamide), binders, dispersants, and solvents are mixed to form a slurry. Then, a crosslinking reaction occurs when an initiator such as ammonium persulfate and a catalyst such as N, N, N', N'-tetramethylene diamine are added to cause the crude body to polymerize in situ. After evaporation of the solvent, the polymer binds the powders and retains the desired shape. The success of this method depends on the production of well-dispersed and highly solid suspensions (up to 50 vol. %). Dispersant concentration, solids content and mixing time are important factors for the successful implementation of the method [6, 24–26].

Rapid prototyping (RP) or freeform solid specimen fabrication techniques are used to fabricate porous structures. In RP, the digital representation of an object is mathematically broken down into several thin layers. Then the layers are built, merged, and form three-dimensional objects. Examples of RP processes include Stereolithography (STL), Selective Laser Sintering (SLS), Fused Deposition Modeling (FDM), and Direct 3D Printer. They provide control over the fabrication of frameworks with reproducible porosity and specific relationships, geometry, orientation, and pore size due to the particular spatial features of the scaffolds. Direct RP is related to anisotropic shrinkage during manufacturing. To remove the limitation of direct RP, indirect freeform solids production (SFF)/RP was developed for biomaterials, including cast ceramic suspensions. The development of molds, casting methods, and mold stripping is an indirect RP task. The difference between direct RP and indirect RP is that the scaffold is directly produced from biomaterial in the first case, while in the second, the scaffolds are cast and processed in the RP mold. The SL technique has been adapted to manufacture 3D ceramics by adding ceramic powders to light-sensitive resins. This technique, ceramic

stereolithography (CSL), requires the preparation of light-sensitive ceramic suspensions [6, 27–31].

A technique uses polymer foam, which is popular in the production of macroporous ceramics and metals. One of the most common synthetic polymeric materials, sponges, which is consumed is polyurethane. The polymer template is moistened several times in a suspension of the corresponding powders to impregnate the templates, and the residues are drained and removed (squeezing out a sponge to get rid of excess suspension). The dried template is then heat-treated to decompose the organic sponges (pyrolysis). After removing the polymer template, ceramic or metal structures are baked at higher temperatures to seal the walls of the posts [32, 33].

3 Research Methodology

3.1 Materials

The chemical formula of hydroxyapatite is $\text{Ca}_{10}(\text{PO}_4)_6(\text{OH})_2$, and the stoichiometric Ca/P ratio is 1.67 [39]. Bioceramics based on HA are biocompatible, corrosion-resistant, have low toxicity, and have good compressive strength [40]. Whereas β -TCP is bioabsorbable, and bioresorption occurs due to osteoclast activity [41]. An example of porous hydroxyapatite is shown in Figure 1 [42].

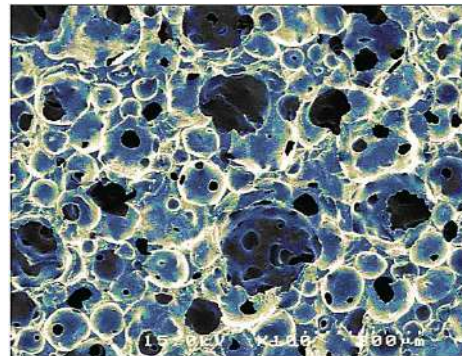


Figure 1 – SEM image of interconnected porous hydroxyapatite (IP-CHA)

Almost all pores are interconnected. HA has mechanical properties: flexural strength, compressive strength, tensile strength, Young's modulus of elasticity, and Vicker's modulus. The hardness values of HA ceramics are in the range of 38–250, 120–150, and 38–300 MPa; 35–120, and 3–7 GPa, respectively [43].

The mass fraction of hydroxyapatite must be at least 95 % of the crystalline phases. The mass fraction of CaO should be no more than 1 % of the crystalline phases. The mass fraction of hydroxyapatite is calculated according to the formula:

$$MF_{HA} = 100\% - MF_{\beta\text{TCP}} - MF_{\alpha\text{TCP}} - MF_{\text{TTCP}} - MF_{\text{CaO}}, \quad (8)$$

where MF_{HA} – the mass fraction of crystalline HA; $MF_{\beta\text{TCP}}$ – a mass fraction of crystalline β TCP; $MF_{\alpha\text{TCP}}$ – a mass fraction of crystalline α TCP; MF_{TTCP} – a mass fraction of crystalline TTCP; MF_{CaO} – a mass fraction of crystalline CaO.

The mass fraction of any phase is considered zero if its value is below the detection threshold [44].

A suspension was prepared with a regulated HA loading. Used cellulose sponges, which can restore their original shape after impregnation and are entirely removed at a temperature of about 600 °C. The cellulose sponges were round samples with a diameter of 1 cm. Hydroxyapatite powder was dissolved in distilled water to obtain a suspension. The powder was gradually placed in water with stirring for uniform dissolution. Then a dispersant in different compositions was added to the solution. Three dispersant compositions were applied to the hydroxyapatite suspensions. After impregnating the slurry, the sponges were dried and heat-treated at 600 °C for 1 hour to remove the organic matrix. The sintering was carried out at 1200 °C for 1 hour.

The influence of three factors (sintering rate, stirring time, and hydroxyapatite concentration) on the porosity, compressive strength, and crystallinity of porous bodies was investigated. For evaluating the sintering rate, samples 1 and 2 were compared. The hydroxyapatite concentration and stirring time were kept constant while the sintering rate was varied. The sizes and weights of all samples were measured before and after heat treatment (Table 4).

Table 4 – Conditions for obtaining porous HA

Sample	Water, g	Concentration of HA, wt. %	Stirring time, min	Sintering speed, °C/h
S1	15.7	44	20	1500
S2	15.7	44	20	220
S3	16.7	42	20	220
S4	16.7	42	4	220
S5	20.0	38	20	220
S6	20.0	38	4	220

3.2 Methods

As already mentioned, the ingrowth of bone substitutes also depends on the porosity of the structure. The macroporosity must be large and interdependent for ingrowth to occur throughout the entire volume of the implant. Porosity affects the rate of resorption of ceramics: the larger the number of micropores, the higher the dissolution rate. The formula calculates the porosity:

$$P = 100 \left(1 - \frac{d_r}{d_{th}} \right), \quad (9)$$

where P is the degree of porosity, %; d_r – calculated by measuring the size and weight of a parallelepiped bone substitute with a minimum volume of 2 cm³. The volume V of the bone substitute is calculated using the measured parameters and then determine d_r by the formula:

$$d_r = \frac{m}{V}; \quad (10)$$

Table 5 – Conditions for preparation of hydroxyapatite and physical properties of porous samples S1, S2, S3, S4, S5 and S6

Sample	Average apparent density, g/cm ³	Total porosity, %	Compressive strength, MPa	Young's modulus, MPa
S1	2.03	35.9	10	655
S2	1.69	46.2	4.3	275
S3	2.08	34.3	10.5	579
S4	1.81	42.7	6.4	385
S5	1.60	49.4	3.2	215
S6	1.27	59.8	1.8	61

d_{th} – insurance for formula insurance for a formula:

$$d_{th} = \frac{d_{HAP} \frac{MF_{HA}}{d_{HA}} + d_{\beta TCP} \frac{MF_{\beta TCP}}{d_{\beta TCP}}}{\frac{MF_{HA}}{d_{HA}} + \frac{MF_{\beta TCP}}{d_{\beta TCP}}}. \quad (11)$$

Young's modulus E_s of cellular materials is defined as follows:

$$E_s = E_b \left(\frac{\rho_s}{\rho_b} \right)^2, \quad (12)$$

where E_b – Young's modulus of the bulk material [26].

4 Results and Discussion

As can be seen from Figure 2 (sample 1) was found to have a high average apparent density, compressive strength, and Young's modulus, while the average porosity was lower. The average compressive strength for sample 1 was 10 MPa, the average apparent density was 2.03 g/cm³, and the average porosity was 35.9 %. It was found experimentally that a higher rate of sintering speed leads to higher apparent density and high compressive strength.

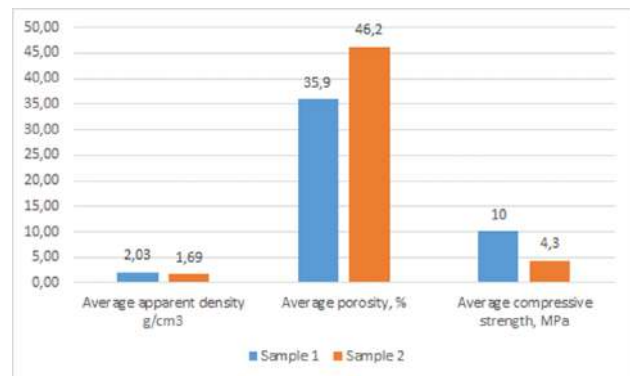


Figure 2 – Average visible density, compressive strength, and porosity of samples 1 and 2

The effect of the mixing period was evaluated by comparing samples 3 and 4, as well as samples 5 and 6. The preparation conditions are shown in Table 3, physical properties – in Table 5.

Figure 3 shows a comparison of samples 3, 4, 5, and 6 in terms of their average apparent density, compressive strength, and porosity. Comparing samples 3 and 4 shows that an increase in the mixing time increased the compressive strength and apparent density but decreased the porosity. The same can be done for samples 5 and 6. Increasing the mixing time leads to the destruction of agglomerates, and the resulting suspension becomes more homogeneous. The relationship of these parameters is shown graphically in Figure 4 a–c.

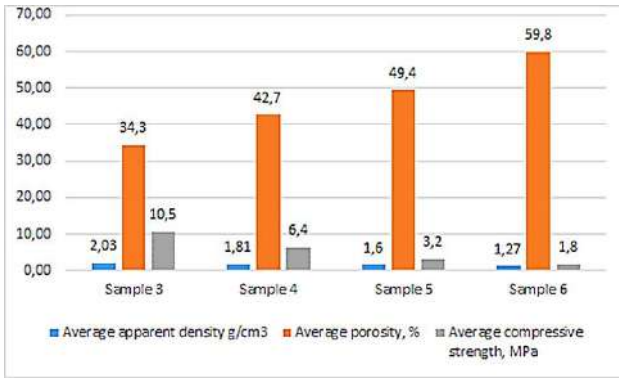
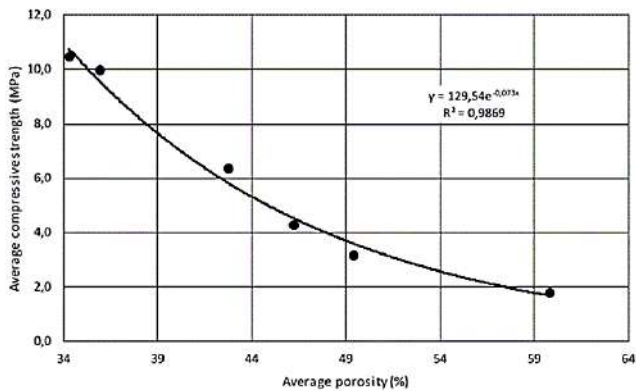
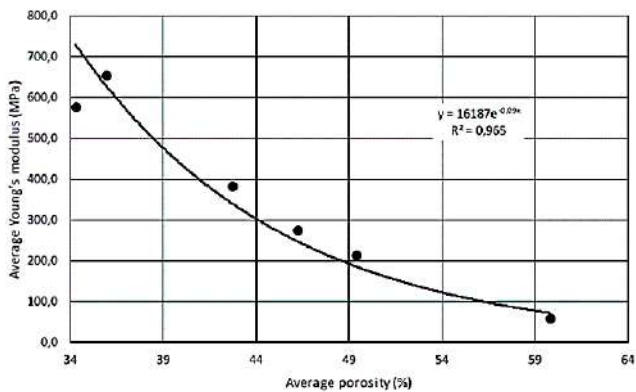


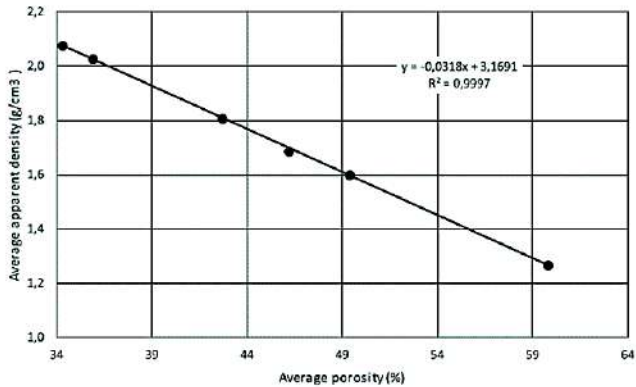
Figure 3 – Average visible density, compressive strength and porosity of samples S3, S4, S5 and S6



a

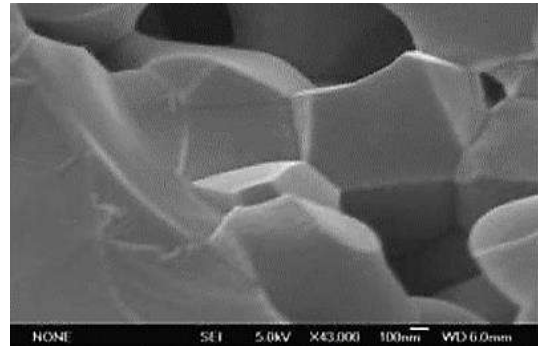


b

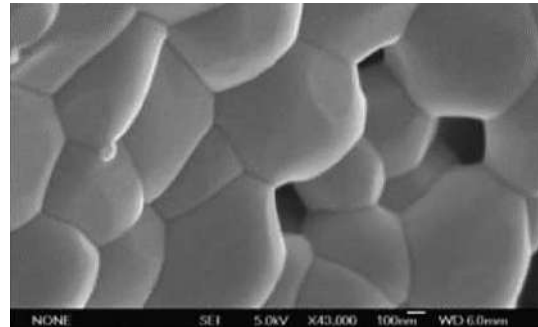


c

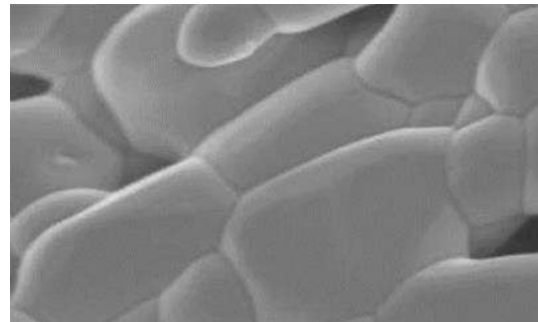
Figure 4 – Dependence of compressive strength, Young's modulus, and average apparent density on porosity



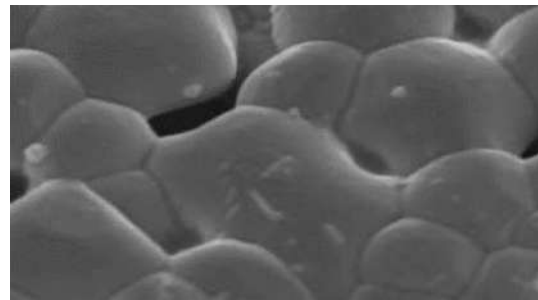
a



b



c

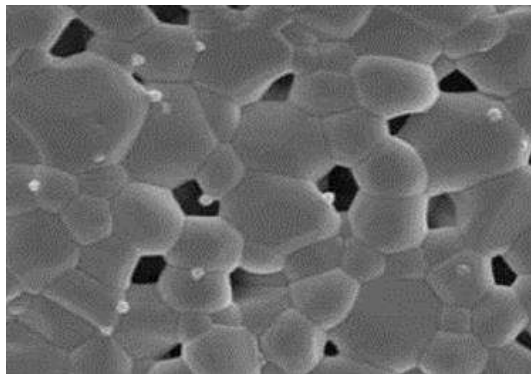


d

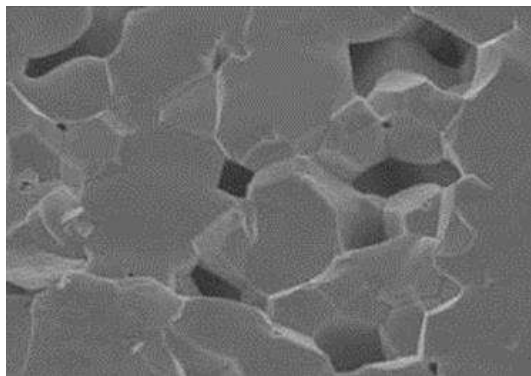
Figure 5 – Microphotographs of samples 3 (a), 4 (b), 5 (c) and 6 (d)

Figure 5 shows images of samples 3–6. With fewer voids shown in Figure 5 a, sample 3 with a longer mixing time has lower porosity and higher density than sample 4 (Figure 5 b). Larger crystal sizes and fewer particle boundaries with more uniform particles visible in sample 3 indicate higher crystallinity. The same results were obtained by comparing micrographs of samples 5 and 6, as shown in Figures 6 c–d. Increasing the mixing time gives a more uniform suspension and increases the crystallinity of the porous structure.

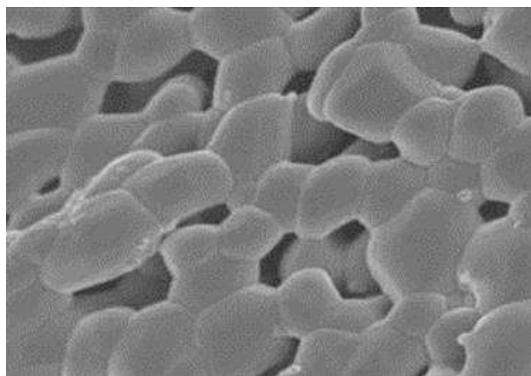
The effect of the concentration of hydroxylapatite on porosity, compressive strength, and crystallinity was evaluated; samples 2, 3, and 5 were compared with material concentrations of 44, 42, and 38 % by weight, respectively.



a



b



c

Figure 6 – Micrographs of samples: a – 2 samples (44 wt. %); b – 3 samples (42 wt. %); c – 5 samples (38 wt. %)

From the images in Figure 6, with an increase in the concentration of hydroxylapatite from 38 to 42 % of the mass fraction, the time became more interconnected with denser and thicker pore walls, which indicates a higher density.

Glass-ceramic materials were prepared using nanostructured BHA (or SCPM) powders and sodium borosilicate glass with a weight ratio of 0.46:1. Powder mixes for SCP/glass composites were prepared by mixing sodium borosilicate glass and SCPM powders ($\text{Ca}_{10}(\text{PO}_4)_6(\text{OH})_2$, $\text{Ca}_4(\text{PO}_4)_2\text{O}$ and $\text{Ca}_2\text{P}_2\text{O}_7$) (less than

160 μm). Samples with a diameter of 3 g and 15 mm were prepared by dry pressing under 150 MPa and sintering at 800 °C for all investigated composites. The resulting SCP powder had the composition $\text{Ca}_{10}(\text{PO}_4)_6(\text{OH})_2$, β -tribasic calcium phosphate (β -TCP, $\beta\text{-Ca}_3(\text{PO}_4)_2$), tetrabasic calcium phosphate (TTCP, $\text{Ca}_4(\text{PO}_4)_2\text{O}$), calcium pyrophosphate (CPP, $\text{Ca}_2\text{P}_2\text{O}_7$).

Table 6 shows the apparent density of SCP. The apparent density is significantly influenced by the particle size of the original mixture and the type of calcium phosphate. SCP/glass is dominated by open porosity. This is due to the launched processes of phase formations in synthetic calcium phosphates during sintering, accompanied by gas formation, leading to the resulting porosity structure.

Table 6 – Number of pores, solubility, and pH change in the material after 48 and 168 hours

Parameter	SCP/glass
Open porosity	24.1 %
Closed porosity	10.4 %
Density	1.75 g/cm ³
pH after 48 h	10.2
pH after 168 h	9.5
Solubility after 2 days	0.036 wt. %
Solubility after 5 days	0.054 wt. %

The apparent density is influenced by both the particle size of the feed mixture and the type of calcium phosphate. In determining the solubility in vitro, the permeability of the porous structure is also essential, which depends, instead, on the open porosity, which is effective in impregnating the material, and the design of capillary-porous channels, characterized by high crimp than on the porosity in general and the pore structure. The permeability of a structure is determined by the coefficient of permeability, which affects the rate of mass transfer when determining the rate of dissolution in vitro. The average diameter of the pore channel, established by studying the microstructure and pore size distribution, is 8.83 μm for SCP/glass. The results obtained in this work are consistent with previous studies [45].

There are many methods for making porous ceramic materials. The pore morphology can be controlled using the size of the initial powder and sintering parameters - temperature, time, pressure. Studies of various materials based on hydroxylapatite have shown that the higher the sintering rate of the material powder, the more apparent density is formed in the final material, and this leads to a higher compressive strength. It was found that increasing the mixing time increased the compressive strength and apparent density but decreased the porosity, because the longer the mixing time leads to the destruction of agglomerates, and the slurry becomes more homogeneous. There are various technologies for the manufacture of bone substitutes (electrospinning and freeze-drying). In milled bioceramics, the pore size can be reduced by increasing the temperature.

5 Conclusions

The study of the porosity of materials for biomedicine has always received considerable attention. Porosity plays an essential role in the process of introducing bone substitutes. A large and interconnected macroporosity is required for bone ingrowth to occur throughout the entire volume. Traditional methods generate random pores. New technologies for processing scaffolds allow the production of porous materials with improved mechanical properties. Since the advent of additive manufacturing technologies, triple periodic minimal surfaces (TPMS) have served as a promising tool for designing microstructures due to their superior intrinsic characteristics such as interconnection, tortuosity, and high surface-to-volume ratio.

The use of a liquid blowing agent creates scaffolds with lamellar morphology with well-defined pore connectivity. The foaming process uses dissolved gas at elevated pressure or a chemical that produces gaseous decomposition products. Rapid prototyping methods provide control over the fabrication of frameworks with

reproducible porosity and specific relationships, geometry, orientation, and pore size. The SCPL method helps produce materials with controlled pore sizes and shapes. During freeze-drying, there are no harmful solvents, and it is possible to clarify the morphology of the frameworks.

Various parameters can control pore sizes during the manufacturing process (temperature, sintering speed, and stirring time). Variations in the content of porosity, pore size, and shape are possible due to changes in various processing parameters (liquid-powder ratio, concentration, the composition of the foaming agent in the solution). The fast-sintering rate of hydroxyapatite results in higher apparent density and high compressive strength. Increasing mixing time increases compressive strength and apparent density but decreases porosity. Also, an increase in the mixing period leads to the destruction of agglomerates, and the resulting suspension becomes more homogeneous. As the concentration of hydroxyapatite increases, the pores become more interconnected with denser and thicker pore walls.

References

1. Sukhodub, L. F., Diadiura, K. O. (2018). Design and fabrication of polymer-ceramic nanocomposites materials for bone tissue engineering. *Journal of Nano- and Electronic Physics*, Vol. 10(6), 06003(11pp), doi: 10.21272/jnep.10(6).06003.
2. Bouler, J. M., Pilet, P., Gauthier., O. (2017). Verron biphasic calcium phosphate ceramics for bone reconstruction: A review of biological response. *Acta Biomaterialia*, Vol. 53, pp. 1–12, doi: 10.1016/j.actbio.2017.01.076.
3. Rustom, L., Boudou, T., Lou, S., Pignot-Paintrand, I., Nemke, B. W., Lu, Y., Markel, M. D., Picart, C., Johnson, A. J. W. (2016). Micropore-induced capillarity enhances bone distribution in vivo in biphasic calcium phosphate scaffolds. *Acta Biomaterialia*, Vol. 44, pp. 144–154, doi: 10.1016/j.actbio.2016.08.025.
4. Johnson, A. J. W., Herschler, B. A. (2011). A review of the mechanical behavior of CaP and CaP/polymer composites for applications in bone replacement and repair. *Acta Biomaterialia*, Vol. 7(1), pp. 16–30, doi: 10.1016/j.actbio.2010.07.012.
5. Miclăuș, T., Valla, V., Koukoura, A., Nielsen, A. A., Dahlerup, B., Tsianos, G.-I., Vassiliadis, E. (2020). Impact of design on medical device safety. *Therapeutic Innovation and Regulatory Science*, Vol. 54(4), pp. 839–849, doi: 10.1007/s43441-019-00022-4.
6. Babaie, E., Bhaduri, S. B. (2017). Fabrication aspects of porous biomaterials in orthopedic applications: A review. *ACS Biomater. Sci. Eng.*, Vol. 4(1), pp. 1–39, doi: 10.1021/acsbiomaterials.7b00615.
7. Diez-Escudero, A., Espanol, M., Ginebra, M. P. (2020). Synthetic bone graft substitutes: Calcium-based biomaterials. *Dental Implants and Bone Grafts*, Woodhead Publishing, pp. 125–157.
8. Ternero, F., Rosa, L. G., Urban, P., Montes, J. M., Cuevas, F. G. (2021). Influence of the total porosity on the properties of sintered materials – A review. *Metals*, Vol. 11(5), 730, doi: 10.3390/met11050730.
9. Gibson, L. J., Ashby, M. F. (1999). *Cellular Solids: Structure and Properties*. Cambridge University Press.
10. Rho, J. Y., Kuhn-Spearing, L., Zioupos, P. (1998). Mechanical properties and the hierarchical structure of bone. *Medical Engineering and Physics*, Vol. 20(2), pp. 92–102, doi: 10.1016/S1350-4533(98)00007-1.
11. Cordell, J. M., Vogl, M. L., Johnson, A. J. W. (2009). The influence of micropore size on the mechanical properties of bulk hydroxyapatite and hydroxyapatite scaffolds. *Journal of the Mechanical Behavior of Biomedical Materials*, Vol. 2(5), pp. 560–570, doi: 10.1016/j.jmbbm.2009.01.009.
12. Prokopiev, O., Sevostianov, I. (2006). Dependence of the mechanical properties of sintered hydroxyapatite on the sintering temperature. *Materials Science and Engineering: A*, Vol. 431(1-2), pp. 218–227, doi: 10.1016/j.msea.2006.05.158.
13. Prokopiev, O., Sevostianov, I. (2006). On the possibility of approximation of irregular porous microstructure by isolated spheroidal pores. *International Journal of Fracture*, Vol. 139(1), pp. 129–136, doi: 10.1007/s10704-006-8370-9.
14. Lutzweiler, G., Halili, A. N., Vrana, N. E. (2020). The overview of porous, bioactive scaffolds as instructive biomaterials for tissue regeneration and their clinical translation. *Pharmaceutics*, Vol. 12(7), pp. 602, doi: 10.3390/pharmaceutics12070602.
15. Montazerian, H., Davoodi, E., Asadi, M., Kadkhodapour, J. (2017). Porous scaffold internal architecture design based on minimal surfaces: A compromise between permeability and elastic properties. *Mater. Des.*, Vol. 126, pp. 98–114, doi: 10.1016/j.matdes.2017.04.009.

16. Bobbert, F. S. L., Lietaert, K., Eftekhari, A. A., Pouran, B., Ahmadi, S. M., Weinans, H., Zadpoor, A. A. (2017). Additively manufactured metallic porous biomaterials based on minimal surfaces: A unique combination of topological, mechanical, and mass transport properties. *Acta Biomaterialia*, Vol. 53, pp. 572–584, doi: 10.1016/j.actbio.2017.02.024.
17. Babaie, E., Ren, Y., Bhaduri, S. B. (2016). Microwave sintering of fine grained MgP and Mg substitutes with amorphous tricalcium phosphate: Structural, and mechanical characterization. *J. Mater. Res.*, Vol. 31(08), pp. 995–1003, doi: 10.1557/jmr.2016.84.
18. Sebastian, T., Preisker, T. R., Gorjan, L., Graule, T., Aneziris, C. G., Clemens, F. J. (2020). Synthesis of hydroxyapatite fibers using electrospinning: A study of phase evolution based on polymer matrix. *Journal of the European Ceramic Society*, Vol. 40(6), pp. 2489–2496, doi: 10.1016/j.jeurceramsoc.2020.01.070.
19. Faridi-Majidi, R., Nezafati, N., Pazouki, M., Hesarakhi, S. (2017). The effect of synthesis parameters on morphology and diameter of electrospun hydroxyapatite nanofibers. *J Aust Ceram Soc.*, Vol. 53, pp. 225–233, doi: 10.1007/s41779-017-0028-8.
20. Czechowska, J., Zima, A., Siek, D., Ślósarczyk, A. (2018). Influence of sodium alginate and methylcellulose on hydrolysis and physicochemical properties of α -TCP based materials. *Ceramics International*, Vol. 44(6), pp. 6533–6540, doi: 10.1016/j.ceramint.2018.01.055.
21. Januariyasa, K., Yusuf, Y. (2020). Porous carbonated hydroxyapatite-based scaffold using simple gas foaming method. *Journal of Asian Ceramic Societies*, Vol. 8(3), pp. 634–641, doi: 10.1080/21870764.2020.1770938.
22. Li, X., Deng, Y., Chen, X., Xiao, Y., Fan, Y., Zhang, X. (2016). Gelatinizing technology combined with gas foaming to fabricate porous spherical hydroxyapatite bioceramic granules. *Materials Letters*, Vol. 185, pp. 428–431, doi: 10.1016/J.MATLET.2016.09.036.
23. Mamat, N., Darus, F., Md Isa, R., Jaafar, M., Kawashita, M. (2017). Hierarchical bioceramic scaffold for tissue engineering: A review. *International Journal of Polymeric Materials and Polymeric Biomaterials*, Vol. 66(17), pp. 877–890, doi: 10.1080/00914037.2017.1291507.
24. Wu, Z., Zhou, Z., Hong, Y. (2018). Isotropic freeze casting of through-porous hydroxyapatite ceramics. *Journal of Advanced Ceramics*, Vol. 8(2), pp. 256–264, doi: 10.1007/s40145-018-0312-2.
25. Mondal, S., Hoang, G., Manivasagan, P., Moorthy, M. S., Nguyen, T. P., Phan, T. T. V., Kim, H. H., Kim, M. H., Nam, S. Y., Oh, Y. (2018). Nano-hydroxyapatite bioactive glass composite scaffold with enhanced mechanical and biological performance for tissue engineering application. *Ceramics International*, Vol. 44 (13), pp. 15735–15746, doi: 10.1016/j.ceramint.2018.05.248.
26. Yuan, B., Zhou, S.-Y., Chen, X.-S. (2017). Rapid prototyping technology and its application in bone tissue engineering. *Journal of Zhejiang University-Science B*, Vol. 18(4), pp. 303–315, doi: 10.1631/jzus.B1600118.
27. Truneca, M., Chlup, Z. (2017). Subtractive manufacturing of customized hydroxyapatite scaffolds for bone regeneration. *Ceramics International*, Vol. 43(14), pp. 11265–11273, doi: 10.1016/j.ceramint.2017.05.177.
28. Sapkal, P. S., Kuthe, A. M., Kashyap, R. S., Nayak, A. R., Kuthe, S. A., Kawle, A. P. (2016). Indirect fabrication of hydroxyapatite/b-tricalcium phosphate scaffold for osseous tissue formation using additive manufacturing technology. *J Porous Mater*, Vol. 23(6), pp. 1567–1574, doi: 10.1007/s10934-016-0217-9.
29. Hassanajili, S., Pour, A. K., Oryan, A., Talaie-Khozani, T. (2019). Preparation and characterization of PLA/PCL/HA composite scaffolds using indirect 3D printing for bone tissue engineering. *Materials Science and Engineering C*, Vol. 104, 109960, doi: 10.1016/j.msec.2019.109960.
30. Houben, A., Van Hoorick, J., Van Erps, J. A., Thienpont, H., Van Vlierberghe, S., Dubruel, P. (2017). Indirect rapid prototyping: opening up unprecedented opportunities in scaffold design and applications. *Ann. Biomed. Eng.*, Vol. 45(1), pp. 58–83, doi: 10.1007/s10439-016-1610-x.
31. Hui, D., Goodridge, R. D., Scotchford, C. A., Grant, D. M. (2018). Laser sintering of nano-hydroxyapatite coated polyamide 12 powders. *Additive Manufacturing*, Vol. 22, pp. 560–570, doi: 10.1016/j.addma.2018.05.045.
32. Khallok, H., Elouahli, A., Ojala, S., Keiski, R. L., Kheribech, A., Hatim, Z. (2020). Preparation of biphasic hydroxyapatite/ β -tricalcium phosphate foam using the replication technique. *Ceramics International*, Vol. 46(14), pp. 22581–22591, doi: 10.1016/j.ceramint.2020.06.019.
33. Wong, W. Y., Noor, A.-F. M., Othman, R. (2016). Sintering of beta-tricalcium phosphate scaffold using polyurethane template. *Key Engineering Materials*, Vol. 694, pp. 94–98, doi: 10.4028/www.scientific.net/KEM.694.94.
34. Gandhimathi, C., Venugopal, J. R., Ramakrishna, S., Srinivasan, D. K. (2018). Electrospun-electrosprayed hydroxyapatite nanostructured composites for bone tissue regeneration. *Journal of Applied Polymer Science*, Vol. 135(42), 46756, doi: 10.1002/app.46756.
35. Seyedmajidi, S., Seyedmajidi, S., Alaghehmand, H., Hajian-Tilaki, K., Haghanifar, S., Zabihi, E., Rayabnia, R., Seyedmajidi, M. (2018). Synthesis and characterization of hydroxyapatite/bioactive glass nanocomposite foam and fluorapatite/bioactive glass nanocomposite foam by gel casting method as cell scaffold for bone tissue. *Eurasian J Anal Chem*, Vol. 13(3), em17, doi: 10.29333/ejac/85078.
36. Miola, M., Verne, E., Vitale-Brovvarone, C., Baino, F. (2016). Antibacterial bioglass-derived scaffolds: Innovative synthesis approach and characterization. *International Journal of Applied Glass Science*, Vol. 7(2), pp. 238–247, doi: 10.1111/ijag.12209.
37. Shao, H., He, J., Lin, T., Zhang, Z., Zhang, Y., Liu, S. (2018). 3D gel-printing of hydroxyapatite scaffold for bone tissue engineering. *Ceramics International*, Vol. 45(1), pp. 1163–1170, doi: 10.1016/j.ceramint.2018.09.300.
38. Gomes, D. S., Santos, A. M. C., Neves, G. A., Menezes, R. R. (2019). A brief review on hydroxyapatite production and use in biomedicine. *Cerâmica*, Vol. 65(374), pp. 282–302, doi: 10.1590/0366-69132019653742706.

39. Siddiqui, H. A., Pickering, K. L., Mucalo, M. R. (2018). A review on the use of hydroxyapatite carbonaceous structure composites in bone replacement materials for strengthening purposes materials. *Materials (Basel)*, Vol. 11(10), 1813, doi: 10.3390/ma11101813.
40. Kamrun, N. U., Shovon, B., Rajib, C. D., Shujit, C. P., Shukanta, B., Muhammed, Y. M., Sydul, I. M. D. (2017). Characterization of beta-tricalcium phosphate (β - TCP) produced at different process conditions. *J Bioengineer and Biomedical Sci*, Vol. 7(221), doi: 10.4172/2155-9538.1000221.
41. Abe, Y., Kobatake, R., Okazaki, Y., Oki, Y., Naito, Y., Prananingrum, W., Tsuga, K. (2017). Novel development of phosphate treated porous hydroxyapatite. *Materials*, Vol. 10(12), 1405. doi: 10.3390/ma10121405.
42. Karyasa, I. W. (2021). Developing renewable thermo-hydrothermic bioinorganic materials from bone wastes of slaughterhouses. *Journal of Physics: Conference Series*, Vol. 1869(1), 012030, doi: 10.1088/1742-6596/1869/1/012030.
43. ISO 13175-3:2012 Implants for surgery – Calcium phosphates – Part 3: Hydroxyapatite and beta-tricalcium phosphate bone substitutes.
44. Pinchuk, N., Parkhomey, O., Sych, O. (2017) In vitro investigation of bioactive glass-ceramic composites based on biogenic hydroxyapatite or synthetic calcium phosphates. *Nanoscale Research Letters*, Vol. 1(111), doi: 10.1186/s11671-017-1895-1.
45. Parkhomei, O. R., Pinchuk, N. D., Sych, O., Tomila, T. (2016). Structural and mechanical properties of bioactive glass–ceramic composites. *Powder Metallurgy and Metal Ceramics*, Vol. 55 (3-4), doi: 10.1007/s11106-016-9792-1.



Javanbakht T., Laurent S., Stanicki D., Salzmann I. (2021). Rheological properties of superparamagnetic iron oxide nanoparticles. *Journal of Engineering Sciences*, Vol. 8(1), pp. C29–C37, doi: 10.21272/jes.2021.8(1).c4

Rheological Properties of Superparamagnetic Iron Oxide Nanoparticles

Javanbakht T.^{1*}, Laurent S.^{2,3}, Stanicki D.², Salzmann I.¹

¹Department of Chemistry and Biochemistry, Department of Physics, Concordia University, Richard J. Renaud Science Complex, 7141, Sherbrooke St., Montreal, Quebec, Canada;

²Laboratory of NMR and Molecular Imaging, University of Mons, Avenue Maistriau, 19, B-7000 Mons, Belgium;

³Center for Microscopy and Molecular Imaging (CMMI), 6041, Gosselies St., Belgium

Article info:

Received: March 25, 2021
 The final version received: June 18, 2021
 Accepted for publication: June 23, 2021

*Corresponding email:

taraneh.javanbakht@concordia.ca

Abstract. The present study focuses on the rheological properties of polyethylene glycol (PEG) modified, positively charged, and negatively charged superparamagnetic iron oxide nanoparticles (SPIONs) at different temperatures. We hypothesized that the surface properties of these nanoparticles in the water did not affect their rheological properties. These nanoparticles had not the same surface properties as SPIONs-PEG had not to charge on their surface whereas positively charged and negatively charged ones with amine and carboxyl groups as their surfaces had positive and negative surface charges, respectively. However, their rheological behaviors were not different from each other. The comparative rheological study of SPIONs revealed their pseudo-Newtonian behavior. The viscosity of SPIONs decreased with the increase in temperature. At low shear rates, the shear stress of SPIONs was independent of rate and increased with the increase of rate. Moreover, at high shear rates, the shear stress for PEG-SPIONs was more than those for positively charged and negatively charged SPIONs. These measurements also revealed that at high shear rates, the shear stress of samples decreased with the increase of temperature. The shear stress of samples decreased with the increase of shear strain and the temperature. We also observed that all the samples had the same amount of shear strain at each shear stress, which indicated the exact resistance of SPIONs to deformation. Furthermore, the shear modulus decreased with time for these nanoparticles. These results suggest that these nanoparticles are promising candidates with appropriate properties for fluid processing applications and drug vectors in biomedical applications.

Keywords: rheology, SPIONs, nanomaterials, surface charge, mechanical engineering.

1 Introduction

Superparamagnetic iron oxide nanoparticles (SPIONs) have been developed for diverse applications such as magnetic drug targeting, magnetic hyperthermia, MRI contrast agent, and photocatalytic applications. These nanoparticles are usually suspended in water. They have been studied for biomedical applications [1–5], whereas a seed-mediated growth method in a nonhydrolytic condition is needed to prepare semiconductor nanocomposites for photocatalytic applications [6].

The physicochemical and biological properties of SPIONs as separated materials or in nanocomposites have been widely studied [7–11]. SPIONs exhibit the phenomenon of superparamagnetism, which corresponds to their magnetization up to their saturation magnetization when an external magnetic field is applied. They no longer exhibit any residual magnetic interaction when the

magnetic field is removed. This property is size-dependent and generally manifests for nanoparticles with sizes smaller than 10 to 20 nm [5]. SPIONs can be targeted to the required area through external magnets and show interesting physical properties such as superparamagnetism, high field irreversibility, high saturation field, extra anisotropy contributions, or shifted loops after field cooling [12].

Two structural configurations are known for SPIONs: 1. a magnetic particle core usually made of magnetite, Fe₃O₄, or maghemite, γ -Fe₂O₃ coated with a biocompatible polymer, 2. nanoparticles precipitated inside a pore biocompatible polymer [13]. A polymer such as polyethylene glycol (PEG) is the best candidate for coating of SPIONs as it can reduce the natural reactivity of these nanoparticles and maintain their physical properties [14]. The coating acts to shield the magnetic particle from the surrounding environment and can also be

functionalized by attaching carboxyl and amine groups [15].

For an appropriate photocatalytic performance, iron oxides should possess a narrow bandgap value. Several techniques improve the photocatalytic performance of iron oxide semiconductor systems, such as composite heterostructure with narrow/wide bandgap, p-n heterojunctions, noble metal loading, plasmonic structure [16–18], magnetite nanoparticles can be either n-type or p-type semiconductors. However, they have the lowest resistivity among iron oxides because their bandgap is small [19].

Rheological properties of the composites of SPIONs with polymers were studied previously [11, 20–23]. However, the rheological behavior of these nanoparticles alone is needed to be investigated. Solubility is an essential characteristic of these nanoparticles for their rheological analysis. The recent synthesis of SPIONs showed that they have high solubility in water [11]. The stability of these nanoparticles depends on various factors such as their concentration, size, size polydispersity, colloidal stabilization efficiency, temperature, and magnetic field intensity [24].

This report describes the rheological behavior of three types of SPIONs at different temperatures. This work aims to investigate the rheological behavior of SPIONs coated with PEG having no charge on their surface, positively and negatively charged SPIONs at 20 °C, 40 °C, and 60 °C. To our knowledge, this is the first time that the rheological behavior of these nanoparticles is reported.

2 Research Methodology

2.1 Chemicals

We used these chemicals for the synthesis of SPIONs: methanol HPLC (ChemLab), acetone (ACS reagent), diethyl ether (ACS reagent), dimethylformamide anhydrous, n-[3-(trimethoxysilyl)propyl] ethylenediamine (TPED), which were purchased from Sigma-Aldrich. Diethylene glycol (DEG) and ferrous chloride tetrahydrate were purchased from Merck. Ferric chloride was purchased from Riedel-de Haën. 1-ethyl-3-(3-dimethylaminopropyl) carbodiimide (EDC) and tetramethylammonium hydroxide were purchased from TCI Chemicals. 3-(triethoxysilyl)propyl succinic anhydride (TEPSA) was purchased from ABCR as described previously [10].

2.2 Synthesis of iron oxide cores

Synthesis of iron oxide cores was performed as described in our previous work [10]. Briefly, magnetite nanoparticles (NPs) were prepared by co-precipitation of iron salts in DEG [19] with mixing 8.9 g of ferrous chloride tetrahydrate salt and 9.1 ml ferric chloride in DEG (250 ml) and heating at 170 °C under a nitrogen atmosphere. After 15 min at that temperature, sodium hydroxide (15 g) was added, and the solution was stirred for 1 h at 170 °C. After cooling the mixture, the magnetic particles were isolated from the solution by magnetic decantation, and the black precipitate was washed with an aqueous solution of nitric acid (200 ml, 1 M). The dispersion of magnetite in deionized water was performed,

and the dispersion was sonicated for 45 minutes and centrifuged (16.5 g; 45 min) to remove aggregates [10].

2.3 Preparation of nanoparticles

PEG-modified nanoparticles, TPED-modified nanoparticles (positively charged SPIONs), and TEPSA-modified magnetic nanoparticles (negatively charged SPIONs) were prepared as described previously [10, 11].

For the preparation of PEG-modified nanoparticles, O-(2-aminoethyl)-O'-methyl-polyethyleneglycol (120 mmol; 90 mg) was added to EDC (200 mmol; 38 mg), and TEPSA-modified ferrofluid (150 mM in iron; 5 ml) was added to the mixture. The pH was then adjusted to 7.5. After stirring the mixture for 15h at room temperature, the suspension was purified by membrane filtration [10].

Preparation of positively charged SPIONs was done with grafting N-[3-(trimethoxysilyl)propyl] ethylenediamine (TPED) to the nanoparticles by adding TPED to a suspension of nanoparticles in nitric acid ([Fe] = 25 mM) at 50 °C. The mixture was stirred for 2 h under boiling conditions. Then it was cooled to room temperature. In the next step, the suspension was purified by membrane filtration and centrifuged (16.5 g; 45 minutes) [11].

For the preparation of negatively charged SPIONs, the suspension of obtained NPs (20 ml; [Fe] 1/4 250 mM) was diluted with dimethylformamide (50 ml). Then water was eliminated under reduced pressure. After adding TEPSA (25 mmol; 7.1 ml) to the nanoparticle dispersion in DMF, water was added (4.3 ml). The solution of TMAOH (1 M; 2.5 mmol; 2.5 ml) was prepared at room temperature under stirring and heated to 100 °C for 24 h. The magnetic nano-objects were collected after pouring the suspension in an acetone/diethyl ether mixture (50/50). Acetone was used for washing the sample, and the precipitate was dispersed in water. Membrane filtration (membrane cut-off: 30 kDa) was performed. The NPs were then centrifuged (16 500g; 45 minutes) [11].

The surface charge measurements of positively charged and negatively charged SPIONs were reported in our previous work [25]. PEG-modified SPIONs were prepared in the current work to neutralize the surface charge of NPs in TEPSA-modified ferrofluid [26].

2.4 Rheological measurements

The rheological properties of SPIONs were studied using an Anton Paar MCR-302 rheometer. 5 mL of each sample in millipore water were prepared. Each sample contained 12 mg of magnetite nanoparticles. The concentration of SPIONs in water was 0.01 M. This concentration of SPIONs was chosen as it was low enough to be appropriate for biomedical applications, and the same concentration coated with polyethylene glycol was studied in our previous work [11]. 4 mL of each prepared sample were used for rheology. The rotational mode was applied for samples. The torque was measured at different temperatures for all the tests [27].

2.5 Statistical analysis

The QtiPlot software was used to determine the mean values and standard deviations [7]. The data were checked to be statistically significant [28]. The errors were calculated with the QtiPlot software. The data were close to each other, and the standard deviation values were small. The error bars bigger than the expected values were

attributed to the presence of polymer in the PEG-SPIONs or that of carboxyl at the surface of the neg-SPIONs, which could affect the rheological properties of nanoparticles.

3 Results

Figure 1 shows the viscosity of SPIONs versus the shear rate at 20 °C, 40 °C, and 60 °C. The applied shear rate was between 0 and 1000 s⁻¹.

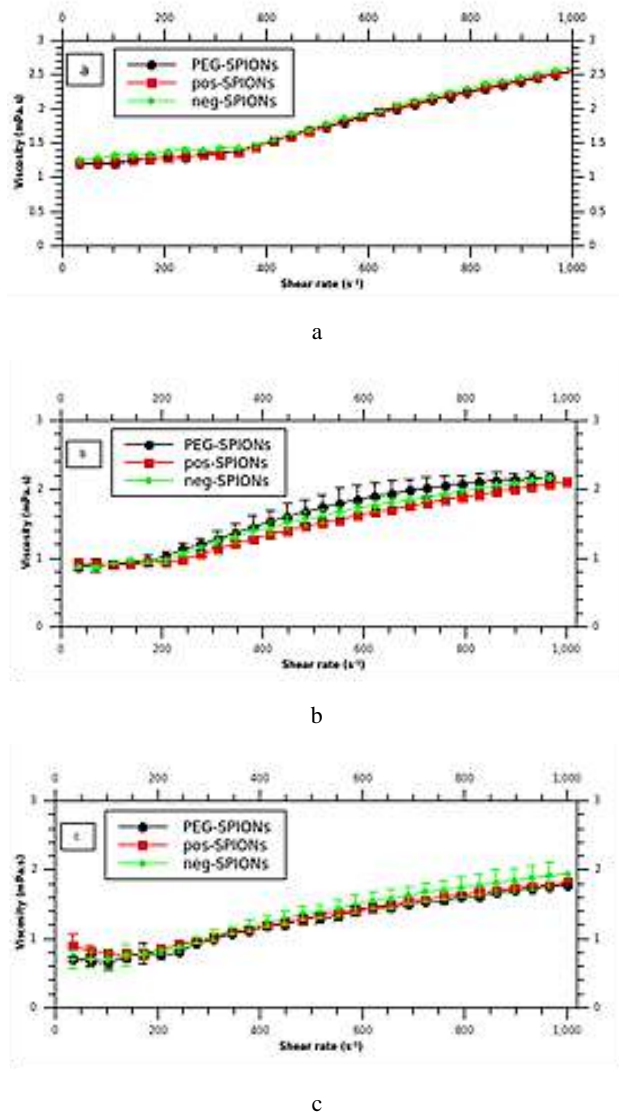


Figure 1 – Viscosity of SPIONs versus shear rate at 20 °C (a), 40 °C (b), and 60 °C (c)

As shown in Figure 1, the viscosity of SPIONs decreased with the increase of temperature by comparison of (a), (b), and (c). Moreover, their viscosity η increased between 100 and 1000 s⁻¹. Pseudo-Newtonian behavior at low shear rate is observed when shear viscosity does not change significantly, and it is invariant with the change of shear rate [29, 30].

Therefore, these nanoparticles showed a pseudo-Newtonian behavior at a shear rate less than 250 s⁻¹, increasing shear viscosity at sufficiently high shear rates.

Figure 2 shows the change of viscosity of each SPION versus shear rate at different temperatures.

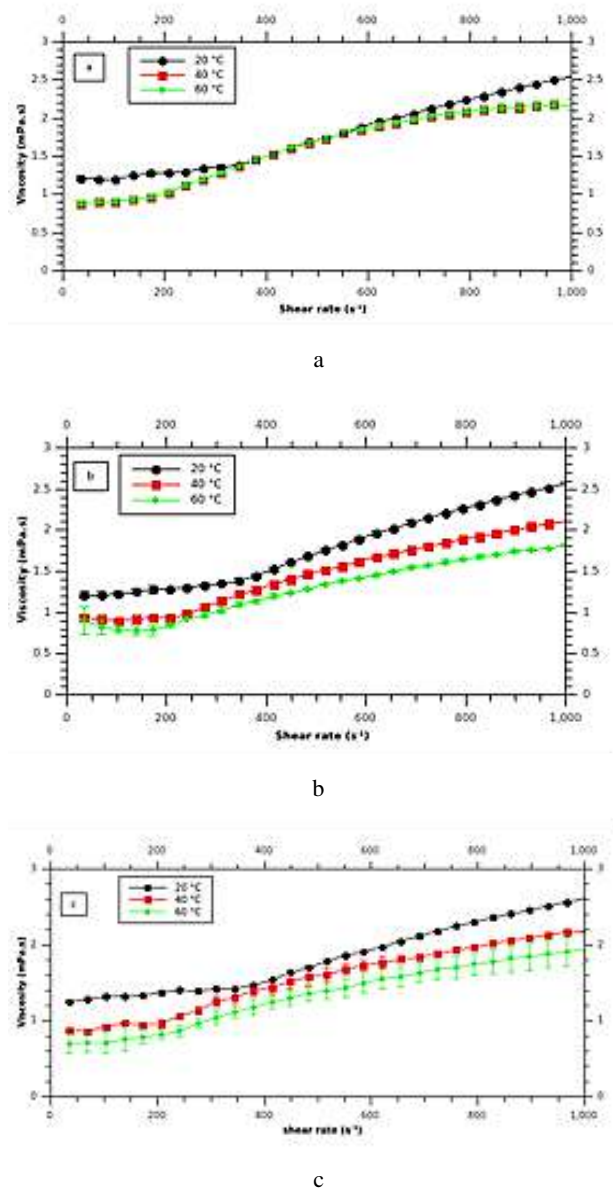


Figure 2 – Dynamic viscosity of PEG-SPIONs, positively charged SPIONs, and negatively charged SPIONs versus shear rate at 20 °C (a), 40 °C (b), and 60 °C (c)

As seen in this figure, the viscosity of SPIONs decreased with the increase of temperature. Although the same expected effect was observed for PEG-SPIONs at 40 °C and 60 °C in comparison with 20 °C, there was not a significant difference between the viscosity of these nanoparticles at 40 °C and 60 °C. This may be due to their aggregation of PEG-SPIONs at 60 °C.

The shear stress versus shear rate curves at 20 °C, 40 °C, and 60 °C are displayed in Figure 3.

As shown in Figure 3, the shear stress of increased with the increase of shear rate. At high shear rates, the shear stress for PEG-SPIONs was more than those for positively charged and negatively charged SPIONs. At high shear rates, the shear stress of samples decreased with the increase of temperature.

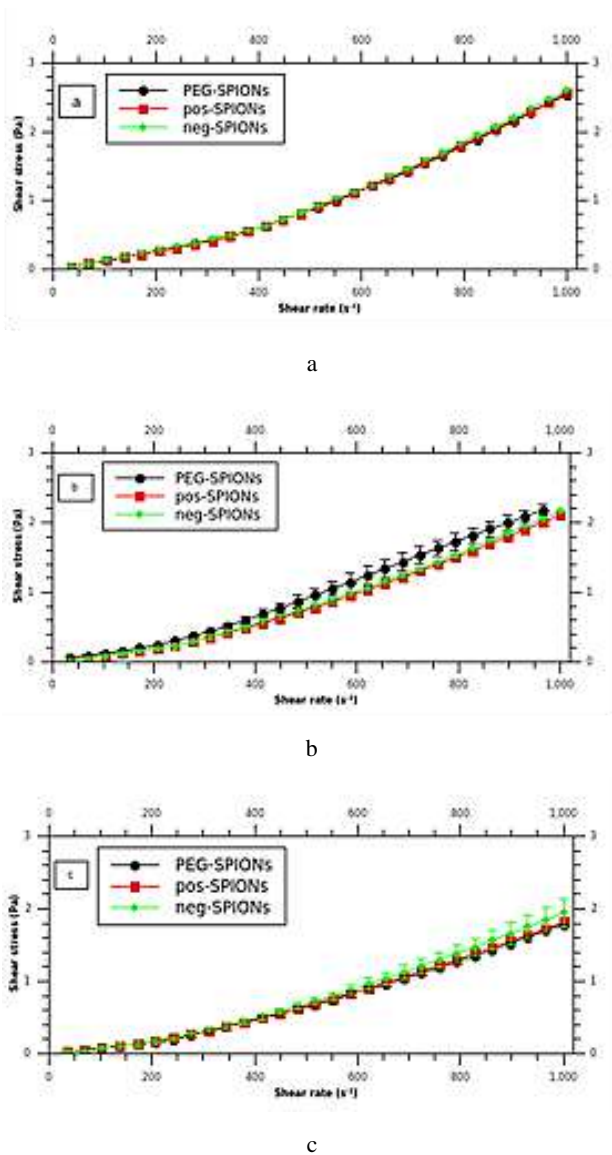


Figure 3 – Shear stress versus shear rate at 20 °C (a), 40 °C (b), and 60 °C (c)

The size ratio values of positively charged and negatively charged SPIONs in nm compared to those of PEG-SPIONs measured previously with dynamic light scattering (DLS) and transmission electron microscopy (TEM) are presented in Table 1.

Table 1 – The size ratio values of positively charged and negatively charged SPIONs in nm compared to those of PEG-SPIONs

Method	Positively charged SPIONs	Negatively charged SPIONs
DLS	1.6	0.8
TEM	0.8	1.0

Comparing the results presented in Table 1, a small difference was observed in the TEM data for the size ratio values of positively and negatively charged SPIONs compared to PEG-SPIONs, whereas this difference was more for their DLS data. The larger size ratio of positively charged SPIONs was reported due to their possible aggregation [10].

Figure 4 shows torque versus time curves at 20 °C, 40 °C, and 60 °C. The torque values increased with time for SPIONs, as seen in this figure. As the concentration of samples was low, their high elasticity caused the increase of torque with time. As expected, the torque values decreased with the increase of time temperature.

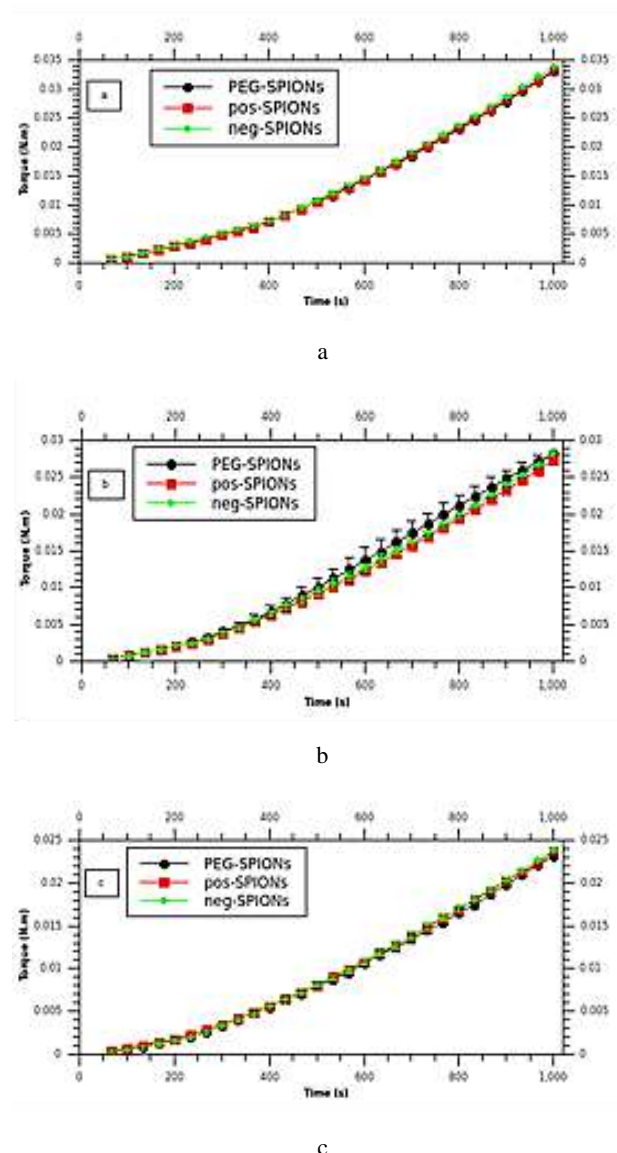
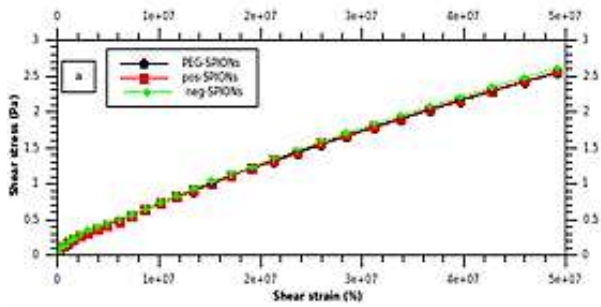


Figure 4 – Torque versus time at 20 °C (a), 40 °C (b), and 60 °C (c)

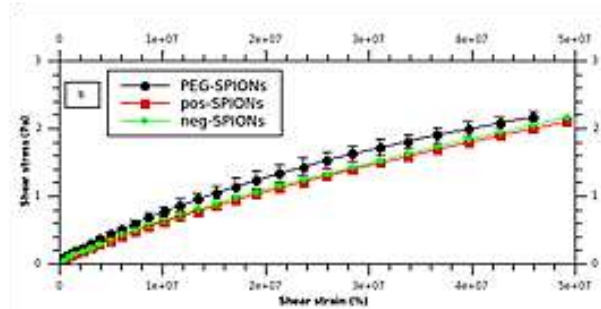
The shear stress versus shear strain curves of SPIONs at 20 °C, 40 °C, and 60 °C are displayed in Figure 5.

As shown in this figure, the shear stress of samples decreased with shear strain and temperature increase. However, all the samples had the same amount of shear strain at each shear stress. This indicates that the nanoparticles were not deformed, and their resistance to the deformation was the same, although they had different surface properties that we analyzed in our previous works [10, 11].

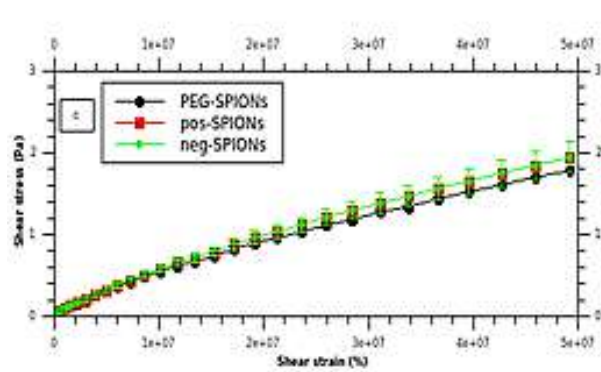
Figure 6 shows shear stress versus shear strain curves of SPIONs at different temperatures.



a



b

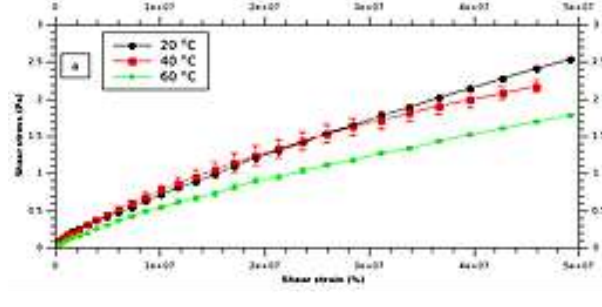


c

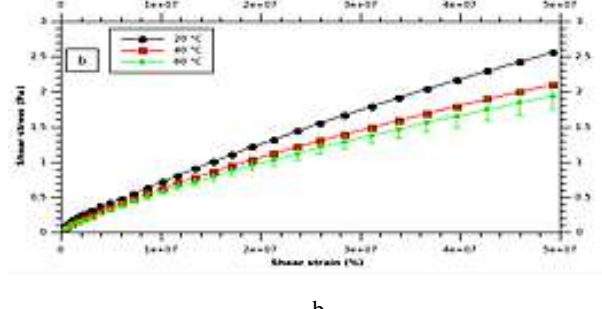
Figure 5 – Shear stress versus shear strain at 20 °C (a), 40 °C (b), and 60 °C (c)

As shown in Figure 6, less shear stress is required with the increase of temperature for the deformation of SPIONs. The deformation of PEG-SPIONs at 60 °C is more than that at 40 °C, whereas no change was observed for the deformation of positively and negatively charged SPIONs at these temperatures. This may be due to the surface charges of these SPIONs that hinder their deformation with the increase of temperature.

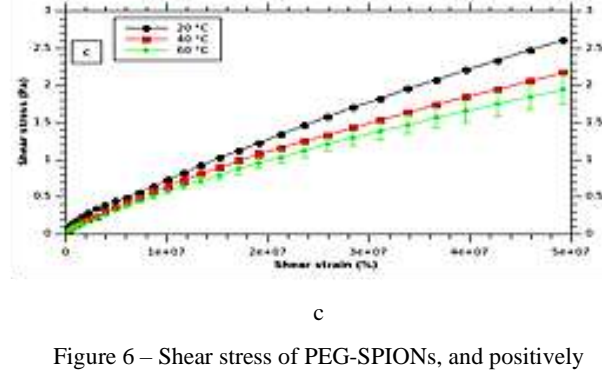
Figure 7 shows the shear modulus versus time of SPIONs at 20 °C, 40 °C, and 60 °C. As shown in this figure, shear modulus, or the ratio of shear stress to shear strain, at a low duration of time (less than 200 s), decreases with the increase of temperature. This behavior has been reported for metal-based materials previously [31]. The trend for SPIONs was not observed at low temperatures in this figure, which may be due to the difference in the surface properties of these nanoparticles. This can explain why different charged SPIONs in comparison with PEG-SPIONs have different responses to shear stress.



a



b



c

Figure 6 – Shear stress of PEG-SPIONs, and positively at 20 °C (a), 40 °C (b), and 60 °C (c)

4 Discussion

Shear modulus was very low for SPIONs, and its values decreased with time for all the samples. Moreover, the shear modulus was independent of time after 400 s because this modulus did not change with time after this duration.

An important parameter that reflects the material's ability to resist deformation is shear modulus, which is the ratio of shear stress to shear strain. Shear modulus decreases with time, but it becomes constant after 8 minutes for all the samples. Moreover, this parameter decreases with the increase of temperature. This means that the deformation of SPIONs can happen by applying less amount of shear stress as the temperature increases.

The decrease of viscosity with the increase of temperature has been previously reported [32]. With the increase of temperature, Brownian motion enhances, which caused the decreased interaction between the nanoparticles. Therefore, the flow resisting force and heat resistance in samples decrease. This phenomenon is helpful to improve the efficiency of SPIONs as solar absorbers at high temperatures [33].

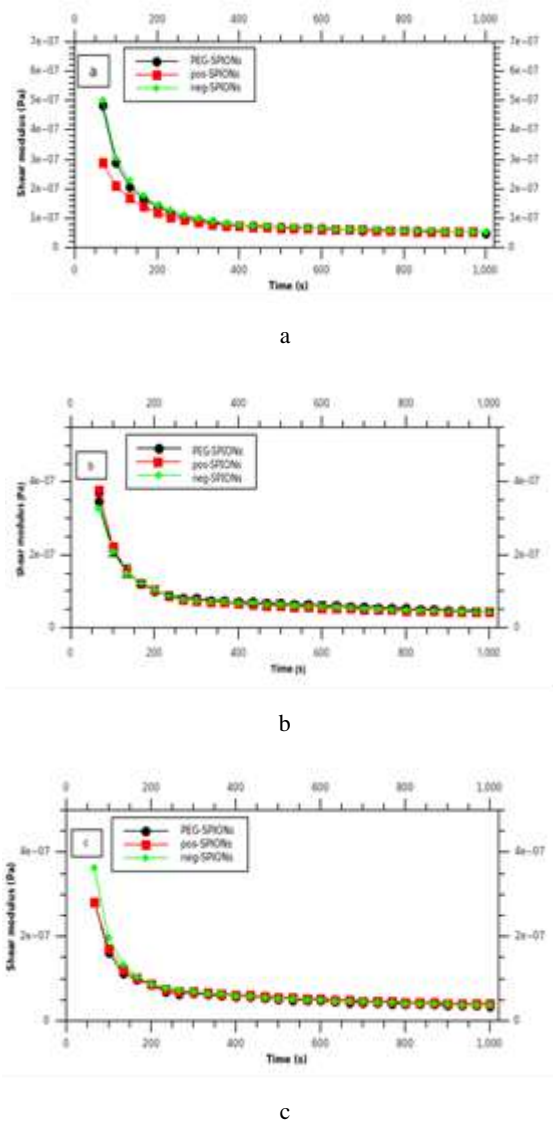


Figure 7 – Shear modulus versus time at 20 °C (a), 40 °C (b), and 60 °C (c)

The rheological behavior of SPIONs depends on their physical properties. Their pseudo-Newtonian behavior can be affected by the volume, size distribution, and shape of the particles. It should be noted that this behavior can also depend on the concentration, in proportion to some maximum packing fraction partly controlled by the form of the particle size distribution [34].

According to our previous investigation with dynamic light scattering, the average sizes of PEG-SPIONs, positively charged and negatively charged SPIONs were 19.3 ± 0.1 nm, 30.6 ± 0.1 nm, and 15.7 ± 0.2 nm, respectively [10].

The independence of shear stress from the shear rate at low rates for SPIONs corresponds to their yield behavior, which is accounted for by their elastic behavior [35].

This was reported for iron oxide suspensions in silicone oil previously [36]. The identical behavior of SPIONs concerning the independence of shear stress from the shear rate at low rates indicates that they have the same rheological behavior at a constant temperature.

At high shear rates for a given shear strain, the flow stress decreases with increasing temperature. This phenomenon is more pronounced at higher strain rates and more significant strains and can be attributed to the temperature rise generated in the samples because of deformation heating [37].

The increase of torque with time, as observed in our experiments, is due to the elasticity of the samples. [38]. More investigation is required to determine the viscoelastic properties of SPIONs with oscillatory rheology.

We observed that the shear modulus for SPIONs decreased with the increase of temperature. The decrease of shear modulus with increased temperature has been reported previously for other materials [39][40]. The rheological analysis of SPIONs in oscillatory mode will be performed in further investigation.

Another important topic to consider is that the optimal surface charge of SPIONs for their diverse applications should be close to neutral or slightly negative [41].

However, the surface charge affects the zeta potential and that, in turn, the zeta potential determines the solution stability of these nanoparticles [7, 11]. We seek to improve the application of these nanoparticles as future semiconductors in solar cell fabrication as similar nanoparticles, when prepared with irradiation, could have a uniform shape appropriate for this application [42]. The next step will be to determine their electrochemical properties. As the nanostructure of materials impacts their electrical characteristics, it would be necessary to investigate the effect of the structure of these nanoparticles or other nanoparticles on their physical properties for their applications in solar cells [42–45].

Previously, some devices' physical and biological properties were studied with different methods [46–49]. The physicochemical properties of some polymers and nanomaterials have also been investigated during recent years [50–53]. The rheological properties of some biological materials [54–57] will be studied in our subsequent investigation.

The viscosity of blood at 37 °C is around 3 mPa·s. The measured viscosity of SPIONs in this study was less than that of blood [58, 59]. Therefore, these nanoparticles have been appropriate tools to be used in biomedical applications. More investigations are required to determine the rheological properties of SPIONs in oscillatory mode and those of the materials used in these devices or conjugation with these nanoparticles.

5 Conclusions

The rheological properties of SPIONs dispersed in water affect their behavior for their various applications. These properties were analyzed and designed to meet the requirements of these applications.

The obtained results indicate that the surface properties of SPIONs do not affect their rheological properties at different temperatures as three types of SPIONs with different surface properties that we reported previously showed the same rheological behavior.

Some issues are required to be addressed, and among these, the viscoelasticity of these nanoparticles is an important rheological property and of great interest as their viscosity affects the drug delivery output when these nanoparticles are used as drug vectors. It is also required to proceed with novel functionalizations of SPIONs to

obtain new nanoparticles with surface modifications that can affect their rheological behavior. Progress in this issue will allow precise tuning of the properties of these nanoparticles for their fluid processing and semiconductor applications.

References

1. Rosensweig, R. W. (1985). *Ferrohydrodynamics (Cambridge Monographs on Mechanics and Applied Mathematics)*. Cambridge, Cambridge University Press.
2. Sabale, S., Kandesar, P., Jadhav, V., Komorek, R., Motkuri, R. K., Yu, W.-Y. (2017). Recent developments in the synthesis, properties, and biomedical applications of core/shell superparamagnetic iron oxide nanoparticles with gold. *Biomaterials Science*, Vol. 5(11), pp. 2212–2225. <https://doi.org/10.1039/c7bm00723j>.
3. Lin, M. M., Kim, D. K., Haj, A. J. E., Dobson, J. (2009). Development of superparamagnetic iron oxide nanoparticles (SPIONs) for translation to clinical applications. *IEEE Transactions on NanoBioscience*, Vol. 7(4), pp. 298–305. <https://doi.org/10.1109/TNB.2008.2011864>.
4. Kaushik, S., Thomas, J., Panwar, V., Ali, H., Chopra, V., Sharma, A., Tomar, R., Ghosh, D. (2020). In situ biosynthesized superparamagnetic iron oxide nanoparticles (SPIONs) induce efficient hyperthermia in cancer cells. *ACS Applied Bio Materials*, Vol. 3(2), pp. 779–788. <https://doi.org/10.1021/acsabm.9b00720>.
5. Wahajuddin, A. S. (2012). Superparamagnetic iron oxide nanoparticles: magnetic nanoplatforms as drug carriers. *International Journal of Nanomedicine*, Vol. 7, pp. 3445–3471. <https://doi.org/10.2147/IJN.S30320>.
6. Chiu, W., Khiew, P., Cloke, M., Isa, D., Lim, H., Tan, T., Huang, N., Radiman, S., Abd-Shukor, R., Hamid, M.A.A., Chia, C. (2010). Heterogeneous seeded growth: synthesis and characterization of bifunctional Fe₃O₄/ZnO core/shell nanocrystals. *Journal of Physical Chemistry C*, Vol. 114(18), pp. 8212–8218. <https://doi.org/10.1021/jp100848m>.
7. Graczyk, H., Bryan, L. C., Lewinski, N., Suarez, G., Coullerez, G., Bowen, P., Riediker, M. (2015). Physicochemical Characterization of Nebulized Superparamagnetic Iron Oxide Nanoparticles (SPIONs). *Journal of Aerosol Medicine and Pulmonary Drug Delivery*, Vol. 28(1), pp. 43–51. <https://doi.org/10.1089/jamp.2013.1117>.
8. Mieloch, A. A., Zurawek, M., Giersig, M., Roswadowska, N., Rybka, J. D. (2020). Bioevaluation of superparamagnetic iron oxide nanoparticles (SPIONs) functionalized with dihexadecyl phosphate (DHP). *Scientific Reports*, Vol. 10(1), 2725. <https://doi.org/10.1038/s41598-020-59478-2>.
9. Belanova, A. A., Gavalas, N., Makarenko, Y. M., Belousova, M. M., Soldatov, A. V., Zolotukhin, P. V. (2018). Physicochemical properties of magnetic nanoparticles: implications for biomedical applications in vitro and in vivo. *Oncology Research and Treatment*, Vol. 41(3), pp. 139–143. <https://doi.org/10.1159/000485020>.
10. Javanbakht, T., Laurent, S., Stanicki, D., Frenette, M. (2020). Correlation between physicochemical properties of superparamagnetic iron oxide nanoparticles and their reactivity with hydrogen peroxide. *Canadian Journal of Chemistry*, Vol. 98(10), pp. 601–608. <https://doi.org/10.1139/cjc-2020-0087>.
11. Javanbakht, T., Laurent, S., Stanicki, D., David, E. (2019). Related physicochemical, rheological, and dielectric properties of nanocomposites of superparamagnetic iron oxide nanoparticles with polyethyleneglycol. *Journal of Applied Polymer Science*, Vol. 137(3), pp. 48280–48289. <https://doi.org/10.1002/app.48280>.
12. Grancharov, S. G., Zeng, H., Sun, S. H., Wang, S. X., O'Brien, S., Murray, C. B., Kirtley, J. R. G., Held, A. (2005). Bio-functionalization of monodisperse magnetic nanoparticles and their use as biomolecular labels in a magnetic tunnel junction based sensor. *Journal of Physical Chemistry B*, Vol. 109(26), pp. 13030–13035. <https://doi.org/10.1021/jp051098c>.
13. Hans, M. L., Lowman, A. M. (2002). Biodegradable Nanoparticles for Drug Delivery and Targeting. *Current Opinion in Solid State and Materials Science*, Vol. 6(4), pp. 319–327. [https://doi.org/10.1016/S1359-0286\(02\)00117-1](https://doi.org/10.1016/S1359-0286(02)00117-1).
14. Solar, P., González, G., Vilos, C., Herrera, N., Juica, N., Moreno, M., Simon, F., Velásquez, L. (2015). Multifunctional polymeric nanoparticles doubly loaded with SPION and ceftiofur retain their physical and biological properties. *Journal of Nanobiotechnology*, Vol. 13(14), pp. 14–25. <https://doi.org/10.1186/s12951-015-0077-5>.
15. Andrade, A., Ferreira, R., Fabris, J., Domingues, R. (2011). Coating Nanomagnetic Particles for Biomedical Applications. *Biomedical engineering - Frontiers and Challenges*, North Dakota, University of North Dakota.
16. Qu, Y., Duan, X. (2013). Progress, challenge and perspective of heterogeneous photocatalysts. *Chemical Society Reviews*, Vol. 42(7), pp. 2568–2580. <https://doi.org/10.1039/C2CS35355E>.
17. Xu, P., Zeng, G. M., Huang, D. L., Feng, C. L., Hu, S., Zhao, M. H., Lai, C., Wei, Z., Huang, C., Xie, G. X., Liu, Z. F. (2012). Use of iron oxide nanomaterials in wastewater treatment: a review. *Science of the Total Environment*, Vol. 424, pp. 1–10. <https://doi.org/10.1016/j.scitotenv.2012.02.023>.
18. Wang, Y., Wang, Q., Zhan, X., Wang, F., Safdar, M., He, J. (2013). Visible light driven type II heterostructures and their enhances photocatalysis properties: a review. *Nanoscale*, Vol. 5(18), pp. 8326–8339. <https://doi.org/10.1039/c3nr01577g>.
19. Boxall, C., Kelsall, G. Zhang, Z. (1996). Photoelectrophoresis of colloidal iron oxides. Part 2. – Magnetite (Fe₃O₄). *Journal of the Chemical Society, Faraday Transactions*. Vol. 92(5), pp. 791–802. <https://doi.org/10.1039/FT9969200791>.

20. Brullot, W., Reddy, N. K., Wouters, J., Valev, V. K., Goderis, B., Vermant, J., Verbiest, T. (2012). Versatile ferrofluids based on polyethylene glycol coated iron oxide nanoparticles. *Journal of Magnetism and Magnetic Materials*, Vol. 324(11), pp. 1919–1925. <https://doi.org/10.1016/j.jmmm.2012.01.032>.
21. Gonçalves, L. C., Seabra, A. B., Pelegrino, M. T., de Araujo, D. R., Bernardes, J. S., Haddad, P. S. (2017). Superparamagnetic iron oxide nanoparticles dispersed in Pluronic F127 hydrogel: potential uses in topical applications. *RSC Advances*, Vol. 7(24), pp. 14496–14503. <https://doi.org/10.1039/C6RA28633J>.
22. Nejatpour, M., Unal, U., Acar, H. Y. (2020). Bidisperse magneto-rheological fluids consisting of functional SPIONs added to commercial MRF. *Journal of Industrial and Engineering Chemistry*, Vol. 91, pp. 25, 110–120. <https://doi.org/10.1016/j.jiec.2020.07.040>.
23. Yoon, K. Y. (2012). *The Design and Control of Stability and Magnetic Properties of Imaging Nanoparticles*. PhD thesis, University of Texas, Austin.
24. Socoliuc, V., Bica, D., Vekas, L. (2011). Magnetically induced phase condensation with asymptotic critical temperature in an aqueous magnetic colloid. *Magneto hydrodynamics*, Vol. 47(2), pp. 201–206. <https://doi.org/10.22364/mhd.47.2.12>.
25. Stanicki, D., Boutry, S., Laurent, S., Wacheul, L., Nicolas, E., Crombez, D., Elst, L. V., Lafontaine, D. L. J., Muller, R. N. (2014). Carboxy-silane coated iron oxide nanoparticles: A convenient platform for cellular and small animal imaging. *Journal of Materials Chemistry B*, Vol. 2(4), pp. 387–397. <https://doi.org/10.1039/C3TB21480J>.
26. Cu, Y., Saltzman, W. M. (2009). Controlled Surface Modification With Poly(ethylene)glycol Enhances Diffusion of PLGA Nanoparticles in Human Cervical Mucus. *Molecular Pharmacology*, Vol. 6(1), pp. 173–181. <https://doi.org/10.1021/mp8001254>.
27. Fathurrohman, M. I., Maspanger, D. R., Sutrisno, S. (2015). Vulcanization Kinetics and Mechanical Properties of Ethylene Propylene Diene Monomer Thermal Insulation. *Bulletin of Chemical Reaction Engineering and Catalysis*, Vol. 10(2), pp. 104–110. <https://doi.org/10.9767/bcrec.10.2.6682.104-110>.
28. Javanbakht, T., Ghane-Motlah, B., Sawan, M. (2020). Comparative study of antibiofilm activity and physicochemical properties of microelectrode arrays. *Microelectronic Engineering*, Vol. 229, 111305. <https://doi.org/10.1016/j.mee.2020.111305>.
29. Haward, S. J., McKinley, J. H. (2012). Stagnation point flow of wormlike micellar solutions in a microfluidic cross-slot device: Effects of surfactant concentration and ionic environment. *Physical Review E*, Vol. 85(3), 031502. <https://doi.org/10.1103/PhysRevE.85.031502>.
30. Jamali, S., Armstrong, R. C., Mc Kinley, G. H. (2019). Multiscale nature of thixotropy and rheological hysteresis in attractive colloidal suspensions under shear. *Physical Review Letters*, Vol. 123(24), 248003. <https://doi.org/10.1103/PhysRevLett.123.248003>.
31. Liu, Z. Y., Wang, G., Chan, K. C., Ren, J. L., Huang, Y. J., Bian, X. L., Xu, X. H., Zhang, D. S., Gao, Y. L., Zhai, Q. J. (2013). Temperature dependent dynamics transition of intermittent plastic flow in a metallic glass. I. Experimental investigations. *Journal of Applied Physics*, Vol. 114, 033520. <https://doi.org/10.1063/1.4815943>.
32. Chen, H. J., Wang, Y. M., Qu, J. M., Hong, R. Y., Li, H. Z. (2011). Preparation and characterization of silicon oil based ferrofluid. *Applied Surface Science*, Vol. 257(24), pp. 10802–10807. <https://doi.org/10.1016/j.apsusc.2011.07.103>.
33. Han, D., Meng, Z., Wu, D., Zhang, C., Zhu, H. (2011). Thermal properties of carbon black aqueous nanofluids for solar absorption. *Nanoscale Research Letters*, Vol. 6(1), pp. 457. <https://doi.org/10.1186/1556-276X-6-457>.
34. Barnes, H.A. (1989). Shear-Thickening (“Dilatancy”) in Suspensions of Nonaggregating Solid Particles Dispersed in Newtonian Liquids. *Journal of Rheology*, Vol. 33(2), pp. 329–366. <https://doi.org/10.1122/1.550017>.
35. Vu-Bac, N., Areias, P., Rabczuk, T. (2016). A multiscale multisurface constitutive model for the thermo-plastic behavior of polyethylene. *Polymer*, Vol. 105, pp. 327–338. <https://doi.org/10.1016/j.polymer.2016.10.039>.
36. Yang, M. C., Scriven, L. E., Makosco, C. W. (1986). Some rheological measurements on magnetic iron oxide suspensions in silicone oil. *Journal of Rheology*, Vol. 30(5), pp. 1015–1029. <https://doi.org/10.1122/1.549892>.
37. Chen, T. -H., Tsai, C. -K., Fang, T. -H. (2013). Dynamic shear characteristic and fracture failure of inconel 690 alloy under different high strain rates and temperatures. *Advances in Material Science and Engineering*, Vol. 2013, 382503. <https://doi.org/10.1155/2013/382503>.
38. Sumith, S., Sangam, K., Kannan, K., Shankar, K. (2020). Prediction of nonlinear viscoelastic behaviour of simulative soil for deep-sea sediment using a thermodynamically compatible model. *Inverse Problems in Science and Engineering*, Vol. 28(6), pp. 1741–5977. <https://doi.org/10.1080/17415977.2019.1648452>.
39. Todd, T. P. (1973). Effect of cracks on elastic properties of low porosity rocks. PhD thesis, University of Toronto.
40. Hua, X., Wang, L., Yang, S. (2019). Molecular dynamics simulation of improving the physical properties of polytetrafluoroethylene cable insulation materials by boron nitride nanoparticle under moisture-temperature-electric fields conditions. *Polymers*, Vol. 11(6), pp. 971–985. <https://doi.org/10.3390/polym11060971>.
41. Durymanov, M. O., Rosenkranz, A. A., Sobolev, A. S. (2015). Current approaches for improving intratumoral accumulation and distribution of nanomedicines. *Theranostics*, Vol. 5(9), pp. 1007–1020. <https://doi.org/10.7150/thno.11742>.
42. Hussain, D. H., Abdulah, H. I., Rheima, A. M. (2016). Synthesis and characterization of γ -Fe₂O₃ nanoparticles photoanode by novel method for dye sensitized solar cell. *International Journal of Scientific Research and Publications*, Vol. 6(10), pp. 26–31.
43. Cai, F., Zhang, S., Yuan, Z. (2015). Effect of magnetic gamma-iron oxide nanoparticles on the efficiency of dye-sensitized solar cells. *RSC Advances*, Vol. 5(53), pp. 42869–42874. <https://doi.org/10.1039/C5RA05936D>.
44. Tuharin, K., Turek, Z., Zanařka, M., Kudrna, P., Tichý, M. (2020). Iron oxide and iron sulfide films prepared for dye-sensitized solar cells. *Materials*, Vol. 13(8), 1797. <https://doi.org/10.3390/ma13081797>.

45. Tharwat, M. M., Almalki, A., Mahros, A. M. (2021). Plasmon-enhanced sunlight harvesting in thin-film solar cell by randomly distributed nanoparticle array. *Materials*, Vol. 14(6), 1380. <https://doi.org/10.3390/ma14061380>.
46. Ghane-Motlagh, B., Javanbakht, T., Shoghi, F., Wilkinson, K. J., Martel, R., Sawan, M. (2016). Physicochemical properties of peptide-coated microelectrode arrays and their in vitro effects on neuroblast cells. *Materials Science and Engineering C*, Vol. 68, pp. 642–650. <https://doi.org/10.1016/j.msec.2016.06.045>.
47. Djavanbakht, T., Carrier, V., André, J. -M., Barchewitz, R., Troussel, P. (2000). Effets d'un chauffage thermique sur les performances de miroirs multicouches Mo/Si, Mo/C et Ni/C pour le rayonnement X mou. *Journal de Physique IV France*, Vol. 10, pp. 281–287. <https://doi.org/10.1051/jp4:20001031>.
48. Tsutsumi, Y., Niinomi, M., Nakai, M., Shimabukuro, M., Ashida, M., Chen, P., Doi, H., Hanawa, T. (2016). Electrochemical surface treatment of a β -titanium alloy to realize an antibacterial property and bioactivity. *Metals*, Vol. 6(4), 76. <https://doi.org/10.3390/met6040076>.
49. Kiran, A. S. K., Sireesha, M., Ramalingam, R., Kizhakeyil, A., Verma, N. K., Lakshminarayanan, R., Kumar, T. S. S., Doble, M., Ramakrishna, S. (2019). Modulation of biological properties by grain refinement and surface modification on titanium surfaces for implant-related infections. *Journal of Materials Science*, Vol. 54(20), pp. 13265–13282. <https://doi.org/10.1007/s10853-019-03811-2>.
50. Javanbakht, T., Bérard, A., Tavares, J. R. (2016). Polyethylene glycol and poly (vinyl alcohol) hydrogels treated with photo-initiated chemical vapor deposition. *Canadian Journal of Chemistry*, Vol. 94(9), pp. 744–750. <https://doi.org/10.1139/cjc-2016-0229>.
51. Javanbakht, T., David, E. (2020). Rheological and physical properties of a nanocomposite of graphene oxide nanoribbons with polyvinyl alcohol. *Journal of Thermoplastic Composite Materials*, 0892705720912767. <https://doi.org/10.1177/0892705720912767>.
52. Javanbakht, T., Hadian, H., Wilkinson, K. J. (2020). Comparative study of physicochemical properties and antibiofilm activity of graphene oxide nanoribbons. *Journal of Engineering Sciences*, Vol. 7(1), pp. C1–C8. [https://doi.org/10.21272/jes.2020.7\(1\).c1](https://doi.org/10.21272/jes.2020.7(1).c1).
53. Javanbakht, T., Sokolowski, W. (2015). *Thiolene/Acrylate Systems for Biomedical Shape-Memory Polymers in Shape Memory Polymers for Biomedical Applications (Ed. L'H Yahia)*, pp. 157–166, Sawston, Cambridge, Woodhead Publishing.
54. Sicilia, G., Grainger-Boulby, C., Francini, N., Magnusson, J. P., Saeed, A. O., Fernández-Trillo, F., Spain, S. G., Alexander, C. (2014). Programmable polymer-DNA hydrogels with dual input and multiscale responses. *Biomaterial Sciences*, Vol. 2, pp. 203–211. <https://doi.org/10.1039/C3BM60126A>.
55. Bravo-Anaya, L. M., Pignon, F., Martínez, F. A. S., Rinaudo, M. (2016). Rheological properties of DNA molecules in solution: molecular weight and entanglement influences. *Polymers*, Vol. 8(8), 279. <https://doi.org/10.3390/polym8080279>.
56. Djavanbakht, T., Jolès, B., Laigle, A. (2000). Intracellular stability of antisense oligonucleotides protected by the d(GCGAAGC). *Biomedical Society Transactions*, Vol. 28, p. A201. <https://doi.org/10.1042/bst028a201c>.
57. Murray, B. S. (2011). Rheological properties of protein films. *Current Opinion in Colloid and Interface Science*, Vol. 16(1), pp. 27–35. <https://doi.org/10.1016/j.cocis.2010.06.005>.
58. Farina, A., Fasano, A., Rossi, F. (2021). Mathematical models for some aspects of blood microcirculation. *Symmetry*, Vol. 13, 1020. <https://doi.org/10.3390/sym13061020>.
59. Hijikata, W., Rao, J., Abe, S., Takatani, S., Shinshi, T. (2015). Estimating flow rate using the motor torque in a rotary blood pump. *Sensors and Materials*, Vol. 27(4), pp. 297–308. <https://doi.org/10.18494/SAM.2015.1128>.



Hurey I., Gurey V., Bartoszek M., Hurey T. (2021). Formation of residual stresses during discontinuous friction treatment. *Journal of Engineering Sciences*, Vol. 8(1), pp. C38–C44, doi: 10.21272/jes.2021.8(1).c5

Formation of Residual Stresses during Discontinuous Friction Treatment

Hurey I.¹[0000-0002-7295-5477], Gurey V.¹[0000-0002-5117-6802], Bartoszek M.²[0000-0002-6964-6921], Hurey T.¹[0000-0002-9017-8309]

¹Lviv Polytechnic National University, 12, Bandera St., 79013 Lviv, Ukraine;

²Opole University of Technology, 76, Prószkowska St., 45758 Opole, Poland

Article info:

Received:

March 14, 2021

The final version received:

June 18, 2021

Accepted for publication:

June 23, 2021

*Corresponding email:

Ihor.V.Hurei@lpnu.ua

Abstract. The tool with grooves on its working surface is used to improve the properties of the strengthened layer. This allows us to reduce the structure's grain size and increase the thickness of the layer and its hardness. Mineral oil and mineral oil with active additives containing polymers are used as a technological medium during friction treatment. It is shown that the technological medium used during the friction treatment affects the nature of the residual stresses' distribution. Thus, when using mineral oil with active additives containing polymers, residual compressive stresses are more significant in magnitude and depth than when treating mineral oil. The nature of the residual stresses diagram depends on the treated surface' shape. After friction treatment of cylindrical surfaces, the highest compressive stresses near the treated surface decreases with depth. And after friction treatment of flat surfaces near the treated surface, the compressive stresses are small. They increase with depth, pass through the maximum, and then decrease to the original values. The technological medium used during friction treatment affects residual stresses in the grains and in the crystal lattice.

Keywords: friction treatment, residual stresses, fatigue, white layer, nanocrystalline structure, technological environment, crystal lattice, grains.

1 Introduction

The current stage of technical development needs increased requirements for the performance of parts. Various parts and assemblies work in friction conditions at high specific loads, temperatures, a wide range of speeds, and exposure to aggressive mediums. Often several factors influence at the same time.

The condition of the surface layer is an essential factor that determines the performance of the product because the destruction of parts begins from its surface. This leads to a decrease in the efficiency and failure of parts due to the processes that take place in the surface layers of parts during operation – friction and wear, plastic deformation, the development of microcracks, and redistribution of residual stresses. The reliability of the parts is directly related to the surface layer's quality and is characterized by geometrical, physical, and mechanical properties. Geometric parameters are determined by the roughness and waviness of the surface and depend on the quality of surface treatment. The properties of materials depend on the chemical composition and structure of the materials. The relationship between the surface layer's quality

characteristics with the parts' performance properties shows that the treated surface must have high hardness, residual compressive stresses, fine structure, etc.

2 Literature Review

Fatigue damage is one of the most common types of metal structures' destruction. Fatigue phenomena occur during the cyclic loading of parts. The material is affected by oscillating stresses and strains, which lead to destruction (failure) due to the accumulation of damage [1]. Fatigue failure is considered the interaction between the metal parts' microstructure, deformations, and mechanical state, especially the surface layer [2]. Avoidance or delay of the parts' damages affected by cyclic loads is an important issue that should be resolved at the design and manufacture of machine parts [1, 2].

Various technological methods improve the quality of surface layers and increase the durability and reliability of machine parts in operation [3–6]. All these technological processes contribute to the formation of high-quality strengthened layers, which slow down the formation and propagation of fatigue cracks. For ensuring appropriate

operating conditions of products and their reliability, it is necessary to study the stresses that occur during the operation of parts, especially in the surface layers [7, 8]. Stresses formed in the parts' surface layers during processing significantly affect the performance properties of parts [9].

The technological processes are required, due to improve parts' performance properties. Such methods include processing methods using highly concentrated energy sources [10, 11].

The application of technologies for machine parts' surface strengthening (hardening) by using highly concentrated energy flows leads to the formation of the complex temperature-phase transformations in the surface layers of the metal. The surface layer is heated at high speeds to temperatures above the point of phase transformation, and after the removal of the thermal energy source is its subsequent rapid cooling in extreme conditions. As a result, the structure, physical-mechanical and electrochemical characteristics of the metal change in the surface layers significantly affect the machine parts' performance during operation [10, 12].

Residual stresses that occur in the parts' surface layers during their manufacturing process significantly affect their performance during operation. They are among the most critical indicators of the parts' surface layers quality. Thus, the residual compressive stresses in the machine parts' surface layers increase their resistance to fatigue failure, and the tensile, on the contrary – decreases [13, 14]. Knowing the patterns of the 1st kind residual stresses formation can predict and the formation of the second or other residual stresses plot in the surface layers of the metal depends on the processing conditions, the applied technological medium, the physical and mechanical properties of the processed material.

The work aims to study the influence of the technological medium on residual stresses formed during the friction treatment production operation of samples' cylindrical and flat surfaces.

3 Research Methodology

Friction treatment refers to surface strengthening (hardening) methods using highly concentrated energy flows. This flow of energy is created by the friction of the tool disk on the workpiece. At the same time, there is a simultaneous high-speed shear deformation. The heating rate reaches $5.0 \cdot 10^5$ – $1.5 \cdot 10^6$ K/s. The surface layers of the metal are heated to temperatures above the point of phase transformation (A_{c3}), cooling occurs at high speeds ($5.0 \cdot 10^5$ – $1.5 \cdot 10^6$ K/s) due to heat dissipation into the part [17]. And the nonequilibrium state of the metal is obtained. The carbon content in martensite is much higher than the concentration corresponding to the point of martensitic transformation. The strengthened white layer with a nanocrystalline structure is formed in the machine parts' surface layer [18].

During the friction treatment, the technological medium is fed into the tool and part contact area. Hydrocarbons are mainly used as a technological medium. The technological

medium decomposes into constituent chemical elements (e.g., carbon and hydrogen), which diffuse into the surface strengthened layer.

Friction treatment of sample' cylindrical surfaces was performed on an upgraded lathe, where instead of a tool holder, a particular device with the autonomous drive for rotation of the tool was mounted. Friction treatment of sample' flat surfaces was performed on an upgraded grinding machine, increasing the tool's rotation speed. On both machines, the tool' rotation speed was 70 m/s. A metal disk made of stainless steel is used as a tool. The tool has transverse grooves on the working surface. Mineral oil and mineral oil with active additives containing polymers were used as the technological medium.

Metallographic analysis showed that after friction treatment of samples of Steel C45 (quench hardening and low-temperature tempering) using as a technological medium mineral oil, a surface strengthened (hardened) layer with a nanocrystalline structure with the thickness of 110–130 μm is formed. The microhardness of the strengthened layer was $H_{\mu} = 6.5$ – 6.8 GPa and the hardness of the base metal – $H_{\mu} = 2.1$ – 2.3 GPa. When used mineral oil with active additives containing polymers as a technological medium, the thickness of the strengthened layer increased to 190–220 μm . The microhardness also increased to $H_{\mu} = 8.6$ GPa.

X-ray analysis showed that the grain size of the surface strengthened layer was 20–40 nm near the surface with a smooth transition to the depth to the structure of the base (source) material. The structure of the obtained strengthened surface layer after friction treatment refers to nanocrystalline.

The first kind of residual stresses, which are formed in the surface layers after friction treatment, were determined by changes in the deflection of the sample during layer-by-layer removal of metal from half of the sample during its electrochemical etching. This disrupts the load balance in opposite parts of the sample, and it bends to restore balance. This principle is the basis for measuring the residual stresses of the first kind by this method. Load balance is changed in opposite parts of the sample, and it is bent to restore the balance. This principle is the basis for measuring the first kind of residual stresses by this method.

The obtained deformations determined residual stresses. Residual stresses were determined on the cylindrical samples with a diameter of 20 mm and a length of 150 mm, and on the flat samples with a size of $6 \times 20 \times 150$ mm. Electrochemical etching and measurement of deflections of the samples were performed on a particular device (Fig. 1). The test samples were placed in the bath on special supports, which provided their free deflection during electrochemical etching. The electrolyte must fill the test sample to half its thickness. The electrode was placed under the sample, which corresponded to the shape of the test sample. Strain gauges (FKPA-20-200 type) were glued to the samples on one side. Before the measurement, the strain gauges were calibrated by loading the samples, mounted on two supports, and a calibration curve was constructed. Using electrochemical etching to

remove thin layers sequentially $\delta_1, \delta_2, \dots, \delta_n$ on one side of the sample, and on the opposite side – measured the deformation value using calibration graphs. For ensuring the etching of only one part of the sample, its sides and top were covered by waterproof varnish. Anodic etching was performed at the current density of 5 A/dm² at a constant rate. During etching, the electrolyte was mixed, and the samples were standing without etching before measuring the deformation, as the temperature that occurs at the metal – medium boundary can add errors.

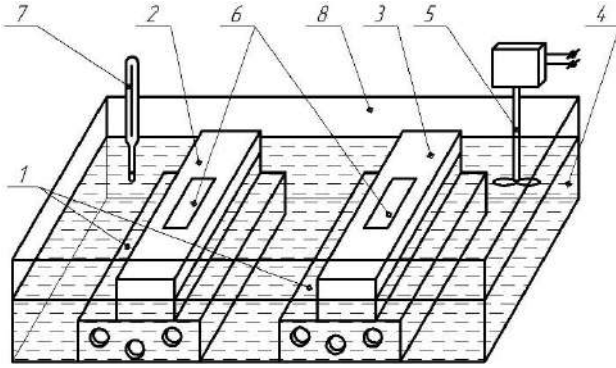


Figure 1 – Scheme of the particular device for determining the first kind residual stresses: 1 – bath; 2 – test sample; 3 – compensating sample; 4 – electrolyte; 5 – mixer; 6 – strain gauges; 7 – thermometer; 8 – bath.

The axial residual stresses that occur in the flat sample after the deformations determined friction treatment according to the formula:

$$\sigma_{rs}(a_i) = \frac{4E}{3l^2} \left[(h-a_i)^2 \frac{df}{da}(a_i) - 4(h-a_i)f(a_i) + 2 \int_0^a f(\xi) d\xi \right]. \quad (1)$$

Parabola formulas were used to determine the derivative $\frac{df}{da}(a_i)$. Then,

$$\frac{df}{da}(a_i) = f_{i-1} \left(\frac{-\Delta_{i+1}}{\Delta_i(\Delta_i + \Delta_{i+1})} \right) + f_i \left(\frac{\Delta_{i+1} - \Delta_{i+1}}{\Delta_i \cdot \Delta_{i+1}} \right) + f_{i+1} \left(\frac{\Delta_i}{\Delta_{i+1}(\Delta_i + \Delta_{i+1})} \right). \quad (2)$$

This formula is valid for all values of a_i , eliminate the first and last values.

For the initial value of $i=0$, $a_0=0$, $f_0=0$.

$$\frac{df}{da}(0) = f_1 \left(\frac{\Delta_1 + \Delta_2}{\Delta_1 \cdot \Delta_2} \right) + f_2 \left(\frac{-\Delta_1}{\Delta_2(\Delta_1 + \Delta_2)} \right). \quad (3)$$

For the last removed layer $i=n$:

$$\frac{df}{da}(a_n) = f_{n-2} \left(\frac{\Delta_n}{\Delta_{n-1}(\Delta_{n-1} + \Delta_n)} \right) + f_{n-1} \left(\frac{-\Delta_{n-1} + \Delta_n}{\Delta_{n-1} \cdot \Delta_n} \right) + f_n \left(\frac{\Delta_n + (\Delta_{n-1} + \Delta_n)}{\Delta_n(\Delta_{n-1} + \Delta_n)} \right). \quad (4)$$

where E – modulus of elasticity, MPa; l – sample length, m; h – sample height, m; Δ_i – the thickness of the etched layer at the i -th stage, m; f_i – deflection of the sample, m.

When determining the first kind of residual stresses, it was assumed that they are constant along the sample length.

The axial residual stresses were determined by the deformations that occur in the cylindrical sample, according to the formula:

$$\sigma = \frac{E}{\left[\frac{2(r-\delta_i) + \pi y_{ci}}{I_{\delta_i}} \cdot I_{\delta_i} \right]} \frac{d\varepsilon}{d\delta_i} + E \int_0^{\delta_i} A \delta_{(i-1)} \frac{d\varepsilon'_e}{d\delta_{(i-1)}} \cdot d\delta_{(i-1)}. \quad (5)$$

where:

$$A \delta_{(i-1)} = \frac{2(r-\delta_{(i-1)}) + \pi y_{c(i-1)} \left(r - \delta_i + y_{c(i-1)} \right) + \frac{\pi}{F \delta_{(i-1)}}}{2(r-\delta_{(i-1)}) + \pi y_{c(i-1)}} \cdot I_{\delta_{(i-1)}} - \frac{\pi}{F \delta_{(i-1)}}; \quad (6)$$

δ_i – the thickness of the i -th layer ($i = 1, 2, 3 \dots n$); $l_{\delta_i} = r - y_{ci}$ – the distance from the center of gravity to the lower fiber after removing the layer whose thickness is equal δ_i ; y_{ci} – displacement of the section' center of gravity relative to the axis of the rod after removal of the layer, the thickness of which is equal δ_i :

$$y_{ci} = \frac{4 \left[(r-\delta_i)^3 - r^3 \right]}{3\pi \left[(r-\delta_i)^2 + r^2 \right]}; \quad (7)$$

I_{δ_i} – the rod' cross-sectional area after removing the layer, the thickness of which is equal δ_i :

$$I_{\delta_i} = \left(\frac{\pi}{8} \right) \left[(r-\delta_i)^4 + r^4 \right]; \quad (8)$$

F_{δ_i} – the rod' cross-sectional area after removing the layer, the thickness of which is equal δ_i :

$$F_{\delta_i} = \left(\frac{\pi}{2} \right) \left[(r-\delta_i)^2 + r^2 \right]. \quad (9)$$

The parabolic approximation method was used to calculate the derivative $\frac{d\varepsilon'_e}{d\delta_i}$ in the equation.

Residual stresses that occur in flat samples were calculated according to the formula:

$$\sigma_{rs}(a_i) = \frac{4E}{3l^2} \left[(h-a_i)^2 \frac{df}{da}(a_i) - 4(h-a_i)f(a_i) + 2 \int_0^a f(\xi) d\xi \right]. \quad (10)$$

Parabola formulas were used to determine the derivative $\frac{df}{da}(a_i)$. Then,

$$\frac{df}{da}(a_i) = f_{i-1} \left(\frac{-\Delta_{i+1}}{\Delta_i (\Delta_i + \Delta_{i+1})} \right) + f_i \left(\frac{\Delta_{i+1} - \Delta_{i+1}}{\Delta_i \cdot \Delta_{i+1}} \right) + f_{i+1} \left(\frac{\Delta_i}{\Delta_{i+1} (\Delta_i + \Delta_{i+1})} \right) \quad (11)$$

This formula is valid for all values of a_i , eliminate the first and last values.

For the initial value of $i=0$, $a_0=0$, $f_0=0$.

$$\frac{df}{da}(0) = f_1 \left(\frac{\Delta_1 + \Delta_2}{\Delta_1 \cdot \Delta_2} \right) + f_2 \left(\frac{-\Delta_1}{\Delta_2 (\Delta_1 + \Delta_2)} \right) \quad (12)$$

For the last removed layer $i=n$:

$$\frac{df}{da}(a_n) = f_{n-2} \left(\frac{\Delta_n}{\Delta_{n-1} (\Delta_{n-1} + \Delta_n)} \right) + f_n \left(\frac{-(\Delta_{n-1} + \Delta_n)}{\Delta_i \cdot \Delta_{i+1}} \right) + f_n \left(\frac{\Delta_n + (\Delta_{n-1} + \Delta_n)}{\Delta_n (\Delta_{n-1} + \Delta_n)} \right) \quad (13)$$

where E – modulus of elasticity, MPa; l – sample length, m; h – sample height, m; Δ_i – the thickness of the etched layer at the i -th stage, m; f_i – deflection of the sample, m.

4 Results

Studies have shown that the applied technological medium significantly affects the nature of the 1st kind residual stresses redistribution during friction treatment. Thus, when strengthening (hardening) the samples' flat surfaces of Steel C45 (quench hardening and low-temperature tempering), there are residual compressive stresses (Fig. 2). When using mineral oil with active additives containing polymers, they extend to a greater depth and are more significant in magnitude than the stresses obtained during strengthening with mineral oil. Their value is small near the surface, but with increasing depth, the stresses increase, pass through the maximum and decrease. The same pattern is observed in the strengthening samples of Steel CT80 after quench hardening and low or high-temperature tempering (Fig. 3). The highest stresses occur on the samples after quench hardening and low-temperature tempering, slightly less after friction treatment of the samples after quench hardening and high-temperature tempering. Notably, the residual stress magnitude is influenced by the structural state of the source metal, but the nature of their distribution is almost the same.

During friction treatment using the mineral oil with active additives containing polymers as the technological medium, it is destroyed, and hydrogen is intensively evolved as a component of hydrocarbons and polymers. Hydrogen plasticizes the metal's surface layer, the shear and impact deformations extend to greater depths than when strengthened by using mineral oil as the technological medium. Therefore, the residual stress increases in magnitude and depth.

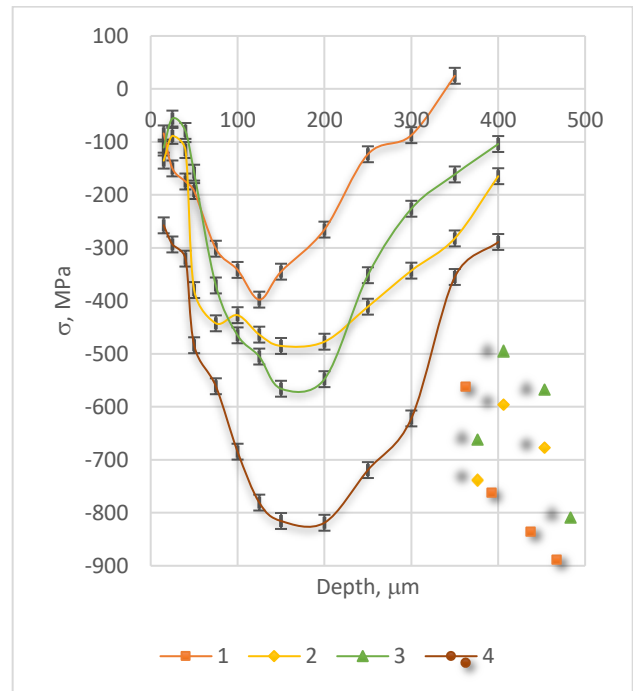


Figure 2 – The first kind of residual stresses obtained on Steel C45 (quench hardening and high-temperature tempering – 1, 2), (quench hardening and low-temperature tempering – 3, 4) after friction treatment: 1, 3 – with mineral oil; 2, 4 – with mineral oil with active additives containing polymers

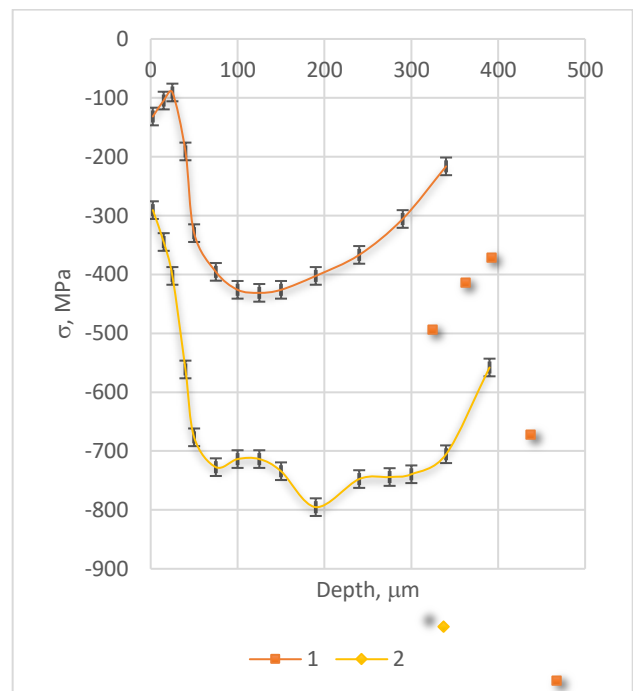


Figure 3 – The first kind of residual stresses obtained on Steel CT80 (quench hardening and low-temperature tempering) after friction treatment: 1 – with mineral oil; 2 – with mineral oil with active additives containing polymers

The nature of the change in residual stresses obtained on cylindrical samples is different from the change in residual stresses obtained after the strengthening of flat samples (Fig. 4). Thus, after friction treatment of samples made of Steel C45 (quench hardening and low-temperature tempering), using the mineral oil with active additives containing polymers as the technological medium, the residual stresses are most significant near the treated surface. With increasing depth, the stresses decrease. The depth of compression stresses is greater than the thickness of the strengthened layer. Compression stresses are observed near the surface, which then turns into tensile stresses. This transition is located outside the white layer on the base metal. After treatment using mineral oil as a process medium, the residual stresses are smaller in value and depth than after treatment with mineral oil with active additives containing polymers, but the nature of the stress distribution is similar.

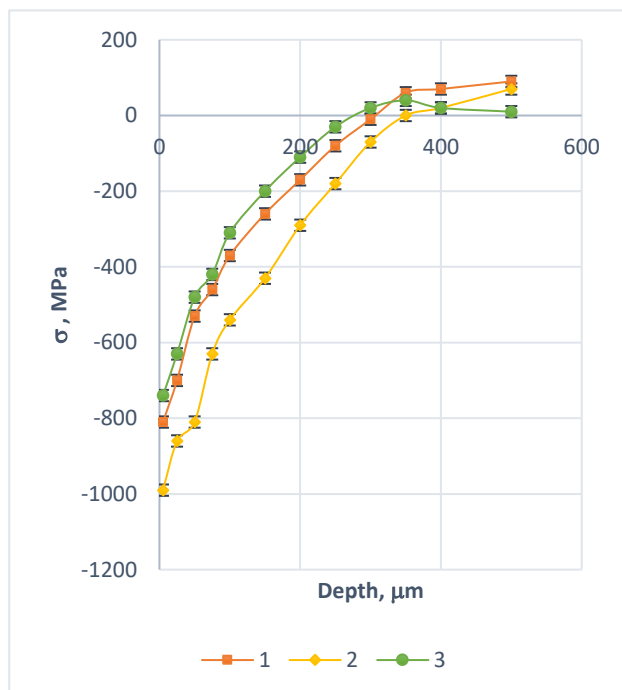


Figure 4 –The first kind of residual stresses obtained on Steel C45 (quench hardening and low-temperature tempering) after friction treatment: 1 – with mineral oil; 2 – with mineral oil with active additives containing polymers; 3 – with mineral oil and stand of 1,5 years.

For determining the effect of the stand on the change in residual stresses, the strengthened samples were stand in the laboratory for 1.5 years. After research, it was found that the stand leads to a slight change in residual stresses, the nature of their distribution is preserved. This allows us to conclude about the high stability of the stress state of the strengthened white layers with a nanocrystalline structure.

The 1st kind of residual stresses obtained on flat surfaces are significantly different from the stresses formed after the frictional treatment of cylindrical surfaces. On the samples' cylindrical surfaces near the treated surface, maximum compressive stresses are

formed, which decrease with depth. After frictional treatment of the samples' flat surfaces, the nature of the stress distribution is different. Near the treated surface, the value of residual stresses is small. With increasing depth, they increase, pass through the maximum, and gradually decrease. The geometric parameters of flat and cylindrical surfaces affect the nature of the 1st kind of residual stresses distribution during frictional treatment.

Frictional treatment refers to methods of obtaining strengthened surface layers with a nanocrystalline structure. Nanocrystallization consists of creating a large number of defects and the demarcation boundary in the surface layer, which are needed for the transition to a structure with nanometric crystal sizes. The necessary conditions for forming the nanocrystalline layer are the provision of high temperatures and stresses in the contact zone. During friction treatment, by using the tool with a discontinuous working surface in the contact area of the tool and part occur the thermoplastic deformation of the treated surface and with heating above the point of phase transformations, cycling of temperatures with high-speed cooling, also shock loads form the nanocrystalline structure. The rate of heating and cooling is 10^3 - 10^4 times higher than with ordinary quench hardening.

During normal quench hardening, a non-equilibrium state of the metal and the corresponding structure are formed, and during high-speed cooling, the time for the formation of such structures and phases is insufficient. As a result, a state is formed, and the individual phases do not have time to separate from the solid solution, or this separation has not yet been finished. At a high cooling rate of the heated iron is fixed γ -phase, carbon does not have time to stand out in the form of cementite formations and remains in solution or partially passes into the tetrahedral pores of Fe_α , and as a result, the martensite is forming. The carbon content in martensite is much higher than the concentration corresponding to the point of martensitic transformation.

The interaction of grains with each other forms residual micro stresses. The action of external load forms unequal deformation of neighboring grains due to their arbitrary orientation and anisotropy.

The study of the technological medium influence during friction treatment on the value of residual micro stresses that occur in grains and crystal lattices was performed on samples made of Steel C45 (quench hardening and low-temperature tempering). Residual micro stresses between grains or crystallites occur due to differences in the microstructure of the material, the presence of different phases or components that have different coefficients of thermal expansion between the phases. Residual microstresses in the metal' crystal lattices are determined by coherence at the demarcation boundary, the presence of various dislocations, lattices defects, dissolved atoms, etc., which cause deformation and stress.

During the friction treatment, the grains of the surface' layer structures sharply decrease to nano-size near the treated surface. With the depth of the layer, the grain size increases to the size of the main structure. The use of different technological mediums during friction treatment

causes various micro distortions in the white layer. Thus, in the white layer obtained on Steel C45 (quench hardening and low-temperature tempering), the most considerable micro distortions occur during friction treatment using a technological medium mineral oil with active additives containing polymers (Fig. 5). After treatment with mineral oil, the stresses are slightly lower. When strengthened using mineral oil, the micro stresses are not much smaller in magnitude than when strengthened using mineral oil with active additives containing polymers but uniform in depth. At depths greater than 100 μm , they begin to decrease towards the initial. Their most considerable value is observed near the surface, at a depth of more than 60 μm . They are close to the initial.

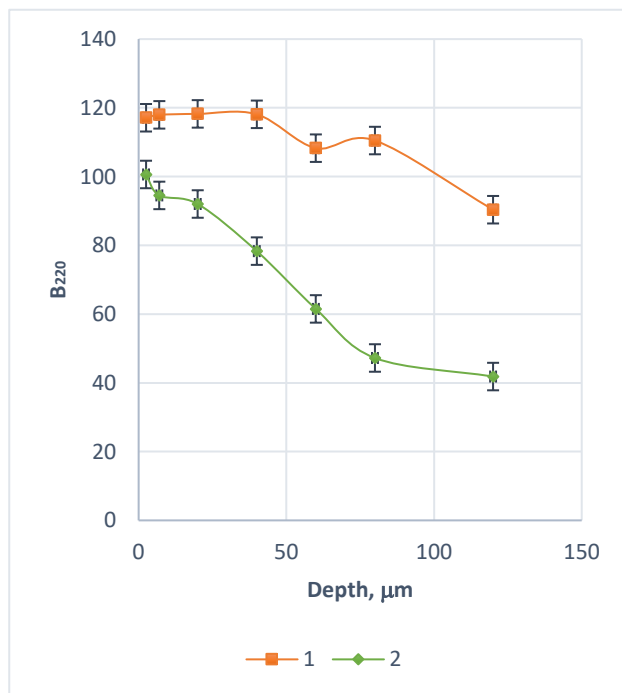


Figure 5 – Changing the width of the diffraction line (220) on Steel C45 (quench hardening and low-temperature tempering) after friction treatment: 1 – with mineral oil; 2 – with mineral oil with active additives containing polymers

In the process of friction treatment in the contact zone of the tool and part under the action of high temperatures and stresses is the decomposition of the technological medium into constituent chemical elements that diffuse into the surface layer. Carbon diffuses into the surface layers, especially during treatment with mineral oil with active additives containing polymers. After friction treatment in the strengthened layer, there is an increased density of dislocations, which on Steel C45 is near the surface of $1.2 \cdot 10^{12} \text{ cm}^{-2}$, and with the depth of the layer decreases to the initial level.

The influence of the technological medium on the residual stresses in the crystal lattice has different effects. Near the treated surface, the technological medium has almost no effect on the distortion of the crystal lattice of the white layer (Fig. 6). With increasing depth of the layer, the stresses in the lattice after friction treatment by using

the mineral oil with active additives containing polymers, first increase, pass through the maximum, and then decrease. After strengthening by using the mineral oil, the most significant stresses are near the treated surface, and the depth of the layer gradually decreases.

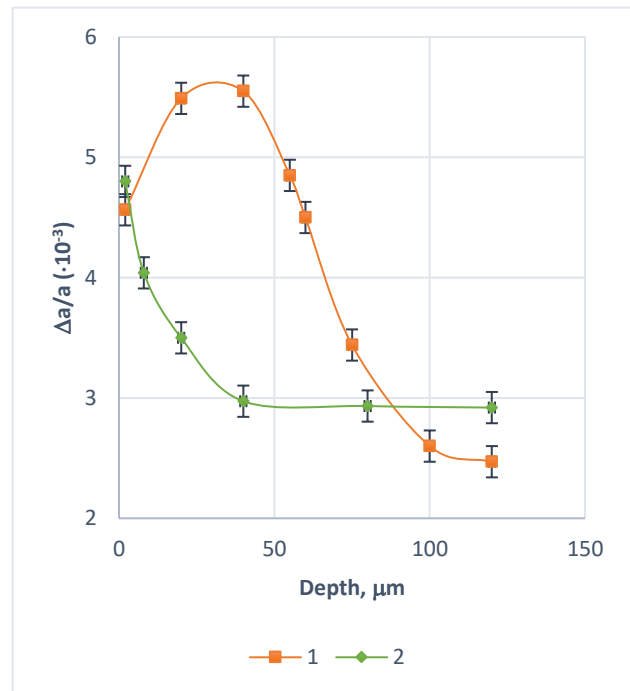


Figure 6 – Distortions of the crystal lattice obtained on Steel C45 (quench hardening and low-temperature tempering) after friction treatment: 1 – with mineral oil; 2 – with mineral oil with active additives containing polymers

Residual stresses are one of the main factors determining the engineering properties of the machined surfaces of machine parts. They should be taken into account when designing and manufacturing various products that are operated under cyclical loads. Although there are many technological methods of processing and strengthening machine parts' working surfaces, developing new processing methods provides a given redistribution of residual stresses.

5 Conclusions

After friction treatment of samples of Steel C45 (quench hardening and low-temperature tempering) using the mineral oil as a technological medium, a surface strengthened layer with a nanocrystalline structure with a thickness of 110-130 μm is formed. The microhardness of the strengthened layer was 7.6 GPa at a hardness of the base metal of 5.1 GPa. When used as a technological medium of mineral oil with active additives containing polymers, the thickness of the strengthened layer increased to 190-220 μm and the microhardness to 8.6 GPa.

The use of mineral oil with polymer-containing additives as a technological medium for frictional treatment increases the magnitude and depth of residual compressive stresses.

The formation of residual stresses is influenced significantly by phase and structural transformations that occur in the surface layers of the metal during the

formation of strengthened white layers with nanocrystalline structures due to high-speed heating and cooling during friction treatment.

References

1. Pineau, A., McDowell, D.L., Busso, E.P., Antolovich S.D. (2016). Failure of metals II: Fatigue, *Acta Materialia*, Vol. 107, pp. 484–507, <https://doi.org/10.1016/j.actamat.2015.05.050>
2. Santecchia, E., Hamouda, A. M. S., Musharavati, F., Zalnezhad, E., Cabibbo, M., El Mehtedi, M., Spigarelli S. (2016). A Review on Fatigue Life Prediction Methods for Metals. *Advances in Materials Science and Engineering*, 9573524, <https://doi.org/10.1155/2016/9573524>
3. Ropyak, L.Y., Pryhorovska, T.O., Levchuk, K.H. (2020). Analysis of materials and modern technologies for PDC drill bit manufacturing. *Progress in Physics of Metals*, Vol. 21 (2), pp. 274–301, <https://doi.org/10.15407/ufm.21.02.274>
4. Prysyazhnyuk, P., Lutsak, D., Shlapak, L., Aulin, V., Lutsak, L., Borushchak, L., Shihab, T.A. (2018). Development of the composite material and coatings based on niobium carbide. *Eastern-European Journal of Enterprise Technologies*, Vol. 6(12-96), pp. 43–49, <https://doi.org/10.15587/1729-4061.2018.150807>
5. Shatskyi, I.P., Perepichka, V.V., Ropyak, L.Y. (2020). On the influence of facing on strength of solids with surface defects. *Metallofizika i Noveishie Tekhnologii*, Vol. 42(1), pp. 69–76, <https://doi.org/10.15407/mfint.42.01.0069>
6. Kalchenko, V.V., Yeroshenko, A.M., Boyko, S.V., Ignatenko, P.L. (2020). Development and research of thermoplastic methods for hardening details, *Naukovyi Visnyk Natsionalnoho Hirnychoho Universytetu*, Vol. 2, pp. 53–60, <https://doi.org/10.33271/nvngu/2020-2/053>
7. Shatskyi, I.P., Ropyak, L.Y., Makoviichuk, M.V. (2016). Strength optimization of a two-layer coating for the particular local loading conditions. *Strength of Materials*, Vol. 48 (5), pp. 726–730, <https://doi.org/10.1007/s11223-016-9817-5>
8. Ropyak, L.Ya., Shatskyi, I.P., Makoviichuk, M.V. (2019). Analysis of interaction of thin coating with an abrasive using one-dimensional model. *Metallofizika i Noveishie Tekhnologii*, Vol. 41(5), pp. 647–654, <https://doi.org/10.15407/mfint.41.05.0647>
9. Hizli, H., Gür C.H. (2018). Comparison of Nondestructive Stress Measurement Techniques for Determination of Residual Stresses in the Heat Treated Steels. *Materials Research Proceedings*, Vol. 6, pp. 165–170, <http://dx.doi.org/10.21741/9781945291890-26>
10. Narayanan, A., Mostafavi, M., Pavier, M., Peel M. (2018). Development of Residual Stresses During Laser Cladding. *Materials Research Proceedings 6*, pp. 39–44, <http://dx.doi.org/10.21741/9781945291890-7>
11. Sakaida, Y., Sasaki, Y., Owashi H. (2018). Influence of Surface Pretreatment on Residual Stress Field of Heat-Treated Steel Induced by Laser Local Quenching. *Materials Research Proceedings*, Vol. 6, pp. 177–182. <http://dx.doi.org/10.21741/9781945291890-28>
12. Hurey I., Hurey T., Lanets O., Dmyterko P. (2021). The Durability of the Nanocrystalline Hardened Layer During the Fretting Wear. *Advances in Design, Simulation and Manufacturing IV*, pp. 23–32, https://doi.org/10.1007/978-3-030-77823-1_3
13. Burley, M., Campbell, J.E., Reiff-Musgrove, R., Dean, J., Clyne T.W. (2021). The Effect of Residual Stresses on Stress–Strain Curves Obtained via Profilometry-Based Inverse Finite Element Method Indentation Plastometry. *Adv. Eng. Mater.*, Vol. 23, 2001478, <https://doi.org/10.1002/adem.202001478>
14. Withers, P.J. (2007). Residual stress and its role in failure. *Rep. Prog. Phys.*, Vol. 70, pp. 2211–2264, <https://doi.org/10.1088/0034-4885/70/12/R04>
15. Development and applications of residual stress measurements using neutron beams. (2014). Vienna : International Atomic Energy Agency.
16. Fardan, A., Berndt, C.C., Ahmed R. (2021). Numerical modelling of particle impact and residual stresses in cold sprayed coatings: A review. *Surface and Coatings Technology*, Vol. 409, 126835, <https://doi.org/10.1016/j.surfcoat.2021.126835>
17. Gurey V., Shynkarenko H., Kuzio I. (2021). Mathematical model of the thermoelasticity of the surface layer of parts during discontinuous friction treatment. *Advanced in Design, Simulation and Manufacturing IV*, Vol. 2, pp. 12–22, https://doi.org/10.1007/978-3-030-77823-1_2
18. Kyryliv V.I., Gurey V.I., Maksymiv O.V., Hurey I.V., Kulyk Yu.O. (2021). The influence of the deformation mode on the force conditions of the formation of the surface nanostructure of steel 40H. *Physico-chemical mechanics of materials*, Vol. 3, pp. 126–131.



Povstyanoy O., MacMillan A. (2021). *Mechatronic system's permeable materials with controlled porosity*. *Journal of Engineering Sciences*, Vol. 8(1), pp. C45–C49, doi: 10.21272/jes.2021.8(1).c6

Mechatronic System's Permeable Materials with Controlled Porosity

Povstyanoy O.¹[0000-0002-1416-225X], MacMillan A.²[0000-0003-4191-096X]

¹Lutsk National Technical University, 75, Lvivska St., 43018, Lusk, Ukraine;

²Institution of Mechanical Engineers, 1, Birdcage Walk, London, UK

Article info:

Received: April 2, 2021
 The final version received: June 19, 2021
 Accepted for publication: June 23, 2021

*Corresponding email:
 povstjanoy@ukr.net

Abstract. Up-to-date directions in the development of modern industry increase the requirements for the quality of technical products. The design and manufacture of competitive process equipment require accuracy, productivity, and efficiency. Therefore, in this article, a new mechatronic system has been designed and developed to help porous, permeable materials with predicted porosity have been produced. The research aims to develop a mechatronic system for technology optimization in manufacturing permeable porous materials with controlled properties. As a result, the method of computer modeling of porous, permeable materials was developed. It allows us to consider the peculiarities of porosity distribution and radial velocity in radial isostatic compression. Additionally, a new mechatronic system for producing permeable materials allows us to determine the porosity distribution and particular characteristics of permeable powder material. The proposed approach allows us to evaluate the impact of technological modes on the main operational characteristics.

Keywords: mechatronic system, porous permeable materials, radial isostatic pressing, industrial wastes, parametric design, modeling, porosity, permeability, manufacturing.

1 Introduction

Industrial development of the technology industry of any industrialized country is impossible without modern mechatronic systems and automation of production. This system is flexible during exploitation, as it allows you to make porous materials of different shapes and sizes by changing the process equipment. The formation of the desired structure of porous products is carried out by radial-isostatic pressing. The existence of traditional technology makes it possible to get new porous permeable materials (PPM). Nevertheless, it is necessary to predict and control the parameters of their structure in the process of manufacturing, which include: granulometric composition of the charge, the shape of particles, the density of the molded workpiece, the quality of the contacts, shaping, porosity, density and their volume of distribution. Today, the development and modeling with using computer-information technologies, mechatronics, and automation of production enable us effectively improve traditional technological processes, introduce low-waste production, improve the quality of manufactured products, save energy, improve production

culture and be able to produce porous permeable materials, with controlled porosity and appropriate sizes [1, 2].

Current problems of creating porous technologies are solved due to computer modeling, automation, and modern computer-aided drafting (CAD) systems, which allow optimizing the technology in obtaining porous permeable materials.

2 Literature Review

The progress and success of creating new porous permeable materials is ensured by improving existing or developing new methods of obtaining them according to the domestic and foreign experience of recent decades [3, 4].

However, prediction, optimization, and modeling in powder metallurgy require further improvement of theoretical concepts and their implementation in qualitative methods and algorithms, which are realized with the help of modern computer information technologies.

Today, the optimization of technological processes for obtaining PPM with controlled porosity is solved based on mechatronic systems using computer simulation. This is

due to the significant development of theoretical ideas and considerations in the behavior of the source material (powder) in its processing and use.

Modeling regularities of forming of structure and properties of materials depend on the geometrical factors of the powder particles [5–9].

Literature review of the processing of metal-containing waste products showed a sufficiently large number of technologies for obtaining powder from sludge waste of tool and bearing steels using mechatronic systems [10, 11].

The research aims to develop a mechatronic system for technology optimization in manufacturing permeable porous materials with controlled properties.

3 Research Methodology

3.1 A method for obtaining porous permeable materials

For obtaining porous materials with high permeability, it is necessary to use powders with large particle sizes. It is necessary to use powders of small particle sizes to obtain the high fineness of cleaning. These contradictions lead to the need to find new technological techniques, automated tools, and computer modeling methods to create such structures of porous materials that provide the best possible combination of operational characteristics [12].

For receiving filtering PPMs, a new installation was designed and manufactured. This device is used for pressing the sealing materials of various kinds: metallic and ceramic powders, graphite, fibers, wire, and wire mesh (Fig. 1).



Figure 1 – Photo of the considered device

To expand the range of porous powder products, save raw materials, and reduce expenditures for production, a solid elastic insert (Fig. 2) can be made by forming a set of inner folded inserts [13]. This allows us to get products with a broader range of sizes and improve the technology and the culture of pressing.

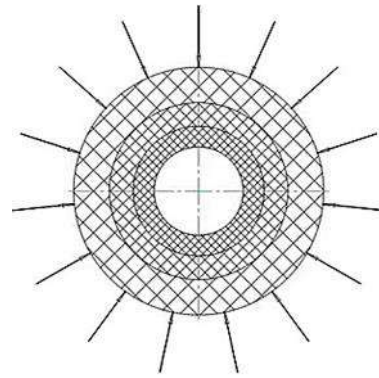


Figure 2 – Scheme of pressing using an elastic insert formed in a set of inner folded inserts

PPMs made with the help of this installation (Fig. 1) meet modern requirements as to the quality of products for this kind.

In the developed object-oriented Computer-aided design (CAD), the parameterization mechanism is implemented by the use of the parametric drawing and modeling system Pro/ENGINEER, which became the basis for the development of a system for modeling the parametric design of installations for the dry radial-isostatic pressing (Fig. 3).

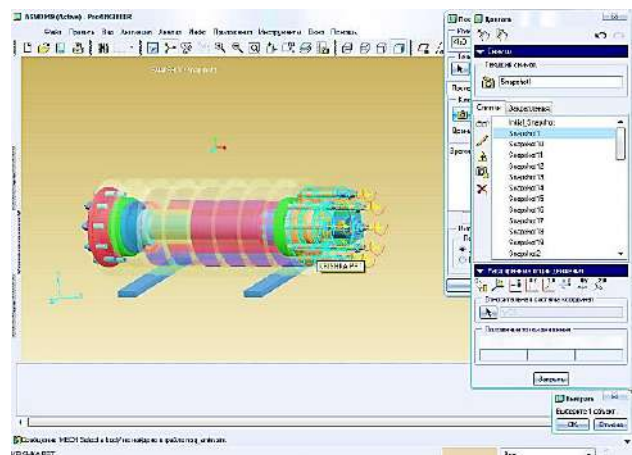


Figure 3 – Design scheme of the developed mechatronic system

One of the essential aspects of the installation design for dry radial isostatic pressing of porous permeable materials is calculating the forces and voltage in detail (Fig. 4).

Modern materials processing technology for pressure and powder metallurgy is required to obtain a wide range of products.

One of the essential aspects of the installation design for dry radial isostatic pressing of porous permeable materials is calculating the forces and voltage in detail (Fig. 5).

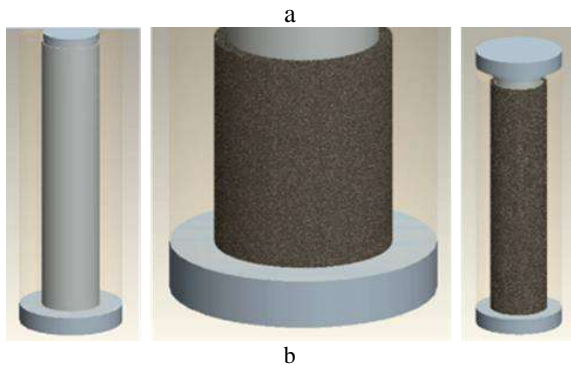
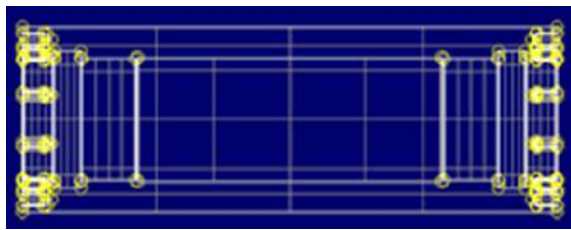


Figure 4 – System of calculation of forces and voltage in details of the design of the installation model for dry radial isostatic pressing of porous permeable materials based (a) and modeling of powder filling process in the form of radial isostatic pressing (b) by using Pro/ENGINEER

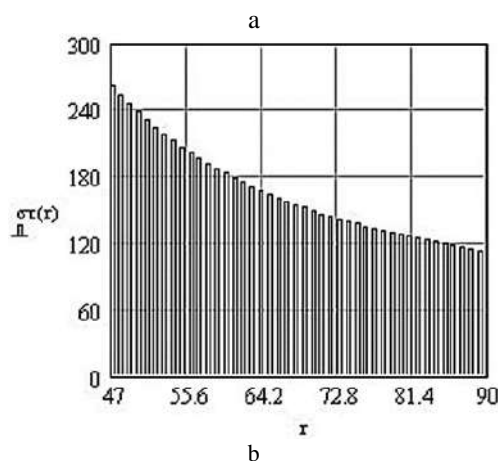
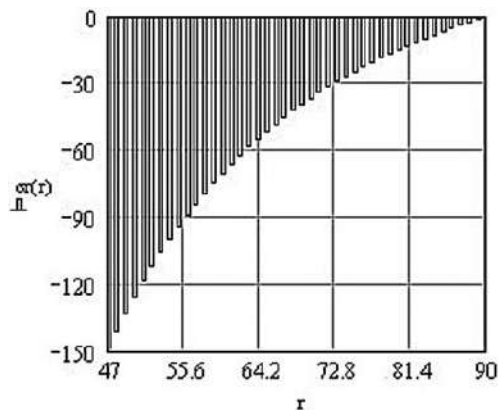


Figure 5 – The curves of radial (a) and tangential (b) stresses variation on the thickness of the isostatic cylinder for pressing

The progress in powder metallurgy and the treatment of materials by pressure is mainly determined by improving pressing processes. They relate to the main phase of production and determine the size, shape, range, power consumption, and effect on properties of the finished product essentially.

Developed and existing technologies do not solve manufacturing PPM products with the optimal combination of structural characteristics and physical and chemical properties. It is essential to control the quality of products, mechanize and automate the pressing, equipment, and tools processes by predicting their properties at the initial stage of formation.

Using the ABAQUS software, a reliable porosity model has been developed (Fig. 6).

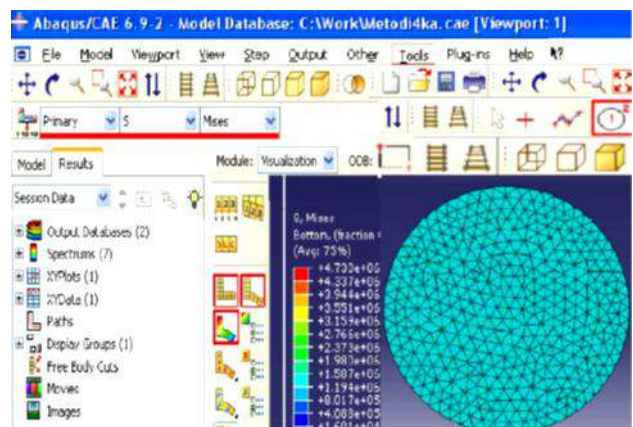


Figure 6 – The porosity model

4 Results and Discussion

The exact particle size distribution of the source powders makes it possible to adequately predict the future structure and properties of the finished PPM due to the logical relationship: the source material – structure – properties (Fig. 7).

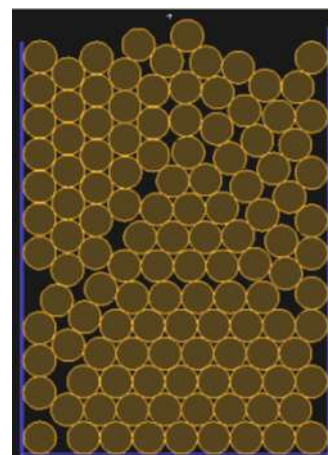


Figure 7 – Variant of filling a two-dimensional the hopper by balls of appropriate size

The modeling of the porous structure of a specific multilayered PPM from a steel powder BBS15 was carried out in the MatLab application package. According to the described methodology, software was developed in the programming language C++ (“FiltrN” program), which allowed modeling the process of radial isostatic pressing with given porosity of the PPM [3]. The initial parameters of the technological process of the mechatronic system for modeling the corresponding structure of the PPM are as follows: the inner diameter of the PPM – 40 mm, the outer diameter – 80 mm (Fig. 8).



Figure 8 – Multilayer PPM made of the steel powder BBS15 $\varnothing 40 \times 220$ mm using the radial isostatic pressing method

A multilayered PPM allows one to analyze the factors contributing to the density of distribution heterogeneity (Fig. 9).

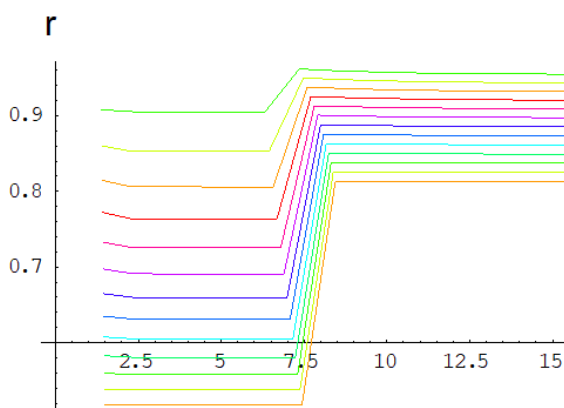


Figure 9 – A generalized distribution of density along the radius of each layer of PPM at different phases of deformation

Determination of the structural characteristics of the metal by the graphic method can be further analyzed using artificial neural networks [19] for ensuring the reliability of the proposed approach.

5 Conclusions

The analysis of existing traditional methods of pressing porous permeable materials showed no technological process, including the main positive features of traditional pressing, which would be non-defective. It is proved that the radial scheme of pressing can be the basis for creating rational equipment and technology for the production of filter materials, including metals, ceramics, graphite and waste industrial production, as it allows to realize the main positive features. In this context, an installation for pressing PPM of the new generation is proposed. The installation comprises technology to produce filter materials based on metals, ceramics, graphite, and industrial production wastes. PPM produced with the help of this installation contains a whole set of properties required for this type of product.

Essentially, the method of computer modeling of porous permeable materials was developed, allowing to consider the peculiarities of the distribution of porosity and radial velocity in radial isostatic compression. As a result, a new modern automation system for manufacturing the permeable materials from wastes of machine-building production was proposed. The method of computer modeling allowed not only to determine the distribution of porosity and other characteristics of the powdered porous units, but also to predict their impact on the operational properties of PPM.

References

1. Bártolo, P. J., Almeida, H. A., Rezende, R. A., Laoui, T., Bidanda, B. (2008). Advanced processes to fabricate scaffolds for tissue engineering. *Virtual Prototyping and Bio Manufacturing in Medical Applications*, pp. 149–170, doi:10.1007/978-0-387-68831-2_8.
2. Belov, S. (1987). *Porous Permeable Materials*. Metallurgy, Moscow, Russia.
3. Povstyanoy, O., Zabolotnyi, O., Rud, V., Kuzmov, A., Herasymchuk, H. (2020). Modeling of processes for creation new porous permeable materials with adjustable properties. In: *Ivanov V. et al. (eds) Advances in Design, Simulation and Manufacturing II. DSMIE 2019. Lecture Notes in Mechanical Engineering*. Springer, Cham, pp. 456–465, 10.1007/978-3-030-22365-6_46.
4. Reut, O., Boginskyi, L., Petiushik, Y. (1998). *Dry Isostatic Pressing of Compactable Materials*. Debora, Minsk, Belarus.
5. Mostafaei, A., Elliott, A. M., Barnes, J. E., Li, F., Tan, W., Cramer, C. L., Nandwana, P., Chmielus, M. (2021). Binder jet 3D printing – Process parameters, materials, properties, modeling, and challenges. *Progress in Materials Science*, Vol. 119, 100707, doi: 10.1016/j.pmatsci.2020.100707.

6. Tofail, S. A. M., Koumoulos, E. P., Bandyopadhyay, A., Bose, S., O'Donoghue, L., Charitidis, C. (2018). Additive manufacturing: Scientific and technological challenges, market uptake and opportunities. *Materials Today*, Vol. 21(1), pp. 22–37, doi: 10.1016/j.mattod.2017.07.001.
7. Jeevanandam, J., Barhoum, Ahmed, Chan, Y. S., Dufresne, A., Danquah, M. K. (2018). Review on nanoparticles and nanostructured materials: history, sources, toxicity and regulations. *Beilstein J Nanotechnol.*, Vol. 9, pp. 1050–1074, doi: 10.3762/bjnano.9.98.
8. Hu, N. (2012). *Composites and Their Properties*. IntechOpen, London, UK, doi: 10.5772/2816.
9. Mourdikoudis, S., Pallares, R. M., Thanh, N. T. K. (2018). Characterization techniques for nanoparticles: comparison and complementarity upon studying nanoparticle properties. *Nanoscale*, Vol. 27, pp. 12871–12934, doi: <https://doi.org/10.1039/C8NR02278J>.
10. Burya, A. I., Lysenko, A. B. (2013). Details of polymeric composites. *International Ukrainian-Japanese Conference on Scientific and Industrial Cooperation*, pp. 42–45.
11. Shetty, D., Manzione, L., Ali, A. (2012). Survey of mechatronic techniques in modern machine design. *Journal of Robotics*, Vol. 2012, 932305, doi: 10.1155/2012/932305.
12. Xiong, Q., Baychev, T. G., Jivkov, A. P. (2016). Review of pore network modelling of porous media: Experimental characterisations, network constructions and applications to reactive transport. *Journal of Contaminant Hydrology*, Vol. 192, pp. 101–117, doi: 10.1016/j.jconhyd.2016.07.002.
13. McMillan, A., Jones, R., Peng, D., Chechkin, G. (2017). A computational study of the influence of surface roughness on material strength. *Mechanics*, Vol. 8, pp. 59–65.



MANUFACTURING 2022

7th International Scientific-Technical Conference

MANUFACTURING 2022

May 16-19, 2022 | Poznan, Poland

Special Session SS_08 Smart Manufacturing Systems

- Smart Manufacturing
- Collaborative Robotics
- Digital Twin
- Vision Systems
- Radio Frequency Identification
- Industrial Internet of Things
- Micro-Electro-Mechanical Systems
- Computational Intelligence, Soft Computing
- Edge Computing
- Big Data, Cloud Computing



ORGANIZERS SS_08

Sławomir Luściński
Kielce University of Technology, Poland
slawomir.luscinski@tu.kielce.pl

Ivan Pavlenko
Sumy State University, Ukraine
i.pavlenko@omdm.sumdu.edu.ua

Ján Piteľ
Technical University of Košice, Slovakia
jan.pitel@tuke.sk

Kamil Židek
Technical University of Košice, Slovakia
kamil.zidek@tuke.sk

<https://manufacturing.put.poznan.pl/>



Demianenko M., Volf M., Pavlenko I., Liaposhchenko O. (2021). *Experimental studies on oscillation modes of vibration separation devices*. *Journal of Engineering Sciences*, Vol. 8(1), pp. D1–D9, doi: 10.21272/jes.2021.8(1).d1

Experimental Studies on Oscillation Modes of Vibration Separation Devices

Demianenko M.¹[0000-0002-4258-0379], Volf M.²[0000-0002-2904-8994],
Pavlenko I.¹[0000-0002-6136-1040], Liaposhchenko O.¹[0000-0002-6657-7051]

¹ Sumy State University, 2, Rymaskogo-Korsakova St., 40007 Sumy, Ukraine;
² University of West Bohemia, 2738/8, Univerzitni St., 301 00 Pilsen, Czech Republic

Article info:

Paper received: February 2, 2020
The final version of the paper received: April 12, 2020
Paper accepted online: April 17, 2020

*Corresponding email:

m.demianenko@omdm.sumdu.edu.ua

Abstract. Despite the rapid development of alternative energy sources, the role of hydrocarbons in the global fuel and energy balance remains significant. For their transportation and further processing, pre-processing is carried out using a set of equipment. In this case, the mandatory devices are separators. In terms of specific energy consumption and separation efficiency, methods based on the action of inertia forces are optimal. However, standard designs have common disadvantages. A method of dynamic separation is proposed to eliminate them. The proposed devices are automatic control systems. The object of regulation is hydraulic resistance, and elastic forces are the regulating actions. Aerohydroelastic phenomena accompany the operation of dynamic separation devices. Among them, the most interesting are flutter and buffeting. Oscillations of adjustable baffles accompany them. It is necessary to conduct a number of multifactorial experiments to determine the operating parameters of dynamic separation devices. In turn, physical experiments aim to identify patterns and features of processes occurring during vibration-inertial separation (i.e., the dependence of various parameters on velocity). Therefore, the article proposes a methodology for carrying out physical experiments on dynamic separation and a designed experimental setup for these studies. As a result, the operating modes of separation devices for different thicknesses of baffle elements were evaluated. Additionally, the dependences of the adjustable element's deflections and oscillation amplitudes on the gas flow velocity were determined for different operating modes of vibration separation devices.

Keywords: gas-liquid mixture, dynamic separation, deformable elements, oscillations, regression model.

1 Introduction

The role of oil and gas in the global fuel and energy balance is constantly growing. In 2018, oil and gas consumption was grown by 4.6 %, which accounted for half of the global increase in energy demand [1].

Notably, oil and natural gas extracted from the well are multiphase multicomponent mixtures. Mainly, the amount of droplet liquid in natural gas, consisting of mineralized water and gas condensate, is usually contained in the amount of 30–40 g/m³, and sometimes even 200–800 g/m³ [2]. Therefore, such gas-dispersed systems are processed before their further transportation and processing. Moisture separation improves the quality of the source product and ensures the reliability of compressor equipment for compression and pumping of gases. The presence of dripping liquids and mechanical impurities in the gas flow leads to emergencies and premature wear of the rotor necks and blades of compressors and

superchargers [3]. The main technological methods of industrial gas preparation are separation, absorption purification, and stabilization. In this case, separation equipment is a mandatory one at industrial gas treatment plants [4].

The extracted oil contains formation water, associated gas, mineral salts, and mechanical impurities. Pure oil is the primary raw material for producing liquid energy, oils and lubricants, bitumen, and coke. For example, flooding crude oil with formation water and dissolved salts leads to a decrease in the quality of the oil itself and its products. [5].

Comprehensive oil preparation for transportation and further processing involves its degassing, dehydration, desalination, and stabilization. The degassing process begins immediately after the gas-liquid mixture enters the apparatus. Associated petroleum gas is usually released in quantities not sufficient for its transportation. Therefore, there is a need to dispose of it by burning it on a torch.

The use of associated petroleum gas as a fuel, which increases its energy efficiency, has become widespread. In the cases of the utilization of associated petroleum gas and its use as a fuel for more efficient combustion, dehydration is carried out to prevent the formation of crystal hydrates. Purification from heavy hydrocarbons prevents fluid blockages. The absence of hydrogen sulfide and carbon dioxide prevents corrosion on the equipment [6].

Therefore, before the transportation and further processing of natural gas and crude oil, the obligatory stage is separating the gas-liquid mixture. For this purpose, separators are used. Their operation is based on the balance of mass forces and aerodynamic drag forces.

2 Literature Review

A method of dynamic separation is proposed to extend the range of effective operation of separation devices designed to purify gas flows from liquid droplets (separation of gas-liquid mixture). According to this method, the gas stream containing the droplet liquid enters the separation channel, in which the elastic elements are cantilevered [7, 8]. These elements distort the flow of the mixture (Figure 1).

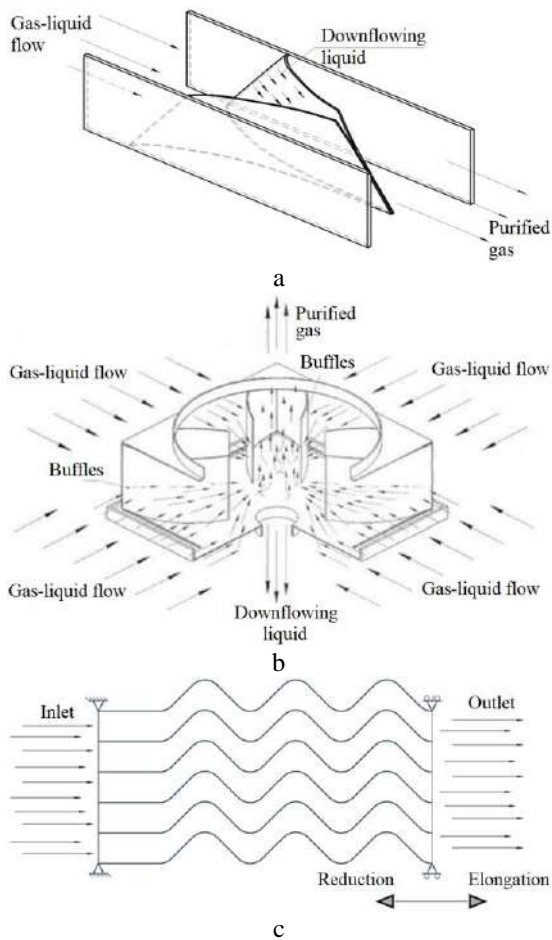


Figure 1 – Design schemes of separation devices

Under the action of inertia forces, the droplets contained in the gas deviate from the curved trajectory of the gas and settle on the walls, forming a film of liquid.

Under dynamic pressure, the elastic elements change their configuration. This causes a change in flow parameters, and therefore, there are aeroelastic phenomena. This approach allows us to adjust the values of dynamic pressure and cross-sectional area automatically.

Figure 2 reflects the main differences in the operation of dynamic separation devices before the loss of static and dynamic stability compared with the traditional louver separation elements.

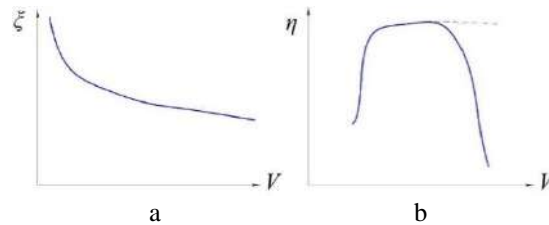


Figure 2 – Operation modes of the dynamic (a) and louver (b) separation devices: a – dependence of the hydraulic resistance coefficient ζ on the flow velocity V for the dynamic separation device; b – dependence of the separation efficiency η on the flow velocity V for the louver (solid line) and dynamic (dashed line) separation devices

An essential parameter of the separation devices is hydraulic resistance. Its value depends on the coefficient of hydraulic resistance, which is determined experimentally [9]. The value of this parameter for louver separation devices can vary from 4 to 400 depending on the design [10, 11]. In turn, dynamic separation devices, in contrast to louvers, have a variable coefficient of hydraulic resistance ζ (depending on the flow velocity V). The primary trend of this dependence is shown in Figure 2 a. Mainly, as the velocity of the gas-liquid flow increases, the cross-sectional area increases too. Therefore, the coefficient of hydraulic resistance decreases.

The primary parameter in assessing the efficiency of a separation device is the degree of separation as the coefficient of separation efficiency. This parameter is the most commonly used as the amount of separated dispersed phase to its content in the gas-liquid mixture at the inlet to the separator. [12].

In traditional designs of louver separation devices, this parameter varies depending on the inlet velocity of the gas-liquid flow. The primary trend of this change is shown in Figure 2 b by solid line [13]. The higher the flow rate, the greater the inertia force acting on the droplet liquid, causing its separation. Therefore, efficiency increases.

On the other hand, the destruction of the droplets leads to a halt in the growth of separation efficiency (a horizontal line in Figure 2 b) at a specific flow rate.

The destruction of droplets is so essential that in combination with the film destruction for the already captured liquid (and consequently, secondary splashing) leads not only to stop the growth of efficiency but also to its sharp decrease [3, 14].

Unlike a louver separation device, avoiding a decrease in separation efficiency in a dynamic separation device can be accomplished by preventing a critical increase in the effective aerodynamic force as the velocity of the gas-

liquid flow increases. This occurs by increasing the cross-section of the channel. As a result, the range of effective operations is expanding. The primary trend for a dynamic separation device is indicated in Figure 2 b by a dashed line. Thus, the primary advantage of dynamic separation devices is working as an automatic control system. In this case, the object of regulation is the hydraulic resistance and the regulating action – elastic forces. Due to this, it is possible to maintain the degree of gas purification in a wide range of possible changes in the flow rate of the gas-liquid mixture. Therefore, increasing the efficiency of the separation of heterogeneous systems through vibration-inertial separation methods is an urgent problem. It is necessary to perform physical modeling of vibration-inertial separation processes to define the essential working characteristics of dynamic separation devices.

3 Research Methodology

3.1 General formulation

Regardless of their design, dynamic separation devices include elastic elements of different types (Figure 1). These elements can change their shape under the action of the gas flow hydrodynamics. The change in the cross-section influences the flow parameters. Therefore, aerohydroelastic phenomena occur.

For developing an engineering method to calculate separation devices, it is necessary to solve the problem of aerohydroelasticity separately, considering the features and appropriate simplifications and assumptions. Given that depending on the content of the liquid phase may change the nature of the interaction of gas-liquid flow and elastic elements, the solution of this problem can be divided into the following four stages [15].

The first stage is conducting full-scale and numerical experiments. It determines and compares the gas flow rate, which causes loss of static and dynamic stability of elastic elements. When the static stability is lost, the numerical experiment is verified using the values of the deviations of the elastic elements and the gas flow velocities that caused them. Due to the numerical experiment gives a better idea of the flow structure and the deflected mode of the elements, the pressure distribution depending on the velocity and deformation is determined. The data can be used to determine the stiffness of the elements and damping of the gas flow. Therefore, the mathematical model can be refined. Verification of a dynamic stability loss by conducting a numerical experiment using oscillation frequency and amplitude of elastic elements is carried out. From the verified numerical experiment, it is possible to determine the pressure distribution over the elastic elements as a function of time and flow rate, and as a consequence, the value of damping as a function of time.

The second stage is conducting experimental studies of the interaction of elastic elements and gas-liquid flow with different liquid phase concentrations. The loss of static and dynamic stability depending on the flow rate in a specific range of the content of the dispersed liquid in the gas flow is investigated. Verification of the numerical experiment is carried out similarly to the first stage and determines the

pressure distribution on the elastic elements depending on the gas-liquid flow rate and the concentration of the liquid phase in case of loss of static stability and as a function of time in case of loss of dynamic stability. The obtained data are used to determine the stiffness of the elastic elements and the damping coefficients of the gas-liquid flow. Comparing the obtained data with the previous stage results, we can conclude about the effect of different concentrations on the stability of elastic elements, determine the separation efficiency, and consider the possibility of using vibrations for coagulation of droplets.

The third stage is studying the influence of mechanical oscillations of elastic elements on the gas-liquid flow. The expected effect is the coagulation of droplets, hence increasing their separation efficiency, similar to the effect of vibroacoustic coagulation. According to features of the specified effect, it is possible to observe both coagulation of drops and their destruction depending on a combination of the following parameters: gas-liquid flow rate, the oscillation frequency, and droplet dispersion.

Therefore, while studying the effect of mechanical oscillations on the flow, we have used a mathematical model, in which the identification was made with all the necessary parameters to find the size of the separation device. Such an approach increases the efficiency of separating the input gas-liquid mixture due to the coagulation of droplets. According to these dimensions, it is necessary to make a separation element to investigate the effect of oscillations.

The fourth stage is conducting a full-scale and numerical experiment to study the mutual effect of installed sequentially dynamic separation devices. Of particular interest is the change in the critical velocities of the gas-liquid flow (buffing and fluttering). These effects cause the phenomenon of dynamic instability, depending on the distance between the devices. The change in critical velocity may differ depending on the location in the gas flow.

Let us consider the features of researching each of the designs of the devices shown in Figure 1. The main differences are the different methods of their manufacture. For example, in a separation device where the elastic elements are truncated parabolic half-cylinders, the elastic elements (plates) are in a pre-deformed state. It must be considered since it affects their rigidity. The elastic elements have no internal stresses in the other two devices before the gas-liquid flow enters the separation channel. This is because in a dynamic device with four inputs, they are not deformed at all at the initial time. In the channel with sinusoidal walls, their shape is planned to be obtained using a vacuum press. Remarkably, one of the main difficulties in developing separation devices with elastic elements of sinusoidal shape is the choice of material. The mechanical properties of the material should provide the necessary deformations while holding the shape.

3.2 Experimental setup

Given the stages of scientific research described above, an experimental stand was developed (Figures 3, 4). It provides the solution to the following problems:

- to provide easy change of modular separation devices;
- to measure the deviation of elastic elements in the subcritical mode;
- to measure oscillation amplitudes and frequencies during the loss of dynamic stability;
- to measure the separation efficiency for a gas-liquid mixture and hydraulic resistance;
- to determine the effect of mechanical oscillations on the gas-liquid flow.

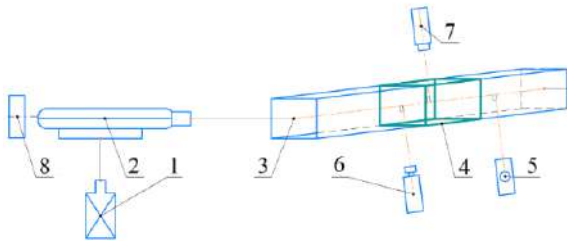


Figure 3 – The design scheme of the experimental stand:
 1 – fog generator; 2 – centrifugal gas blower; 3 – test section;
 4 – test model of the dynamic modular separation device;
 5 – anemometer; 6 – high-speed camera; 7 – stroboscope;
 8 – frequency regulator

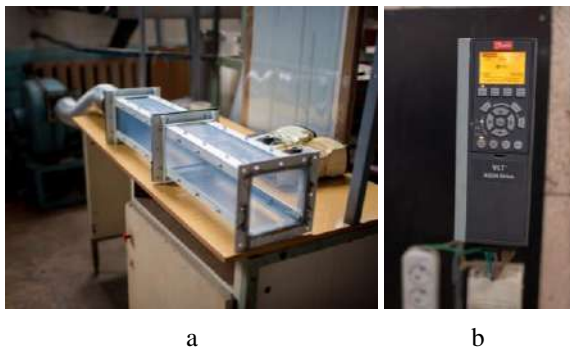


Figure 4 – Photo of test section (a) and frequency regulator (b)

Let us consider in detail the operation of the experimental stand, the design scheme of which is given in Figure 3 and the photo – in Figure 4. Dispersed liquid generated by the fog generator “Longray 2680A-II” 1 is fed to the centrifugal blower 2, where it mixes with the gas flow. Under the action of pressure, it is sent to the channel of the experimental stand, where the model of the modular dynamic separation device is installed. The deformation of an elastic element concerning the scale put on the channel walls is fixed using the high-speed camera. The camera is mounted on a tripod. The level gauge measures its position. In test section 3, the gas-liquid flow passes the modular dynamic separation device 4, where the capture of dispersed particles occurs. The captured film liquid is removed from the separator. The purified gas is released into the atmosphere. The airflow of the centrifugal blower is regulated by the frequency regulator “Aqua Drive FC 200”. The cold mist generator 1 allows us to adjust the dispersion of the liquid in a range from 5 to 50 μm . Therefore, the separation efficiency can be determined for different particle sizes.

Figure 4 a shows that the test section consists of two parts having a square cross-section of 125 mm \times 125 mm and a length of 400 mm. Such geometric dimensions were selected to ensure uniformity of flow at the inlet of the modular dynamic separation device. For this purpose, the transition nozzle from a round cross-section to a square one is used as a diffuser with an angle of 15°. The elastic elements of the modular separation device are fixed between the two parts of the test section. This fastening was chosen to minimize the impact of the housing rigidity on the oscillations of the elastic elements when they lose dynamic stability. The elements specified in Figure 1 a without inclination are considered. Therefore, their shape is a parabolic half-cylinder. The length of the plates is 210 mm.

The procedure for conducting a physical experiment at the first stage of research is as follows. Firstly, the frequency regulator is switched on, and the rotation speed of the electric motor’s rotor connected to a centrifugal gas blower is exposed. An anemometer measures the flow rate at the inlet to the modular separation device. As a result, dependence between the velocity of the gas-liquid flow and the speed of the motor is built.

Secondly, the gas flow enters the test section, where a modular separation device is installed. If the gas flow does not cause loss of dynamic stability, they are measured using a scale on the body and are tabulated. If oscillations of the elastic elements occur, recording is performed for one minute using a high-speed camera with 240 frames per second shooting speed. After, the resulting video is decomposed into frames. Comparing every two adjacent frames allows us to measure the speed of the elastic elements and determine the oscillation frequency.

Thirdly, a series of experiments are performed for the thicknesses of elastic elements of 0.4, 0.5, and 0.6 mm for different values of gas flow rate, liquid volume fraction, and dispersion. Notably, in the case of the stability loss (at a particular input flow velocity), it is necessary to wait until the mode is set because a particular time is required for damping the oscillations.

After carrying out the measurements mentioned above, new plates are installed. In this case, the frequency is set on the frequency regulator, at which the velocity of the gas-liquid flow causes oscillations of the elastic elements. The obtained time allows us to investigate the fatigue strength of elastic elements, particularly the number of bends before their destruction.

Let us consider the difference between conducting experimental research in the first and second stages. At the first stage (switching on the gas blower), the fog generator is switched on. The dispersion of droplets is established, and the resulting mist is fed to the centrifugal blower. After, the deviation of elastic elements to the loss of stability is measured. Also, the velocity of their movement, the oscillation frequency, the critical flow velocity, and the time before the destruction of the elastic element are determined. The obtained results are tabulated and compared with the corresponding results of the first stage. Additionally, the separation efficiency before the stability loss is measured.

At the third stage of research, the separation efficiency after the loss of dynamic stability is measured. In this case, a series of experiments are performed for different combinations of fluid dispersion and oscillation frequency of elastic elements. The obtained results are tabulated too.

Fourthly, two modules of dynamic separation elements are installed in the housing. At this research stage, the fog generator does not switch on but only adjusts the speed of the blower's rotor. Studying is made on both modules, and the critical input velocity that causes oscillations is determined for each module.

Simultaneously, experimental studies were carried out within the research program and methodology developed according to DSTU 3974-2000 "System of Product Development and Launching into Manufacture".

4 Results

Experimental studies of elastic baffles with a thickness of 0.4, 0.5, and 0.6 mm and a length of 200 mm have been carried out to determine the gas flow rate, at which there is a loss of dynamic and static stability. The height of baffle elements corresponds to the height of the channel. Baffle elements are made from polyvinyl chloride with the following mechanical properties: Young's modulus 2.8 GPa; Poisson's ratio 0.385 [1].

The plates had no preliminary deformation before installing them in the channel. A thermoanemometer "Hot Wire Anemometer HT-9829" is used to determine the flow velocity. Velocity measurements were performed without the installation of elastic baffles in the channel.

After carrying out measurements, it is possible to allocate some modes of work of an elastic baffle element. The symbols indicated in Figure 5 were introduced to facilitate the analysis of the results.

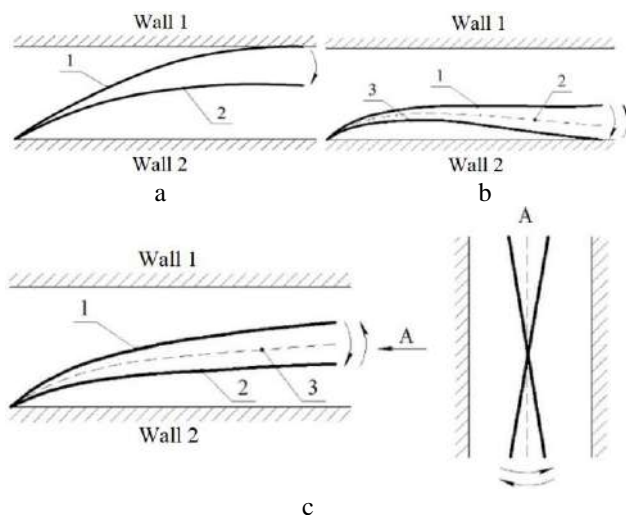


Figure 5 – Experimentally obtained operating modes for baffle element with thickness of 0.5 mm

There are no oscillations at the first mode (gas flow velocity is less than 4 m/s). Only a static deflection appears, as shown in Figure 5 a. In this case, at an inlet velocity of less than 2.2 m/s, the deviation of the element

is not observed because the gas flow passes through the gaps between the upper and lower walls of the channel and the elastic baffle element.

At the second stage (velocity range of 4.0–7.4 m/s), oscillations of the baffle element occur. It touches the upper and lower walls due to the occurrence of bending and torsional oscillations, schematically shown in Figure 5 b. As a result, the oscillating plate approaches wall 2.

At the third stage (velocity range of 7.4–11.6 m/s), the element begins to touch wall 2 (Figure 5 c), including bending torsional oscillations. The speed of 11.6 m/s was taken as a limiting value when the elastic baffle element is pressed to wall 2 and stops moving.

Let us consider the dependence of each oscillation parameter on the gas flow velocity. Three functions have been used to describe the relationship between the deviation of the elastic element (or equilibrium position) A depending on the speed V in each of the three modes mentioned above.

Let us start with the first mode, in which there are static deviations from the starting position. It includes the first six points. A linear function is applied:

$$A = b_1 V + b_0. \quad (1)$$

We did not set element b_0 to zero because noticeable deviations appear at a velocity above 2.2 m/s. Before that, the gas flow passes over the upper and lower part of the plate.

The least-squares method was used to determine the regression coefficients:

$$F = \sum_{i=1}^n (A_i - b_0 - b_1 \cdot V_i)^2 \rightarrow \min. \quad (2)$$

Since the problem of determining the coefficients of a linear polynomial is reduced to finding the minimum of the function, we have equated to zero the partial derivatives with respect to the evaluated coefficients:

$$\begin{cases} \frac{\partial F}{\partial b_0} = -2 \cdot \sum_{i=1}^n (A_i - b_0 - b_1 \cdot V_i) = 0, \\ \frac{\partial F}{\partial b_1} = -2 \cdot \sum_{i=1}^n (A_i - b_0 - b_1 \cdot V_i) \cdot V_i = 0. \end{cases} \quad (3)$$

The transformation to obtain the resulting system of linear equations with two unknowns b_0 and b_1 are performed:

$$\begin{cases} b_0 \cdot n + b_1 \cdot \sum_{i=1}^n V_i = \sum_{i=1}^n A_i, \\ b_0 \cdot \sum_{i=1}^n V_i + b_1 \cdot \sum_{i=1}^n V_i^2 = \sum_{i=1}^n (V_i \cdot A_i). \end{cases} \quad (4)$$

The inverse matrix method is used to determine them:

$$\begin{pmatrix} b_0 \\ b_1 \end{pmatrix} = \begin{pmatrix} n & \sum_{i=1}^n V_i \\ \sum_{i=1}^n V_i & \sum_{i=1}^n V_i^2 \end{pmatrix}^{-1} \cdot \begin{pmatrix} \sum_{i=1}^n A_i \\ \sum_{i=1}^n (V_i \cdot A_i) \end{pmatrix}. \quad (5)$$

Therefore, the following regression coefficients were obtained using the computer algebra system "MahtCAD" for the first mode of operation: $b_0 = -44.6$, $b_1 = 18.8$. As a result, regression (1) takes the following form:

$$A = 18.8 \cdot V - 44.6. \quad (6)$$

Equating this equation to zero, the velocity at which deviations occur can be determined. Its value equals 2.4 m/s, which differs by 0.2 m/s from the experimentally obtained value of 2.2 m/s.

For linear polynomials, the correlation coefficient is used to quantify the closeness of the relationship between the quantities. Its value is equal to 0.98. According to the Chaddock scale, this value corresponds to a very high direct relationship between velocity and deviation.

In the oscillation modes of operation, the description of the equilibrium position depending on the gas velocity is described. The polynomial coefficients are determined using the least-squares method: $b_0 = -17.0$, and $b_1 = 12.2$. The resulting regression equation is as follows:

$$A = 12.2 \cdot V - 17.0. \quad (7)$$

The correlation coefficient is equal to 0.97. According to the Chaddock scale, this value corresponds to a very high direct relationship between speed and equilibrium.

Figure 6 presents the dependence of the plate's position on the velocity of the incoming gas flow. The vertical lines show the limits of the modes in the operation of the separation element described above.

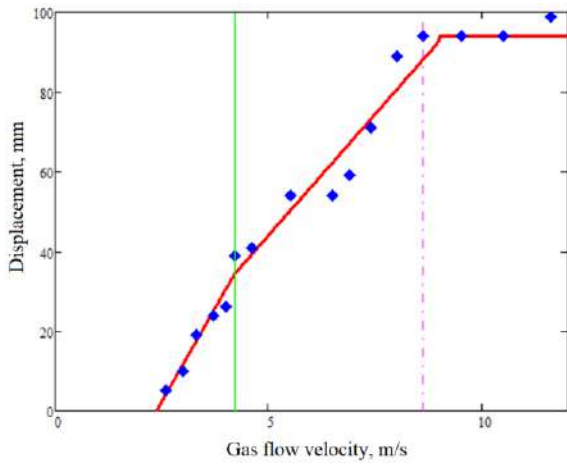


Figure 6 –Dependence of the plate's deflection on the gas flow velocity

The following parameter, the dependence of which was considered on the gas flow velocity V , is the amplitude of oscillations X . Notably, to describe the dependence on the second mode of operation (velocity range of 4.2–7.4 m/s), a polynomial of the second degree is used:

$$X = a_0 + a_1 \cdot V + a_2 \cdot V^2. \quad (8)$$

As for a linear polynomial, the determination of the unknown coefficients of a polynomial of the second degree can be performed using the least-squares method:

$$F = \sum_{i=1}^n \sum_{j=1}^n (X_i - a_0 - a_1 \cdot V - a_2 \cdot V^2)^2 \rightarrow \min. \quad (9)$$

It is necessary to equate to zero three partial derivatives with respect to the coefficients a_0 , a_1 , and a_2 :

$$\begin{aligned} \frac{\partial F}{\partial a_0} &= -2 \cdot \sum_{i=1}^n (X_i - a_0 - a_1 \cdot V_i - a_2 \cdot V_i^2) = 0, \\ \frac{\partial F}{\partial a_1} &= -2 \cdot \sum_{i=1}^n (X_i - a_0 - a_1 \cdot V_i - a_2 \cdot V_i^2) \cdot V_i = 0, \quad (10) \\ \frac{\partial F}{\partial a_2} &= -2 \cdot \sum_{i=1}^n (X_i - a_0 - a_1 \cdot V_i - a_2 \cdot V_i^2) \cdot V_i^2 = 0. \end{aligned}$$

In this case, when performing transformations, a system of linear equations with three unknowns a_0 , a_1 , and a_2 is obtained:

$$\begin{cases} a_0 \cdot n + a_1 \cdot \sum_{i=1}^n V_i + a_2 \cdot \sum_{i=1}^n V_i^2 = \sum_{i=1}^n X_i, \\ a_0 \cdot \sum_{i=1}^n V_i + a_1 \cdot \sum_{i=1}^n V_i^2 + a_2 \cdot \sum_{i=1}^n V_i^3 = \sum_{i=1}^n (X_i \cdot V_i), \\ a_0 \cdot \sum_{i=1}^n V_i^2 + a_1 \cdot \sum_{i=1}^n V_i^3 + a_2 \cdot \sum_{i=1}^n V_i^4 = \sum_{i=1}^n (X_i \cdot V_i^2). \end{cases} \quad (11)$$

Therefore, the solution of the above system using the inverse matrix method has the following form:

$$\begin{pmatrix} a_0 \\ a_1 \\ a_2 \end{pmatrix} = \begin{pmatrix} n & \sum_{i=1}^n V_i & \sum_{i=1}^n V_i^2 \\ \sum_{i=1}^n V_i & \sum_{i=1}^n V_i^2 & \sum_{i=1}^n V_i^3 \\ \sum_{i=1}^n V_i^2 & \sum_{i=1}^n V_i^3 & \sum_{i=1}^n V_i^4 \end{pmatrix}^{-1} \cdot \begin{pmatrix} \sum_{i=1}^n X_i \\ \sum_{i=1}^n (X_i \cdot V_i) \\ \sum_{i=1}^n (X_i \cdot V_i^2) \end{pmatrix}. \quad (12)$$

For the second mode of operation, using the computer algebra system “MahtCAD”, the following values of regression coefficients were obtained: $a_0 = 121.2$, $a_1 = -39.8$, and $a_2 = 4.9$. The resulting regression equation (8) takes the following form:

$$X = 121.1 - 39.8 \cdot V + 4.9 \cdot V^2. \quad (13)$$

Fisher's criterion is used to verify the significance of the regression model.

Given that the number of explanatory variables is equal to 1, the number of degrees of freedom of the explained variance is also equal to 1. The number of degrees of freedom for unexplained variance is calculated depending on the number of experimental points and the number of explanatory variables. So, it is equal to $5 - 1 - 1 = 3$. Therefore, the obtained correlation coefficient is 0.999, and Fisher's criterion is $F = 1806$. The Fisher's criterion is defined according to the corresponding table for the accepted significance level 0.05 and the above-stated degrees of freedom. It is equal to $F_{tab} = 10.13$. Since the actual value $F > F_{tab}$, the regression equation (13) is statistically reliable.

At the next stage (velocity range of 7.4–11.6 m/s), the relationship between the oscillation amplitude and the gas flow velocity was carried out using a polynomial of the second degree too, with the determination of its coefficients by the least-square method. The resulting dependence takes the following form:

$$X = 286.2 - 41.5 \cdot V + 1.9 \cdot V^2. \quad (14)$$

As in the previous case, we evaluated the accuracy of the relationship between the amplitude and the gas flow velocity using Fisher's criterion. In this case, the number of degrees of freedom for unexplained variance is equal to 5. The correlation coefficient is 0.902, Fisher's criterion $F = 21.9$, and its table value $F_{tab} = 6.61$. Therefore, the regression equation (14) is also statistically reliable.

The obtained relationships between the gas flow velocity and the oscillation amplitude for both operation modes are shown in Figure 7. Vertical lines indicate the boundaries of these modes.

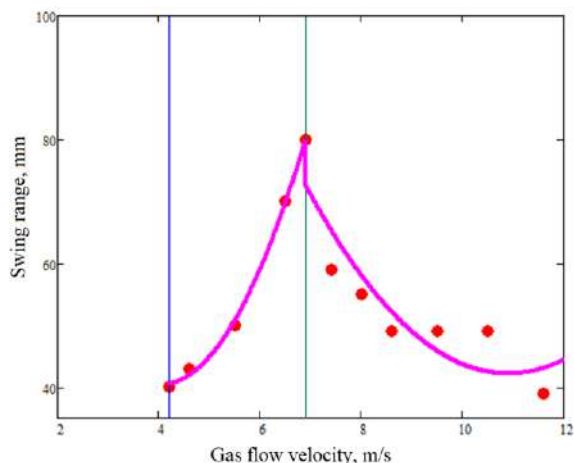


Figure 7 – Dependence of the swing range on the inlet gas flow velocity

The last parameter of oscillations studied during the experiment is the oscillation frequency. To estimate its change from increasing speed, we have found the percentage of its minimum value from the maximum. For the data obtained at the first stage of research, it is equal to 96.7 %. This parameter in the studied speed range does not change significantly. Therefore, the frequency can be considered constant when using a dynamic separation element for vibrocoagulation of droplets.

Additionally, the frequency and amplitude of the elastic baffle element with a thickness of 0.4 mm were measured. The least-squares method was used to process the results of the experiment. There are three operation modes, as in the case of a baffle element with a thickness of 0.5 mm.

Let us consider the operation of an elastic baffle element with a thickness of 0.6 mm in more detail. Its feature is the presence of four operation modes (Figure 8), differing from the plates with 0.4 and 0.5 mm thickness.

At the first stage (velocity range of 3.3–4.8 m/s), the oscillations of the baffle element occur. It does not touch any wall of the channel, which is schematically shown in Figure 8 a. Необхідно відмітити, що при швидкості входу меншій за 3.3 м/с відхилення елемента не спостерігаються, а у випадку їх виникнення являються надто малими для вимірювання.

At the second stage (velocity range of 4.8–6.6 m/s), oscillations of the elastic baffle element continue. In this case, the element begins to touch wall 1, as shown in Figure 8 b. The element's position is close to wall 2; touches occur by increasing the amplitude of oscillations.

At the third stage (velocity range of 6.6–9.9 m/s), bending-torsional oscillations occur, as evidenced by touching the upper and lower walls of the channel. Since the element's position approached with increasing speed to wall 2, the element stopped touching wall 1. This operation mode is schematically shown in Figure 8 c.

At the fourth mode (velocity range of 9.9–13.1 m/s), the element touches wall 2. In this case, bending-torsional oscillations continue (Figure 8 d).

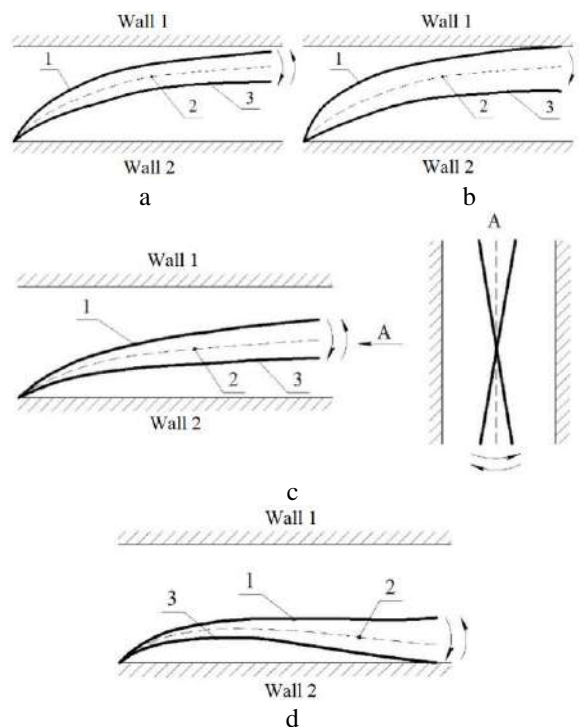


Figure 8 – Operating modes of the baffle element with the thickness of 0.6 mm: 1 – small displacements; 2 – large displacements; 3 – position of equilibrium

Notably, the gas flow velocity of 13.1 m/s is the maximum one while studying this design.

The obtained results were analyzed using the least-square method to find the coefficients of polynomials of the first and second degrees, describing the relationship between the amplitude of oscillations, the position of the elastic baffle element, and the velocity of the gas flow.

As a result, the graph of the plate's position on the velocity of the incoming gas flow is built in Figure 9.

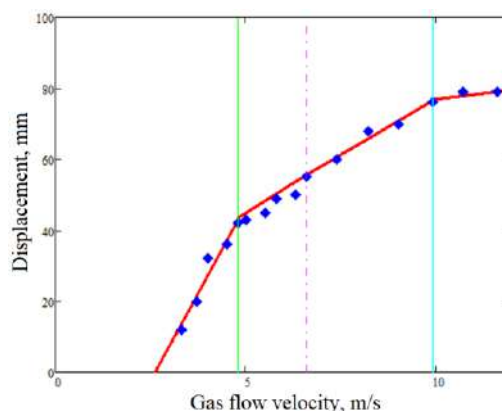


Figure 9 – Dependence of the plate's position on the gas flow velocity

Vertical lines show the mode boundaries. At the fourth mode, it should be noted that the line (as in previous cases) is almost horizontal.

Let us consider in more detail the obtained graph of the dependence of the amplitude of the elastic baffle element on the speed of the oncoming gas flow (Figure 10).

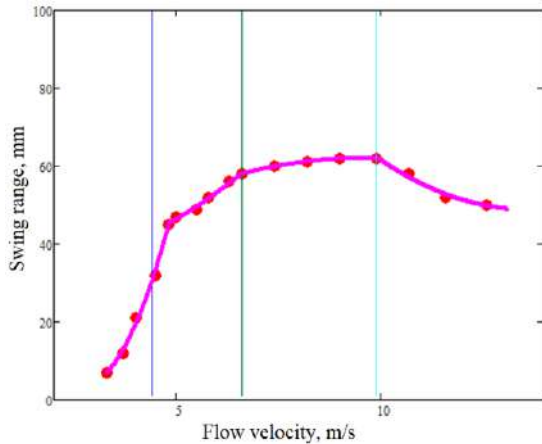


Figure 10 – Dependence of the swing range on the inlet flow velocity

In the operating modes of the separation element, in which there is no contact with the wall of channel 2, the dependence of the amplitude of oscillations on the flow velocity is increasing. In the last mode, it decreases, as in all previous cases. It should be noted that in the third mode, the dependence is almost linear, given the coefficient near the variable squared.

The percentage of the elastic baffle element's minimum and the maximum oscillation frequency is 78.8%, which may affect the coagulation of droplets.

An alternative material, ABS plastic, was proposed to manufacture elastic baffles with a thickness of 0.4 mm. This material has the following mechanical properties: Young's modulus 1.7 GPa, and Poisson's ratio 0.30. As in the case of elastic baffles made of polyvinyl chloride with a thickness of 0.4 and 0.5 mm, the operation of the above elements from ABS plastic can be divided into similar three modes.

5 Discussion

As can be seen from the results of experimental studies, the operation of the separation element from ABS plastic has a few features, mainly as follows. A wide first operating mode (коливання відсутні): velocity range of 1.1–5.3 m/s. In the first mode, there are significant deviations of the elastic element: 15–60 mm. A narrow second operating mode: velocity range of 5.5–6.3 m/s. A wide third operating mode (the element performs torsional oscillations while touching the wall 2): velocity range of

6.3–11.6 m/s. Notably, the operation is limited by the gas flow velocity of 11.8 m/s, at which the element under the action of the flow is pressed against wall 2. Thus, the regression equations for the dependence of various parameters on the flow rate were obtained. For a plate with a thickness of 0.4 mm from polyvinyl chloride, the regression equation for the deviation on the gas flow velocity is as follows: $A = 10.6V - 1.0$. The regression equation for the dependence of the equilibrium position on the velocity is as follows: $A = 6.1V - 24.0$.

In the second operating mode, the regression equation for the dependence of the swing range on the speed is as follows: $X = 36.1 - 6.9V + 6.9V^2$. Fisher's criterion calculated on the given mode takes $F = 53$ compared to tabular value $F_{tab} = 18.51$. In the third operating mode, the regression equation for the dependence of the swing range on the speed is as follows: $X = 666.2 - 118.9V + 5.8V^2$. Fisher's criterion calculated on the given mode takes $F = 6337$ compared to tabular value $F_{tab} = 6.61$.

6 Conclusions

The paper considers dynamic separation devices that operate as automatic control systems. Due to this, they allow increasing the efficiency of the separation process in heterogeneous systems. The method of conducting physical experiments of these devices and experimental setup for their study are presented.

As a result of experimental research, the operation modes of separation devices were determined for different plate thicknesses, i.e., 0.4, 0.5, and 0.6 mm. The obtained dependencies of the plate's position on the oncoming gas flow velocity and the oscillation amplitudes on different operation modes have been estimated.

The following regression equations for different parameters of flow rate were also obtained. E.g., for a plate of 0.4 mm thick from polyvinyl chloride, deviation, the position of equilibrium, and swing range on the 2nd and 3rd modes have been obtained. Fisher's criteria confirm the adequacy of the proposed model.

The obtained results verify the mathematical model and substantiate the primary parameters of studied separation devices.

7 Acknowledgments

The developed methodology was realized within the research project "Creation of new granular materials for nuclear fuel and catalysts in the active hydrodynamic environment" (State reg. No. 0120U102036). The authors also appreciate the support of the International Association for Technological Development and Innovations.

References

1. Shah, S., Koralewicz, P., Gevorgian, V., Liu, H., Fu, J. (2021). Impedance methods for analyzing stability impacts of inverter-based resources: Stability analysis tools for modern power systems. *IEEE Electrification Magazine*, Vol. 9(1), pp. 53–65.
2. Sujan, S., Jamal, M., Hossain, M., Khanam, M., Ismail, M. (2015). Analysis of gas condensate and its different fractions of Bibiyana gas field to produce valuable products. *Bangladesh Journal of Scientific and Industrial Research*, Vol. 50(1), 59.
3. Liaposhchenko, O. O., Sklabinskyi, V. I., Zavalov, V. L., Pavlenko, I. V., Nastenko, O. V., Demianenko, M. M. (2017). Appliance of inertial gas-dynamic separation of gas-dispersion flows in the curvilinear convergent-divergent channels for compressor equipment reliability improvement. *IOP Conference Series: Materials Science and Engineering*, Vol. 233(1), 012025.
4. Eremenko, O., Novikova, A. (2019). Improvement of technologies as a basis for effective development of mature field. *Tyumen 2019: 6th Conference*, Vol. 2019, pp. 1–5, doi: 10.3997/2214-4609.201900625.
5. Stewart, M., Arnold, K. (2008). Two-phase gas-liquid separators. Gas-liquid and liquid-liquid separators. In: Stewart, M., Arnold, K. (Eds.) *Gas-Liquid And Liquid-Liquid Separators*. Gulf Professional Publishing, pp. 65–130.
6. Gaile, A. A., Chistyakov, V. N., Koldobskaya, L. L., Kolesov, V. V. (2012). Extraction purification of light gas oils of secondary oil refining processes. *Chemistry and Technology of Fuels and Oils*, Vol. 48(3), pp. 187–194, doi: 10.1007/s10553-012-0357-9.
7. Liaposhchenko, O. O., Pavlenko, I. V., Nastenko, O. V., Usyk, P. Yu., Demianenko, M. M. (2015). *Method of Capturing Highly Dispersed Droplet Liquid from Gas-Liquid Stream*. Patent of Ukraine, 102445 U, B01D 45/04 (2006.01), Sumy State University.
8. Liaposhchenko, O. O., Nastenko, O. V., Pavlenko, I. V., et al. (2016). *Method of Capturing Highly Dispersed Droplet Liquid from Gas-Liquid Stream*. Patent of Ukraine, 111039 U, B01D 45/00 (2006.01), Sumy State University.
9. Kohl, A. L., Nielsen, R. (1997). *Gas Purification*. Elsevier, Amsterdam, Netherlands.
10. Fang, C., Zou, R., Luo, G., Ji, Q., Sun, R., Hu, H., Li, X., Yao, H. (2021). CFD simulation design and optimization of a novel zigzag wave-plate mist eliminator with perforated plate. *Applied Thermal Engineering*, Vol. 184, 116212.
11. Luan, Y., Sun, H. (2010). Application of numerical simulation in the design of wire-mesh mist eliminator. *2010 International Conference On Computer Design and Applications*, pp. 5-95–5-98, doi: 10.1109/iccda.2010.5540870.
12. Perry, R. H., Green, D. W. (2007). *Perry's Chemical Engineers' Handbook*. McGraw-Hill, New York, NY, USA.
13. Kharoua, N., Khezzar, L., Nemouchi, Z. (2010). Hydrocyclones for deoiling applications – A review. *Petroleum Science and Technology*, Vol. 28(7), pp. 738–755, doi: 10.1080/10916460902804721.
14. Vaidya, M. M., Duval, S., Hamad, F., O'Connell, J., Ghulam, S., Al-Talib, A., Bahamdan, A. A., Al-Otaibi, F. D. (2020). Improving the operation of split-flow sulfur recovery plants with membrane technology. *The Society of Petroleum Engineers - Abu Dhabi International Petroleum Exhibition and Conference 2020, ADIP 2020*, 165204.
15. Demianenko, M., Liaposhchenko, O., Pavlenko, I., Luscinski, S., Ivanov, V. (2020). Methodology of experimental research of aeroelastic interaction between two-phase flow and deflecting elements for modular separation devices. *Advanced Manufacturing Processes. InterPartner 2019. Lecture Notes in Mechanical Engineering*. Springer, Cham, pp. 489–499.



SPONSOR

**ACADEMY OF SCIENCES AND ARTS
OF BOSNIA AND HERZEGOVINA**

**ORGANIZER
AND
CO-ORGANIZER**

 UNIVERSITY OF SARAJEVO	 UNIVERSITY "Džemal Bijedić" OF MOSTAR	 UNIVERSITY OF TUZLA	 UNIVERSITY OF ZENICA	 SARAJEVO SCHOOL OF SCIENCE AND TECHNOLOGY OF SARAJEVO	 INTERNATIONAL UNIVERSITY OF SARAJEVO
 SOCIETY FOR ROBOTICS OF B & H	 INTERNATIONAL BURCH UNIVERSITY OF SARAJEVO	 INTERNATIONAL ASSOCIATION FOR TECHNOLOGICAL DEVELOPMENT AND INNOVATIONS UKRAINA	 FOREIGN TRADE CHAMBER OF BOSNIA AND HERZEGOVINA	 TEHNOLOGY PARK INTERA MOSTAR	

are organizing

**8th International Conference
"New Technologies,
Development and Application"**

NT-2022

CALL FOR PAPERS



Sarajevo, 23th - 25th, June 2022
ACADEMY OF SCIENCES AND ARTS
OF BOSNIA AND HERZEGOVINA

www.icnt.ba



Kanagasabai L. (2021). Heat transfer and simulated coronary circulation system optimization algorithms for real power loss reduction. *Journal of Engineering Sciences*, Vol. 8(1), pp. E1–E8, doi: 10.21272/jes.2021.8(1).e1

Heat Transfer and Simulated Coronary Circulation System Optimization Algorithms for Real Power Loss Reduction

Kanagasabai L.

¹ Department of EEE, Prasad V. Potluri Siddhartha Institute of Technology, Kanuru, Vijayawada, 520007 Andhra Pradesh, India

Article info:

Received: January 27, 2021
 The final version received: April 19, 2021
 Accepted for publication: April 25, 2021

*Corresponding email:

gklenin@gmail.com

Abstract. In this paper, the heat transfer optimization (HTO) algorithm and simulated coronary circulation system (SCCS) optimization algorithm has been designed for Real power loss reduction. In the projected HTO algorithm, every agent is measured as a cooling entity and surrounded by another agent, like where heat transfer will occur. Newton's law of cooling temperature will be updated in the proposed HTO algorithm. Each value of the object is computed through the objective function. Then the objects are arranged in increasing order concerning the objective function value. This projected algorithm time "t" is linked with iteration number, and the value of "t" for every agent is computed. Then SCCS optimization algorithm is projected to solve the optimal reactive power dispatch problem. Actions of human heart veins or coronary artery development have been imitated to design the algorithm. In the projected algorithm candidate solution is made by considering the capillaries. Then the coronary development factor (CDF) will appraise the solution, and population space has been initiated arbitrarily. Then in the whole population, the most excellent solution will be taken as stem, and it will be the minimum value of the Coronary development factor. Then the stem crown production is called the divergence phase, and the other capillaries' growth is known as the clip phase. Based on the arteries leader's coronary development factor (CDF), the most excellent capillary leader's (BCL) growth will be there. With and without L-index (voltage stability), HTO and SCCS algorithm's validity are verified in IEEE 30 bus system. Power loss minimized, voltage deviation also reduced, and voltage stability index augmented.

Keywords: optimal reactive power, transmission loss, heat transfer, simulated coronary circulation system.

1 Introduction

Power loss minimization and voltage stability enhancement with voltage deviation minimization is the key objectives of this work. Newton's method, interior point method; successive quadratic programming method [1–6]. Nevertheless, there are enormous difficulties found in handling the in-equality constraints. These ten years, there is a massive growth in the swarm and evolutionary algorithms [7–39] for solving the problem. Algorithms like genetic, ant colony, wolf search, cuckoo search, birds swarm, fish swarm, gravitational search, particle swarm optimization, symbiotic organism search algorithm [41–52] are already solved the problem. The central aspect is to maintain the exploration and exploitation in the flow of the process. Many algorithms failed to tradeoff between exploration and exploitation. This paper projects the Heat Transfer Optimization (HTO) algorithm and the Simulated Coronary Circulation System (SCCS)

optimization algorithm to solve the optimal reactive power problem. In the proposed HTO algorithm, every agent is measured as a cooling entity, and it is surrounded by another agent, like where heat transfer will occur. Newton's law of cooling temperature will be updated in the proposed HTO algorithm. Object's temperature is considered the position's position, and the heat energy will be transferred to objects surrounding it. Then new-fangled positions are modernized through new temperature conditions. Each value of the object is computed through the objective function. Then the objects are arranged in increasing order concerning the objective function value. In algorithm Control variable₁ direct the random step size and Control variable₂ organize (1 – t). In the conclusion of the procedure, the value of "t" will be augmented, leading to a linear decrease in arbitrariness and escalating the exploitation. Objects are grouped into two modes concerning temperature as *Temperature*₁

is ecological one for another object $Temperature_{\frac{n}{2}+1}$ which is in cooling condition. This paper proposes Simulated Coronary Circulation System (SCCS) optimization algorithm to solve the optimal reactive power problem. SCCS algorithm has been modeled by imitating the actions of human heart veins or coronary artery development. In the projected algorithm, few capillaries which form the preliminary group is designated as the population. Then the main arteries are taken as the variables of the problem. The divergence phase and clip phase are considered as the global search of the procedure. Then the gofer and clip phase is taken as local search in the procedure. The most excellent capillary leader (BCL) is taken as a key leader of the arteries, which will be transformed to a stem through which that coronary tree will expand. A new-fangled solution is obtained from the coronary tree branch, and the objective function cost is obtained from the end of the coronary tree's total cost. Through these for the obtained solution, the Coronary development factor (CDF) will be computed, and it will act as the fitness value of the problem. This work Heart memory parameter (HMP) is taken as a 5.0 and Heart memory parameter considering rate (HMPCR) taken as 0.955, respectively. HMP will save the most excellent solutions, and it will be sequentially modernized iteration by iteration. Proposed HTO, SCCS algorithms evaluated in IEEE 30 bus system with and without L-index. Real power loss and voltage deviation minimized with voltage stability index enhancement.

2 Research Methodology

2.1 Problem formulation

Power loss minimization is defined by

$$\text{Min } \overline{OBF}(\bar{r}, \bar{u}) \quad (1)$$

subject to

$$L(\bar{r}, \bar{u}) = 0; \quad (2)$$

$$M(\bar{r}, \bar{u}) = 0; \quad (3)$$

$$r = [VLG_1, \dots, VLG_{N_g}; QC_1, \dots, QC_{N_c}; T_1, \dots, T_{N_T}]; \quad (4)$$

$$u = [PG_{slack}; VL_1, \dots, VL_{N_{load}}; QG_1, \dots, QG_{N_g}; SL_1, \dots, SL_{N_T}]; \quad (5)$$

The fitness function (F_1, F_2, F_3) is designed for power loss (MW) reduction, Voltage deviation, voltage stability index (L-index) is defined by

$$F_1 = P_{\text{Minimize}} = \text{Minimize} \left[\sum_{m=1}^{N_{TL}} G_m [VL_i^2 + VL_j^2 - 2 * VL_i VL_j \cos \theta_{ij}] \right]; \quad (6)$$

$$F_2 = \text{Minimize} \left[\sum_{i=1}^{N_{LB}} |VL_{Lk} - VL_{Lk}^{\text{desired}}|^2 + \sum_{i=1}^{N_g} |QG_k - Q_{kG}^{\text{lim}}|^2 \right]; \quad (7)$$

$$F_3 = \text{Minimize } L_{\text{Maximum}}; \quad (8)$$

$$L_{\text{Maximum}} = \text{Maximum} [L_j]; j = 1, \dots, N_{LB}; \quad (9)$$

$$\begin{cases} L_j = 1 - \sum_{i=1}^{N_{PV}} F_{ji} \frac{VL_i}{VL_j}; \\ F_{ji} = -[Y_1]^{-1} [Y_2]; \end{cases} \quad (10)$$

$$L_{\text{Maximum}} = \text{Maximum} \left[1 - [Y_1]^{-1} [Y_2] \times \frac{VL_i}{VL_j} \right]. \quad (11)$$

Equality constraints:

$$0 = PG_i - PD_i - VL_i \sum_{j \in N_B} VL_j [G_{ij} \cos[\theta_i - \theta_j] + B_{ij} \sin[\theta_i - \theta_j]]; \quad (12)$$

$$0 = QG_i - QD_i - VL_i \sum_{j \in N_B} VL_j [G_{ij} \sin[\theta_i - \theta_j] + B_{ij} \cos[\theta_i - \theta_j]]. \quad (13)$$

Inequality constraints:

$$P_{g_{slack}}^{\text{minimum}} \leq P_{g_{slack}} \leq P_{g_{slack}}^{\text{maximum}}; \quad (14)$$

$$Q_{gi}^{\text{minimum}} \leq Q_{gi} \leq Q_{gi}^{\text{maximum}}, i \in N_g; \quad (15)$$

$$VL_i^{\text{minimum}} \leq VL_i \leq VL_i^{\text{maximum}}, i \in N_L; \quad (16)$$

$$T_i^{\text{minimum}} \leq T_i \leq T_i^{\text{maximum}}, i \in N_T; \quad (17)$$

$$Q_c^{\text{minimum}} \leq Q_c \leq Q_c^{\text{maximum}}, i \in N_C; \quad (18)$$

$$|SL_i| \leq S_{L_i}^{\text{maximum}}, i \in N_{TL}; \quad (19)$$

$$VG_i^{\text{minimum}} \leq VG_i \leq VG_i^{\text{maximum}}, i \in N_g. \quad (20)$$

Multi-objective fitness (MOF) function has been defined by

$$\text{MOF} = F_1 + r_1 F_2 + u F_3 = F_1 + \left[\sum_{i=1}^{N_L} x_v [VL_i - VL_i^{\text{min}}]^2 + \sum_{i=1}^{N_C} r_g [QG_i - QG_i^{\text{min}}]^2 \right] + r_f F_3; \quad (21)$$

$$VL_i^{\text{minimum}} = \begin{cases} VL_i^{\text{max}}, & VL_i > VL_i^{\text{max}}; \\ VL_i^{\text{min}}, & VL_i < VL_i^{\text{min}}; \end{cases} \quad (22)$$

$$QG_i^{\text{minimum}} = \begin{cases} QG_i^{\text{max}}, & QG_i > QG_i^{\text{max}}; \\ QG_i^{\text{min}}, & QG_i < QG_i^{\text{min}}; \end{cases} \quad (23)$$

2.2 Heat transfer optimization (HTO) algorithm

Heat transfer characteristics between the objects have been imitated to model the Heat Transfer Optimization (HTO) algorithm. In the proposed algorithm, every agent is measured as a cooling entity, and it is surrounded by another agent, like where heat transfer will occur. Newton's law of cooling temperature will be updated in the proposed HTO algorithm.

Generally, heat exchange coefficient symbolized as "h", and at time $t=0$ particular objects in highly elevated temperature $Temperature_0$ has been positioned or surrounded by cooling objects. Then there will be a transfer of heat between the objects $Tempaerature_b$. Concerning volume and surface, the heat loss rate is determined by

$$\frac{dq}{dt} = h(Temperature_a - Temperature_b) \text{ surfave area}(SA). \quad (24)$$

In the time dt $h(Temperature_a - Temperature_b) \text{ surfave area}(SA)dt$ is the heat loss which indicates the decrease in temperature dT as follows:

$$\text{volume}(v) * \text{density}(\rho) * \text{specific heat}(c) * Dt = -h * SA(Temperature - Temperature_b)dt. \quad (25)$$

Then

$$\frac{\text{Temperature} - \text{Temperature}_b}{\text{Temperature}_0 - \text{Temperature}_b} = \exp\left(-\frac{h * SA}{\text{volume}(v) * \text{density}(\rho) * \text{specific heat}(c)} t\right); \quad (26)$$

$$\beta = \frac{h * SA}{\text{volume}(v) * \text{density}(\rho) * \text{specific heat}(c)}; \quad (27)$$

Then equation (12) can be written as

$$\frac{Temperature - Temperature_b}{Temperature_0 - Temperature_b} = \exp(-\beta t). \quad (28)$$

Then temperature mathematically defined as follows:

$$Temperature = Temperature_b + (Temperature_0 - Temperature_b) \exp(-\beta t). \quad (29)$$

In the exploration of space objects, initial temperature is defined by:

$$Temperature_{initial}^0 = Temperature_{minimum} + random \cdot (Temperature_{maximum} - Temperature_{minimum}). \quad (30)$$

Objects are grouped into two modes concerning temperature as $Temperature_1$ is ecological one for another object $Temperature_{\frac{n}{2}+1}$ which is in cooling condition.

Then the value of β (higher or lower) determines the transfer of heat (variation of temperature between objects), and by the status of β , that position will be altered. The β value for each object is computed by

$$\beta = \frac{cost(object)}{cost(poor_object)}. \quad (31)$$

In this projected algorithm, time “ t ” is linked with iteration number, and the value of “ t ” for every agent is computed by

$$t = \frac{iteration}{maximum\ number\ of\ iteration}. \quad (32)$$

To avoid the solution getting trapped in the local solution ecological temperature of the object has been adjusted as follows:

$$Temperature_i^{ecological} = (1 - (Control\ variable_1 + Control\ variable_2 \times (1 - t)) \times random) \times Previous\ Temperature_i^{ecological}. \quad (33)$$

In equation (33) Control variable₁ direct the random step size and Control variable₂ organize (1 - t). In the conclusion of the procedure, the value of “ t ” will be augmented, leading to a linear decrease in arbitrariness and escalating the exploitation.

Then the new-fangled temperature object is updated by

$$Temperature_i^{new} = Temperature_i^{ecological} + (Temperature_i^{old} - Temperature_i^{new}) \exp(-\beta t); \quad (34)$$

Then j -th variable agent upper and lower bound defined by

$$Temperature_{i,j} = Temperature_{j,minimum} + random \times (Temperature_{j,maximum} - Temperature_{j,minimum}). \quad (35)$$

a. Start.

b. Agents are initiated by,

$$Temperature_{initial}^0 = Temperature_{minimum} + random \cdot (Temperature_{maximum} - Temperature_{minimum}).$$

c. The objective functional value will be computed.

d. Modernization of population and memory.

e. Grouping of the object is engendered.

f. Value of β , t is computed by,

$$\beta = \frac{cost(object)}{cost(poor_object)};$$

$$t = \frac{iteration}{maximum\ number\ of\ iteration}.$$

g. Ecological values altered by,

$$Temperature_i^{ecological} = (1 - (Control\ variable_1 + Control\ variable_2 \times (1 - t)) \times random) \times Previous\ Temperature_i^{ecological}$$

h. Temperature values are modernized by,

$$Temperature_i^{new} =$$

$$= Temperature_i^{ecological} +$$

$$+ (Temperature_i^{old} -$$

$$- Temperature_i^{new}) \exp(-\beta t)$$

$$Temperature_{i,j} =$$

$$= Temperature_{j,minimum} + random \cdot$$

$$(Temperature_{j,maximum} -$$

$$- Temperature_{j,minimum})$$

i. Is the end condition satisfied? If “yes”, stop the process or else go to step “c”.

2.3 Simulated coronary circulation system optimization algorithm

In this work Simulated Coronary Circulation System (SCCS) optimization algorithm has been modeled by imitating the actions of human heart veins or coronary artery development. In the projected algorithm candidate solution is made by considering the capillaries. Then the Coronary development factor (CDF) will appraise the solution, and population space has been initiated arbitrarily. Then the stem crown production is called the divergence phase, and the other capillaries’ growth is known as the clip phase. In the projected algorithm, few capillaries which form the preliminary group is designated as the population. Then the main arteries are taken as the variables of the problem. A new-fangled solution is obtained from the coronary tree branch, and the objective function cost is obtained from the end of the coronary tree’s total cost. Through these for the obtained solution, the Coronary development factor (CDF) will be computed, and it will act as the fitness value of the problem. Then in the whole population, the most excellent solution will be taken as stem, and it will be the minimum value of the Coronary development factor.

The divergence phase and clip phase are considered as the global search of the procedure. In the period at the ending of the stem, the capillary leader will expand, and for iteration “ t ”, there will be $N_{variable}$, ($j = 1, 2, \dots, N_{variable}$). Capillaries are the population $N_{population}$, ($i = 1, 2, 3, \dots, N_{population}$). Then the j -th capillaries in the present population is indicated by $Y_c^{i,j}$. Through the stem, the most excellent capillary leader (BCL) will be identified. Then for BCL, the Coronary development factor (CDF) is computed by

$$CDF_i^t = \frac{1/fitness_i}{\sum 1/fitness_i}, i = 1, 2, \dots, N_{population}; \quad (36)$$

$$CDF_c^t = \frac{1/fitness_c}{\sum 1/fitness_i}; \quad (37)$$

$$fitness_c = mean(fitness_i). \quad (38)$$

In the divergence phase, the present solution is modernized by

$$Y_{i,j}^{t+1} = Y_{i,j}^t + development\ direction \cdot Divergence\ factor(D_f) \times (Y_{c,j}^t - Random \cdot Y_{i,j}^t), i = 1 \text{ and } N_{population}, j = 1 \text{ and } N_{variable}; \quad (39)$$

$$\begin{cases} development\ direction = -1; & \text{if } CDF_c^t < CDF_i^t; \\ development\ direction & \text{else} \end{cases} \quad (40)$$

$$Y_{c,j} = mean(Y_j^t); j = 1, 2, \dots, N_{variable}. \quad (41)$$

Then the gofer and clip phase is taken as local search in the procedure. The most excellent capillary leader (BCL) is taken as a key leader of the arteries, which will be transformed to stem through the coronary tree will expand. Based on the coronary development factor (CDF) of the arteries leader, the most excellent capillary leader's (BCL) growth will be there, and for this development, the exemplar factor is computed by

$$Y_j^{t+1} = Y_{i,j}^t + \alpha \cdot random \cdot (Y_{best,j}^t - Y_{worst,j}^t). \quad (42)$$

Each capillary leader will explore the newfangled growth as capillaries. Sequentially best (most excellent) and worst are found, and preceding values will be modernized continuously. Then through the Heart memory parameter (HMP) solution which violates the boundary will be identified. HMP possesses the BCL and its CDF values. Heart memory parameter considering rate (HMPCR) varies between 0 and 1 and will select the new-fangled value from the stored values. In this work, HMP is taken as 5.0, and HMPCR is taken as 0.955, respectively. Heart memory parameter (HMP) will save the most excellent solutions, and it will be sequentially modernized iteration by iteration. HMP exploration has been balanced in the projected algorithm.

- a. Start.
- b. In the exploration space, the preliminary position of the capillary leader is arbitrarily initialized by,

$$Y_{i,j}^0 = Y_{minimum} + random \cdot (Y_{maximum} - Y_{minimum}).$$

- c. For every capillary leader, the Coronary development factor (CDF) value is computed by,

$$CDF_i^t = \frac{1/fitness_i}{\sum 1/fitness_i}, i = 1, 2, \dots, N_{population};$$

$$CDF_c^t = \frac{1/fitness_c}{\sum 1/fitness_i}.$$

- d. Heart memory parameter (HMP) will be utilized for storing the most excellent capillary leader and its Coronary development factor (CDF) value. The stored capillary leader will be added to the population, and equivalent to that poor (worst) capillary leader will be removed.

- e. Then the capability of the exploration has been augmented by adding a particular parameter "SP" inside the value of (0, 1), and it also evades the early convergence (during exploration, the beginning value is 0.1, and it increased to 0.3 to induce the superior exploitation), mainly it will specify about the changing the mechanism of the capillary leader, and is defined as follows:

$$SP = \omega_{minimum} + \left(\frac{iteration}{iteration_{maximum}} (\omega_{maximum} - \omega_{minimum}) \right).$$

- f. Apply the equations below when $Random_i < SP$;

$$Y_{i,j}^{t+1} = Y_{i,j}^t + development\ direction \cdot$$

$$Divergence\ factor(D_f) \cdot (Y_{c,j}^t - Random \cdot Y_{i,j}^t), i = 1 \text{ and } N_{population}, j =$$

$$1 \text{ and } N_{variables};$$

$$\begin{cases} development\ direction = -1; & \text{if } CDF_c^t < CDF_i^t; \\ development\ direction & \text{else} \end{cases}$$

$$Y_{c,j} = \frac{\sum_{i=1}^{N_{population}} \frac{Y_j}{fitness_i}}{\sum_{i=1}^{N_{population}} \frac{1}{fitness_i}},$$

$$j = 1, 2, \dots, N_{variable}.$$

or else

$$Y_{i,j} = Y_{minimum,j} + random \cdot (Y_{maximum,j} - Y_{minimum,j}).$$

- g. Concerning the objective function values, the capillary leader will be modernized and classified.
- h. Then the modernization and classification of the capillary leader is done by $Y_j^{t+1} = Y_{i,j}^t + \alpha \cdot random \cdot (Y_{best,j}^t - Y_{worst,j}^t)$.
- i. Concerning the objective function values, the capillary leader will be modernized and classified.
- j. Through the heart memory parameter (HMP), the most excellent capillary leader (BCL) will be preserved.
- k. The procedure will be stopped once the predefined value is reached or else go to step "c".
- l. End.

3 Results and Discussion

Projected HTO, SCCS algorithms have been tested in the standard IEEE 30 bus system [60]. Tables 1–4 compare values between proposed and reported algorithms for the IEEE 30 bus system. Figures 1–3 give a graphical comparison between the methodologies regarding power loss, voltage stability improvement, voltage deviation, and multi-objective problem formulation. Real power loss reduction has been achieved with voltage stability enhancement with minimization of voltage deviation.

Table 1 – Comparison of total power loss

Method	Power loss (MW)
Hybrid PSO-TS [53]	4.5213
TS [53]	4.6862
Basic PSO [53]	4.6862
ALO [54]	4.5900
QO-TLBO [55]	4.5594
TLBO [55]	4.5629
Standard GA [56]	4.9408
S.PSO [56]	4.9239
HAS [56]	4.9059
S-FS [57]	4.5777
IS-FS [57]	4.5142
SFS [59]	4.5275
HTO	4.5080
SCCS	4.5089

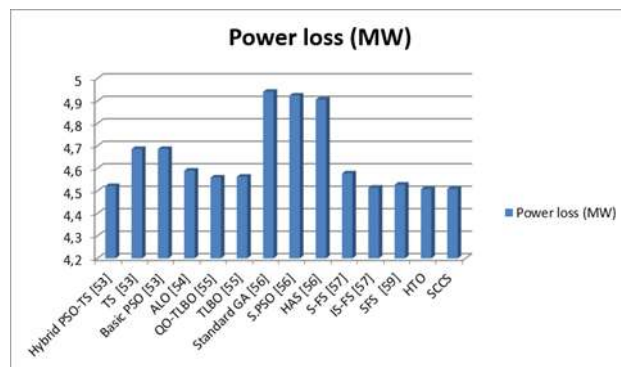


Figure 1 – Comparison of real power loss

Table 2 – Comparison of voltage deviation

Method	Voltage deviation (PU)
BPSO-TVIW [58]	0.1038
BPSO-TVAC [58]	0.2064
SPSO-TVAC [58]	0.1354
BPSO-CF [58]	0.1287
PG-PSO [58]	0.1202
SWT-PSO [58]	0.1614
PGSWT-PSO [58]	0.1539
MPG-PSO [58]	0.0892
QO-TLBO [55]	0.0856
TLBO [55]	0.0913
S-FS [57]	0.1220
ISFS [57]	0.0890
SFS [59]	0.0877
HTO	0.0869
SCCS	0.0867

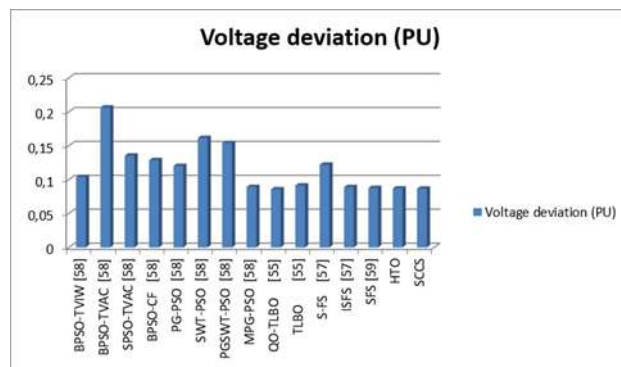


Figure 2 – Comparison of voltage deviation

Table 3 – Comparison of L-Index

Method	L-index (PU)
BPSO-TVIW [58]	0.1258
BPSO-TVAC [58]	0.1499
SPSO-TVAC [58]	0.1271
BPSO-CF [58]	0.1261
PG-PSO [58]	0.1264
SWT-PSO [58]	0.1488
PGSWT-PSO [58]	0.1394
MPG-PSO [58]	0.1241
QO-TLBO [55]	0.1191
TLBO [55]	0.1180
ALO [54]	0.1161
ABC [54]	0.1161
GWO [54]	0.1242
BA [54]	0.1252
S-FS [57]	0.1252
IS-FS [57]	0.1245
SFS [59]	0.1007
HTO	0.1004
SCCS	0.1003

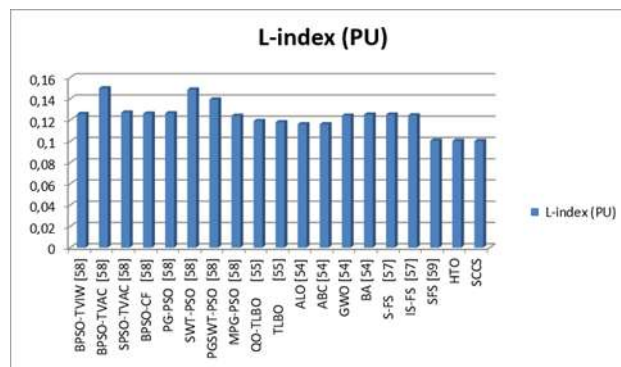


Figure 3 – Comparison of L-index

HTO, SCCS algorithms have been evaluated in IEEE 30 bus system without considering L-index [40]. In Table 4, comparisons of results are presented.

Figure 4 gives a graphical comparison between the methodologies concerning power loss. Power loss reduction has been achieved. Percentage of power loss reduction improved concerning the base case.

Table 4 – Power loss comparison

Parameters	Value of base case [47]	Modified particle swarm optimization [47]	Basic particle swarm optimization [46]	Standard evolutionary programming [45]	Self-adaptive real coded genetic algorithm [45]	HTO	SCCS
Percentage of power loss reduction	0.000	8.400	7.400	6.600	8.300	17.94	17.77
Real power loss, MW	17.550	16.070	16.250	16.380	16.090	14.40	14.43

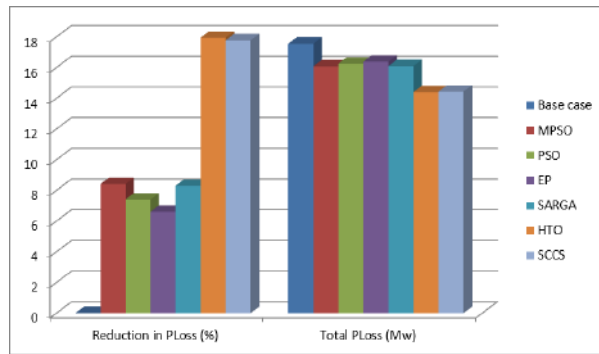


Figure 4 – Comparison of real power loss

From the above results and comparison, it is evident that real power loss has been reduced comparatively. Voltage stability enhancement and voltage deviation minimization are attained. The percentage of power loss reduction has been improved substantially. Overall comparison has been made with standard algorithms – Differential evolution, Gravitational search algorithm, Hybrid Artificial Physics–Particle Swarm Optimization, Modified particle swarm optimization, Basic particle swarm optimization Hybrid PSO-Tabu search (PSO-TS), Ant lion (ALO), quasi-oppositional teaching learning-based (QOTBO), improved stochastic fractal search optimization algorithm (ISFS), harmony search (HS) and improved pseudo-gradient search particle swarm optimization. The projected Heat Transfer Optimization (HTO) algorithm and the Simulated Coronary Circulation System (SCCS) optimization algorithm reduced the power loss effectively.

4 Conclusions

In this paper, the heat transfer optimization (HTO) algorithm and simulated coronary circulation system (SCCS) optimization algorithm successfully solved the problem. In HTO object's temperature is considered as the position is its position, and the heat energy will be transferred to objects surrounding it. Then new-fangled positions are modernized through new temperature conditions. Newton's law of cooling temperature will be updated in the proposed HTO algorithm. Then the objects are arranged in increasing order concerning the objective function value. Objects are grouped into two modes concerning temperature as $Temperature_1$ is ecological one for another object $Temperature_{\frac{n}{2}+1}$ which is in cooling condition. In the SCCS optimization algorithm, few capillaries which form a preliminary group is designated as the population. Then the main arteries are taken as the variables of the problem.

References

1. Lee, K. Y..(1984). Fuel-cost minimisation for both real and reactive-power dispatches. *Proceedings Generation, Transmission and Distribution Conference*, Vol. 131(3), pp. 85–93.
2. Deeb, N. I. (1998). An efficient technique for reactive power dispatch using a revised linear programming approach. *Electric Power System Research*, Vol. 15(2), pp. 121–134.
3. Bjelogric, M. R., Calovic, M. S., Babic, B. S. (1990). Application of Newton's optimal power flow in voltage/reactive power control. *IEEE Trans Power System*, Vol. 5(4), pp. 1447–1454.
4. Granville, S. (1994). Optimal reactive dispatch through interior point methods. *IEEE Transactions on Power System*, Vol. 9(1), pp. 136–146, <http://dx.doi.org/10.1109/59.317548>.

Through the Heart memory parameter (HMP) solution which violates the boundary will be identified. HMP possesses the most excellent capillary leader (BCL) and Coronary development (CDF) values. Heart memory parameter considering rate (HMPCR) varies between 0 and 1 and will select the new-fangled value from the stored values. The capability of the exploration has been augmented by adding a particular parameter “SP” inside the value of (0, 1), and it also evades the early convergence (during exploration, the beginning value is 0.1, and it increased to 0.3 to induce the superior exploitation), mainly it will specify about the changing the mechanism of the capillary leader. Proposed HTO, SCCS algorithms verified in standard IEEE 30- bus test system with L-index. Then algorithms are evaluated in the IEEE 30 bus test system devoid of L-index. Power loss minimization, voltage deviation minimization, and voltage stability enhancement have been attained.

Nomenclature

- OBJF* – minimization of the objective function;
L, M – control and dependent variables of the optimal reactive power problem;
r – consist of control variables;
(Q_c) – reactive power compensators;
T – dynamic tap setting of transformers;
(V_g) – level of the voltage in the generation units;
u – consist of dependent variables;
PG_{slack} – slack generator;
V_L – voltage on transmission lines;
Q_G – generation unit's reactive power;
S_L – apparent power;
N_{TL} – number of transmission line indicated by the conductance of the transmission line between the *ith* and *jth* buses;
 \emptyset_{ij} – phase angle between buses *i* and *j*;
V_{Lk} – load voltage in *kth* load bus;
V_{Lk}^{desired} – voltage desired at the *kth* load bus;
Q_{GK} – reactive power generated at *kth* load bus generators;
Q_{KG}^{Lim} – reactive power limitation;
N_{LB}, Ng – number load and generating units;
Tt – transformer tap;
Gen volt – generator voltage;
DE – differential evolution;
GSA – gravitational search algorithm;
APOPSO – Adapted Particle Swarm Optimization;
MPSO – Modified Particle Swarm Optimization;
PSO – Particle Swarm Optimization;
EP – evolutionary programming;
SARGA – self-adaptive real coded genetic algorithm.

5. Grudin, N. (1998). Reactive power optimization using successive quadratic programming method. *IEEE Transactions on Power System*, Vol. 13(4), pp. 1219–1225, <http://dx.doi.org/10.1109/59.736232>.
6. Arifoglu, U., Yalçin, F. (2018). System constrained active power loss minimization in practical multi-terminal HVDC systems through GA. *Sakarya University Journal of Science*, Vol. 22(4), pp. 1163–1173, <https://doi.org/10.16984/sofenbilder.421351>.
7. Kamel, S., Abdel-Fatah, S., Ebeed, M., Yu, J., Xie, K., Zhao, C. (2019). Solving optimal reactive power dispatch problem considering load uncertainty. *2019 IEEE Innovative Smart Grid Technologies - Asia (ISGT Asia), 2019*, pp. 1335–1340, <https://doi.org/10.1109/ISGT-Asia.2019.8881322>.
8. Bhattacharyya, B., Karmakar, N. (2020). Optimal reactive power management problem: A solution using evolutionary algorithms. *IETE Technical Review*, Vol. 37(5), pp. 540–548, doi: 10.1080/02564602.2019.1675541.
9. Kamel, S., Abdel-Fatah, S., Ebeed, M., Yu, J., Xie, K., Zhao, C. (2019). Solving optimal reactive power dispatch problem considering load uncertainty. *2019 IEEE Innovative Smart Grid Technologies - Asia (ISGT Asia), Chengdu, China, 2019*, pp. 1335–1340, doi: 10.1109/ISGT-Asia.2019.8881322.
10. Aljohani, T. M., Ebrahim, A. F., Single, O. M. (2019). Multiobjective optimal reactive power dispatch based on hybrid artificial physics–Particle swarm optimization. *Energies*, Vol. 12(12), 2333, <https://doi.org/10.3390/en12122333>.
11. Mahate, R. K., Singh, H. (2019). Multi-objective optimal reactive power dispatch using differential evolution. *International Journal of Engineering Technologies and Management Research*, Vol. 6(2), pp. 27–38, <https://doi.org/10.5281/zenodo.2585477>.
12. Nguyen, T. T., Vo, D. N. (2020). Improved social spider optimization algorithm for optimal reactive power dispatch problem with different objectives. *Neural Computing and Applications*, Vol. 32(10), <https://doi.org/10.1007/s00521-019-04073-4>.
13. Yang, S., Wang, W., Liu, C., Huang, Y. (2015). Optimal reactive power dispatch of wind power plant cluster considering static voltage stability for low-carbon power system. *J. Mod. Power Syst. Clean Energy*, Vol. 3(1), pp. 114–122, <https://doi.org/10.1007/s40565-014-0091-x>.
14. Emiroglu, S., Uyaroglu, Y., Ozdemir, G. (2017). Distributed reactive power control based conservation voltage reduction in active distribution systems. *Advances in Electrical and Computer Engineering*, Vol. 17(4), pp. 99–106, doi: 10.4316/AECE.2017.04012.
15. Ghasemi, M., Taghizadeh, M., Ghavidel, S., Aghaei, J., Abbasian, A. (2015). Solving optimal reactive power dispatch problem using a novel teaching–learning-based optimization algorithm. *Engineering Applications of Artificial Intelligence*, Vol. 39, pp. 100–108.
16. Wei, Y.-L., Nguyen, T. T., Vo, D. N., Van Tran, H., Van Dai, L. (2019). Optimal dispatch of reactive power using modified stochastic fractal search algorithm. *Complexity*, Vol. 2019, <https://doi.org/10.1155/2019/4670820>.
17. Padilha-Feltrin, A., Rodezno, D. A. Q., Mantovani, J. R. S. (2015). Volt-VAR multiobjective optimization to peak-load relief and energy efficiency in distribution networks. *IEEE Transactions on Power Delivery*, Vol. 30(2), pp. 618–626.
18. Khan, I., Li, Z., Xu, Y., Gu, W. (2016). Distributed control algorithm for optimal reactive power control in power grids. *International Journal of Electrical Power & Energy Systems*, Vol. 83, pp. 505–513.
19. Castillo, A., Lipka, P., Watson, J.-P., Oren, S. S., O'Neill, R. P. (2016). A successive linear programming approach to solving the IV-ACOPF. *IEEE Transactions on Power Systems*, Vol. 31(4), pp. 2752–2763.
20. Olabode, O. E., Okakwu, I. K., Alayande, A. S., Ajewole, T. O. (2020). A two-stage approach to shunt capacitor-based optimal reactive power compensation using loss sensitivity factor and cuckoo search algorithm. *Energy Storage*, Vol. 2, <https://doi.org/10.1002/est2.122>.
21. Bhattacharyya, B., Raj, S. (2017). Differential evolution technique for the optimization of reactive power reserves. *Journal of Circuits, Systems and Computers*, Vol. 26(10), <https://doi.org/10.1142/S0218126617501559>.
22. Dutta, S., Roy, P. K., Nandi, D. (2016). Optimal location of STATCOM using chemical reaction optimization for reactive power dispatch problem. *Ain Shams Engineering Journal*, Vol. 7(1), pp. 233–247, <https://doi.org/10.1016/j.asej.2015.04.013>.
23. Cong, Z., Haoyong, C., Honwing, N., Zipeng, L., Manlan, G., Dong, H., Solution of reactive power optimization including interval uncertainty using genetic algorithm. *IET Generation Transmission Distribution*, Vol. 11(5), pp. 3657–3664.
24. Valipour, K., Ghasemi, A. (2015). Using a new modified harmony search algorithm to solve multi-objective reactive power dispatch in deterministic and stochastic models. *Journal of AI and Data Mining*, Vol. 5(1), pp. 89–100.
25. Baziareh, A., Kavousi-Fard, F., Zare, A., Abasizade, A., Saleh, S. (2015). Stochastic reactive power planning in distribution systems considering wind turbines electric power variations. *IOS Press Content Library*, Vol. Jan.2015, pp. 1081–1087.
26. Roy, P. K., Dutta, S. (2019). Economic load dispatch: Optimal power flow and optimal reactive power dispatch concept. *Optimal Power Flow Using Evolutionary Algorithms, IGI Global*, pp. 46–64, <https://doi:10.4018/978-1-5225-6971-8.ch002>.
27. Nagendra, P., Halder Nee Dey, S., Paul, S. (2014). Voltage stability assessment of a power system incorporating FACTS controllers using unique network equivalent. *Ain Shams Engineering Journal*, Vol. 5(1), pp. 103–111.
28. Nagendra, P., Halder Nee Dey, S. and Paul, S. (2015). Location of static VAR compensator in a multi-bus power system using unique network equivalent. *Adv. Energy Res.*, Vol. 3(4), pp. 235–249.
29. Zhang, H., Lei, X., Wang, C., Yue, D., Xie, X. (2017). Adaptive grid based multi-objective Cauchy differential evolution for stochastic dynamic economic emission dispatch with wind power uncertainty. *PLOS One*, Vol. 12(9), <https://doi.org/10.1371/journal.pone.0185454>.
30. Li, J., Wang, N., Zhou, D., Hu, W., Huang, Q., Chen, Z., Blaabjerg, F. (2020). Optimal reactive power dispatch of permanent magnet synchronous generator-based wind farm considering levelised production cost minimization. *Renewable Energy*, Vol. 145, pp. 1–12.
31. Prasad, C. D., Kumar, G. P. (2015). Effect of load parameters variations on AGC of single area thermal power system in presence of integral and PSO-PID controllers. *2015 Conf. Power, Control. Common. Compute. Technol. Sustain. Growth, PCCCTSG 2015*, pp. 64–68.
32. Morsal, J., Zare, K., Hagh, M. T. (2015). *Performance Comparison of TCSC with TCPS and SSSC Controllers in AGC of Realistic Interconnected Multi-Sources Power System*. Elsevier.
33. Fadel, W., Kilic, U., Ayan, K. (2021). Optimal reactive power flow of power systems with two-terminal HVDC and multi distributed generations using backtracking search algorithm. *International Journal of Electrical Power & Energy Systems*, Vol. 127, 106667, <https://doi.org/10.1016/j.ijepes.2020.106667>.

34. Wei, H., Lin, C., Wang, Y. (2018). The optimal reactive power flow model in mixed polar form based on transformer dummy nodes. *IEEJ Trans Elec Electron Eng*, Vol. 13, pp. 411–416.
35. Fang, S., Cheng, H., Xu, G., Zhou, Q., He, H., Zeng, P. (2017). Stochastic optimal reactive power reserve dispatch considering voltage control areas. *Int. Trans. Electr. Energ. Syst.*, Vol. 27, <https://doi.org/10.1002/etep.2269>.
36. Dozein, M. G., Monsef, H., Ansari, J., Kazemi, A. (2016) An effective decentralized scheme to monitor and control the reactive power flow: A holonic-based strategy. *Int. Trans. Electr. Energ. Syst.*, Vol. 26, pp. 1184–1209.
37. Du, Z., Nie, Y., Liao, P. (2014). PCPDIPM-based optimal reactive power flow model using augmented rectangular coordinates. *Int. Trans. Electr. Energ. Syst.*, Vol. 24, pp. 597–608.
38. Liu, B., Liu, F., Zhai, B., Lan, H. (2019). Investigating continuous power flow solutions of IEEE 14-bus system. *IEEJ Trans Elec Electron Eng*, Vol. 14, pp. 157–159.
39. Soodi, H. A., Vural, A. M. (2018). STATCOM estimation using back-propagation, PSO, shuffled frog leap algorithm, and genetic algorithm based neural networks. *Comput Intell Neurosci.*, Vol. 2018, 6381610.
40. Illinois Center for a Smarter Electric Grid (ICSEG). Available online: <https://icseg.iti.illinois.edu/ieee-30-bussystem>.
41. El Ela, A. A., Abido, M. A., Spea, S. R. (2011). Differential evolution algorithm for optimal reactive power dispatch. *Electr. Power Syst. Res.*, Vol. 81, pp. 458–464.
42. Duman, S., Sönmez, Y., Güvenç, U., Yörükeren, N. (2012). Optimal reactive power dispatch using a gravitational search algorithm. *IET Gener. Transm. Distrib.*, Vol. 6, pp. 563–576.
43. Aljohani, T. M., Ebrahim, A. F., Mohammed, O. (2019). Single and multiobjective optimal reactive power dispatch based on hybrid artificial physics–particle swarm optimization. *Energies*, Vol. 12, 2333.
44. Dai, C., Chen, W., Zhu, Y., Zhang, X. (2009). Seeker optimization algorithm for optimal reactive power dispatch. *IEEE T. Power Syst.*, Vol. 24(3), pp. 1218–1231.
45. Subbaraj, P., Rajnarayan, P. N. (2009). Optimal reactive power dispatch using self-adaptive real coded genetic algorithm. *Electr. Power Syst. Res.*, Vol. 79(2), pp. 374–381.
46. Pandya, S., Roy, R. (2015). Particle swarm optimization based optimal reactive power dispatch. *Proceeding of the IEEE International Conference on Electrical, Computer and Communication Technologies (ICECCT)*, pp. 1–5.
47. Hussain, A. N., Abdullah, A. A., Neda, O. M. (2018). Modified Particle swarm optimization for solution of reactive power dispatch. *Research Journal of Applied Sciences, Engineering and Technology*, Vol. 15(8), pp. 316–327, doi: 10.19026/rjaset.15.5917.
48. Mahadevan, K., Kannan, P. S. (2010). Comprehensive learning particle swarm optimization for reactive power dispatch. *Appl. Soft Comput.*, Vol. 10(2), pp. 641–652.
49. Reddy, S. S. (2017). Optimal reactive power scheduling using cuckoo search algorithm. *International Journal of Electrical and Computer Engineering*, Vol. 7(5), pp. 2349–2356.
50. Reddy, S. S. (2014). Faster evolutionary algorithm based optimal power flow using incremental variables. *Electrical Power and Energy Systems*, Vol. 54, pp. 198–210.
51. Saddique, M. S., Bhatti, A. R., Haroon, S. S., Sattar, M. K., Amin, S., Sajjad, A. I., ul Haq, S. S., Awan, A. B., Rasheed, N. (2020). Solution to optimal reactive power dispatch in transmission system using meta-heuristic techniques – Status and technological review. *Electr. Power Syst. Res.*, Vol. 178, 106031.
52. Packiasudha, M., Suja, S., Jerome, J. (2017). A new cumulative gravitational search algorithm for optimal allocation of FACTS device to minimize system loss in deregulated electrical power environment. *Int. J. Electr. Power Energy Syst.*, Vol. 84, pp. 34–46.
53. Sahli, Z., Hamouda, A., Bekrar, A., Trentesaux, D. (2014). Hybrid PSO-tabu search for the optimal reactive power dispatch problem. *Proceedings of the IECON 2014-40th Annual Conference of the IEEE Industrial Electronics Society*, pp. 3536–3542, doi: 10.1109/IECON.2014.7049024.
54. Mouassa, S., Bouktir, T., Salhi, A. (2017). Ant lion optimizer for solving optimal reactive power dispatch problem in power systems. *Engineering Science and Technology, an International Journal*, Vol. 20(3), pp. 885–895.
55. Mandal, B., Roy, P. K. (2013). Optimal reactive power dispatch using quasi-oppositional teaching learning based optimization. *International Journal of Electrical Power & Energy Systems*, Vol. 53, pp. 123–134.
56. Khazali, H., Kalantar, M. (2011). Optimal reactive power dispatch based on harmony search algorithm. *International Journal of Electrical Power & Energy Systems*, Vol. 33(3), pp. 684–692.
57. Tran, H. V., Pham, T. V., Pham, L. H., Le, N. T., Nguyen, T. T. (2019). Finding optimal reactive power dispatch solutions by using a novel improved stochastic fractal search optimization algorithm. *Telecommunication Computing Electronics and Control*, Vol. 17(5), pp. 2517–2526.
58. Polprasert, J., Ongsakul, W., Dieu, V. N. (2016). Optimal reactive power dispatch using improved pseudo-gradient search particle swarm optimization. *Electric Power Components and Systems*, Vol. 44(5), pp. 518–532.
59. Duong, T. H., Duong, M. Q., Phan, V.-D., Nguyen, T. T. (2020). Optimal reactive power flow for large-scale power systems using an effective metaheuristic algorithm. *Journal of Electrical and Computer Engineering*, Vol. 2020, <https://doi.org/10.1155/2020/6382507>.
60. MATPOWER 4.1 IEEE 30-Bus and 118-Bus Test System. Retrieved from: <http://www.pserc.cornell.edu/matpower>.



Eze P. C., Ugoh C. A., Inaibo D. S. (2021). Positioning control of DC servomotor-based antenna using PID tuned compensator. *Journal of Engineering Sciences*, Vol. 8(1), pp. E9–E16, doi: 10.21272/jes.2021.8(1).e2

Positioning Control of DC Servomotor-Based Antenna Using PID Tuned Compensator

Eze P. C.^{1*}, Ugoh C. A.², Inaibo D. S.²

¹ Department of Electrical and Electronic Engineering, Covenant Polytechnic, Aba, Nigeria;

² Department of Power Plant and Utilities Gas Turbine Unit, NNPC WRPC, Ekpan, Warri, Nigeria

Article info:

Received: December 14, 2020
 The final version received: April 26, 2021
 Accepted for publication: May 1, 2021

*Corresponding email:

paulinuseze1@gmail.com

Abstract. Direct current (DC) servomotor-based parabolic antenna is automatically positioned using control technique to track satellite by maintaining the desired line of sight for quality transmission and reception of electromagnetic wave signals in telecommunication and broadcast applications. With several techniques proposed in the literature for parabolic antenna position control, there is still a need to improve the tracking error and robustness of the control system in the presence of disturbance. This paper has presented positioning control of DC servomotor-based antenna using proportional-integral-derivative (PID) tuned compensator (TC). The compensator was designed using the control and estimation tool manager (CETM) of MATLAB based on the PID tuning design method using robust response time tuning technique with interactive (adjustable performance and robustness) design mode at a bandwidth of 40.3 rad/s. The compensator was added to the position control loop of the DC servomotor-based satellite antenna system. Simulations were carried out in a MATLAB environment for four separate cases by applying unit forced input to examine the various step responses. In the first and second cases, simulations were conducted without the compensator (PID TC) in the control loop assuming zero input disturbance and unit input disturbance. The results obtained in terms of time-domain response parameters showed that with the introduction of unit disturbance, the rise time improved by 36 % (0.525–0.336 s) while the peak time, peak percentage overshoot, and settling time deteriorate by 16.3 % (1.29–1.50 s), 43.5 % (34.7–49.8 %), and 7.6 % (4.35–4.68 s), respectively. With the introduction of the PIDTC for the third case, there was an improvement in the system's overall transient response performance parameters. Thus to provide further information on the improved performance offered by the compensator, the analysis was done in percentage improvement. Considering the compensated system assuming zero disturbance, the time-domain response performance parameters of the system improved by 94.1, 94.7, 73.1, and 97.1 % in terms of rising time (525–30.8 ms), peak time (1.290–67.9 ms), peak percentage overshoot (34.7–9.35 %), and settling time (4.35–0.124 s), respectively. In the fourth case, the compensator's ability to provide robust performance in the presence of disturbance was examined by comparing the step response performance parameters of the uncompensated system with unit input disturbance to the step response performance parameters of the compensated system tagged: with PID TC + unit disturbance. The result shows that PID TC provided improved time-domain transient response performance of the disturbance handling of the system by 91.0, 95.4, 80.0, and 93.1 % in terms of rising time (336–30.5 ms), peak time (1500–69.1 ms), peak percentage overshoot (34.7–10.0), and settling time (4.68–0.325 s), respectively. The designed compensator provided improved robust and tracking performance while meeting the specified time-domain performance parameters in the presence of disturbance.

Keywords: antenna, compensator, direct current servomotor, proportional-integral-derivative tuned compensator, positioning control.

1 Introduction

Parabolic antennas are mechanical structures that serve as essential telecommunication and broadcast equipment components used to transmit and receive signals. These antennas are used to establish communication between observers on the earth and

satellite in space. Usually mounted at earth stations, parabolic antennas are employed in satellite tracking applications and are subject to environmental actions such as wind disturbance.

One of the environmental disturbance effects is the changes it can cause on the azimuth positioning control of a satellite dish. Thus, this problem has attracted

research attention in the positioning control of antennas [1]. The interests elicited by azimuth positioning control can be attributed to the significant roles and enhance performances that it would provide for efficient satellite dish communication. With many control methods proposed to achieve optimum azimuth position, such positioning remains a control problem [2].

Direct current (DC) servomotor-based control techniques have been used to position parabolic antenna for satellite tracking automatically. The application of fuzzy proportional-integral-derivative (Fuzzy-PID) control technique and conventional PID controller to achieve optimum satellite tracking performance has been proposed by Hoi et al. [3]. The step response of the Fuzzy-PID and conventional PID revealed the presence of chattering. A discrete control system using a PID control algorithm to get enhanced control of satellite dish angle was proposed by Xuan et al. [4]. The weakness of this work can be attributed to the lack of proper tuning of the PID gains for accurate results. Considering the case of overseas satellite telecommunication, Soltani et al. [5] applied a control system to direct onboard motorized antenna towards a selected satellite using Fault Tolerant Control (FTC) technique. However, the FTC scheme was not sufficiently robust to address the detected fault in the response. The uses of PID and Linear Quadratic Gaussian (LQG) or Linear Quadratic Regulator (LQR) for positioning control of antenna azimuth were presented by [6, 7]. The performance of either PID-LQG or PID-LQR degrades due to nonlinearity and delay as the system approaches the setpoint. Although a much-improved performance in terms of reduced settling time and reduced overshoot was reported by Okumus et al. [8] to have been achieved using Fuzzy Logic Controller (FLC) and Self-Tuning Fuzzy Logic Controllers (STFLC), the chattering process was said to be the weakness of the system. Uthman and Sudin [2] used the PID controller and state feedback controller technique for the control of satellite antenna azimuth position control. However, the system is prone to a nonlinear effect. Fandak and Okumus [9] applied PID, FLC, and Sliding Model Control (SMC) techniques for antenna azimuth position control. It was reported that the performances of the PID and FLC controllers were affected by periodic noise, while the SMC controller was not affected. However, the weaknesses of SMC

control is the chattering effect. In order to improve the performance of the antenna position control system, Onyeka et al. [10] used a Model Predictive Controller (MPC). Though the design specifications were realized in work, the designed MPC parameter seems inadequate to offer robust performance in the presence of disturbance. Application of PID controller and a low pass filter applied to setpoint input aim at improving the performance response of mobile satellite antenna network within Nigeria was presented by Eze et al. [11]. Though the system was reported to have achieved better response performance than the existing system, there was weakness in providing optimum performance in terms of rising time and peak time compared to the existing system, and the effect of disturbance was not considered. Because of these proposed systems and the nonlinear characteristics of the satellite antenna due to the uncertainties caused by wind actions and other environmental disturbances, there is still a control problem. There is a need for improved robustness to disturbance handling while maintaining reduced tracking error for effective antenna azimuth position control, which justifies this study.

In this paper, the objective is to design a compensator to address the problem of antenna azimuth position control deterioration caused by disturbance for quality communication and achieving the design requirements standard of a practical industrial system in the time domain given as the rising time of less than or equal to 4 s, peak percentage overshoot of less than or equal to 10 % and settling time of less than or equal to 5 s [7]. A controller is proposed to ensure robust performance for effective satellite tracking and line of sight operation even in the presence of disturbance. The remaining part of this paper is divided into four sections, namely, system description and DC servomotor modeling, design of PID TC, simulation results and discussion, and conclusion.

2 Research Methodology

2.1 System description

The structure of a DC servomotor-based antenna positioning control system is presented in the form of a block diagram in Figure 1.

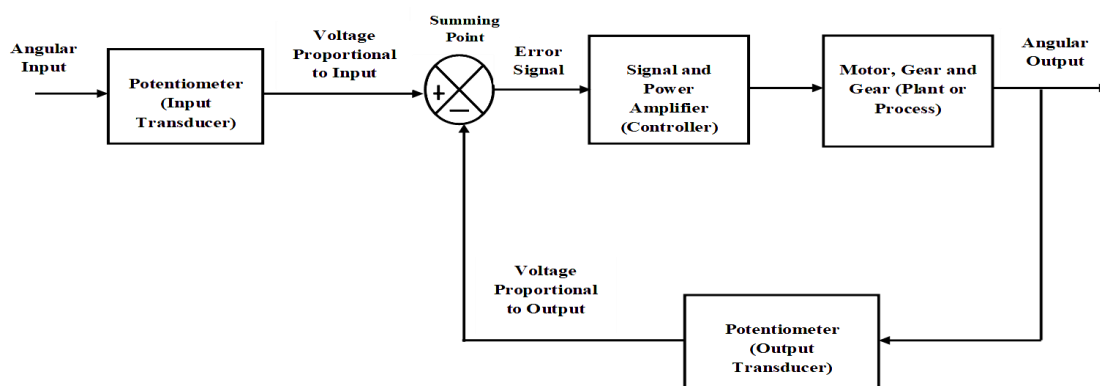


Figure 1 – Block diagram of position control satellite antenna

The system has two transducers, which are potentiometers for converting angular input and angular output (mechanical quantities) to equivalent voltage values (electrical quantities) at the input and output. The angular input is the reference position, which is the first input to the summing point after being converted to equivalent voltage magnitude (voltage proportional to input) by the input potentiometer and serves as the azimuth's desired position or elevation motor is required to attain. The second input to the summing point is the voltage proportional to the output obtained from the angular output (output position) conversion by the feedback potentiometer. The difference between the two inputs to the summing point is the error signal fed into the controller that manipulates the error signal and gives out an appropriate manipulated or control signal to rotate the motor in either direction in line with the sign of the error signal, positive or negative [7]. The error signal reduces to zero as the desired position is approached, thereby bringing the motor to a stop [7].

2.2 DC servomotor modeling

It is necessary to provide the mathematical expression of the dynamics of the DC motor, which is very important in realizing the paper's objective. Figure 2 is an illustration of an armature-controlled DC motor for the antenna positioning control system.

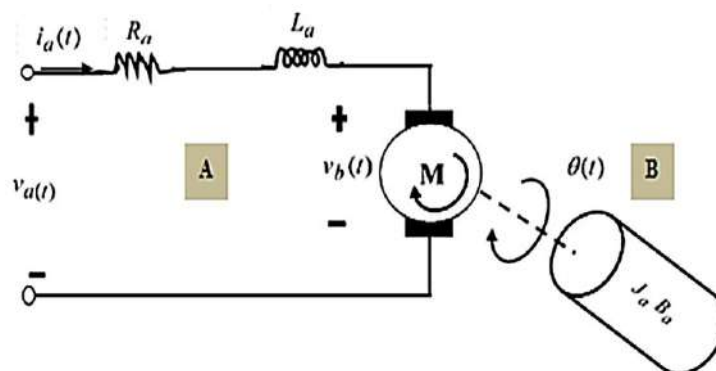


Figure 2 – DC motor diagram

The equation of the torque is given by:

$$J_a \frac{d^2\theta(t)}{dt} + B_a \frac{d\theta(t)}{dt} = K_T I_a(t). \quad (5)$$

Taking the Laplace transform of equations (4) and (5) assuming zero initial conditions give:

$$V_a(s) = L_a s I_a(s) + R_a I_a(s) + K_B s \theta(s) \quad (6)$$

$$J_a s^2 \theta(s) + B_a \theta(s) = K_T I_a(s) \quad (7)$$

Making current the subject in (6) and (7), and equating both gives:

The DC motor diagram in Figure 2 consists of two main parts: the electrical components (part A) and the mechanical components (part B). The applied voltage to the motor's armature varies without changing the applied voltage to the field in armature controlled separately excited DC motor. Applying Kirchhoff's voltage law (KVL) and the law of dynamic motion to the DC motor in Figure 2 gives the following mathematical expressions:

$$V_a(t) = R_a I_a(t) + L_a \frac{dI_a(t)}{dt} + E_b(t); \quad (1)$$

$$E_b(t) = K_B \omega_m(t) = K_B \frac{d\theta(t)}{dt}; \quad (2)$$

$$T_m(t) = K_T I_a(t), \quad (3)$$

where $V_a(t)$ – applied voltage; $E_b(t)$ – back electromotive force (emf); $T_m(t)$ – motor torque; R_a – armature resistance; $I_a(t)$ – armature current; L_a – armature inductance; K_B – back-emf constant; K_T – motor torque constant, $\omega_m(t)$ – the angular velocity; $\theta(t)$ – the angular position.

Substituting equation (2) into (1) gives

$$V_a(t) = L_a \frac{dI_a(t)}{dt} + R_a I_a(t) + K_B \frac{d\theta(t)}{dt}. \quad (4)$$

$$\frac{V_a(s) - K_B s \theta(s)}{R_a + L_a s} = \frac{J_a s^2 \theta(s) + B_a s \theta(s)}{K_T}. \quad (8)$$

The ratio of the output (angular output) to the applied voltage is given by:

$$\frac{\theta(s)}{V_a(s)} = \frac{K_T}{s[(R_a + L_a s)(J_a s + B_a) + K_T K_B]}. \quad (9)$$

The block model of the DC servomotor dynamic is shown in Figure 3.

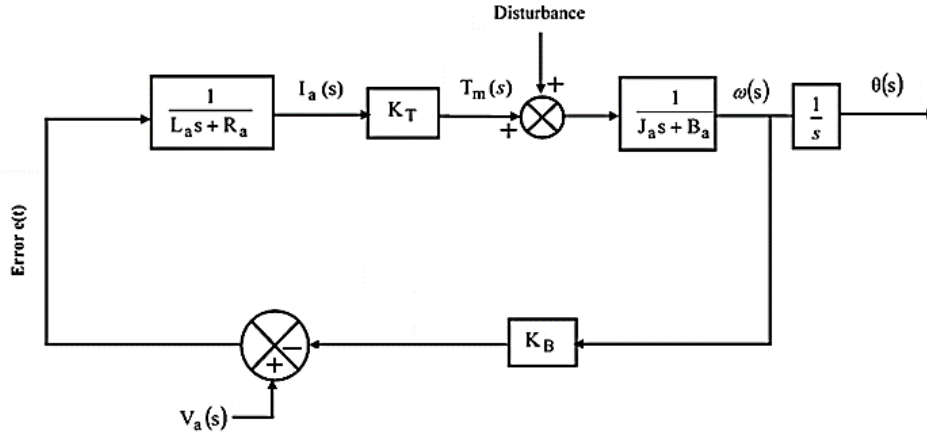


Figure 3 – Closed-loop block model of DC motor dynamic

The transfer function from reference input (applied voltage) to the angular velocity as shown in Figure 3 (assuming disturbance is zero) is given by:

$$\frac{\omega(s)}{V_a(s)} = \frac{K_T}{[(R_a + L_a s)(J_a s + B_a) + K_T K_B]} \quad (10)$$

The transfer function expressions in equations (9) and (10) are relevant to the electrical-mechanical motion analysis of the DC motor responsible for the antenna's azimuth/elevation positioning.

The armature circuit inductance L_a is usually negligible in a fixed motor [13] and $K_T = K_a$, $R_a \gg L_a$ [7]. Thus, equation (10) is reduced to:

$$\frac{\theta(s)}{V_a(s)} = \frac{K_T/R_a}{J_a s^2 + s(B_a + K_T K_B/R_a)} \quad (11)$$

Substituting the equivalent values for the moment of inertia and the viscous friction coefficient, equation (11) is expressed:

$$\frac{\theta(s)}{V_a(s)} = \frac{K_T/R_a J_m}{J_m s^2 + s(B_m + K_T K_B/R_a)} \quad (12)$$

Dividing numerator and denominator by J_m , equation (12) is expressed given by:

$$\frac{\theta(s)}{V_a(s)} = \frac{K_m}{s(s + a_m)} \quad (13)$$

where B_m – the equivalent viscous friction coefficient; J_m – the equivalent moment of inertia; K_m – motor and load gain; a_m – the motor and load pole:

$$K_m = \frac{K_T}{R_a J_m}, \quad a_m = \frac{B_m R_a + K_T K_B}{J_m R_a}$$

The parameters of the system, as well as the DC servomotor, are given in Table 1. Using a gear ratio, the transfer function relating the angular position and armature voltage is given by:

$$\frac{\theta(s)}{V_a(s)} = 0.1 \times \frac{K_m}{s(s + a_m)} = \frac{0.2083}{s(s + 1.71)} \quad (14)$$

With $a = 100$, $K_1 = 100$, and $K_{pot} = 0.318$ defined in Table 1, the closed-loop diagram shown in Figure 4 has a transfer function for antenna DC servomotor system given by:

$$G_p(s) = \frac{\theta_o(s)}{\theta_i(s)} = \frac{6.63K}{s^3 + 101.71s^2 + 171s + 6.63K} \quad (15)$$

According to the Routh-Hurwitz criterion, the system will give a stable response with a gain K of the preamplifier in the range $0 < K < 2,623$ [1, 7, 12]. The gain has been chosen in this paper to be 100 for design convenience and energy consumption reduction.

Table 1 – Parameters of the model with DC servomotor [1, 4, 7]

Quantity	Definition	Value
a	Power amplifier pole	100
a_m	Motor and load pole	1.71
b_a	Motor dampening constant	0.01 N·m/rad
B_L	Load dampening constant	1 N·m·s/rad
B_m	Viscous friction coefficient	0.02 N·m·s/rad
J_a	Motor inertia constant	0.02 kg·m ²
J_L	Load inertia constant	1 kg·m ²
J_m	Equivalent moment of inertia	0.03 kg·m ²
K	preamplifier gain	–
K_1	Power amplifier gain	100
K_B	Back emf constant	0.5 V·s/rad
K_g	Gear ratio	0.1
K_m	Motor and load gain	2.083
K_{pot}	Potentiometer gain	0.318
K_T	Motor torque constant	0.5 N·m/A
L_a	Motor armature inductance	0.45 H
N	Turns on potentiometer	10
$N_1/N_2/N_3$	Gear teeth, respectively	25/250/250
R_a	Motor armature resistance	8 Ohm
V	Voltage across potentiometer	10 V

The closed-loop block diagram of the antenna DC servo motor control system is shown in Figure 4.

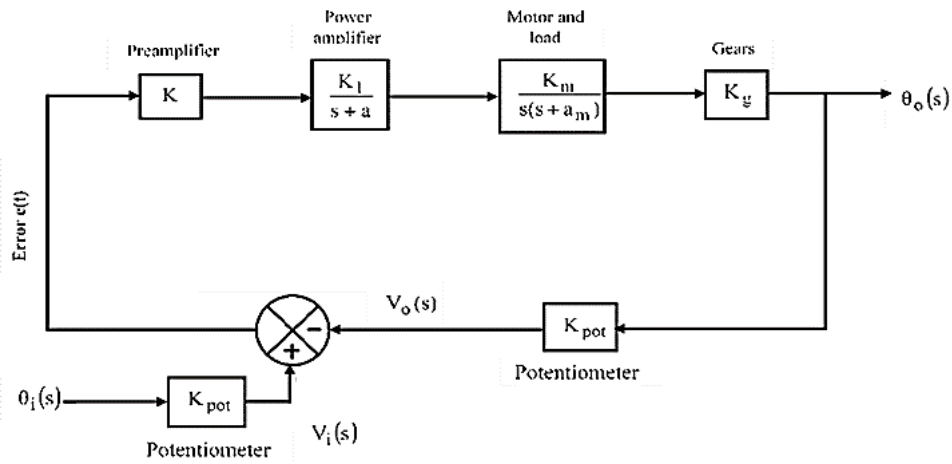


Figure 4 – Closed-loop block diagram of antenna DC servomotor control system

2.3 Design of PID tuned compensator and system configuration

The compensator is used in a control system when the response is very unstable and required to be stabilized to achieve specified performance. Since the studied DC servomotor-based satellite antenna shows some degree of instability and it is prone to environmental disturbance, a compensator has been designed using the Control and Estimation Tool Manager (CETM) of

MATLAB and added to the position control loop to achieve improved transient response and robustness with better stability performance. The design method is based on PID Tuning using robust response time as the tuning method with interactive (adjustable performance and robustness) design mode in the frequency domain. The tuning bandwidth is 40.3 rad/s. The closed diagram of the system with the designed compensator and an input disturbance is shown in Figure 5.

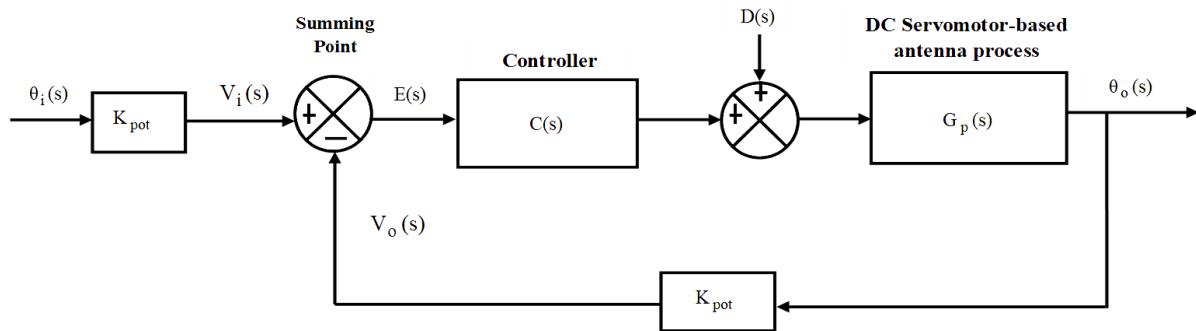


Figure 5 – Block diagram of DC servomotor-based position control

The compensator is given by:

$$C(s) = 7.2507 \frac{(1 + 0.32s)(1 + 2.8s)}{s(1 + 0.0024s)}. \quad (16)$$

$$G_d = \frac{1326s^9 + 4.046e05s^8 + 4.183e07s^7 + 1.537e09s^6 + 7.869e09s^5 + 4.941e10s^4 + 1.319e11s^3 + 3.992e11s^2 + 4.984e11s + 7.729e11}{s^{12} + 406.8s^{11} + 6.275e04s^{10} + 4.421e06s^9 + 1.296e08s^8 + 8.809e08s^7 + 6.441e09s^6 + 2.466e10s^5 + 9.742e10s^4 + 2.222e11s^3 + 5.228e11s^2 + 5.98e11s + 7.729e11} \quad (17)$$

The closed-loop transfer function with the compensator assuming zero disturbance is given by:

$$G_{cp}(s) = \frac{C(s) \times G_p(s)}{1 + C(s) \times G_p(s)}. \quad (18)$$

Hence substituting the expressions in equations (15) and (16) into (18) gives:

The closed-loop transfer function without the compensator assuming unit disturbance is given by:

$$G_{cp}(s) = \frac{1.7947e06(s + 0.3571)(s + 3.125)}{(s + 429.3)(s + 3.443)(s^2 + 85.28s + 3989)}. \quad (19)$$

Using a similar approach for closed-loop transfer function assuming a step input disturbance $D(s)$ in [14], the expression for the closed-loop representation of the DC servomotor-based antenna position control system in Figure 5 is given by:

$$\theta_o(s) = G_{cp}(s) + G_{dp}(s); \quad (20)$$

$$\theta_o(s) = \theta_i(s) \left[\frac{C(s) \times G_p(s)}{1 + C(s) \times G_p(s)} \right] + D(s) \left[\frac{G_p(s)}{1 + C(s) \times G_p(s)} \right], \quad (21)$$

where $G_{dp}(s)$ is the expression for the transfer function due to unit disturbance $D(s)$ in equation (21), and it is given by:

$$G_{dp}(s) = \left[\frac{G_p(s)}{1 + C(s) \times G_p(s)} \right]. \quad (22)$$

Therefore,

$$G_{dp}(s) = \frac{3.6942e-4(s+416.7)(s+100.1)(s^2+1.643s+6.626)}{(s+100.1)(s+3.125)(s^2+1.643s+6.626)} \quad (23)$$

Hence, equation (20) becomes:

$$\theta_o(s) = \frac{3.6942e-4(s+2010)(s+100.1)(s^2+0.6936s+0.1205)(s^2+6.405s+10.3)}{(s^2-1082s+2.426e06)(s+429.3)(s+100.1)(s+3.443)(s+3.125)(s+0.3571)(s+0.3397)(s^2+1.643s+6.626)(s^2+85.28+3989)} \quad (24)$$

A detailed dynamic representation of the loop configuration of a DC servomotor-based satellite

antenna position control system with unit step input applied to it represents the reference position the system is required to attain for an optimum line of sight to ensure quality communication is required achieved. When subject to environmental disturbance (using unit input), the dynamic of the system has been presented as well.

3 Results

In this section, the results and analysis of the system's performance based on simulation conducted in terms of unit step input in the MATLAB environment are presented as follows. The simulations conducted are basically for four cases and include the system without a compensator (zero disturbance), without compensator (plus unit input disturbance), with compensator (zero disturbance), and with compensator (plus unit input disturbance). The time-domain step response performance analysis of the system for each case is presented in Table 2.

Parameters t_r , t_p , POS , and t_s are the rise time in second, peak time in second, peak percentage overshoot, and settling time in second, respectively.

Table 2 – Time domain transient response performance parameters of the system to the unit step input

System	t_r (s)	t_p (s)	POS(%)	t_s (s)
Without a compensator (zero disturbance)	0.525	1.29	34.7	4.35
Without compensator (plus unit input disturbance)	0.336	1.50	49.8	4.68
with compensator (zero disturbance)	0.0308	0.0679	9.35	0.124
with compensator (plus unit input disturbance)	0.0305	0.0691	10	0.325

The responses of the system are presented in Figures 6–11.

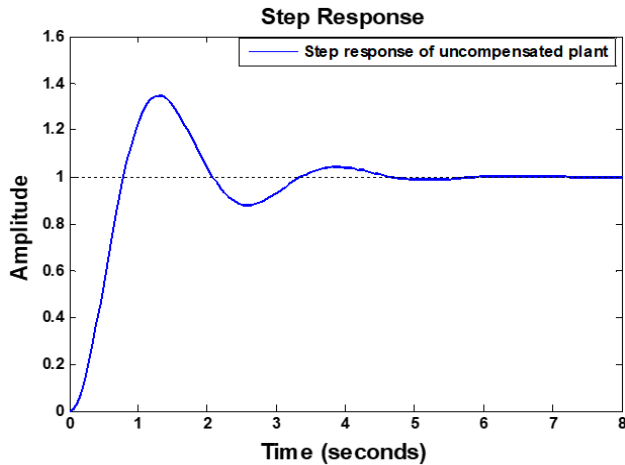


Figure 6 – Step response of the system (uncompensated)

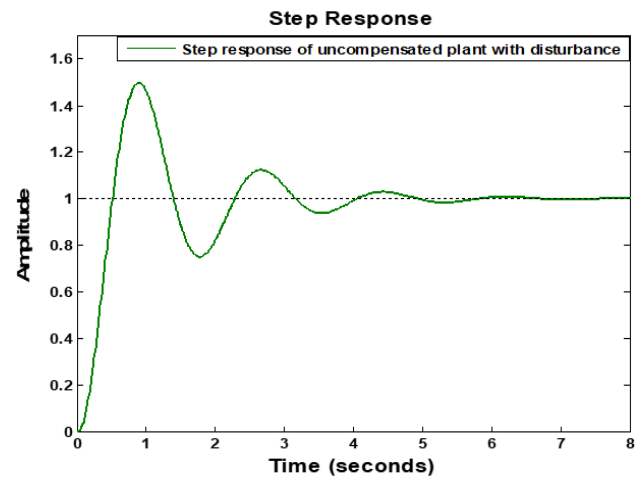


Figure 7 – Step response of the system with unit input disturbance (uncompensated)

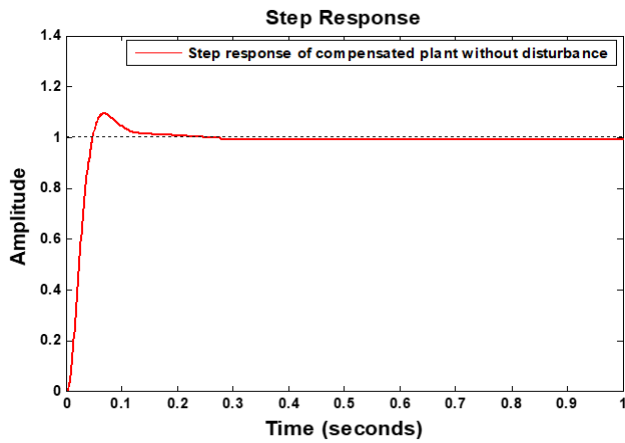


Figure 8 – Step response of the system with PID TC (zero disturbance)

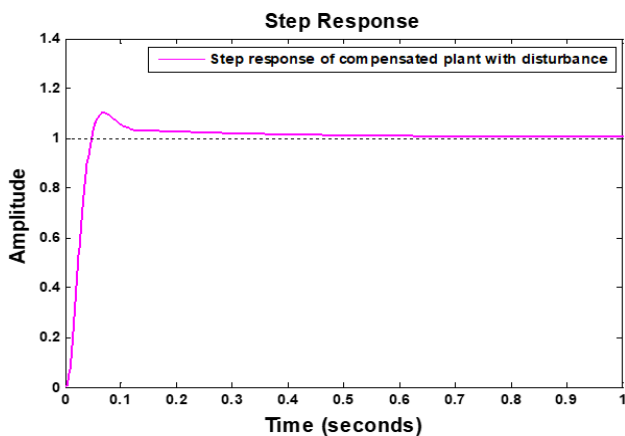


Figure 9 – Step response of the system with PID TC plus disturbance

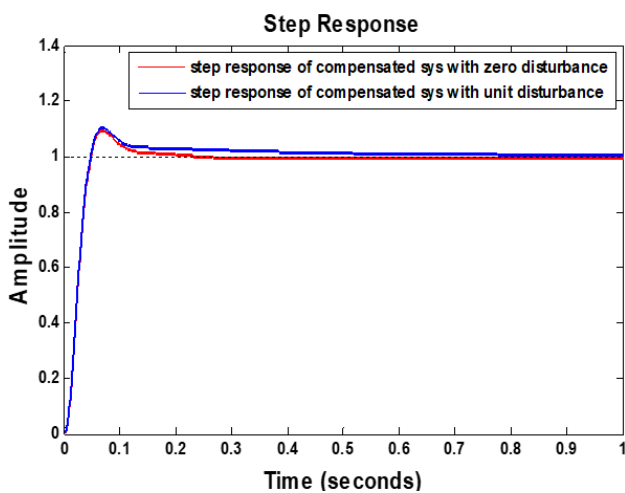


Figure 10 – Step responses of the system with PID TC (with and without disturbance)

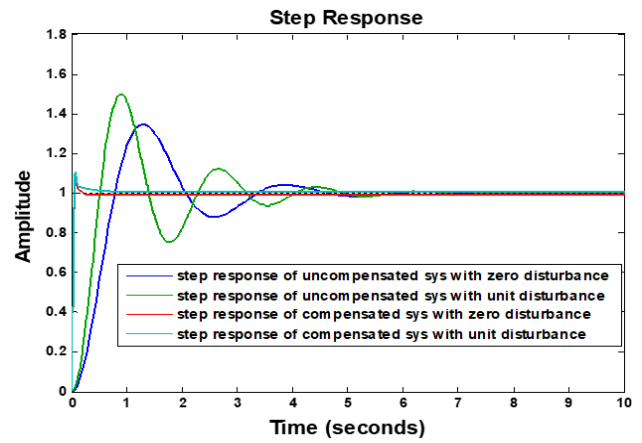


Figure 11 – Step responses of the system for uncompensated and compensated with and without disturbance

The percentage improvement in time domain performance parameters of the system with the introduction of PID TC is presented in Table 3.

The analysis was done using expression

$$\% \text{Improvement} = \frac{P_{\text{uncompensated}} - P_{\text{compensated}}}{P_{\text{uncompensated}}} \times 100, \quad (25)$$

where $P_{\text{uncompensated}}$, and $P_{\text{compensated}}$ are the performance of the system without and with PID TC, respectively.

4 Discussion

The time-domain step response performance characteristics of the system for each case simulated in this paper are shown in Table 1. While Table 2 shows the percentage improvement of the system based on the introduction of PID TC in terms of system with compensator and system plus disturbance with compensator. It can be deduced from Table 2 that with the uncompensated system, considering the high peak percentage overshoot, there is a considerable instability effect associated with the performance of the antenna positioning for optimum response. From the point of view of the uncompensated system, it can be seen looking at Table 2 that with the introduction of unit disturbance, the rise time improved by 36 % (0.525 s to 0.336 s) while the peak time, peak percentage overshoot, and settling time deteriorate by 16.3 % (1.29 s to 1.50 s), 43.5 % (34.7 % to 49.8 %), and 7.6 % (4.35 s to 4.68 s), respectively.

With the introduction of the PID TC, it can be seen in Table 1 that there is an improvement in the overall transient response performance of the time domain parameters of the system. Thus to provide further information on the improved performance offered by the compensator, the analysis has been done in percentage, as shown in Table 3.

Table 3 – Percentage improvement in time domain performance parameters based on PID TC introduction, %

System	Rise time	Peak time	Peak overshoot	Settling time
With PIDTC (zero disturbance)	94.1	94.7	73.1	97.1
With PIDTC + unit disturbance	91.0	95.4	80.0	93.1

Considering zero-disturbance compensated systems, it can be deduced from Table 2 that the time-domain response performance parameters of the system improved by 94.1, 94.7, 73.1, and 97.1 % in terms of rising time (0.525 s to 0.0308 s), peak time (1.29 s to 0.0679 s), peak percentage overshoot (34.7 % to 9.35 %), and settling time (4.35 s to 0.124 s), respectively.

The compensator's ability to provide robust performance in the presence of disturbance can be seen in Table 2 by comparing the step response performance parameters of the uncompensated system with unit disturbance to the step response performance parameters of the compensated system with unit disturbance, tagged: with PID TC + unit step disturbance. The result shows that PID TC provided improved time-domain transient response performance of the disturbance handling of the system by 91.0, 95.4, 80.0, and 93.1 % in terms of rising time (0.336 s to 0.0305 s), peak time (1.50 s to 0.0691 s), peak percentage overshoot (34.7 to 10.0), and settling time (4.68 s to 0.325 s).

References

1. Nise, N. S. (2011). *Control System Engineering*. 6th ed. John Wiley & Sons.
2. Uthman, A., Sudin, S. (2018). Antenna azimuth position control system using PID controller & state-feedback controller approach. *International Journal of Electrical and Computer Engineering*, Vol. 8(8), pp. 1539–1550, <https://doi.org/10.11591/ijece.v8i3.pp1539-1550>.
3. Hoi, T. V., Xuan, N. T., Duong, B. G. (2015). Satellite tracking control system using Fuzzy PID controller. *VNU Journal of Science: Mathematics and Physics*, Vol. 31(1), pp. 36–46.
4. Xuan, L., Estrada, J., Di Giacomandrea, J. (2009). *Antenna Azimuth Position Control System Analysis and Implementation*. Design Problem.
5. Soltani, M. N., Zamanabadi, R., Wisniewski, R. (2010). Reliable control of ship-mounted satellite tracking antenna. *IEEE Transactions on Control Systems Technology*, Vol. 19(1), pp. 221–228, <https://doi.org/10.1109/TCST.2010.2040281>.
6. Ahmed, M., Mohd Noor, S. B., Hassan, M. K., he Soh, A. B. (2014). A Review of strategies for parabolic antenna control. *Australian Journal of Basic and Applied Sciences*, Vol. 8(7), pp. 135–148.
7. Aloo, L. A., Kihato, P. K., Kamau, S. (2016). DC servomotor-based antenna positioning control system design using hybrid PID-LQR controller. *European International Journal of Science and Technology*, Vol. 5(2), pp. 17–31.
8. Okumus, H. I., Sahin, E., Akyazi, O. (2013). Antenna azimuth position control with fuzzy logic and self-tuning fuzzy logic controllers. *IEEE International Conference on Electrical and Electronics Engineering (ELECO)*, pp. 477–481.
9. Fandakl, S. A., Okumus, H. I., (2016). Antenna azimuth position control with PID, fuzzy logic and sliding mode controller. *2016 International Symposium on Innovations in Intelligent Systems and Applications (INISTA)*, pp. 1–5, <https://doi.org/10.1109/INISTA.2016.7571821>.
10. Onyeka, E. B., Chidiebere, M., Nkiruka, A. P. (2018). Performance improvement of antenna positioning control system using model predictive controller. *European Journal of Advances in Engineering and Technology*, Vol. 5(9), pp. 722–729.
11. Eze, P. C., Jonathan, A. E., Agwah, B. C., Okoronkwo, E. A. (2020). Improving the performance response of mobile satellite dish antenna network within Nigeria. *Journal of Electrical, Electronics, Control and Computer Science*, Vol. 6(21), pp. 25–30.
12. Ogata, K. (2010). *Modern Control Engineering*. 5th ed. Prentice-Hall Inc. USA, pp. 95–96.
13. Mbaocha, C., Eze, P., Uchegbu, V. (2015). Positioning control of drilling tool device for high speed performance. *International Journal of Electrical and Electronics Research*, Vol. 3(2), pp. 138–145.
14. Eze, P. C., Onuora, A. E., Ekengwu, B. O., Muoghalu, C., Aigbodioh, F. A. (2017). Design of a robust PID controller for improved transient response performance of a linearized engine idle speed model. *American Journal of Engineering Research*, Vol. 6(8), pp. 305–513.

5 Conclusions

The primary objective of this paper is to design a compensator that will provide robust response performance in the presence of disturbance so as to achieve improved error tracking and robustness. In this case, the tracking of unit step input represents the desired position for a DC servomotor-based satellite antenna position control system and corresponds to an effective line of sight operation for quality communication. With the modeling of the system and the subsequent design of PID TC, simulations were conducted basically for two categories. The first category of simulations is when the PID TC has not been added to the control loop, while the second category is when the PID TC has been added into the loop. The results obtained show that the designed compensator provided improved robust and tracking performance while meeting the specified time-domain performance parameters in the presence of disturbance.



Design Optimization of the Modified Planetary Carrier

Janigová S., Schürger B.*

Technical University in Košice, Faculty of Mechanical Engineering, Department of Applied Mechanics and Mechanical Engineering, 1/9, Letná St., 042 00 Košice, Slovak Republic

Article info:

Received: February 20, 2021
 The final version received: May 24, 2021
 Accepted for publication: May 29, 2021

*Corresponding email:

sara.janigova@tuke.sk

Abstract. This paper aims to design a new model of the third-stage carrier assembly used in a planetary gearbox as a single part component with improved strength and fatigue life properties and lower production costs. First, the mounting carrier assembly is subjected to static, fatigue, and modal analysis, and based on obtained results, the operating conditions that ensure its trouble-free operation are proposed. In the next step, new designs of the carrier as a single piece component are proposed and subjected to similar analyses. The proper numerical analysis method is chosen to evaluate the fatigue life, total deformation, and von Misses stress for each new model. Based on these results, the best design is chosen and submitted to further improvement, ensuring a weight reduction of 5 %. This last model of the carrier assembly is the most optimal solution since the maximum deformation values decreased by more than 55 %, and the maximum von Misses stresses decreased by almost 38 %, which increased fatigue life. A more comprehensive range of operating conditions for the optimized carrier is proposed to ensure its suitability for use in each gearbox. The finite element method analysis is performed in ANSYS.

Keywords: planetary carrier, planetary gearbox, finite elements method, numerical analysis.

1 Introduction

Finite element method (FEM) analysis is a computer-based analytical tool used to simulate and analyze systems and products, especially those used in mechanical engineering. Its ability to replace physical tests and predict the material behavior more effectively based on the given input parameters has become an integral part of the production process. One of the many applications of FEM is the numerical analysis of gearboxes – design improvement, an increase of the fatigue life, damage prediction, etc. [1].

The main task of the gearboxes, in general, is the transformation of the mechanical energy and rotary motion between the driveshaft and the driven shaft. There are numerous advantages of the planetary gears compared to the parallel gears, especially in terms of their power density, relatively low weight, compact structure, kinematic flexibility, or self-centering ability [2].

Planetary gears are used in systems where high torque production is necessary because their construction enables the uniform distribution of load between several planet gears, which makes them also more resistant to damage. They are part of the systems and machines used in the

automotive and aerospace industry, and in general, they are usually applied in the final stages of major transmissions [3].

The tasks are to perform numerical analysis of a mounted planetary carrier used as a crusher machine drive. The carrier assembly is subjected to the prescribed acting forces. After a detailed evaluation of the results, it will be possible to determine whether the carrier can transfer the prescribed load without failure. Both static and fatigue life analyses are performed in ANSYS.

In the next step, new carrier designs as a single part component are modeled and submitted to numerical analysis. Based on the obtained results, the most suitable variant is recommended to replace the mounted carrier. Subsequently, the primary operating conditions are defined based on the fatigue life and modal analysis.

2 Literature Review

Planetary gearboxes are the most complex types of gear arrangements. They are applied in systems where it is necessary to use gears with low weight or small dimensions because of the lack of space and reduce high speed and torque. This requirement applies to a wide range

of industries, including turbine engines, tractors, automatic transmissions, construction equipment, and even electric screwdrivers [4].

These systems basically consist of 4 main parts (Figure 1): sun gear, carrier, planet gears, ring gear [3]:

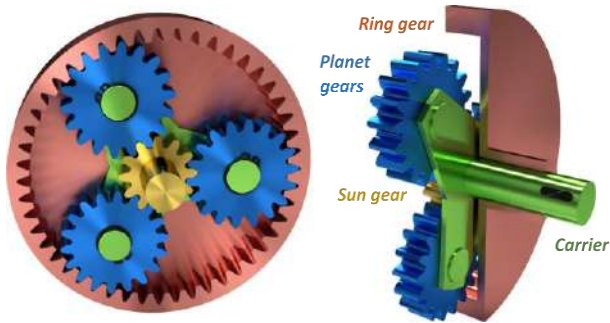


Figure 1 – Planetary gear parts

By fixing one of the coaxial elements, it is possible to achieve different gear ratios depending on which members are fixed. The remaining two elements are used as input and output, so we get three types of planetary gears summarized in Table 1 [5].

Table 1 – Planetary gear ratios determined for different fixed elements [5]

Input	Output	Fixed part	Calculation	Gear ratio
Sun gear	Carrier	Ring gear (R)	$1 + K/C$	3.4:1
Carrier	Ring gear	Sun gear (S)	$1/(1 + C/K)$	0.71:1
Sun gear	Ring gear	Carrier (C)	$-K/C$	-2.4:1

The third stage carrier analyzed in this paper is a part of a gearbox with an arrangement where the fixed member is the ring gear, the input is on the sun gear, and the output then passes through the carrier. This arrangement provides the highest gear ratio but based on other researches focusing on the analysis of a similar carrier assembly, the effect of high load causes the pins to protrude from the body of the carrier what leads to their failure, formation of the plastic deformation area and eventually cranks [6].

When designing a planetary gear, several conditions must be met to avoid interference between the ring and planet gears. Interference can result in unworkable conditions caused by the teeth of gears cutting into each other because of the insufficient number of planet gears teeth or inaccurate difference in the number of teeth between planet and ring gears [6].

$$\frac{z_1 + z_2}{x} = \text{integer number}; \quad (1)$$

$$z_2 = (z_1 + 2) \cdot z_3, \quad (2)$$

where z_1 represents the number of the sun gear teeth, z_2 is the number of the ring gear teeth, z_3 is the number of the planet gear teeth, and x is the number of planet gears [5].

A complete dynamic analysis of planetary gears is demanding even under ideal geometric conditions because of the singularities that occur at the points of contact between the teeth of the sun gear and planet gears as well as between the teeth of planet gears and the ring gear, leading to very different values of contact stress [7].

In the planetary gearbox, the torque is transmitted from the central wheel via satellites to the carrier and the main rotor shaft. One of the tools for assessing the condition of these components is vibration analysis. The vibrations of planetary gears are difficult to analyze. It is necessary to consider the influence of several factors, e.g., similar vibrations of the planet wheels, multiple and time-varying transmission paths from the transmission to the transducers, which are usually attached to the transmission housing. When these factors are combined, they reduce the efficiency of conventional fault detection algorithms, so these data sets have been adapted specifically for the case of planetary gearboxes and applied to the time-synchronous averages of the planetary carrier vibrations [8].

Today an increasing number of gear designers are using loaded tooth contact analysis (LTCA) methods to get precise information on the load distribution in both dimensions of the flank (lead and profile direction) on the entire gear flank. The use of the algorithm is a good solution to get proper values for the face load factor $K_{H\beta}$ of spur and helical gears, but it has also proved to be efficient when adapted for planetary systems [9].

The current trend is to minimize the weight and the cost, and since the structures become lighter, their flexibility is more and more critical. Static calculations of stresses in the wind gearbox have been widely performed with only rigid assumptions. Therefore it is necessary to update the calculation methods. A gear element is developed and tested in FEM software to be linked to flexible components. In typical methods, the gear points and the local loads are calculated separately, but with the gear elements, the input of the calculation is only the torque and the speed [10].

The present studies also address having more planet gears, which significantly increases the input torque density while using flexible pins. In this type of design, the pin stiffness and position tolerances are essential parameters as they affect the dynamic performances significantly. This issue is solved by modeling a double cantilevered flexible pin and analyzing the contributions of pin stiffness and misalignment applying the lumped parameter approach [11].

3 Research Methodology

The analyzed carrier assembly is a part of the planetary gearbox manufactured by the Slovak company. It is used as a part of a driving mechanism in the crusher machine with an axial distance of 650 mm between the crushing rollers. Two front-planet towers drive the gearbox while

each of them has two hydraulic motors. The output transmission ratio is 1:1, so the torque is distributed from the planet gearbox equally between two output shafts connected to the crushing rollers mounted in a common bearing.

The carrier is made of low-alloy stainless chrome-molybdenum steel 42CrMo4+QT characterized by resistance to abrasive wear and medium shock of dynamic forces, higher hardenability for stressed machine parts and components such as shafts and couplings. After simplifying the geometry of the mounted planetary carrier and applying the appropriate adjustments, the resulting model has been subjected to analysis (Figure 2).

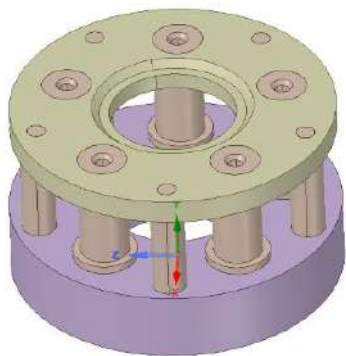


Figure 2 – Modification of the mounted planetary carrier geometry for static analysis

The automatic meshing method called MultiZone meshing was used for the model because of its complexity. A finer mesh was applied to the pins and other active load-bearing components using the mesh size definition function to achieve the most accurate results. This unevenly distributed mesh of the finite elements is shown in Figure 3.

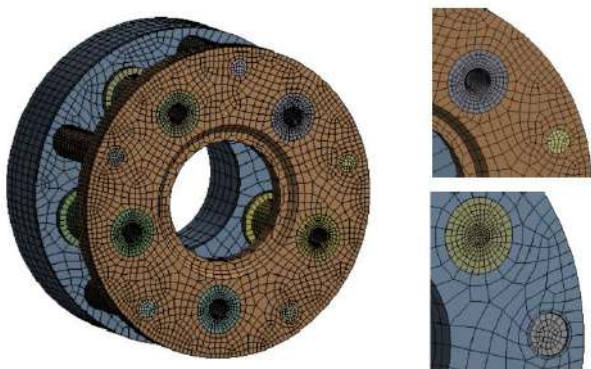


Figure 3 – Assembly model with finite element mesh

In the last step, the prescribed load was applied by a circumferential force perpendicular to each pin. This is the force transmitted to the carrier assembly via planet gears and pins from the sun gear.

4 Results

4.1 Numerical analysis of the mounted carrier assembly

We subjected the carrier assembly to static, modal, and fatigue life analysis to predict its service life under a given load.

The most considerable deformations reach a value of 0.73 mm at the outer edge of the carrier plate. The deformations on the main body of the carrier are compared to that much smaller as the main body is significantly stiffer. The deformation of the screw joint is approximately 20 % greater than the deformation of the pins, and they are both more deformed at the point of contact with the carrier plate (Figure 4).

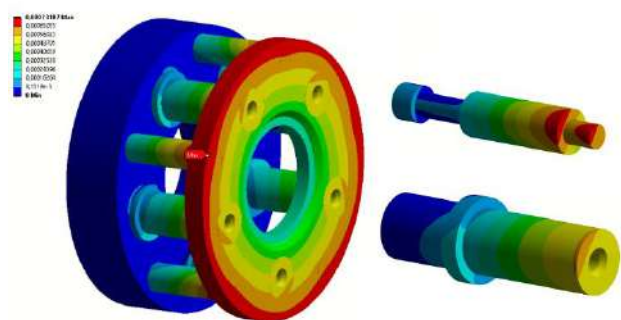


Figure 4 – Total deformation of the mounted carrier assembly

The stress is concentrated at the edge of the pinhole on the main body of the carrier, wherein practice the most frequently the zone of wear and subsequent failure occurs. (Figure 5). Since the pin is pressed into the main body of the carrier with a more extensive interference, the stress concentration is lower at the hole in the carrier plate. The maximum von Mises stress value exceeds the prescribed value of the yield stress for the given material by almost 4 % at the edge of the hole in the main body of the carrier. This is the place where the highest probability of failure due to fatigue processes is expected.

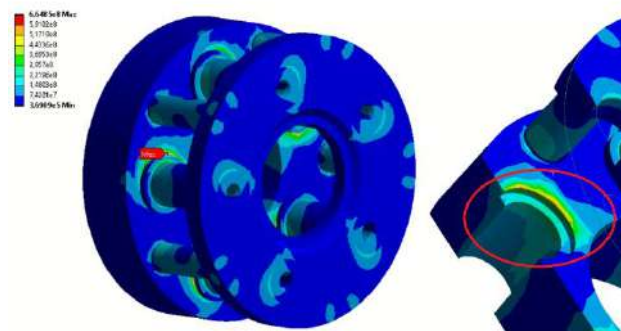


Figure 5 – Von Mises stress distribution on the mounted carrier assembly

The mounted carrier can be used in the crusher machines designed for 8 hours of continuous trouble-free daily operation. Based on a fatigue life analysis, the carrier is suitable for this basic operation. However, repeated

switching on and off the crusher machine would lead to premature failure (formation of the plastic deformation areas, cracks, etc.).

In the last step, the natural frequencies, natural shapes of oscillations, and deformations are obtained through the modal analysis. The main task is to evaluate the results to determine whether the resonance may occur in the system in conjunction with the operating frequencies. The results of the modal analysis for the first six natural shapes are summarized in Table 2.

Table 2 – Modal parameters of the mounted carrier assembly

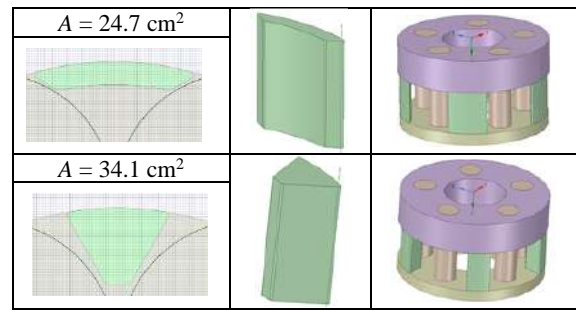
ω , Hz	Natural shapes	ω , Hz	Natural shapes
902		2118	
1091		2262	
2091		2738	

The input angular velocity is 70 Hz, and the output velocity is only 1.5 Hz, so based on the results, it is safe to say that resonance will not occur in this assembly because the mounted carrier is sufficiently rigid and characterized by high natural frequencies.

4.2 Design and numerical analysis of the carrier assembly as a single part component

Based on the evaluation of the graphical representation of the natural shapes, it can be assumed that the outer and inner edge of the carrier plate is prone to deformation because of their lower stiffness. These and several other aspects like the available information about the options for the carrier construction are considered when designing the model as a single part component. The main research objective is to improve strength properties, fatigue life and provide a broader operating condition. At the same time, there must be no significant increase in weight, which would lead to an increase in production costs. The material of the product does not change. Two new designs are created with the screw connections replaced by the supports at the outer edge of the carrier plate, while the cross-sectional area of the screw joint is used as a reference value for the design of the new supports to prevent excessive weight gain. Their 3D shape and the resulting assembly are shown in Table 3.

Table 3 – Two new designs of the carrier with supports



The basic parameters of the analysis like the material, model simplification, contact types, and meshing methods remain unchanged. A new type of contact is used between the supports and the carrier plate to prevent their displacement and separation. The results of these analyzes are shown in Figures 6–7.

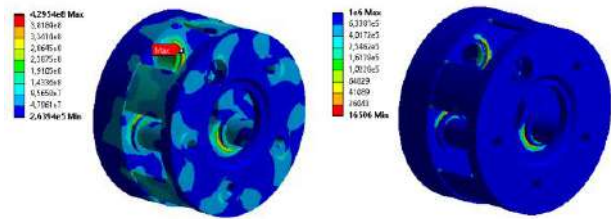


Figure 6 – Von Mises stress distribution and fatigue life of model no. 1

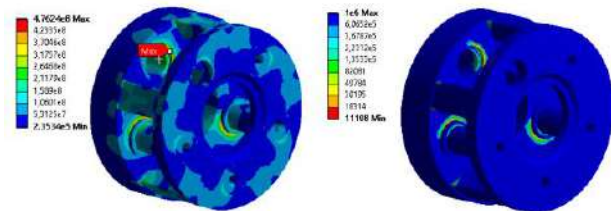


Figure 7 – Von Mises stress distribution and fatigue life of model no. 2

In the next step, new designs were subjected to the fatigue life analysis to determine the new range of operation conditions. The modal analysis was not performed because the carrier proved to be sufficiently rigid. The main results for all models submitted to the static and fatigue life analysis are shown for better comparison in Table 4.

Table 4 – Results summarization

Model	Deformation, mm	von Mises stress, MPa	Fatigue life, 10 ³ cycles
Original	0.732	665	3.2
no. 1	0.354	430	16.5
no. 2	0.478	476	11.1

In both models, there is a significant improvement in all properties. Even though model no. 2 has a larger cross-sectional area of supports, the most significant improvement can be observed in model no. 1. The main body diameter is then reduced so that it is equal to the diameter of the carrier plate. This reduction ensures a weight loss of 5%, which can positively affect production costs. The results of static and fatigue life analysis for the final model with reduced diameter are shown in Figure 8.

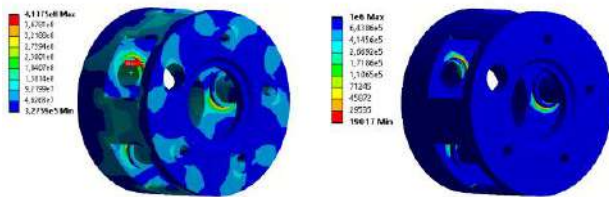


Figure 8 – Von Misses stress distribution and fatigue life of the optimized model with reduced diameter

5 Discussion

This paper represents a specific use of computer-aided FEM in practice, which requires the solution of very complex problems. FEM enables testing and optimization of machine parts, while the costs are significantly lower than performing physical tests. On the other hand, it is also beneficial to supplement this method with the results obtained from experimental measurements if possible. The experimental methods, when applied correctly, represent the actual state of the part in specific operating conditions.

New operating conditions are proposed based on the results of numerical analysis (Table 5). Compared to the original model, they include a more comprehensive range of applications and the use of the crusher machine in practice.

Table 5 – New operating conditions proposal for the optimized carrier assembly

Daily operation time	No. of switch on per hour	Cycles until failure, 10^3	Suitability
8 hrs	0	0.73	Suitable
up to 8 hrs	1	5.84	Suitable
8–12 hrs	1	8.76	Suitable
12 - 24 hrs	1	17.5	Suitable
up to 8 hrs	2–3	17.5	Suitable
8–12 hrs	2	17.5	Suitable

Planetary gearboxes need to have a large load capacity, compact size, and high power density. Therefore, they are vulnerable to fatigue crack even when they are well designed. Fatigue crack caused mainly by a harsh working environment may eventually cause failures of planetary gearboxes if not detected early. Many studies also investigate the behavior of a planetary gear system with a crack. The crack can increase the relative displacement

between the carrier and ring gear and induce more difference in response frequency with gravity and clearance [12]. This may lead to a smaller range of operating conditions.

In another study, vibration data from a number of US Army UH-60A Black Hawk helicopter transmissions were used to test two new methods of detecting a fatigue crack in a planet carrier. Vibration measurements of faulted and un-faulted transmissions over a range of torque levels in controlled test-cell and on-aircraft conditions showed that new methods are reliable under test-cell conditions but less effective under low-torque on-aircraft conditions [13].

These studies could be used for further analysis of the optimized carrier assembly to test its reliability in less-than-ideal conditions when the fatigue crack evolves.

6 Conclusions

In this paper, a numerical analysis of the planetary carrier assembly was performed in ANSYS. The main aim was to evaluate the obtained results and design a new carrier model as a single part component with improved strength and fatigue life properties.

The results for equivalent stresses of the mounted carrier assembly showed that the stress exceeded the yield strength of the material by almost 5 % at the point of contact between the pin with the main body of the carrier. This is an area where the formation of a plastic deformation zone and subsequent failure can be expected. The fatigue analysis proved that the maximum number of cycles until failure is sufficient only for the continuous operation (eight hours a day), and the repeated switching on and off would lead to premature failure due to fatigue processes. The modal parameters obtained from the modal analysis showed that the carrier assembly has high natural frequencies and is sufficiently rigid. It is also safe to say that resonance will not occur as the operating frequencies are significantly lower.

The new designs were created based on the previous results and subjected to analysis. Model no. 1 proved to be the most efficient one since the maximum equivalent stress was reduced significantly, resulting in an increase in the number of cycles until failure. Furthermore, model no. 1 was modified by reducing its main body diameter to minimize its weight. This modification ensured a weight reduction of 5 %.

The last model of the carrier assembly designed as a single part component is the most optimal solution for the application in the given gearbox. The maximum values of deformation decreased by more than 55%. The maximum von Misses stresses decreased by almost 38%, while the most important is that their value in critical places fell below the value of the yield strength of the material. Fatigue life has increased almost six times compared to the original model, which resulted in a new proposal of the operating conditions for the optimized carrier, including a broader range of the crusher machines applications in practice. The overall summary of the results from the mounted carrier to its most optimal shape as a single part component is shown in Table 6.

Table 6 – Final comparison between the mounted carrier assembly, model no. 1, and optimized model

	Deformation, mm	von Mises stress, MPa	Fatigue life 10 ³ cycles
Original	0.732	665	3.2
no. 1	0.354	430	16.5
Optimized model	0.325	414	19.0

7 Acknowledgments

This research was funded by Ministry of Education of Slovakia Foundation, grant project VEGA no. 1/0500/20.

References

- Nielsen, C. V., Zhang, W., Alves, L. M., Bay, N., Martins, P. A. F. (2013). *Finite Element Formulations. Modeling of Thermo-Electro-Mechanical Manufacturing Processes*. Springer Briefs in Applied Sciences and Technology, https://doi.org/10.1007/978-1-4471-4643-8_2.
- Talbot, D., Kahraman, A. (2014). A methodology to predict power losses of planetary gear sets. *International Gear Conference 2014, 26–28 August 2014, Lyon, France*, pp. 625–635, <https://doi.org/10.1533/9781782421955.625>.
- Fan, L., Wang, S. H., Wang, X., Han, F., Lyu, H. (2016). Nonlinear dynamic modeling of a helicopter planetary gear train for carrier plate crack fault diagnosis. *Chinese Journal of Aeronautics*, Vol. 29(3), pp. 675–687, <https://doi.org/10.1016/j.cja.2016.04.008>.
- Boyce, M. P. (2012). *Gears. Gas Turbine Engineering Handbook*. Elsevier, pp. 605-625, <https://doi.org/10.1016/B978-0-12-383842-1.00014-7>.
- Browell, R., Hancq, A. (2006). *Calculating and Displaying Fatigue Results*. ANSYS® Online White Papers. Available online: <https://support.ansys.com/staticassets/ANSYS/staticassets/resourcelibrary/whitepaper/fatigue.pdf>.
- Hd el Morsy, M. (2011). Dynamic analysis of wind turbine gearbox planet gear carrier using finite elements approach. *International Journal of Current Research*, Vol. 12, pp. 220–225.
- Hao, D., Wang, D. (2013). Finite-element modeling of the failure of interference-fit planet carrier and shaft assembly. *Engineering Failure Analysis*, Vol. 33, pp. 184–196, <https://doi.org/10.1016/j.engfailanal.2013.04.029>.
- August, R., et al. (1984). *Dynamics of Planetary Gear Trains*. NASA Contractor Report. Available online: <https://ntrs.nasa.gov/archive/nasa/casi.ntrs.nasa.gov/19840017959.pdf>.
- Kissling, U., Dinner, H. (2014). A procedure to determine the optimum flank line modifications for planetary gear configurations. *International Gear Conference 2014, 26–28 August 2014, Lyon, France*, pp. 65–75, <https://doi.org/10.1533/9781782421955.65>.
- Moreau, R., Mevel, B. (2014). A gear element in a wind-turbine gearbox. *International Gear Conference 2014, 26–28 August 2014, Lyon, France*, pp. 495–505, <https://doi.org/10.1533/9781782421955.495>.
- Zhu, C. C., Xu, X. Y., Lim, T. C., Du, X. S., Liu, M. Y. (2013). Effect of flexible pin on the dynamic behaviors of wind turbine planetary gear drives. *Proceedings of the Institution of Mechanical Engineers, Part C: Journal of Mechanical Engineering Science*, Vol. 227(1), pp. 74–86, <https://doi.org/10.1177/0954406212447029>.
- Chen, X., Chen, Y., Zuo, M. J. (2020). Dynamic modelling of a planetary gear system with sun gear crack under gravity and carrier-ring clearance. *Procedia Manufacturing*, Vol. 49, pp. 55–60, <https://doi.org/10.1016/j.promfg.2020.06.011>.
- Blunt, D. M., Keller, J. A. (2006). Detection of a fatigue crack in a UH-60A planet gear carrier using vibration analysis. *Mechanical Systems and Signal Processing*, Vol. 20(8), pp. 2095–2111, <https://doi.org/10.1016/j.ymsp.2006.05.010>.



Prydalnyi, B. I. (2021). *Mathematical model of the tensioning in the collet clamping mechanism with the rotary movable input link on spindle units. Journal of Engineering Sciences, Vol. 8(1), pp. E23–E28, doi: 10.21272/jes.2021.8(1).e4*

Mathematical Model of the Tensioning in the Collet Clamping Mechanism with the Rotary Movable Input Link on Spindle Units

Prydalnyi B. I.¹[0000-0001-8565-5986], Sulym H. T.²[0000-0003-2223-8645]

¹ Lutsk National Technical University, 75 Lvivska street, 43018 Lutsk, Ukraine;

² Bialystok University of Technology, 45C, Wiejska St., 15-351 Bialystok, Poland

Article info:

Received:

March 30, 2021

The final version received:

May 25, 2021

Accepted for publication:

June 2, 2021

*Corresponding email:

b.prydalnyi@lutsk-ntu.com.ua

Abstract. Increasing machining productivity causes the cutting forces acting on tools or workpieces to grow and requires extra clamping forces for their fixation reliably. In the research, a mathematical model of the operation of the clamping mechanism for fixating cylindrical objects on the spindle of machine tools at the stage of tension is presented. The presented design of the mechanism contains screw gear and provides self-braking. Based on the calculation model, mathematical dependencies are developed to describe the relationship among the movements of the parts of the mechanism when clamping forces are growing. The presented analytical dependencies allow considering the stage of growing clamping forces separately when the conservative type of forces are prevailing in the mechanism's operation. That stage of work when both types of forces of dissipative and potential characters exist is considered. The developed dependencies describe the position of parts of the clamping mechanism depending on the generalized coordinate. The angle of rotation of the input rotating link is used as the generalized coordinate. This fact allows calculating the position of the elements of the clamping mechanism of this type depending on time. Results of the research enhance understanding the pattern of the change in the interaction of the elements and forces that act in the mechanism during the final stage of clamping. The obtained mathematical dependencies are a precondition for the development of design methodology for mechanisms of this type.

Keywords: machining, clamping drive, clamping forces, calculation model, screw gear.

1 Introduction

One of the essential characteristics of metalworking machines is the productivity of machining, which determines their competitiveness. The ability to increase the feed and allowance of machining requires an increase in the power of the cutting process and, consequently, the amount of effort to fix the tool and workpieces.

The fixation effort has to ensure the absence of uncontrolled movements of tools and workpieces under the cutting forces, leading to many negative consequences. Most metalworking machines use clamping mechanisms that work in an automatic mode for fixing workpieces and tools. The clamping process can be divided into two stages: a sampling of gaps and creating a stress state of the system (tension).

The characteristics of the second stage of clamping determine the conditions of creating the required amount of clamping forces. The process that occurs during the creation of clamping forces can be described generally as converting the kinetic energy of the moving elements of the clamping mechanism into the potential deformation energy of its links. The clamping mechanism is part of the structure of the spindle assembly of machines, and as one of its largest subsystems, affects its dynamic characteristics.

Promising are the designs of clamping mechanisms that provide self-braking in the clamped position. This helps to avoid the need to supply energy to retain the fixation object in a clamped state, prevents uncontrolled release of the fixation object in case of power loss, and provides stability of clamping forces (as opposed to geometric lock) when the size of the fixation object

deviates from nominal values. One example of such a design is a clamping mechanism with a screw transmission and a rotating input link.

The structure of any clamping mechanism for clamping tools or workpieces on spindle units can be divided figuratively into two systems: clamping chuck and clamping actuator. A clamping actuator can be presented as a mechanism designed for converting and transmitting mechanical energy in the form of forces from the input link to the clamping collet chuck. Characteristics of clamping actuators influence the work characteristics of clamping mechanisms.

2 Literature Review

Many theoretical studies relate mainly to the operation of the spindle assemblies as a whole, without highlighting the clamping mechanism as a separate subsystem. The adaptive clamping control has been developed to improve the work-piece-holding process in the research [1]. The article [2] is devoted to considering bending and translational-angular vibrations of spindles of metal-cutting machine tools. Developed in [3], the mathematical model of spindle unit bearing assembly describes the mechanism of vibration signal formation analytically. The paper [4] aims to improve the spindle's output torque and propose a novel electromagnetic structure design to improve the output torque of the spindle motor. The dynamic model of the clamping mechanism is presented in [5] as a lumped parameter system of rigid bodies connected by elastic and dissipative links. The article [6] examines the influence of different clamping chucks on energy consumption parameters and focuses on essential sustainability indicators in machining. The paper [7] deals with kinematic designing clamping mechanism with reciprocating linear motion and dead-position closed positions. The dynamic simulation analysis of the clamping and stretching processes are performed using the article's finite element method [8]. In the paper [9], the clamping-unclamping principle of the automatic collet chuck holders in their initial static state describes analytically and presents the finite element method of static analysis. In the research work [10], the spindle unit model was studied [10] and used to calculate the required adjustments to the spindle unit to eliminate loss of stability, excessive vibrations, and cracks on production pieces. A procedure intended to examine a spindle drive unit using numerical models and experimental data has been developed in work [11]. In the research [12], the contact interaction between the tooltip and the workpiece surface is investigated considering the submicrometer level through the proposed spindle. The paper [13] is a study case for a clamp mechanism design, solving both analysis and synthesis problems. The research [14] is devoted to machining thin-walled workpieces, including static workpiece displacements and large deformations caused by local indentations at contacts. It is obtained that machining strategy is essential for obtaining proper surface finish and fine control over dimensions and form. To improve the spindle system in the designing stage and

predict the tool point dynamics, the paper [15] proposes modeling of spindle-holder assembly and investigates the contact characteristic under clamping and centrifugal forces. The study [16] aims explicitly to model a spindle-holder taper joint to predict the stiffness and stress distribution under different clamping and centrifugal forces. It was noted that an understanding of the contact characteristics of a spindle-holder joint in machine tools calls for an in-depth analysis of its performance, in particular under machining conditions. In work [17], the idea that measuring the clamping forces on cylindrical workpieces is a critical factor in the geometrical tolerances of such components, especially if they are slender as the case of thin rings, is expressed. The lower the clamping force, the better tolerances will be achieved, but with the disadvantage of reducing friction and increasing the risk of slipping. Therefore, achieving a minimum but safe clamping force is a critical factor in controlling the process. The operation principles of both new and improved clamping mechanisms of the CNC lathe with the automatic reinstallation workpiece manipulation are described in the article [18].

3 Research Methodology

3.1 Schemes of the calculation

The study [5] presents a scheme of calculation and dependencies that describe some kinematic characteristics of clamping mechanisms with screw self-braking transmission. The general scheme (Fig. 1) of this type of mechanism for clamping cylindrical objects on spindle units of metalworking machines is developed.

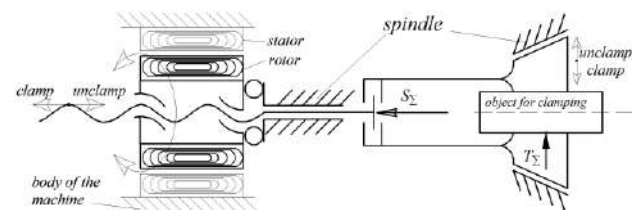


Figure 1 – The scheme of the design of the clamping mechanism with screw gear

The operation of clamping mechanisms can be separated into at least two stages. Separation occurs according to the type of forces (dissipative or potential) acting in these clamping mechanisms at a particular stage of the clamping process. For example, there is backlash elimination in the clamping mechanisms at the first stage when only active dissipative forces act. At the second stage, there is a creation of tension (mechanical stress). At this stage, potential forces' action prevails due to significant deformation of a flexible system of the mechanism with insignificant forces of dissipative character.

The relation among the kinematic parameters of the design of the clamping mechanism with screw gear can be calculated accordingly to the scheme (Fig. 2). It can be performed based on the equality between the magnitude

of the rotation angle ϕ_o of the input link in the form of rotor and the movement x_m of the drawbar in the form of a tube connected to the collet [5]:

$$x_m = \frac{\phi_o \cdot h}{2\pi} \quad (1)$$

where h – the pitch of the screw gear. As a result of differentiation (1) regarding time t , obtain the speed of movement of the drawbar $V_m = \frac{\partial x_m}{\partial t} = \frac{\partial \phi_o}{\partial t} \cdot \frac{h}{2\pi}$ and

$$V_m = \omega_o \cdot \frac{h}{2\pi} = 0,5\omega_o \frac{h}{\pi} = \omega_o \cdot 0,5d_1 \cdot \text{tg}\psi \quad \text{where } d_1 \text{ – the diameter of the thread of the screw gear; } \Psi \text{ – the angle of the rise of the thread of the screw gear. As a result of substitution, we receive } 0,5d_1 \cdot \text{tg}\psi = i_z. \text{ After putting into the previous equation, we get } V_m = \omega_o \cdot i_z = \dot{\phi}_o \cdot i_z.$$

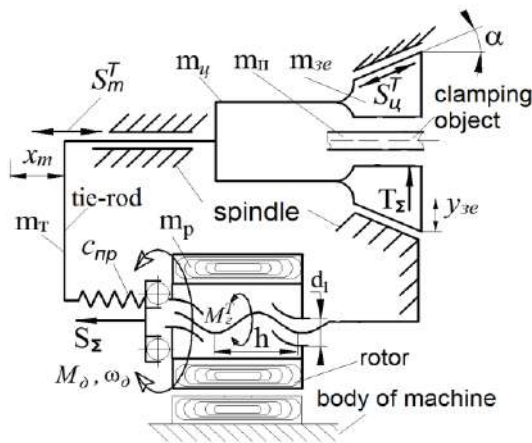


Figure 2 – The scheme for the calculation of parameters of the clamping mechanism

The relation between the elementary rotation angle $\delta\phi_o$ of the input link (rotor) and the elementary displacements of drawbar $\delta x_m = \delta\phi_o \frac{h}{2\pi}$ and clamping jaw of the collet $\delta y_{ze} = \delta x_m \cdot \text{tg}\alpha$ is represented by analogy with the previous equations, therefore $\delta y_{ze} = \delta\phi_o \frac{h}{2\pi} \cdot \text{tg}\alpha$, where α – the angle of a half of the clamping collet cone.

3.2 Power characteristics

The torque M_z^T of friction in the thread from the tangential friction force $F_t = S_z \cdot \text{tg}\phi^T$ with arm $0,5d_1$:

$$M_z^T = 0,5 \cdot d_1 \cdot S_z \cdot \text{tg}\phi^T, \quad (2)$$

where $S_z = \frac{2M_o}{d_1 \text{tg}\psi}$ – the axial force acting from the collet; ϕ^T – the friction angle in the thread; M_o – the

torque supplied to the input link of the mechanism..

The force of friction S_u^T in the connection between conical surfaces of the collet and the spindle:

$$S_u^T = \frac{z \cdot S_z}{\cos \alpha + (\sin \alpha) / f_u}, \quad (3)$$

where f_u – friction coefficient in the connection of the collet and the spindle; z – the quantity of clamping jaws in clamping chuck.

The magnitude of the friction force S_m^T in the connection of the tie-rod made in the form of a tube and the spindle can be calculated from the expression:

$$S_m^T = g \cdot m_\Sigma \cdot f_m, \quad (4)$$

where g – free-fall acceleration; $m_\Sigma = m_m + m_n$ – the sum of masses of the object for clamping and the tie-rod; f_m – friction coefficient in the connection of the spindle with the tie-rod.

4 Results

The stage of creating tension in the clamping mechanisms is characterized by a significant increase in the magnitude of the radial clamping force T_Σ , which is associated with the appearance of contact approximations at the junction of a clamping segment and an object of clamping. That is assumed that during the clamping time t the force T_Σ goes to its maximum value T_{\max} exponentially:

$$T_\Sigma = T_{\max} (1 - e^{-kt}). \quad (5)$$

The coefficient k collectively reflects the design features of the mechanism that affect the speed of reaching the maximum values of the clamping force. It also depends on the individual characteristics of mechanisms such as the contact stiffness of the joints of parts, settings, operating conditions etc. Therefore, the coefficient may change during exploitation.

During the operation of the clamping mechanisms, its kinetic energy E does not depend on the angle ϕ_o of the input link rotation. The partial derivative of the mechanism kinetic energy E on the angle ϕ_o is equal zero $\partial E / \partial \phi_o = 0$. At the stage of creation tension, the significant deformations of the clamping mechanisms' flexible system and conservative forces (potential elastic forces) at a small movement of elements appear. For this case, the differential equation of motion of the elements of the clamping mechanisms can be obtained based on the theorem on the change of the total mechanical energy of the holonomic system. The Lagrange equation, in this case, has the form:

$$\frac{d}{dt} \left(\frac{\partial E}{\partial \dot{\phi}_o} \right) - \frac{\partial E}{\partial \phi_o} = -\frac{\partial \Pi}{\partial \phi_o} + M_{II}^n, \quad (6)$$

where $\Pi = \frac{c \cdot x_m^2}{2}$ – the potential energy of elastic deformation forces of clamping mechanism elements, c – stiffness of the elastic system of the clamping mechanism. M_{II}^n – generalized force in the form of reduced torque at the stage of creating a mechanical tension system. The kinetic energy of the clamping mechanism as a rotation system can be described by the expression $E = J_{II} \dot{\phi}_o^2 / 2$, where J_{II} – the inertia moment of the clamping mechanism is reduced to the input link (rotor). The partial derivative of the previous mathematical expression of the kinetic energy E at the generalized speed $\dot{\phi}_o$ can be presented in the form $\dot{\phi}_o J_{II} = \partial E / \partial \dot{\phi}_o$. Taking into account the fact that when the time t is changing, it causes changes only the angle ϕ_o the partial derivative of the previous expression on time is:

$$\frac{d}{dt} \left(\frac{\partial E}{\partial \dot{\phi}_o} \right) = \ddot{\phi}_o J_{II}. \quad (7)$$

Considering (1) and $\Pi = \frac{c}{2} \left(\frac{\phi_o \cdot h}{2\pi} \right)^2 = \frac{\phi_o^2 h^2 c}{8\pi^2}$ we obtain:

$$\frac{\partial \Pi}{\partial \phi_o} = \phi_o \frac{h^2 c}{4\pi^2}. \quad (8)$$

Generalized force M_{II}^n in the form of the reduced moment, which represents the action of non-potential forces in the clamping mechanisms at the stage of creating mechanical tension system, can be described as equality of small works of forces that are acting in the clamping mechanism on small movements:

$$\begin{aligned} M_{II}^n \delta \phi_o &= M_o \delta \phi_o - M_z^T \delta \phi_o \\ -\delta x_m (S_m^T + S_u^T) - T_\Sigma \delta y_{3e}, \end{aligned} \quad (9)$$

where M_z^T – the torque of friction forces in the thread of the screw transmission; S_u^T and S_m^T – the friction forces between surfaces respectively: the cone of the collet and the spindle; the tie-rod and the spindle.

As a result of substitution (1) (2), (3), and (4) into (9) and taking into account previously defined kinematic parameters of the clamping mechanism, we get:

$$\begin{aligned} M_{II}^n &= M_o - 0,5d_1 S_\Sigma \operatorname{tg} \phi^T \\ -\frac{h}{2\pi} \left(gm_\Sigma f_m + \frac{z S_\Sigma}{\cos \alpha + \sin \alpha / f_u} \right) - T_\Sigma \left(\frac{h}{2\pi} \operatorname{tg} \alpha \right). \end{aligned} \quad (10)$$

If include $S_\Sigma = \frac{2M_o}{d_1 \operatorname{tg} \psi}$, $\frac{h}{\pi} = d_1 \operatorname{tg} \psi$ and (5) into (10):

$$\begin{aligned} M_{II}^n &= M_o \left(1 - \frac{\operatorname{tg} \phi^T}{\operatorname{tg} \psi} - \frac{z}{\cos \alpha + \sin \alpha / f_u} \right) \\ -\frac{h}{2\pi} gm_\Sigma f_m - T_{\max} \frac{h}{2\pi} \operatorname{tg} \alpha + e^{-kt} T_{\max} \frac{h}{2\pi} \operatorname{tg} \alpha. \end{aligned} \quad (11)$$

After denotation of the summands of (11) by symbols

$$\begin{aligned} \beta_2 &= T_{\max} \frac{h}{2\pi} \operatorname{tg} \alpha \quad \text{and} \quad \theta_2 = M_o \left(1 - \frac{\operatorname{tg} \phi^T}{\operatorname{tg} \psi} - \frac{z}{\cos \alpha + \sin \alpha / f_u} \right) \\ -\frac{h}{2\pi} gm_\Sigma f_m - T_{\max} \frac{h}{2\pi} \operatorname{tg} \alpha \quad \text{it takes a form:} \end{aligned}$$

$$M_{II}^n = \theta_2 + \beta_2 e^{-kt}. \quad (12)$$

Substituting (7), (8), and (12) for (6), we obtain a differential equation:

$$\ddot{\phi}_o J_{II} = -\phi_o \frac{h^2 c}{4\pi^2} + \theta_2 + \beta_2 e^{-kt}. \quad (13)$$

After denotation $\lambda_0 = \frac{h^2 c}{4\pi^2} \cdot \frac{1}{J_{II}}$, $\theta_0 = \frac{\theta_2}{J_{II}}$ and

$\beta_0 = \frac{\beta_2}{J_{II}}$ we obtain:

$$\ddot{\phi}_o + \phi_o \lambda_0 = \theta_0 + \beta_0 e^{-kt}. \quad (14)$$

Solution (14) can be represented as a solution to a non-homogeneous equation of the form:

$$\phi_{o_{3H}} = \phi_{o_{3O}} + \phi_{o_{3H}}, \quad (15)$$

where $\phi_{o_{3H}}$ – the general solution of the non-homogeneous equation, $\phi_{o_{3O}}$ – the general solution of the homogeneous equation, $\phi_{o_{3H}}$ – the partial solution of the non-homogeneous equation. To find $\phi_{o_{3O}}$, consider the equation $\ddot{\phi}_o + \phi_o \lambda_0 = 0$. Its characteristic equation

$k^2 + \lambda_0 = 0$; $k^2 = -\lambda_0$ and assume that $\lambda_0 = \frac{h^2 c}{4\pi^2} \cdot \frac{1}{J_{II}} > 0$

– constant, $k_1 = \sqrt{\lambda_0} i$, $k_2 = -\sqrt{\lambda_0} i$. Therefore, the solution of the homogeneous equation has the form $\phi_{o_{3O}} = C_1 \cos(\sqrt{\lambda_0} t) + C_2 \sin(\sqrt{\lambda_0} t)$.

The solution of $\phi_{o_{3H}}$ is found in the following form (according to the theory of differential equations):

$$\phi_{o_{3H}} = A + \beta e^{-kt}. \quad (16)$$

After substitution of $\dot{\phi}_{o_{3H}} = -\beta e^{-kt}$, $\ddot{\phi}_{o_{3H}} = \beta e^{-kt}$ with the initial equation (14) we obtain $\beta e^{-kt} + \lambda_0 (A + \beta e^{-kt}) = \theta_0 + \beta_0 e^{-kt}$, $e^{-kt} (\beta + \lambda_0 \beta) + \lambda_0 A =$

$= \theta_0 + \beta_0 e^{-kt}$ where $A = \frac{\theta_0}{\lambda_0}$, $\beta = -\frac{\beta_0}{k^2 + \lambda_0}$. According

to (16), $\phi_{\partial_{3H}} = \frac{\theta_0}{\lambda_0} - \frac{\beta_0}{k^2 + \lambda_0} e^{-kt}$, and

$$\phi_{\partial_{3H}} = C_1 \cos(\sqrt{\lambda_0} t) + C_2 \sin(\sqrt{\lambda_0} t) + \frac{\theta_0}{\lambda_0} - \frac{\beta_0}{k^2 + \lambda_0} e^{-kt}. \quad (17)$$

Expression (17) describes the dependence of the generalized coordinate ϕ_{∂} on time at the second stage of clamping the workpiece under the action of non-conservative (dissipative) and conservative forces in the clamping mechanisms. The constants C_1 and C_2 can be found from the two corresponding initial conditions and in our initial conditions $C_1 = C_2 = 0$. After denotation of the summands of (17) by symbols $A = \sqrt{C_1^2 + C_2^2}$ and $\phi_0 = \arctg \frac{C_2}{C_1}$ it can be rewritten as:

$$\phi_{\partial_{3H}} = A \sin(\sqrt{\lambda_0} t + \phi_0) + \frac{\theta_0}{\lambda_0} - \frac{\beta_0}{k^2 + \lambda_0} e^{-kt}. \quad (18)$$

The part of (18) $A \sin(\sqrt{\lambda_0} t + \phi_0)$ describes a simple harmonic motion that does not define the limits of change of rotation angle $\phi_{\partial_{3H}}$. Given the initial conditions and the mechanical content of the processes taking place, we take $A=0$. As a result, the dependence for determining the angle of rotation of the input rotary link ϕ of the clamping mechanism on-time t has the form:

$$\phi = \frac{\theta_0}{\lambda_0} - \frac{\beta_0}{k^2 + \lambda_0} e^{-kt}. \quad (19)$$

The beginning of tension creation starts after the completion of backlashes elimination and proceeds until the moment of achievement of the maximum set magnitude of the clamping force T_{\max} .

5 Discussion

The change of the generalized coordinate in the form of the angle of rotation ϕ of the input link of the clamping mechanism at the stage of creating tension in time is presented in the graph (Fig. 3). The graph is built under the dependence (19) for the parameters of the mechanism: $h = 1.5 \cdot 10^{-3} m$; $g = 9.81 m/s^2$; $m_{\Sigma} = 3.2 kg$; $f_m = 0.3$; $z = 3$; $\alpha = 15^\circ$; $tg \phi^T = 0.15$; $ctg \psi = 5$; $c = 80 \cdot 10^6 N/m$; $T_{\max} = 85 kN$; $f_u = 0.1$; $M_{\partial} = 7 Nm$; $J_{II} = 0.02 kg \cdot m^2$. Values of the factors λ_0 , θ_0 and β_0 are determined by the mass-geometrical characteristics of the parts of the mechanism and its specified force parameters.

As shown in the graph (Fig. 3), the movement of the machine elements during clamping takes most of the time at the final stage, while at the beginning of the clamping force creation, rotation of the input link of the clamping mechanism is much faster. Therefore, to reduce the clamping duration, it is advisable to reduce the duration of tension creation. According to the obtained dependence (19), it is possible to assess the mass-geometrical characteristics of the parts of the clamping mechanism to reduce the duration of the process of creating tension in the clamping mechanism for reliable fixation of workpieces or tools.

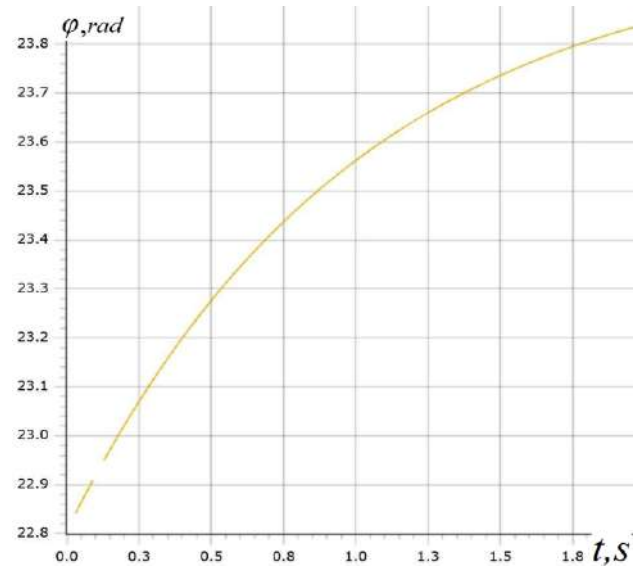


Figure 3 – The change of generalized coordinate at the stage of creating tension in the clamping mechanism

6 Conclusions

The research is part of a theoretical study of the automatic clamping mechanisms with the self-brake transmission for spindle units of metalworking machines. The dependence obtained due to the research describes the relationship of the generalized coordinate in the form of the angle ϕ of rotation of the input link and time t at the stage of increasing the clamping forces and creating tension. This mathematical dependence takes into account the specified values of the coefficients λ_0 , θ_0 and β_0 . The values of the coefficients are determined by the magnitudes of the geometric-mass parameters of the elements of the clamping mechanism under the obtained mathematical dependences.

The obtained dependence provides additional opportunities to assess the impact of the design characteristics of the clamping mechanisms of this type on the characteristics of their work conditions. The result of the research can be used to identify more appropriate characteristics of the mechanism's design to obtain the specified performance characteristics. It is also a prerequisite for the creation of design optimizing methodology.

7 Acknowledgments

The work has been accomplished under the research activity of Borys Prydalnyi at the Faculty of Mechanical Engineering, the Bialystok University of Technology, Poland, in the frame of the PROM Project: “International Scholarship Exchange of PhD Candidates and Academic

Staff” within the Operational Programme Knowledge Education Development, co-financed from the European Social Fund.



References

1. Szepesi, D., van't Erve, A. H. (1984). Adaptive clamping control on high performance CNC lathes. *Twenty-Fourth International Machine Tool Design and Research Conference*. Palgrave, London, pp. 177–186, doi: 10.1007/978-1-349-81247-9_25.
2. Denisenko, A. F., Yakimov, M. V. (2019). Dynamics of spindle assembly metal-cutting machine tool with anisotropic elastic support. *The 4th International Conference on Industrial Engineering*. Springer, Cham, pp. 1647–1655, doi: 10.1007/978-3-319-95630-5_176.
3. Gasparov, E. S., Gasparova, L. B. (2020). Mathematical model of spindle unit bearing assembly. *The 5th International Conference on Industrial Engineering*. Springer, Cham. doi: 10.1007/978-3-030-22041-9_78.
4. Liu, C. S., Chang, Y. H. (2017). Development of novel spindle motor with dual air gaps to improve output torque. *Microsyst Technol*, Vol. 23, pp. 371–379, doi: 10.1007/s00542-015-2685-2.
5. Prydalnyi, B. (2021). The dynamic model of the automatic clamping mechanism with a rotating input link. *Advances in Design, Simulation and Manufacturing IV*. Springer, Cham, pp. 95–103, doi: 10.1007/978-3-030-77719-7_10.
6. Thorenz, B., Westermann, H. -H., Kafara, M., Nuetzel, M., Steinhilper, R. (2018). Evaluation of the influence of different clamping chuck types on energy consumption, tool wear and surface qualities in milling operations. *Procedia Manufacturing*, Vol. 21, pp. 575–582, doi: 10.1016/j.promfg.2018.02.158.
7. Hsieh, L.-C., Chen, T.-H., Lai, P.-C. (2020). The kinematic design of mold clamping mechanism with minimal maximum acceleration. *Advances in Mechanical Engineering*, Feng Chia University, Po-Cheng Lai, Vol. 12(6), doi: 10.1177/1687814020926280.
8. Song, B., Wang, H., Cui, W., Zhang, J., Liu, H. (2019). Dynamic simulation and optimization of clamping mechanism of online tension testing machine for wire ropes. *Engineering Failure Analysis*, Vol. 95, pp. 181–190, doi: 10.1016/j.engfailanal.2018.09.015.
9. Soriano, E., Rubio, H., García-Prada, J.C. (2013). Analysis of the clamping mechanisms of collet-chucks holders for turning. *New Trends in Mechanism and Machine Science*, Springer, Dordrecht, Vol. 7, pp. 391–398, doi: 10.1007/978-94-007-4902-3_42.
10. Sabirov, F., Suslov, D., Savinov, S. (2012) Diagnostics of spindle unit, model design and analysis. *The International Journal of Advanced Manufacturing Technology*, Vol. 62, pp. 861–865, doi: 10.1007/s00170-011-3848-7.
11. Shitov, A. M., (2011) Complex examination of a spindle drive unit of a profile-grinding machine. *Journal of Machinery Manufacture and Reliability*, Vol. 40, doi: 10.3103/S1052618811010195.
12. Murakami, H., Katsuki, A., Sajima, T., Uchiyama, K., Houda, K., Sugihara Y. (2021). Spindle with built-in acoustic emission sensor to realize contact detection. *Precision Engineering*, Vol. 70, pp. 26–33, doi: 10.1016/j.precisioneng.2021.01.017.
13. Pozdřrcă, A. (2010). Design of a clamp mechanism. *International Symposium on Science of Mechanisms and Machines*. Springer, Dordrecht, pp. 687–698, doi: 10.1007/978-90-481-3522-6_58.
14. Yadav, M. H., Mohite, S. S. (2018). Controlling deformations of thin-walled Al 6061-T6 components by adaptive clamping. *Procedia Manufacturing*, Vol. 20, pp. 509–516, doi: 10.1016/j.promfg.2018.02.076.
15. Shaoke, W., Jun, H., Fei, D. (2019). Modelling and characteristic investigation of spindle-holder assembly under clamping and centrifugal forces. *Journal of Mechanical Science and Technology*, Vol. 33(5), pp. 2397–2405, doi: 10.1007/s12206-019-0438-3.
16. Chao, Xu, Jianfu, Z., Pingfa, F. (2014). Characteristics of stiffness and contact stress distribution of a spindle-holder taper joint under clamping and centrifugal forces. *International Journal of Machine Tools and Manufacture*, Vol. 82-83, pp. 21–28, doi: 10.1016/j.ijmachtools.2014.03.006.
17. Estrems, M., Arizmendi, M., Cumbicus, W.E., López, A. (2015). Measurement of clamping forces in a 3 jaw chuck through an instrumented aluminium ring. *Procedia Engineering*, Vol. 132, pp. 456–463, doi: 10.1016/j.proeng.2015.12.519.
18. Alquraan, T., Kuznetsov, Yu., Tsvyd, T. (2016). High-speed clamping mechanism of the CNC lathe with compensation of centrifugal forces. *Procedia engineering*, Vol. 150, pp. 689–695, doi: 10.1016/j.proeng.2016.07.081.



FCC Algorithm for Power Loss Diminution

Kanagasabai L.

Department of EEE, Prasad V. Potluri Siddhartha Institute of Technology, Kanuru, Vijayawada, 520007 Andhra Pradesh, India

Article info:

Received:

February 19, 2021

The final version received:

May 29, 2021

Accepted for publication:

June 7, 2021

*Corresponding email:

gklenin@gmail.com

Abstract. In this work, the FCC algorithm has been applied to the power problem. Real power loss reduction, voltage deviation minimization, and voltage stability enhancement are the key objectives of the proposed work. The proposed FCC algorithm has been modeled based on the competition, communication among teams, and training procedure within the team. The solution has been created based on the team, players, coach, and substitution tactic. A preliminary solution of the problem is produced, and the initialization of the teams depends on the team's formation with substitute tactics. Mainly fitness function for each solution is computed, and it plays an imperative role in the process of the algorithm. With the performance in the season, promotion and demotion of the teams will be there. Most excellently performed teams will be promoted to a senior division championship, and the most poorly performed team will be demoted to the top lower division league. Ideas and tactics sharing procedure, repositioning procedure, Substitution procedure, seasonal transmit procedure, Promotion and demotion procedure of a team which plays in the confederation cup has been imitated to solve the problem. Similar to an artificial neural network, a learning phase is also applied in the projected algorithm to improve the quality of the solution. Modernization procedure employed sequentially to identify the best solution. With and without voltage stability (L-index) FCC algorithm is evaluated in IEEE 30, bus system. Then the Proposed FCC algorithm has been evaluated in standard IEEE 14, 57,118,300 bus test systems without L-index. Power loss minimization and voltage stability index improvement have been achieved with voltage deviation minimization.

Keywords: optimal reactive power, transmission loss, FCC algorithm.

1 Introduction

Real power loss and voltage deviation minimization with voltage stability augmentation are the main objectives of this work. Previously conventional methods [1–6] are applied to solve the problem. Then these decades, many enhanced versions of genetic algorithm, variant of particle swarm optimization, ant colony algorithm, Frog leaping search algorithm, wolf search algorithm, ant lion algorithm, Butterfly algorithm, honeybee mating algorithm, black hole algorithm, bat algorithm, harmony search algorithm, whale optimization algorithm, water flow algorithm, artificial bee colony algorithm, mine blast algorithm [7–39] are utilized to solve the problem. But the central aspect is balancing the exploration and exploitation in the process of the algorithm. Many evolutionary and swarm-based algorithms fail to balance exploration and exploitation to

reach an optimal solution. In this work, the football confederation cup (FCC) algorithm has been applied to solve the optimal reactive power problem. The main aim of the work is to reduce the actual power loss. In the transmission and distribution of the Electrical system, power loss is a significant issue. Reduction of the real power loss along with voltage stability enhancement is a difficult task. Previously many researchers around the world have applied conventional methods for this task, but many difficulties have been faced in handling the constraints, and these decades' evolutionary computation algorithms have been sequentially applied to solve the problem. Many algorithms have been applied, but shortcomings have been identified in balancing the exploration and exploitation. Since a fair trade between exploration and exploitation will guide the process to reach the best solution. The proposed FCC algorithm has been modeled based on the competition, communication

among football teams, and training procedure within the team. The solution has been created based on the team, players, coach, and substitution tactic. Mainly fitness function for each solution is being computed, and it will play a vital role. Repositioning procedure, Substitution procedure, Seasonal transmit procedure, Promotion and demotion procedure of a team and the match between any two teams playing in the Confederation Cup is unknown; any team can win at the end a weak team will win over the strong team. The following high strength of the individual team will reflect in the match, and it will make the team conquer the rival team in the match. The respective team will analyze the past results attained and concentrate on the forthcoming match alone by examining the bench strength with controlled tactics. Coaches are playing the lead role in giving valid input to the team. They share the knowledge and experience to players whenever possible. Also, coaches alter the tactics during the match towards the goal of winning. In team repositioning of the players in the game is done. It will alter and sequentially upgrade the process of the game in a particular match. With and without considering voltage stability index proposed FCC algorithm is tested in IEEE 30, bus system. Then with considering voltage stability index criterion Proposed FCC algorithm has been tested in standard IEEE 14, 30, 57, 118, 300 bus test systems without considering the voltage stability index. Projected algorithms reduced the power loss effectively. Mainly percentage of real power reduction has been improved when compared to other specified standard algorithms.

2 Research Methodology

2.1 Problem formulation

Linearized steady-state system power flow equations are given by:

$$\begin{bmatrix} \Delta P \\ \Delta Q \end{bmatrix} = \begin{bmatrix} J_{p\theta} & J_{pV} \\ J_{q\theta} & J_{qV} \end{bmatrix} \begin{bmatrix} \Delta \theta \\ \Delta V \end{bmatrix}, \quad (1)$$

where ΔP – incremental change in real bus power; ΔQ – incremental change in bus reactive Power injection; $\Delta \theta$ – incremental change in bus voltage angle; ΔV – incremental change in bus voltage Magnitude; $J_{p\theta}$, J_{pV} , $J_{q\theta}$, J_{qV} – Jacobian matrix are the sub-matrixes of the system voltage stability is affected by both P and Q .

However, P is kept constant at each operating point and evaluate voltage stability by considering the incremental relationship between Q and V .

To reduce (1), let $\Delta P = 0$, then

$$\Delta Q = [J_{qV} - J_{q\theta} J_{p\theta}^{-1} J_{pV}] \Delta V = J_R \Delta V; \quad (2)$$

$$\Delta V = J^{-1} - \Delta Q, \quad (3)$$

where the reduced Jacobian matrix of the system:

$$J_R = (J_{qV} - J_{q\theta} J_{p\theta}^{-1} J_{pV}). \quad (4)$$

Voltage Constancy characteristics of the system can be identified by calculating the eigenvalues and eigenvectors. Let

$$J_R = \xi \Lambda \eta, \quad (5)$$

where ξ – right eigenvector matrix of J_R ; η – left eigenvector matrix of J_R ; Λ – diagonal eigenvalue matrix of J_R and

$$J_R^{-1} = \xi \Lambda^{-1} \eta. \quad (6)$$

From (3) and (6), we have

$$\Delta V = \xi \Lambda^{-1} \eta \Delta Q \quad (7)$$

or

$$\Delta V = \sum_i \frac{\xi_i \eta_i}{\lambda_i} \Delta Q, \quad (8)$$

where ξ_i – the i -th column right eigenvector; η – i -th row left eigenvector of J_R ; λ_i – the i th eigenvalue of J_R .

The i -th modal reactive power variation is

$$\Delta Q_{mi} = K_i \xi_i, \quad (9)$$

where

$$K_i = \sum_j \xi_{ij}^2 - 1; \quad (10)$$

ξ_{ji} – the j -th element of ξ_i .

The corresponding i -th modal voltage variation is

$$\Delta V_{mi} = [1/\lambda_i] \Delta Q_{mi}. \quad (11)$$

In (8), let $\Delta Q = e_k$, where e_k has all its elements zero except the k -th one being 1. Then

$$\Delta V = \sum_i \frac{\eta_{ik} \xi_i}{\lambda_i}, \quad (12)$$

η – k -th element of η_i ; $V - Q$ sensitivity at bus k .

$$\frac{\partial V_k}{\partial Q_k} = \sum_i \frac{\eta_{ik} \xi_i}{\lambda_i} = \sum_i \frac{P_{ki}}{\lambda_i}. \quad (13)$$

The key objective is to diminish the real power loss P_{loss} in transmission lines of a power system. This is mathematically stated as follows:

$$P_{loss} = \sum_{k=1}^n g_k (V_i^2 + V_j^2 - 2V_i V_j \cos \theta_{ij}), \quad (14)$$

where n – the number of transmission lines; g_k – the conductance of branch k ; V_i and V_j – voltage magnitude at bus i and j ; θ_{ij} – the voltage angle difference between bus i and j .

It is aimed in this objective that minimizing the Deviations in voltage magnitudes VD at load buses. This is mathematically stated as follows:

$$VD = \sum_{k=1}^{nl} |V_k - 1.0| \rightarrow \min, \quad (15)$$

where nl – the number of load busses; V_k – the voltage magnitude at bus k .

In the minimization process of objective functions, some problem constraints which one is equality, and

others are inequality had to be met. Objective functions are subjected to these constraints shown below.

Load flow equality constraints:

$$P_{Gi} - P_{Di} - V_i \sum_{j=1}^{nb} v_j \left[\begin{matrix} G_{ij} & \cos \theta_{ij} \\ +B_{ij} & \sin \theta_{ij} \end{matrix} \right] = 0, i = 1, 2, \dots, nb; \quad (16)$$

$$Q_{Gi} - Q_{Di} V_i \sum_{j=1}^{nb} v_j \left[\begin{matrix} G_{ij} & \cos \theta_{ij} \\ +B_{ij} & \sin \theta_{ij} \end{matrix} \right] = 0, i = 1, 2, \dots, nb; \quad (17)$$

where nb – the number of buses; P_G and Q_G – the real and reactive power of the generator; P_D and Q_D – the real and reactive load of the generator; G_{ij} and B_{ij} – the mutual conductance and susceptance between bus i and bus j .

Generator bus voltage V_{Gi} inequality constraint:

$$V_{Gi}^{min} \leq V_{Gi} \leq V_{Gi}^{max}, i \in ng. \quad (18)$$

Load bus voltage V_{Li} inequality constraint:

$$V_{Li}^{min} \leq V_{Li} \leq V_{Li}^{max}, i \in nl. \quad (19)$$

Switchable reactive power compensations Q_{Ci} inequality constraint:

$$Q_{Ci}^{min} \leq Q_{Ci} \leq Q_{Ci}^{max}, i \in nc. \quad (20)$$

Reactive power generation Q_{Gi} inequality constraint:

$$Q_{Gi}^{min} \leq Q_{Gi} \leq Q_{Gi}^{max}, i \in ng. \quad (21)$$

Transformers tap setting T_i inequality constraint:

$$T_i^{min} \leq T_i \leq T_i^{max}, i \in nt. \quad (22)$$

Transmission line flow S_{Li} inequality constraint:

$$S_{Li}^{min} \leq S_{Li} \leq S_{Li}^{max}, i \in nl. \quad (23)$$

2.2 FCC algorithm

In this work, Football Confederation Cup (FCC) algorithm has been modeled based on the competition, communication among football teams, and training procedure within the team. The solution has been created based on the team, players, coach, and substitution tactic. Mainly fitness function for each solution will be computed, and it will play an important role. The match between any two teams playing in the Confederation Cup is unknown; any team can win at the end also even a weak team will win over the strong team. The next high strength of the individual team will reflect in the match, and it will make the team conquer the rival team in the match. The respective team will analyze the past results attained and concentrate on the forthcoming match alone by examining the bench strength with controlled tactics. Naturally, when team i beat team j its due to the power or strength of the winning team; similarly, it will be a weak point for the losing team.

A preliminary solution of the problem is created, and the initialization of the teams depends on the team's formation with substitute tactics. Then the preliminary set of teams is denoted as $football_team^0$ with the population of a number of teams. At first $y_j^{formation}$, $y_j^{substitute}$ of the j -th variable is defined by

$$y_j^{formation} = lower\ bound_j + random() \times (upper\ bound_j - lower\ bound_j); \quad (24)$$

$$y_j^{substitute} = lower\ bound_j + random() \times (upper\ bound_j - lower\ bound_j). \quad (25)$$

Then the formation, substitute creation can be symbolized in the matrix as follows:

$$formation = \begin{bmatrix} y_{1,1}^{formation} & \dots & y_{1,j}^{formation} \\ \vdots & \ddots & \vdots \\ y_{i,1}^{formation} & \dots & y_{i,j}^{formation} \end{bmatrix}; \quad (26)$$

$$substitute = \begin{bmatrix} y_{1,1}^{substitute} & \dots & y_{1,j}^{substitute} \\ \vdots & \ddots & \vdots \\ y_{i,1}^{substitute} & \dots & y_{i,j}^{substitute} \end{bmatrix}. \quad (27)$$

Normally there will be a game per week, and each team i formation defined as $y_i^{formation}$ and the strength or power index is described by

$$\varphi(i) = \frac{f(y_i^{formation})}{sum\ of\ fitness\ value\ in\ a\ week}; \quad (28)$$

$$sum\ of\ fitness\ value\ in\ a\ week = \sum_{i=1}^n f(y_i^{formation}). \quad (29)$$

When two teams j and l are playing a match with formations $y_i^{substitute}$ and $y_i^{formation}$ then the power or strength index value of the teams will be calculated by

$$\varphi(j) = \frac{f(y_j^{formation})}{sum\ of\ fitness\ value\ in\ a\ week}; \quad (30)$$

$$\varphi(l) = \frac{f(y_l^{formation})}{sum\ of\ fitness\ value\ in\ a\ week}. \quad (31)$$

Probability for the team j winning the match:

$$probability(j, l) = \frac{\varphi(j)}{\varphi(j) + \varphi(l)}. \quad (32)$$

Probability of the Match between the teams l and j :

$$probability(j, l) + probability(l, j) = 1; \quad (33)$$

$$probability(l, j) = 1 - \frac{\varphi(j)}{\varphi(j) + \varphi(l)}. \quad (34)$$

Match between team i and l is given by:

```

Function match (i, l)
Compute  $\varphi(j)$  and
sum of fitness value in a week by
 $\varphi(i) = \frac{f(y_i^{formation})}{sum\ of\ fitness\ value\ in\ a\ week}$ 
sum of fitness value in a week =
 $\sum_{i=1}^n f(y_i^{formation})$ 
If  $probability(j, l) < r$ 
Then team "j" will be the winner and team "l" will
be loser
Otherwise
Team "l" will be the winner and team "j" will be
loser
End if
Apply the winning tactic for the winner
Apply the losing stratagem for the loser
End
    
```

Coaches are playing a lead role in giving effective input to the team. They share the knowledge and experience with players whenever needed. Also, coaches modify the tactics during the match towards the goal of winning, and it has been mathematically defined as

$$y_j^{formation}(t+1) = y_j^{formation}(t) + \text{random}_1 \lambda^{formation} (\text{upper bound}_j - \text{lower bound}_j); \quad (35)$$

$$y_j^{substitute}(t+1) = y_j^{substitute}(t) + \text{random}_1 \lambda^{substitute} (\text{upper bound}_j - \text{lower bound}_j). \quad (36)$$

How many numbers of ideas, game tactics are shared with the team is given by

$$\text{Number}_{idea\ sharing} = [\text{Total positions}(J) \delta_{idea\ sharing}]. \quad (37)$$

Ideas and tactics sharing procedure:

For $k=1$: $\text{Number}_{idea\ sharing}$
 Choose arbitrarily a position
 For $J=1$: j
 Formation possessions of Position “ j ” modernization is done through,
 $y_j^{formation}(t+1) = y_j^{formation}(t) + \text{random}_1 \lambda^{formation} (\text{upper bound}_j - \text{lower bound}_j)$
 Substitute possessions of Position “ j ” modernization is done by,
 $y_j^{substitute}(t+1) = y_j^{substitute}(t) + \text{random}_1 \lambda^{substitute} (\text{upper bound}_j - \text{lower bound}_j)$
 End for

In team repositioning of the players in the game is a natural aspect. It will modify and consecutively elevate the procedure of the game in a specific match, and this process is mathematically defined by

$$\text{Number}_{repositioning} = [\text{Total positions}(J) \delta_{repositioning}]. \quad (38)$$

Sequentially after choosing two probable position i and j then two variables C and D with “2” modes of formation and substitute is given by:

$$C^{formation} = y_i^{formation}; \quad (39)$$

$$C^{substitute} = y_i^{substitute}; \quad (40)$$

$$D^{formation} = y_j^{formation}; \quad (41)$$

$$C^{substitute} = y_j^{substitute}. \quad (42)$$

Then

$$y_i^{formation} = D^{formation}; \quad (43)$$

$$y_i^{substitute} = D^{substitute}; \quad (44)$$

$$y_j^{formation} = C^{formation}; \quad (45)$$

$$y_j^{substitute} = C^{substitute}. \quad (46)$$

Repositioning procedure:

For $k=1$ to $\text{Number}_{repositioning}$
 Positions i and j are arbitrarily chosen by
 $C^{formation} = y_i^{formation}$; $C^{substitute} = y_i^{substitute}$
 $D^{formation} = y_j^{formation}$; $C^{substitute} = y_j^{substitute}$
 Position i and j are reversed by
 $y_i^{formation} = D^{formation}$; $y_i^{substitute} = D^{substitute}$
 $y_j^{formation} = C^{formation}$; $y_j^{substitute} = C^{substitute}$
 End

During the game, there will be substitution in teams, and the number of substitutions is mathematically defined by

$$\text{Number}_{substitution} = [\text{random number} \cdot \text{position}(J)]. \quad (47)$$

Substitution procedure:

Compute the sum of substitution number by
 $\text{Number}_{substitution} = [\text{random number} \cdot \text{position}(J)]$
 Describe the sets
 For $k=1$ to $\text{Number}_{substitution}$
 $y_{h(idea)}^{formation} = \text{substitute}(idea)$
 $y_{h(idea)}^{substitute} = \text{formation}(idea)$
 End

The winning team will determine the position within the exploration space, and it defined mathematically by including inertia weight Ψ :

$$y^{formation}(t+1) = y^{formation}(t) + \text{random}_1 \cdot (\Psi^{formation})_x \cdot (y^{formation}(t)^* - y^{formation}(t)); \quad (48)$$

$$y^{substitute}(t+1) = y^{substitute}(t) + \text{random}_1 \cdot (\Psi^{substitute})_x \cdot (y^{substitute}(t)^* - y^{substitute}(t)). \quad (49)$$

In any football team, the learning phase is significant, and it substantively progresses the performance of the game

$$\theta = d \cdot b \cdot \text{random}_1 - b; \quad (50)$$

$$v = d \cdot \text{random}_2; \quad (51)$$

$$b = \beta - \text{current iteration} \left(\frac{\beta}{\beta / \text{maximum number of iteration}} \right). \quad (52)$$

Then

$$y_j^m(t+1)_\phi = (y_j^m(t))_\phi - \theta \left(\left| v(y_j^m(t))_\phi - (y_j^m(t))_\phi \right| \right). \quad (53)$$

After few games, top teams in the rank table after few games, for example first “3” in the points table, will possess a good quality of learning. Since those three teams have virtuous strategy and amalgamation of players:

$$y_j^{formation}(t+1)_1 = \left(y_j^{formation}(t)\right)_1 - \theta \left(\left|v(y_j^{formation}(t))_1 - (y_j^{formation}(t))\right|\right); \quad (54)$$

$$y_j^{formation}(t+1)_2 = \left(y_j^{formation}(t)\right)_2 - \theta \left(\left|v(y_j^{formation}(t))_2 - (y_j^{formation}(t))\right|\right); \quad (55)$$

$$y_j^{formation}(t+1)_3 = \left(y_j^{formation}(t)\right)_3 - \theta \left(\left|v(y_j^{formation}(t))_3 - (y_j^{formation}(t))\right|\right). \quad (56)$$

With orientation to the most excellent team properties, the current solution modernization is done:

$$y_j^{substitute}(t+1)_1 = \left(y_j^{substitute}(t)\right)_1 - \theta \left(\left|v(y_j^{substitute}(t))_1 - (y_j^{substitute}(t))\right|\right); \quad (57)$$

$$y_j^{substitute}(t+1)_2 = \left(y_j^{substitute}(t)\right)_2 - \theta \left(\left|v(y_j^{substitute}(t))_2 - (y_j^{substitute}(t))\right|\right); \quad (58)$$

$$y_j^{substitute}(t+1)_3 = \left(y_j^{substitute}(t)\right)_3 - \theta \left(\left|v(y_j^{substitute}(t))_3 - (y_j^{substitute}(t))\right|\right); \quad (59)$$

$$y_j^{substitute}(t+1) = \frac{y_j^{substitute}(t+1)_1 + y_j^{substitute}(t+1)_2 + y_j^{substitute}(t+1)_3}{3}. \quad (60)$$

Usually, many players are getting transformed before the commencing of a particular season. This procedure is mathematically defined as follows:

$$number_{seasonal\ transfer} = [number \cdot percentage\ of\ teams \cdot participating\ in\ seasonal\ transfer]. \quad (61)$$

Seasonal transmit procedure:

```

For k=1 to numberseasonal transfer
G = {chose arbitrary index i from |i ≠ h}
End for
For k=1 to numberseasonal transfer
For j=1 to J
r = random ()
if r > 0.5
Gjformation(idea) = ojformation
Gjsubstitute(idea) = ojsubstitute
o = chose randomly for the present teams
End if
End for
cost function (idea) = f(yformation(idea))
End for

```

With orientation to the performance in the matches, promotion and demotion of the teams will be there. Most excellently performed teams will be promoted to a senior division championship, and most poor performed teams will be demoted to top lower division league:

$$number_{teams\ movement} = total\ number\ of\ teams \times \delta_{teams\ moved\ to\ another\ confederation}. \quad (62)$$

Promotion and demotion procedure:

```

Eliminate worst teams numberteams movement
Describe with formation and substitute
For k= 1 to numberteams movement
For j=1 to J
number of teamjformation(idea) = Ejformation
number of teamjsubstitute(idea) = Ejsubstitute
End for
cost function (idea) =
f(number of teamsformation(idea))
End for
Add number of teams to the confederation

```

Every football team has its private strategy; the formations of the team members are rendering to their prearranged tactics. Each Football team will analyze the conclusion of the Football match. The analysis will be based on strength, blemish, fortuitous, and stress, which unambiguously allies with inner strength and blemish with exterior aspects of fortuitous and stress. This investigation will be the basement for the progress of Football team performance in the play.

- a. Begin.
- b. Parameters are initialized.
- c. Spot the most excellent team.
- d. $number\ of\ season = number\ of\ season + 1, i = 1$
- e. Engender the Confederation timetable.
- f. Match between team C and D.
- g. Strength or power index computed for teams C and D.
- h. The winner and loser are determined.
- i. Applying different tactics.
- j. Modernization of most excellent team.
- k. The learning phase will be applied.
- l. When the maximum number of weeks = number of the week.
- m. If yes, remove the top worst teams.
- n. If no, go to step “e”.
- o. Add a new team to the confederation.
- p. Applying the transfer process.
- q. Modernization of the best team.
- r. The maximum number of seasons = number of seasons.
- s. If yes, determine the most excellent solution.
- t. Otherwise, go to step “d”.
- u. End.

3 Results and Discussion

In this work, the FCC algorithm has been applied to solve the problem. Real power loss reduction has been achieved. Competition and communication among the football teams have been imitated to design the algorithm. Previously many types of conventional algorithms have been applied to solve the problem. But many difficulties have occurred while handling the constraints. Then evolutionary algorithms are sequentially applied to the problem, and the primary point is that balancing the exploration and exploitation in the algorithm is the key to reach the nearby global optimal solution. But unfortunately, many evolutionary algorithms have been failed. In work, exploration and exploitation have been balanced. At first, the FCC algorithm is tested in the IEEE 30 bus system at Illinois Center for a Smarter Electric Grid, considering voltage stability index. Tables 1–4 show the comparisons with other standard algorithms. Figures 1–4 give a graphical comparison between the methodologies.

Table 1 – Comparison of real power loss with different metaheuristic algorithms

Parameter	DE [42]	GSA [41]	APOPSO [40]	FCC
Real Power Loss in MW	4.56	4.51	4.40	4.23
Voltage deviation in PU	1.96	0.88	1.05	1.04
L stability index	0.55	0.14	0.13	0.120

Table 2 – Comparison of different algorithms with reference to voltage stability improvement

Parameter	DE [42]	GSA [41]	APOPSO [40]	FCC
Real Power Loss in MW	6.48	6.91	5.70	5.42
Voltage deviation in PU	0.09	0.07	0.09	0.08
L stability index	0.14	0.13	0.14	0.13

Table 3 – Comparison with the reference to voltage deviation minimization

Parameter	DE [42]	GSA [41]	APOPSO [40]	FCC
Real Power Loss in MW	7.07	4.98	4.48	4.23
Voltage deviation in PU	1.42	0.22	1.86	1.82
L stability index	0.12	0.14	0.12	0.12

Table 4 – Comparison of values with reference to multi-objective formulation

Parameter	APOPSO [40]	FCC
Real Power Loss in MW	4.84	4.73
Voltage deviation in PU	1.01	1.00
L stability index	0.12	0.12

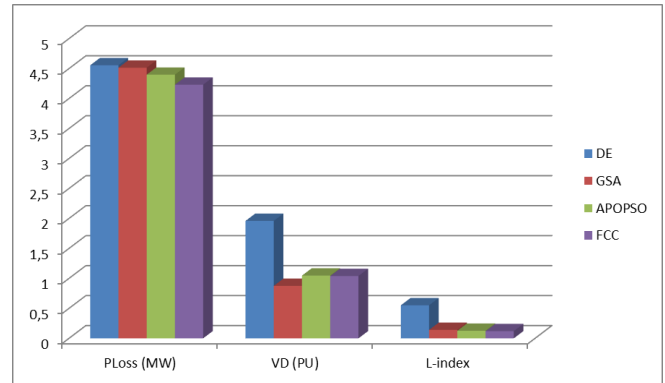


Figure 1 – Comparison of real power loss

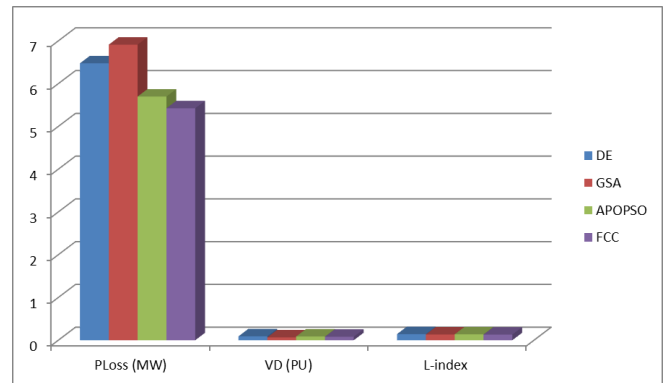


Figure 2 – Comparison with reference to voltage stability improvement

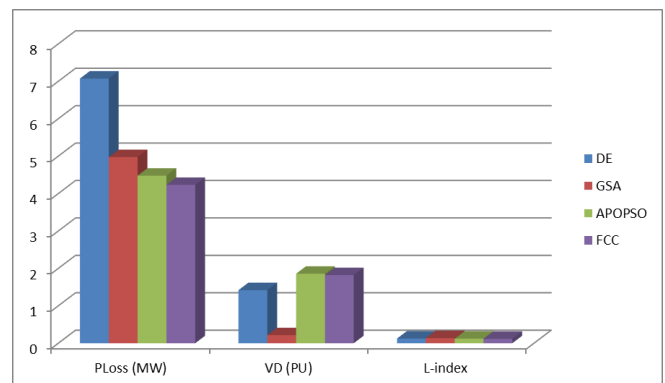


Figure 3 – Comparison with the reference to voltage deviation minimization

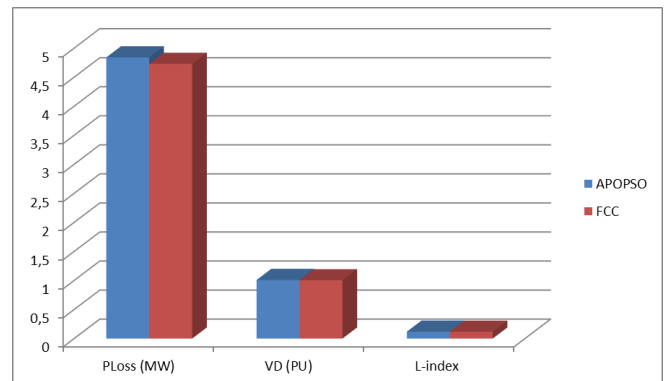


Figure 4 – Comparison with the reference to multi-objective formulation

Validity of the projected FCC algorithm has been tested without considering voltage stability index in standard IEEE 14, 30, 57, 118, and 300 bus systems. Tables 5–9 show the comparison of power loss. Figures 5–9 gives graphical comparison between the methodologies.

Table 5 – Comparison of parameters (IEEE 14 system)

Parameters	Base case [45]	MPSO [45]	PSO [44]	EP [43]	SARGA [43]	FCC
Percentage of reduction in power loss	0.00	9.20	9.10	1.50	2.50	23.69
Total power loss	13.55	12.29	12.32	13.35	13.22	10.34

Table 6 – Comparison of parameters (IEEE 30 system)

Parameters	Base case [45]	MPSO [45]	PSO [44]	EP [43]	SARGA [43]	FCC
Percentage of reduction in power loss	0.00	8.40	7.40	6.60	8.30	19.03
Total power loss	17.55	16.07	16.25	16.38	16.09	14.21

Table 7 – Comparison of parameters (IEEE 57 system)

Parameters	Base case [45]	MPSO [45]	PSO [44]	EP [43]	SARGA [43]	FCC
Percentage of reduction in power loss	0.00	15.40	14.10	9.20	11.60	26.57
Total power loss	27.80	23.51	23.86	25.24	24.56	20.41

Table 8 – Comparison of parameters (IEEE –118 system)

Parameters	Base case [45]	MPSO [45]	PSO [44]	EP [43]	SARGA [43]	FCC
Percentage of reduction in power loss	0.00	11.70	10.10	0.60	1.30	14.39
Total power loss	132.8	117.19	119.3	131.9	130.96	113.6

Table 9 – Comparison of real power loss (IEEE – 300 system)

Parameter	EGA [47]	EEA [47]	CSA [46]	FCC
Power loss	646.30	650.60	635.89	610.20

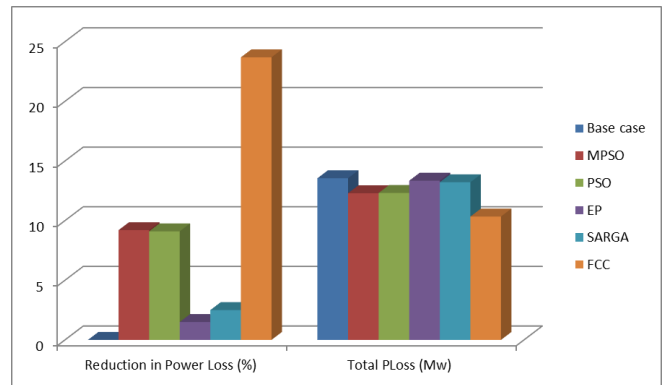


Figure 5 – Comparison of real power loss between methodologies (tested in IEEE 14 bus system)

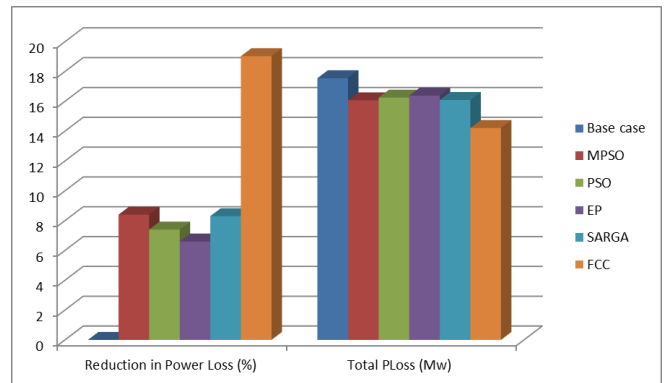


Figure 6 – Comparison of real power loss between methodologies (tested in IEEE 30 bus system)

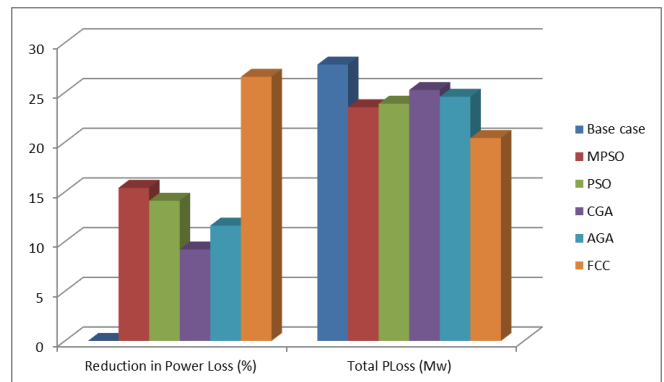


Figure 7 – Comparison of real power loss between methodologies (tested in IEEE 57 bus system)

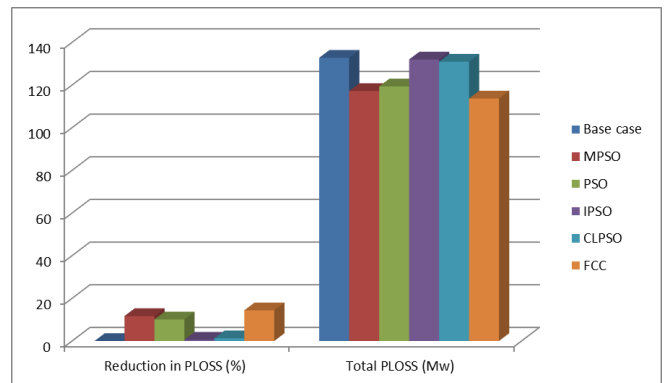


Figure 8 – Comparison of real power loss between methodologies (tested in IEEE 118 bus system)

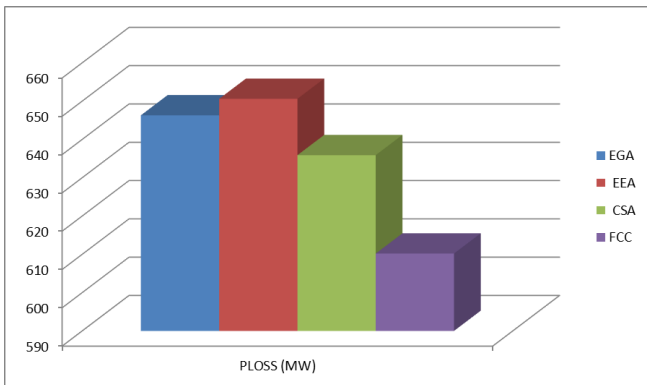


Figure 9 – Comparison of real power loss between methodologies (tested in IEEE 300 bus system)

4 Conclusions

In this work, the FCC algorithm successfully solved the optimal reactive power problem. Primary solution formation and initialization of the teams are based on the team's tactic. The winning team discovered the position through exploration space by including inertia weight Ψ . Primarily fitness function of the solution is computed to improve the process of finding the optimal solution. Key properties of the team have been successfully imitated to solve the problem. The transfer and modernization process improved the algorithm to find an excellent solution. The proposed FCC algorithm is tested in IEEE 30, bus system – real power loss minimization, voltage deviation minimization, and voltage stability index enhancement has been attained. Then with considering L-index alone Proposed FCC algorithm has been tested in standard IEEE 14, 57, 118, and 300 bus test systems. The percentage of power loss reduction has been enhanced when compared to other standard algorithms. Real power loss reduction has been attained effectively with voltage stability enhancement and minimization voltage deviation achieved.

References

- Lee, K. Y. (1984). Fuel-cost minimisation for both real and reactive-power dispatches. *Proceedings Generation, Transmission and Distribution Conference*, Vol. 131(3), pp. 85–93.
- Deeb, N. I. (1998). An efficient technique for reactive power dispatch using a revised linear programming approach. *Electric Power System Research*, Vol. 15(2), pp. 121–134.
- Bjelogrlic, M. R., Calovic, M. S., Babic, B. S. (1990). Application of Newton's optimal power flow in voltage/reactive power control. *IEEE Trans Power System*, Vol. 5(4), pp. 1447–1454.
- Granville, S. (1994). Optimal reactive dispatch through interior point methods. *IEEE Transactions on Power System*, Vol. 9(1), pp. 136–146, <http://dx.doi.org/10.1109/59.317548>.
- Grudin, N. (1998). Reactive power optimization using successive quadratic programming method. *IEEE Transactions on Power System*, Vol. 13(4), pp. 1219–1225, doi: 10.1109/59.736232.
- Roy, P. K., Dutta, S. (2019). Economic load dispatch: Optimal power flow and optimal reactive power dispatch concept. *Optimal Power Flow Using Evolutionary Algorithms*, IGI Global, Vol. 2019, pp. 46–64, doi: 10.4018/978-1-5225-6971-8.ch002.
- Bingane, C., Anjos, M. F., Le Digabel, S. (2019) Tight-and-cheap conic relaxation for the optimal reactive power dispatch problem. *IEEE Transactions on Power Systems*, doi: 10.1109/TPWRS.2019.2912889.
- Prasad D., Mukherjee, V. (2018). Solution of optimal reactive power dispatch by symbiotic organism search algorithm incorporating FACTS devices. *IETE Journal of Research*, Vol. 64(1), pp. 149–160, doi: 10.1080/03772063.2017.1334600.
- Aljohani, T. M., Ebrahim, A. F., Single, O. M. (2019). Multiobjective optimal reactive power dispatch based on hybrid artificial physics – Particle swarm optimization. *Energies*, Vol. 12(12), 2333, doi: 10.3390/en12122333.
- Mahate, R. K., Singh, H. (2019). Multi-objective optimal reactive power dispatch using differential evolution. *International Journal of Engineering Technologies and Management Research*, Vol. 6(2), pp. 27–38, doi: 10.5281/zenodo.2585477.
- Yalçın, E., Taplamacıoğlu, M., Çam, E. (2019). The adaptive chaotic symbiotic organisms search algorithm proposal for optimal reactive power dispatch problem in power systems, *Electrica*, Vol. 19, pp. 37-47.
- Mouassa, S., Bouktir, T. (2019). Multi-objective ant lion optimization algorithm to solve large-scale multi-objective optimal reactive power dispatch problem. *COMPEL - The International Journal for Computation and Mathematics in Electrical and Electronic Engineering*, Vol. 38(1), pp. 304–324, doi: 10.1108/COMPEL-05-2018-0208.
- Basu, M. (2016). Quasi-oppositional differential evolution for optimal reactive power dispatch. *Electrical Power and Energy Systems*, Vol. 78, pp. 29–40.
- Teeparthi, K., Kumar, D. V. (2017). Multi-objective hybrid PSO-APO algorithm-based security constrained optimal power flow with wind and thermal generators. *Eng. Sci. Technol. Int. J.*, Vol. 20, pp. 411–426.
- Teeparthi, K., Kumar, D. V. (2017). Dynamic power system security analysis using a hybrid PSO-APO algorithm. *Eng. Technol. Appl. Sci. Res.*, Vol. 7, pp. 2124–2131.

16. Ramírez, M., Castellanos, R., Calderón, G., Malik, O. (2018). Placement and sizing of battery energy storage for primary frequency control in an isolated section of the Mexican power system. *Electric Power Systems Research*, Vol. 160, pp. 142–150.
17. Rodríguez-Gallegos, C. D., Yang, D., Gandhi, O., Bieri, M., Reindl, T., Panda, S. K. (2018). A multi-objective and robust optimization approach for sizing and placement of PV and batteries in off-grid systems fully operated by diesel generators. An Indonesian case study. *Energy*, Vol. 160, pp. 410–429.
18. Beigvand, S. D., Abdi, H., La Scala, M. (2016). Combined heat and power economic dispatch problem using gravitational search algorithm. *Electr. Power Syst. Res.*, Vol. 133, pp. 160–172.
19. Narang, N., Sharma, E., Dhillon, J. S. (2017). Combined heat and power economic dispatch using integrated civilized swarm optimization and Powell's pattern search method. *Appl. Soft Comput.*, Vol. 52, pp. 190–202.
20. Warid, W., Hizam, H., Mariun, N., Wahab, N. I. A. (2018). A novel quasi-oppositional modified Jaya algorithm for multi-objective optimal power flow solution. *Applied Soft Computing Journal*, Vol. 65, pp. 360–373.
21. Herbadji, O., Slimani, L., Bouktir, T. (2017). Multiobjective optimal power flow considering the fuel cost, emission, voltage deviation and power losses using multi-objective dragonfly algorithm. *International Conference on Recent Advances in Electrical Systems*, pp. 191–197.
22. Vaisakh, K., Rao, P. K. (2008). *Optimum Reactive Power Dispatch Using Differential Evolution for Improvement of Voltage Stability*, IEEE.
23. Chavan, S. D., Adgokar, N. P. (2015). An overview on particle swarm optimization: Basic concepts and modified variants. *International Journal of Science and Research*, Vol. 4(5), pp. 255–260.
24. Nagendra, P., Dey, S. H. N., Paul, S. (2014). Voltage stability assessment of a power system incorporating FACTS controllers using unique network equivalent. *Ain Shams Eng. J.*, Vol. 5(1), pp. 103–111.
25. Nagendra, P., Dey, S. H. N., Paul, S. (2015). Location of static VAR compensator in a multi-bus power system using unique network equivalent. *Adv. Energy Res.*, Vol. 3(4), pp. 235–249.
26. Zhang, H., Lei, X., Wang, C., Yue, D., Xie, X. (2017). Adaptive grid based multi-objective Cauchy differential evolution for stochastic dynamic economic emission dispatch with wind power uncertainty. *PLOS ONE*, Vol. 12(9), e0185454, doi: 10.1371/journal.pone.0185454.
27. Bindu, K. N., Kumar, K. K. (2016). Combined economic and emission dispatch using random drift particle swarm optimization. *International Journal for Modern Trends in Science and Technology*, Vol. 2(11), pp. 134–139.
28. Rupa, J. M., Ganesh, S. (2014). Power flow analysis for radial distribution system using backward/forward sweep method. *Inter J Electr, Comput, Electron Commun Eng*, Vol. 8, pp. 1540–1544.
29. Abdel-Akher, M. (2013). Voltage stability analysis of unbalanced distribution systems using backward/forward sweep load-flow analysis method with secant predictor. *IET Gener, Transm Distrib*, Vol. 7, pp. 309–317.
30. Prasad, C. D., Kumar, G. P. (2016). Effect of load parameters variations on AGC of single area thermal power system in presence of integral and PSO-PID controllers. *2015 Conf. Power, Control. Common. Compute. Technol. Sustain. Growth, PCCCTSG 2015*, Vol. 1, pp. 64–68.
31. Morsali, J., Zare, K., Hagh, M. T. (2016). Performance comparison of TCSC with TCPS and SSSC controllers in AGC of realistic interconnected multi - sources power system. *Ain Shams Engineering Journal*, Vol. 7(1), pp. 143–158, doi: 10.1016/j.asej.2015.11.012.
32. Arifoğlu, U., Yalçın, F. (2018). System constrained active power loss minimization in practical multi-terminal HVDC systems through GA. *Sakarya University Journal of Science*, Vol. 22(4), pp. 1163–1173, doi: 10.16984/saufenbilder.421351.
33. Wei, H., Lin, C. and Wang, Y. (2018). The optimal reactive power flow model in mixed polar form based on transformer dummy nodes. *IEEJ Trans Elec Electron Eng*, Vol. 13, pp. 411–416.
34. Fang, S, Cheng, H, Xu, G, Zhou, Q, He, H, Zeng, P. (2017). Stochastic optimal reactive power reserve dispatch considering voltage control areas. *Int. Trans. Electr. Energ. Syst.*, Vol. 27, e2269.
35. Dozein, M. G., Monsef, H., Ansari, J., Kazemi, A. (2016). An effective decentralized scheme to monitor and control the reactive power flow: a holonic-based strategy. *Int. Trans. Electr. Energ. Syst.*, Vol. 26, pp. 1184–1209.
36. Du, Z., Nie, Y. and Liao, P. (2014). PCPDIPM-based optimal reactive power flow model using augmented rectangular coordinates. *Int. Trans. Electr. Energ. Syst.*, Vol. 24, pp. 597–608.
37. Liu, B., Liu, F., Zhai, B. and Lan, H. (2019). Investigating continuous power flow solutions of IEEE 14-bus system. *IEEJ Trans Elec Electron Eng*, Vol. 14, pp. 157–159.
38. Soodi, H. A., Vural, A. M. (2018). STATCOM estimation using back-propagation, PSO, shuffled frog leap algorithm, and genetic algorithm based neural networks. *Comput Intell Neurosci.*, Vol. 2018, 6381610.
39. Dai, C., Chen, W., Zhu, Y., Zhang, X. (2009). Seeker optimization algorithm for optimal reactive power dispatch. *IEEE T. Power Syst.*, Vol. 24(3), pp. 1218–1231.
40. El Ela, A. A., Abido, M. A., Spea, S. R. (2011). Differential evolution algorithm for optimal reactive power dispatch. *Electr. Power Syst. Res.*, Vol. 81, pp. 458–464.
41. Duman, S., Sönmez, Y., Güvenç, U., Yörükeren, N. (2012). Optimal reactive power dispatch using a gravitational search algorithm. *IET Gener. Transm. Distrib.*, Vol. 6, pp. 563–576.
42. Aljohani, T. M., Ebrahim, A. F., Mohammed, O. (2019). Single and multiobjective optimal reactive power dispatch based on hybrid artificial physics–particle swarm optimization. *Energies*, Vol. 12, 2333.

43. Subbaraj, P., Rajnarayan, P. N. (2009). Optimal reactive power dispatch using self-adaptive real coded genetic algorithm. *Electr. Power Syst. Res.*, Vol. 79(2), pp. 374–381.
44. Pandya, S., Roy, R. (2015). Particle swarm optimization based optimal reactive power dispatch. *Proceeding of the IEEE International Conference on Electrical, Computer and Communication Technologies (ICECCT)*, pp. 1–5, doi: 10.1109/ICECCT.2015.7225981.
45. Hussain, A. N., Abdullah, A. A., Neda, O. M. (2018). Modified particle swarm optimization for solution of reactive power dispatch. *Research Journal of Applied Sciences, Engineering and Technology*, Vol. 15(8), pp. 316–327, doi: 10.19026/rjaset.15.5917.
46. Reddy, S. S. (2017). Optimal reactive power scheduling using cuckoo search algorithm. *International Journal of Electrical and Computer Engineering*, Vol. 7(5), pp. 2349–2356.
47. Szepesi, D., van't Erve, A.H. (1984). Adaptive clamping control on high performance CNC lathes. In: *Davies B.J. (eds) Proceedings of the Twenty-Fourth International Machine Tool Design and Research Conference. Palgrave, London*, pp. 177–186, doi: 10.1007/978-1-349-81247-9_25.



Pawar, R. S., Patil, J. (2021). *Improvement in seismic performance of building with BRBs*. *Journal of Engineering Sciences*, Vol. 8(1), pp. E39–E49, doi: 10.21272/jes.2021.8(1).e6

Improvement in Seismic Performance of Building with BRBs

Pawar R. S., Patil, J.*

MIT World Peace University (MIT-WPU), 124, Paud Road, Kothrud, 411038 Maharashtra, Pune, India

Article info:

Received: April 6, 2021
The final version received: June 7, 2021
Accepted for publication: June 12, 2021

*Corresponding email:

jagruti.patil@mitwpu.edu.in

Abstract. Buckling restrained braces (BRBs) are a somewhat ongoing improvement in the field of seismic-safe steel structures. Their unmistakable component is the non-clasping conduct regularly accomplished by encasing a steel center in a substantially filled cylinder. However, choices have been proposed. Controlling the support from clasping improves malleability essentially and permits symmetric reaction under pressure or pressure powers. The plan of BRB outlines should consider various explicit issues that are not covered by Indian norms and guidelines. This specific task looks at utilizing BRB inside fortifying of built-up substantial casing developments to meet seismic details dependent on the Indian seismic plan and style code. Flexible reaction range examination just as nonlinear period verifiable past assessment is finished by taking a real designing model which experiences feeble first-floor inconsistency because of extra expansion and heaps of only one story. With all the way to deal with comparable solidness just as removal-based plan technique, clasping limited support factors are reasoned and accordingly are familiar with model BRB in ETABS using plastic wen form. 3 arrangements of clasping limited sections are breaking down alongside normal supports. The relationship in the middle of the fundamental cross piece of customary supports and BRB is concluded because of the definition of computing versatile bearing ability precisely where it's shown that the spot of the run of the mill supports must be 1.25 events that of BRB for guaranteeing the very same by and large execution. The outcome uncovers that Inverted V support design shown much better usefulness over single support just as V support setups just as X support arrangement, however not exhorted by Indian code, is mimicked just as applied to this undertaking and contains exhibited preferred execution moreover some different arrangements. The extra exploration about the practical use of this support is generally suggested. Moreover, under the movement of significant seismic tremors, by nonlinear time chronicled past assessment, clasping controlled supports showed much better usefulness of reinforcing the construction just as success runs over the need for code. Under this specific condition, conventional supports misfortunes their bearing limit because of unnecessary buckling.

Keywords: nonlinear time history analysis; RC frame structure, response spectrum, flexible first story, buckling restrained brace.

1 Introduction

Steel supports have for some time been utilized for both breeze and seismic-safe designs. In the seismic field of utilization, continued locking in pressure is the wellspring of solidarity and solidness debasement. A generally ongoing improvement is the “clasping controlled support” (BRB), an extraordinary kind of support with worldwide clasping restrained by a suitable framework. The evasion of worldwide clasping suggests

pressure power uprooting conduct is the same as the reaction displayed under strain powers.

Tremors bring about monetary misfortunes, notwithstanding misfortunes of lives considering the breakdown of structures. All through a genuine seismic tremor occasion, the essential underlying components as bars just as sections are influenced essentially. An improvement is put through the seismic pattern. An incredible degree of energy is circulated inside the level, and the structure of mischief supported by the construction relies on the scattering of the energy. In this

way, an underlying specialist includes fantastic worry inside planning seismic tremor opposing framework to dissipative force proficiently in the construction.

The principal highlight of an energy dispersal segment is diminishing the harm inside essential underlying parts. Bracings are generally familiar with balance out the system against the sidelong loads made due to wind, seismic tremors, and so forth principal burden to standard propping might be the corruption of support strength under pressure on account of clasping of the entirety of the support. BRB is a decent answer for this specific issue. Clasping a limited supported casing gadget is nevertheless one of these tremors opposing as that is undeniably more compelling than regular concentric supports. 1.2 restrained buckling braces (BRB).

BRBs are a reason as of late accessible headway inside the space of sidelong burden opposing constructions. The central creation of BRB started in the 1980s, just as its evaluation got the site in the profound mid-80. While in the 1990s, it was applied around Japan just as because of its great reaction, this specific mechanical development was moved in the US inside 1998 whose evaluation just as recreation required spot in profound 1999 after which appropriately applied wearing undertakings that are significant just after 2000. In 2000, the absolute first BRB gadget was utilized in North America as a principle parallel opposing project at UC Davis. Figure 1 uncovers the various stages of the improvement of BRB. Wakabayashi, a Japanese designer, first conceptualized the possibility of BRB. The absolute initially clasping controlled support which was involved a dull steel plate sandwiched between substantial built-up boards.

The essential component of BRBs comprises a steel place encased by substantial that is shown in Figure 2. The region in the middle of the cylinder just as support is stacked with a substance-like material, just as an exceptional covering is utilized to hold on the substantial. In this manner here, the help can undoubtedly slide concerning the substantially filled cylinder. The substantial stacked tubing supplies the total control all through cyclic stacking. The essential burden opposing perspective in BRB could be the steel community, and the general clasping on the essential steel is gone against through the limiting component provided by the external panel.

Buckling restrained brace is schematically presented in Figure 1. BRBs offer the following advantages: simple demonstrating of the cyclic conduct of its for inelastic assessment; effective connection to the primary program utilizing a shot or even stuck connection with gusset plates; stable hysteretic conduct just as generous energy dispersal limit; limited affectability to harmless to the ecosystem circumstance changes; design adaptability inside the quantity of similarly strength and solidness of whole underlying arrangement of a development. Also, they do not require the primary establishment and individuals fortifying; they produce inside every pressure and strain; it is easy to embrace for seismic retrofitting.

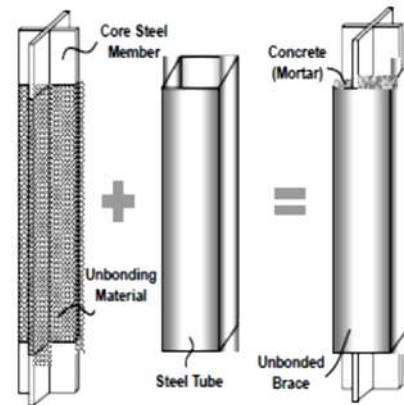


Figure 1 – Schematic of buckling restrained brace

Finally, the BRB activity is like a primary breaker, and through seismic events, harm is concentrated inside the BRB segment. The BRB segment can, without much of a stretch, if necessary, be supplanted following an actual seismic event.

Based on the arrangement used, BRBs will give decreased establishment parcels than comparable shear divider structure strategies.

However, BRBs have some disadvantages: lack of conditions for recognizing just as looking at harmed supports; ductility characteristics unmistakably affected by the math just as material kind on the yielding steel essential fragment.

BRBs have been used on a few sorts of structures like business, medical clinics, retail, vehicle leaves, multi-story private schools, strict fields and arenas, and mechanical and non-building structures.

Buckling restrained braced frames (BRBFs) appeal exceptionally seismic safe primary framework considering the significant proportion between seismic viability and low to medium expense compared with other non-customary energy scattering measures. The adequacy is the moderately high solidness, contrasted and traditional second safe casings, and the huge energy scattering limit, contrasted with old-style concentrically propped outlines.

One deficiency of BRBFs is the penchant for enormous lingering relocations, trademark conduct of any versatile plastic gadget. Be that as it may, adaptable MRFs utilized in mix with BRBFs can give huge post-yield solidness and resulting re-centering capacity.

The detailed study of BRB elements and systems are as follows: experimental and theoretical may be split into research investigations on BRB components, sub-assemblies, and full-scale structure. Several subjects might be recognized within each of the two main subjects, for example:

Experimental tests:

- minimum casing stiffness. This subtopic involves research on the needed minimum casing stiffness. This subtopic includes the intensity and distribution of forces transferred from the steel core to the casing;

– low cycle fatigue and deformation capacity. This subtopic entails determining the ductility capacity for various cyclic loading histories;

– connections. This subtopic entails determining how the strength and flexibility of connections between braces and neighboring frame parts may affect the overall system's seismic performance;

– the effect of an unbonding layer or void. This subtopic investigates how different steel core-casing interfaces affect brace performance.

Numerical studies:

– seismic performance of frames with BRBs. Numerical investigations of the overall seismic performance of frames with BRBs are included in this subtopic. The ductility and energy dissipation demands for BRBs, as well as the force demands for non-dissipative parts and connections, are all statistically evaluated;

– BRB finite element models. This subtopic entails the creation of finite element models that reproduce experimentally observed behavior.

A few theoretical studies have been conducted in the recent decade to examine the seismic performance of steel buildings equipped with BRBs. BRBs are prone to rather substantial residual drifts and plastic deformation demand concentration at one or a few storeys. The low post-yield rigidity of BRBs is to blame for these flaws. We propose developing dual systems with BRBs and moment-resistant frames (MRFs), which give some post-yield rigidity (thus re-centering capacity). The determination of the highest predicted ductility demand for braces is another critical aspect that has been addressed via numerical simulation. Maximum ductility requirement values up to 26 were calculated using six ground motions scaled to the maximum predicted design intensity (i.e., 1.5 times larger than the design level intensity).

Many existing RC buildings and Steel Frames do not fulfill current seismic code lateral strength standards, making them vulnerable to considerable damage in the case of a future earthquake. Nonlinear time history analysis was used to evaluate a steel moment-resisting frame (SMRF). Energy dissipating devices (EDD) were used to strengthen the lateral strength of the building. These devices might be used alone or in combination. The restrained buckling braces (BRB) are effective at all levels of seismic study, considerably improving the RCC and steel frame performance.

Buckling Restrained Braces (BRB) are ongoing created underlying framework which has a steady energy dissemination property. The real benefit of BRB is its capacity to yield both pressure and pressure without clapping, in this way getting a steady hysteresis circle. The BRB support set in a concentric edge is named as BRBF framework. Clapping limited supported edges (BRBFs) are an exceptionally alluring seismic safe underlying framework due to the significant proportion between seismic adequacy and low to medium expense compared with other non-ordinary energy dissemination measures.

The objectives of the study are as follows:

1) looks at how BRB can be used to enhance reinforced concrete frame structures to meet seismic requirements;

2) conduct a structural analysis using Etabs software if the materials are found to be acceptable.

3) by analyzing all of the data, recommending the use of the content inside earthquake-resistant structures. By performing nonlinear historical research, you can save time and money.

2 Literature Review

A literature review presented below summarizes the various works done by different scholars and researchers on BRB.

According to the author, Baca et al. [1] stated that control of vibrations and damage in classic reinforced concrete (RC) buildings during earthquakes is problematic. It necessitates the adoption of novel techniques to improve the seismic behavior of concrete structures. To achieve this goal, we develop RC buildings with buckling restrained braces (BRBs) in this work. For this aim, three traditional RC framed structures with 3, 6, and 9 story levels are designed using the well-known technique no dominated sorting genetic algorithm (NSGA-II) to reduce the cost and maximize the seismic performance. Equivalent RC buildings are designed but including buckling restrained braces. Both structural systems are subjected to several narrow-band ground motions recorded at soft soil sites of Mexico City scaled at different levels of intensities in terms of the spectral acceleration at the first mode of vibration of the structure. Incremental dynamic analysis, seismic fragility, and structural reliability in terms of the maximum inter-story drift are computed for all the buildings. For the three selected structures and the equivalent models with BRBs, it is concluded that the annual rate of exceedance is significantly reduced when BRBs are incorporated. As a result, compared to ordinary reinforced concrete buildings, the structural reliability of RC buildings with BRBs performs better. The usage of BRBs is a good alternative for improving the strength and seismic behavior of RC buildings subjected to strong earthquake ground vibrations, and hence the structural reliability of these structures.

Li et al. [2] resulted that damage to a concrete wall generated by a major earthquake is typically concentrated near the bottom of the wall, posing a serious threat to the steel-concrete hybrid structure's safety and making earthquake rehabilitation extremely difficult. A steel-concrete hybrid structure with buckling restrained bracing is built and tested on a shaking table at a size of 1/10 in this study. The mechanical properties of the BRBs are acquired through a static reacting to stacking test. The unique properties and seismic reaction of the steel-substantial half and half design with BRBs are acquired through shaking table tests. Results show the following:

– the energy dispersal limit of the BRBs is generally excellent, and none of the BRBs clasp during the shaking table tests;

– the steel shafts and segments are fundamentally in a flexible state;

– every break on the substantial divider are miniature breaks, which are broadly disseminated in floors 1–8 of the substantial dividers;

– the most extreme bury story float point arrives at 1/40, which demonstrates that the malleability of the steel-substantial mixture structure is incredible.

Finally, BRBs can increase the seismic performance of steel-concrete hybrid structures significantly.

Patil et al. [3] obtained that BRBs allow for extremely high compression strength in this material. The effective length of the core can be deemed zero because there is no change in available material strength owing to instability. The brace can achieve high ductility by restricting inelastic behavior to axial yielding of the steel core. In this way, the hysteretic execution of these supports is like that of the material of the steel center. Supports with center materials that have huge strain solidifying will display strain solidifying. Since the strains are not amassed in a restricted locale like a plastic pivot, the supports can disseminate much energy. Testing has set up the supports low-cycle exhaustion life; this limit is well in abundance of requests set up from unique nonlinear examination. Such examinations likewise show that utilizing supports with this kind of hysteretic conduct prompts frameworks with incredible execution. Floats are required to be essentially lower than the mainly concentric propped outline (SCBF) due BRBs conduct. BRBFs reaction to seismic stacking gives a lot higher certainty level in a sufficient execution than the conduct of concentrically supported edge (CBF). Scientific investigations of the reaction of BRBF additionally have been utilized to appraise the most significant flexibility requests on BRBs. BRBs should be planned and itemized to oblige inelastic mishappenings without allowing bothersome methods of conduct, like unsteadiness of the support or direction of the non-yielding zones of the center on the sleeve.

Alborzi et al. [4] stated that a buckling-restrained brace (BRB) is a type of bracing system that has an appropriate energy dissipation behavior and does not buckle when subjected to compression pressures. However, because of the BRBs' low post-yield stiffness, significant residual deformations are observed in intense ground vibrations. The seismic presentation of a cutting-edge sidelong burden opposing framework known as the mixture BRB and its traditional partner is evaluated and thought about in this paper. Various plates with various pressure strain conduct are utilized in the center of this new imaginative framework, and this is its distinction with the existent BRBs. Nonlinear static and gradual unique examinations are done for three structure outlines with various primary statures, which utilize traditionally and a half and half BRB frameworks. The FEMA P695 far-field tremor recordset was embraced in various risk levels to do reaction history investigations. The half breed

BRBs are displayed to have predominant seismic execution in examination with the traditional frameworks dependent on the reaction change factor and the harm measures, including lingering removals and between story float proportions

Ozcelik et al. [5] presented a trial examination of (BRBs) with new end limitations and packaging individuals (CMs). The part tests for ten BRBs with CMs comprising of cement-filled steel tube (unbounded), plain concrete, plain cement wrapped with Fiber-Reinforced Polymer (FRP), supported concrete, and a developed segment was tried up to a center plate (CP) strain of 2 %. In unbounded BRBs, an excessive part usually is accessible on the CP. This part might be a contender for clasping during cyclic trips. Henceforth the two finishes of the BRBs at the over-the-top piece of the CP should be controlled even more viably. The developments of BRBs in the current examination were that extra end restrictions were added at the intemperate aspect of the CP at the two finishes, separation material was utilized, and a more efficient CM was utilized. These new end restrictions comprised empty steel areas and steel plates welded to one another and connected to the CM. The testing of the further developed BRBs showed that the cyclic presentation of the BRBs was good up to a CP strain of 2 %. The energy scattering limit of the BRBs was discovered to be essentially reliant upon pressure strength change factor and strain solidifying change factor. Therefore, the further developed BRBs with adequate firmness to oppose out-of-plane clasping at the two closures have satisfactory cyclic execution as per the test outcomes. Besides, the association subtleties, particularly slip basic, segregation materials, and their application procedures, have also been examined for the further developed BRB plan in this investigation.

Nassani et al. [6] presented an examination of the seismic reaction of steel outlines is completed utilizing various kinds of propping frameworks to be specific X braced outlines, V supported edges, modified V supported frames, Knee propped edges, and zipper propped outlines. The steel outlines are displayed nonlinear static, and dynamic investigation is completed in four diverse tallness levels. The casings comprise three inlets, and steel supports were embedded in the center sound of each edge. The underlying reactions of casings are concentrated to limit bend, float proportion, worldwide harm list, base shear, story removals, rooftop uprooting time history, and plastification. The outcomes showed a decent improvement in the seismic opposition of edges with the fuse of propping. The outcomes uncovered that the supporting components were highly successful in lessening floats since the decrease of bury story floats for unbraced edges was on the standard 58 %. Additionally, steel supports impressively decreased the worldwide harm record.

Hamdy et al. [7] assessed the seismic updating of a 6-story RC building utilizing single corner to corner clasping limited supports. Here seismic assessment study is done utilizing static weakling examination and time history investigation. Ten ground movements with

various PGA levels are utilized in the investigation. In addition to one standard deviation upsides of the rooftop float proportion, the most extreme story float proportion, the support pliability factors, and the part strain reactions are utilized as the reason for the seismic exhibition assessments. The outcomes got in this investigation show that fortifying RC structures with clasping controlled supports is a proficient method as it essentially expands the PGA limit of the RC structures. The increment in the PGA limits the RC working with the expansion in the measure of the supports

Guerrero et al. [8] proposed a strategy for starter Performance-Based Seismic Design (PBSD) of low-ascent structures gave Buckling Restrained Braces (BRBs). It is accepted that an edge structure secured with BRBs, named as a double construction, is reasonably addressed by a double single-level of opportunity (SDOF) oscillator whose parts yield at various removal levels. The definition of the strategy is introduced for SDOF structures. Here this improvement is approved utilizing a contextual analysis model. Correlation of the reactions among traditional and double constructions shows that, when planning double constructions, the regular act of utilizing customary plan spectra may prompt one-sided plans. One of the primary benefits of the technique is that, during its application, data valuable for primer and fast evaluation of designs are produced, working with the use of the PBSD reasoning. A contextual investigation model is directed to show its materialness and its potential for the actual appraisal of constructions. Here the principal limit is that this strategy is substantial for low-ascent standard structures with unbending in-plane stomachs and whose unique reaction is constrained by their primary vibration method.

Hosseinzadeh et al. [9] obtained that all-steel clasping limited supports (BRBs) are a recently evolved principal variety is that here common BRBs attributes, for example, weight and restoring of center mortar are upgraded. In these examinations, finite element (FE) models of all steel BRBs with changed calculations were exposed to cyclic investigations. The agreeable support calculations that limited the flimsiness of the center segment while boosting the energy scattering limit were then recognized. Bilinear FE-determined spine bends of the chosen BRBs were utilized in the delegate support components to retrofit three 4-, 8-, and 12-story outlines. The upsides of these supports were featured by drawing execution correlations against customary supports. Nonlinear static and dynamic reactions of the casings with all-steel BRBs were also surveyed as far as boundaries, such as the most significant inelastic disfigurement interest.

Bai et al. [10] examined that an exhibition-based plastic plan (PBPD) strategy for the double arrangement of clasping limited propped supported substantial second opposing casings (RC-BRBFs) is created. The trilinear power deformity relationship of the double RC-BRBF framework was approximated as the bilinear limit bend to infer the yield removal. The plan base shear was resolved dependent on the energy balance condition, which

represented the energy dissemination limit evaluated by the Large Takeda model. The plastic plan technique was introduced to determine the part interior powers.

Patil et al. [11] substantiated that nonlinear time history analysis was used to examine a modified steel moment-resisting frame (SMRF). The basic bare SMRF was first lowered in strength and then increased by installing passive energy dissipation devices (EDDs) to build a modified frame. Both rate-dependent and rate-independent devices are included in passive EDDs. A rate-dependent device is a viscous fluid damper (VFD), whereas a rate-independent device is a buckling-restrained brace. The use of these devices, either alone or in combination, improved the lateral strength of the structure. For incremental dynamic analysis, seven scaled time-history records were used. The lateral displacement profile of the skyscraper demonstrates the stiffness influence on the stories. The VFD was proven to be an effective EDD since it increased the frame's performance at all stages of seismic analysis.

Atlayan et al. [12] presented another underlying steel framework called half and half clasping limited propped outline (BRBF). The "half breed" term for the BRBF framework comes from the utilization of various steel materials, including carbon steel (A36), superior steel (HPS), and low yield point (LYP) steel in the center of the support. In this examination Variety of BRBF models are investigated with nonlinear static sucker, and nonlinear gradual unique examination and correlation is completed with seismic conduct of standard and crossover BRBF frameworks. Results show that Hybrid BRBF frameworks are displayed to have a considerable improvement over standard BRBF frameworks as far as different harm measures remembering a considerable decrease for the risky leftover removals of the standard BRBFs.

Finally, Gua et al. [13] showed the determination of reaction sensitivities for a hysteretic model explicitly produced for clasping limited supports (BRBs) to give a device that can be utilized to assess the impact of BRB constitutive boundaries on underlying reaction just as a device in angle-based strategies in primary streamlining, underlying unwavering quality investigation, and model refreshing. A contextual investigation comprising of a steel outline with BRBs exposed to seismic info is accounted for to represent the impact on worldwide and neighborhood primary reaction amounts of the BRB constitutive boundaries. Likewise, the inferred reaction sensitivities are utilized in a mimicked limited component model refreshing issue to show the productivity of DDM over FDM.

This work opens the best approach to numerous applications and possibilities, for example, affectability examination of complex BRB plan arrangements, execution-based determination of ideal BRB properties, improvement and utilization of advancement-based plan techniques.

3 Research Methodology

3.1 Engineering case study

A flowchart of the research methodology is presented in Figure 2.

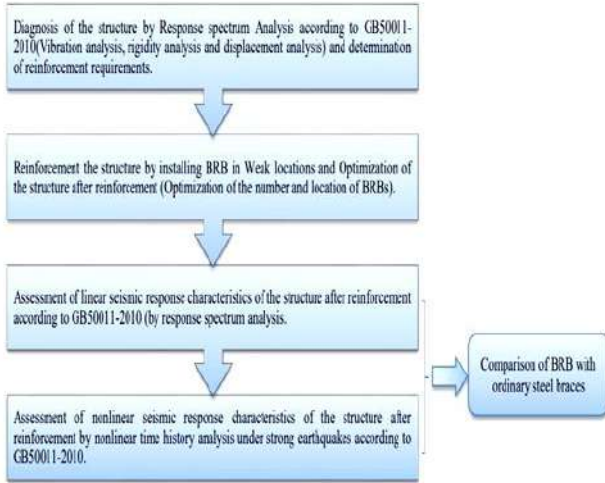


Figure 2 – The flowchart of the research methodology

The basis for this project is a three-story reinforced concrete frame building (Figure 3) with a height of 16.5 m, which was completed in 2008.

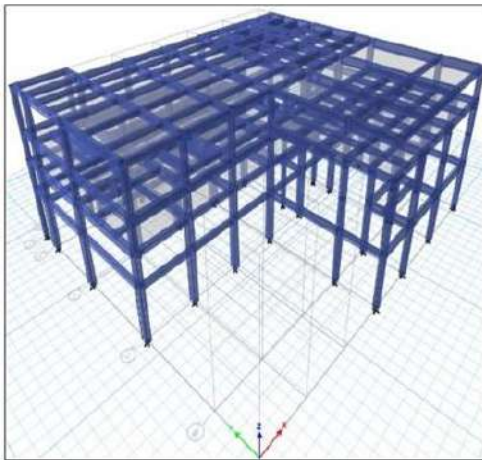


Figure 3 – Engineering model (ETABS)

The structure was built under Indian regulations. After construction, a large machine was installed on the rooftop that had not been anticipated during the analysis and design stage, and another floor was built to cover the machine, necessitating rechecking and strengthening the original structure against new loads. The building is in seismic fortification intensity of 7, and seismic acceleration of the building's 0.1g and the structural design service life is 50 years. The structure has a seismic fortification intensity of 7 and a seismic acceleration of 0.1 g, and the building's structural design service life is 50 years. The building comprises columns and beams of various sizes, with the most significant columns

measuring 700 mm and the most significant beam being 350–950 mm, and the slab measuring 200 mm. All parameters from engineering drawings are considered when modeling the structure, which is made entirely of M30 concrete.

3.2 Structural diagnosis of engineering model

ETABS software calculates maximum displacement, maximum drifts, and frame stiffness utilizing response spectrum analysis of the engineering model. The highest displacement is on the last level, as shown by three modal shapes: translation in X direction (Figure 4 a), translation in the Y-direction (Figure 4 b), and rotation (Figure 4 c).

Table 1 – First three modal periods

Mode	1	2	3
Period, s	0.866	0.748	0.700

The period ratio of the structure is 0.8 and meets the vibration requirements. The story displacement results (Table 2), maximum story drift (Table 3), the frame stiffness (Table 4), and inverted V BRB (Table 5) frame are shown below.

Table 2 – Maximum story drift

Story	Elevation, m	Location	X-Dir, mm	Y-Dir, mm
4	16.5	Top	19.185	15.041
3	12.0	Top	16.620	13.066
2	9.0	Top	12.671	10.851
1	5.8	Top	9.569	7.365
Base	0.0	Top	0.000	0.000

Table 3 – Story displacement

Story	X-Dir, mm	Y-Dir, mm	GB50011-2010
4	0.0006	0.0005	“conform”
3	0.0019	0.0014	“not conform”
2	0.0018	0.0013	“conform”
1	0.0015	0.0013	“conform”
Base	0.0000	0.0000	–

Table 4 – Frame stiffness

Story	X-Dir, 10 ⁸ N/m	Y-Dir, kN/m	GB50011-2010
4	3.51	4.53	“conform”
3	3.26	4.57	“conform”
2	3.41	4.73	“conform”
1	2.23	3.12	“weak 1st story”
Base	0.00	0.00	–

Table 5 – Frame stiffness

Model	Single BRB	X BRB frame	Inverted V BRB Frame
1	0.498	0.415	0.480
2	0.468	0.401	0.438
3	0.356	0.3000	0.330

Weak areas are identified by comparing the results to the “Code for Seismic Design of Buildings” GB50011-2010, which states that the maximum drift ratio must be less than 1/550, the maximum period ratio must be less than 0.9, and the storey stiffness of the floor must not be less than 70 % of the upper floor stiffness and 80% of the average of all above floors). The modal results (Table 1, Figure 4) reveal that the building complies with the code’s vibration criteria.

According to the elastic response spectrum analysis results, the frame construction will have a weak first storey, which will result in concentrated deformation of

the first storey with horizontal stiffness that does not meet Indian standards. This is because the first level lacks appropriate lateral bearing features due to the structure's planned usage.

Furthermore, the third storey does not meet the standard's criterion for elastic storey drift, causing the building to fail before reaching the elastic-plastic stage. This is due to the added load and one storey, increasing the total mass.

As a result, reinforcement of the frame structure is required to improve the stiffness of the flexible floor and reduce the structure's lateral displacement.

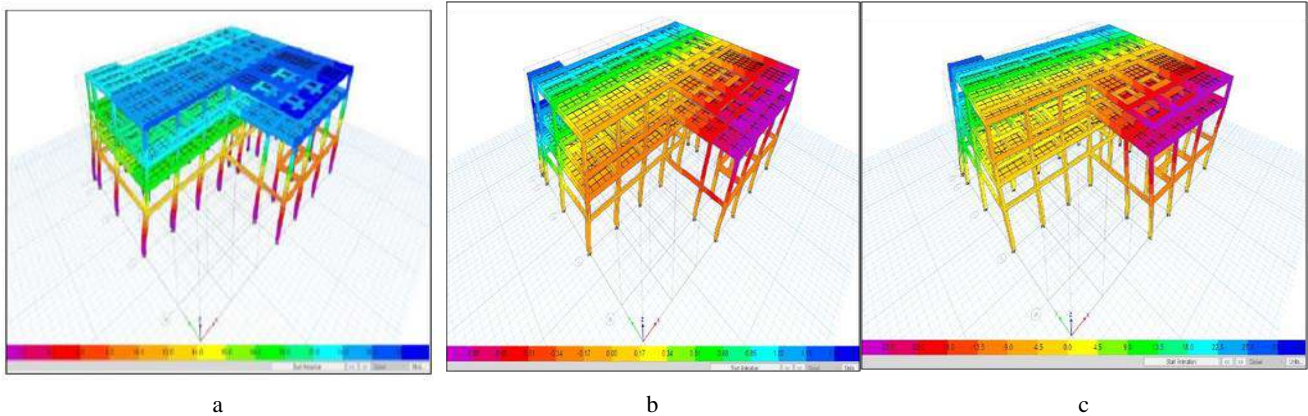


Figure 4 – 1st (a), 2nd (b), and 3rd (c) vibration modes, respectively

4 Results and Discussion

The response characteristics of the strengthened building were determined using response spectrum analysis under the identical stress conditions as the original frame.

For both models, including strengthened and original frames, there is a continual vibration of the structure. The vibration time of a single brace plan, on the other hand, is longer than that of other methods.

All the models are subjected to a linear time history analysis utilizing the direct linear technique of integration with the Hilber Hughes Taylor method in the x-direction. Figure 5 depicts the utilization of ground motion data.

The overall stiffness of the structure improved by BRB has increased, while the vibration period has decreased (Figure 6).

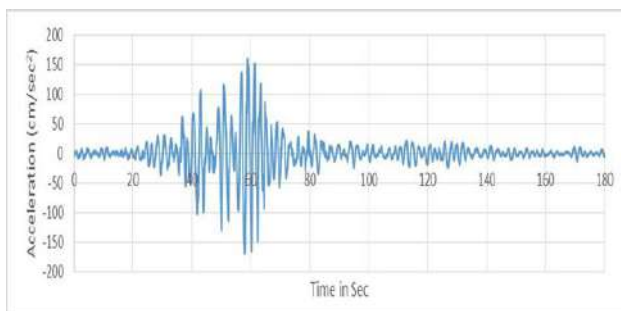
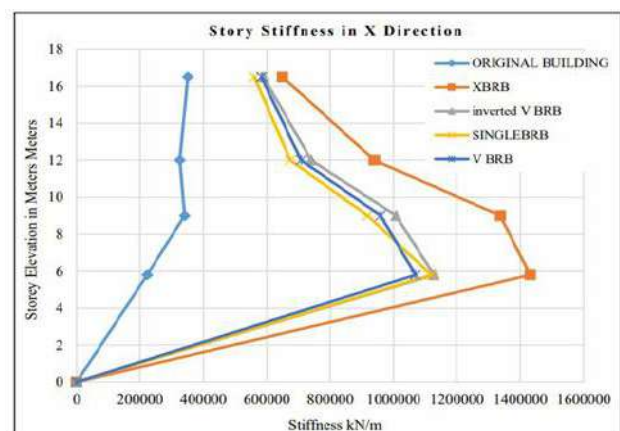


Figure 5 – Ground acceleration time history



a



b

Figure 6 – Stiffness of original (a) and strengthened (b) buildings

The period ratios of both the X and V BRB schemes are less than 0.9, satisfying the requirement that the structure's torsional stiffness be less than its lateral deformation stiffness.

Compared to other configurations, the X-direction stiffness (Figure 6 a) and Y direction stiffness (Figure 6 b) of the frame structure enhanced by X BRB configurations have substantially risen.

The findings reveal that the four BRB configurations strengthened the structure while still adhering to the Indian design code.

Compared to other configuration types, the lateral displacement of the reinforced concrete frame structure enhanced by X BRB (Figure 7) drops the most.

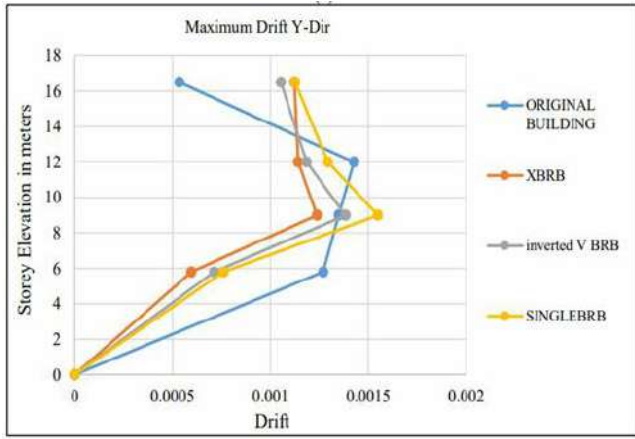
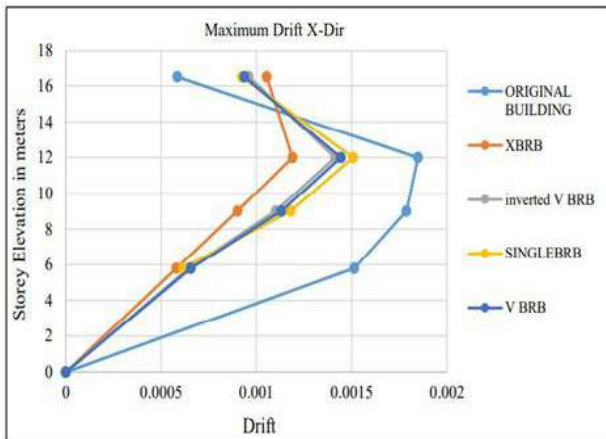
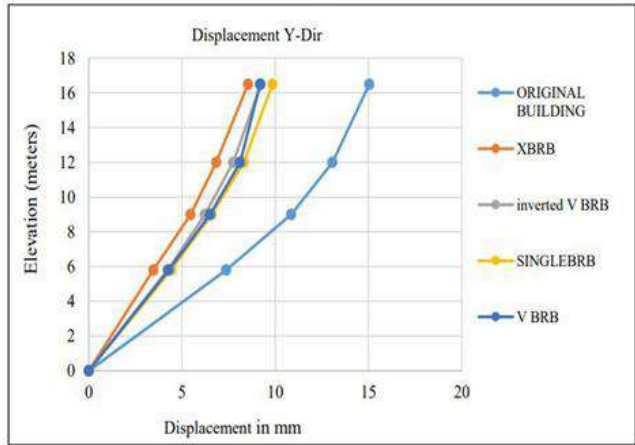
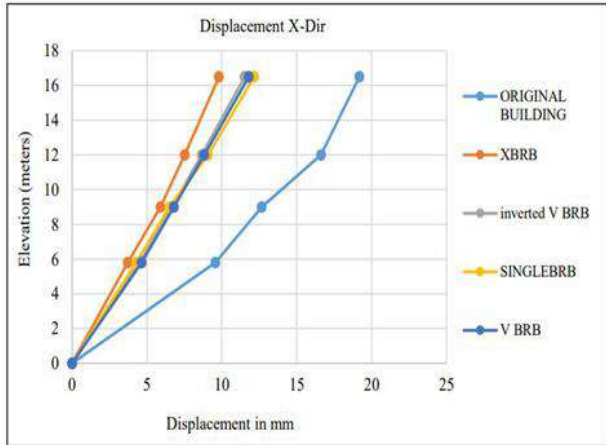


Figure 7 – Maximum floor displacement (a, b) and drift ratio (c, d) of original (a, c) and strengthened (b, d) buildings

Furthermore, a single BRB strengthened frame has a higher drift ratio, implying that, while all BRB reinforcement configurations comply with the standard, a single BRB reinforced frame is not a good choice compared to others.

Under frequent earthquakes, the inter-story drift ratio of reinforced concrete frame structures shall not exceed 1/550 (approximately 0.0018), according to the Indian seismic code for buildings. It can be observed in Figures 7 c–d that the drift ratio of the strengthened building fits the requirements. The structure strengthened by X, V, and single BRB meets the criteria of the appropriate design parameters, with the minimum drift ratio for the X BRB configuration. The stiffness of the frame reinforced by a single brace configuration is lower than that of other configurations, implying that the single brace still has the advantage of a minor increase in the

stiffness of the frame structure after reinforcement compared to other configurations. This single BRB layout may be advantageous for the tallest building when the topmost floors must be fortified to lessen the seismic effect of the enhanced structure

The bearing capacity of ordinary braces is determined by:

$$N_b = \frac{\phi Af}{1 + 0.35\gamma_n}, \quad (1)$$

and that of BRB is determined by $Nb = 0.9Afy$.

where ϕ – stability coefficient of compression members; Af – the cross-section area of the brace; γ_n – adjusted slenderness ratio of the brace:

$$\gamma_n = \left(\frac{L}{\pi}\right) \sqrt{\frac{f_{ay}}{E}}; \quad (2)$$

f_{ay} – the steel’s yield strength; E – the steel’s elastic modulus.

In the plan of standard support, the steadiness coefficient and slinness proportion are basic. As indicated by GB50017-2003, the steadiness coefficient for class an and class “b” FE500 steel is not exactly or equivalent to 1. When a similar steel material and comparing regions are utilized for both standard and clasping limited supports, the bearing limit of the clasping-controlled support will be more noteworthy than that of the standard support, as indicated by the two flexible bearing limit equations. By comparing the two

bearing limit equations, accepting a similar material is utilized for both clasping controlled supports and BRB, and taking the most extreme worth of the security coefficient, the necessary space of customary support to accomplish a similar bearing limit as BRB is discovered to be 1.215 occasions that of BRB.

The results in Figure 8 show that when subjected to small earthquakes, the reinforced concrete frame with standard braces meets displacements (Figure 8 a–b) and maximum drift ratio (Figure 8 c–d) requirements for the Indian building seismic code.

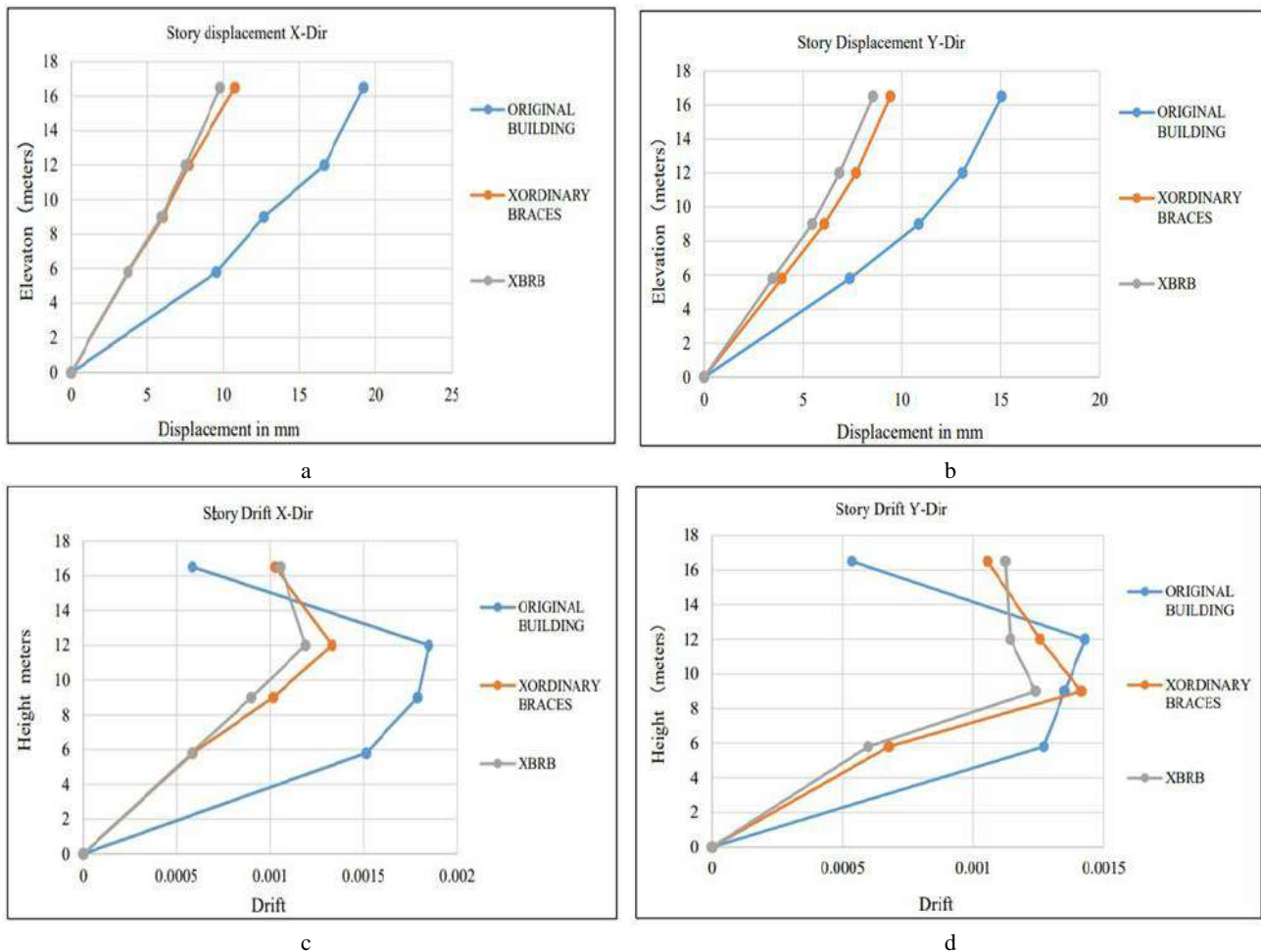


Figure 8 – Stiffness of original binding and strengthened building by ordinary braces and BRB

Ordinary braces with the same configuration (X type), material, and dimensions as BRB are installed at the exact location in reinforced concrete frame construction as BRB to effectively compare the two types of braces’ seismic effect.

Both the frame structure strengthened by ordinary braces and the BRB brace meet the specification’s interlayer displacement requirements, but the drift for the structure strengthened by ordinary braces is greater than the drift for the BRB brace (Figure 4.4.c, d). Because the project examines identical cross-section areas, this is the case.

Because all braces are designed to remain elastic during mild earthquakes, conventional braces with Indian requirements will have a greater area and higher stiffness than BRB, resulting in a lower drift ratio and building horizontal displacement than BRB.

Because the larger cross-section area of a conventional brace is expensive, it may be recommended when project cost is not considered.

When just unbending nature and bearing limit are required, both BRB and standard supports can be used. Anyway, the previous is more financially savvy while the last has a superior inflexibility sway

The structure reaction is accepted to react in a solely flexible way during versatile reaction range investigation. However, because of the mathematical nonlinearity of the structure, material nonlinearity of some primary individuals, and reasonable seismic nonlinearity practices of some underlying individuals. It is helpful to perform a non-direct reaction range examination.

The nonlinear time history examination of the fortified structure under solid tremors is inspected in this investigation.

According to the Code for Seismic Design of Buildings in India, the genuine five severe earthquake recordings and two synthetic earthquakes were chosen based on building sites and design earthquakes grouping.

The spectral features of the selected seismic waves were as close as possible to the building site's characteristic period, and the seismic waves' duration was chosen in line with the code.

The reinforced structure's earthquake resistance was evaluated, and the joint displacement, acceleration, and base shear of the two types of braces were compared.

Figure 9 presents the time history results of building strengthened by BRB and by ordinary braces.

The results show that under rare earthquakes, the base shear (Figure 9 c), peak acceleration (Figure 9 b), and peak displacement time history (Figure 9 a) of BRB structure are smaller than those of ordinary braces. The restrained buckling braces provide an additional damping ratio for the structure, which reduces the displacement response of the structure under earthquakes and reduces the damage of the main structure caused by earthquakes.

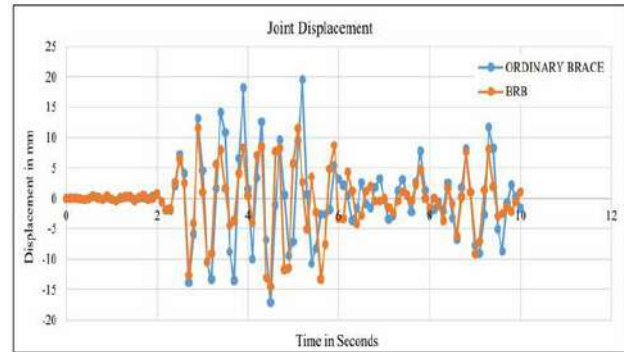
5 Conclusions

According to Indian seismic design requirements, both restrained buckling braces and regular braces can be employed to strengthen reinforced concrete frame structures under the action of mild earthquakes, according to the results of elastic response spectrum analysis. This is since typical bracing will not buckle during mild earthquakes. When comparing the stiffness performance of standard braces with BRB braces, ordinary braces will require a larger cross-section area than BRB braces.

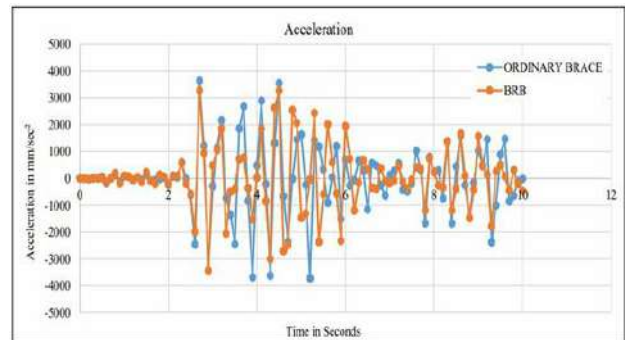
Regular braces fail more frequently due to excessive buckling, whereas buckling restricted braces remain stable, as seen by the superior performance of the frame structure constrained by buckling restrained braces compared to that of ordinary braces are not a safe option for bracing concrete frame constructions in areas where significant earthquakes are forecast.

Different BRB configurations are investigated. The results demonstrate that inverted V buckling restrained braces perform better than V BRB. This is because while

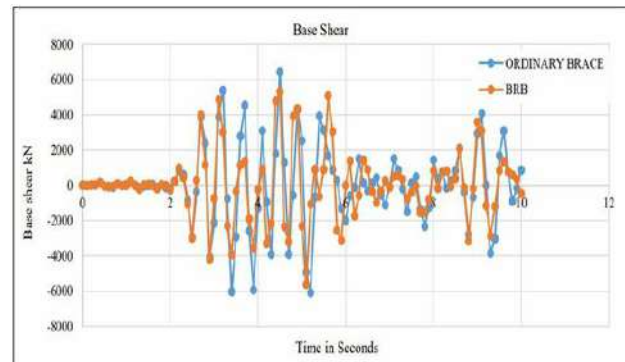
one member is under tension, another is under compression, and the force is directly passed to the column of the next lower floor in an inverted V brace. However, in the case of a V brace, the load will be passed to the beam and then to the column, affecting the bearing capacity.



a



b



c

Figure 9 – Time history results of building strengthened by BRB and by ordinary braces

References

1. Baca, V., Bojórquez, J., Bojórquez, E., Leyva, H., Reyes-Salazar, A., Ruiz, S. E., Formisano A., Palemon, L., Chavez, R., Barraza, M. (2021). Enhanced seismic structural reliability on reinforced concrete buildings by using buckling restrained braces. *Shock and Vibration*, Vol. 2021, 8816552, doi: 10.1155/2021/8816552.
2. Li, L., Li, G., Zhou, T. (2020). Experimental study on the seismic behavior of a steel-concrete hybrid structure with buckling restrained braces. *Advances in Civil Engineering*, Vol. 2020, 9232138.
3. Patil, D. V., Deshmukh, C. M., Kadam, S. S. (2019). Comparative study of conventional braces and buckling restrained braces in steel frame structure. *International Journal of Engineering Research and Technology*, Vol. 8(11), pp. 739–743.
4. Tahghighi, A. M. H., Azarbakht, A. (2019). Numerical comparison of the efficiency of conventional and hybrid buckling-restrained bracing for seismic protection of short-to-midrise steel buildings. *International Journal of Advanced Structural Engineering*, Vol. 11, pp. 439–454.
5. Ozcelik, R., Dikiciasik, Y., Erdil, E. F. (2017). The development of buckling restrained braces with innovative end restrains. *Journal of Constructional Steel Research*, Vol. 138, pp. 208–220.
6. Nassani, D. E., Hussein, A. K., Mohammed, A. H. (2017). Comparative response assessment of steel frames with different bracing systems under seismic effect. *Structures*, Vol. 11, 229–242.
7. Abou-Elfath, H., Ramadan, M., Alkanai, F. O. (2017). Upgrading the seismic capacity of existing RC buildings using buckling restrained braces. *Alexandria Engineering Journal*, Vol. 56, pp. 251–262.
8. Guerrero, H., Ji, T., Teran-Gilmore, A., Escobar, J. A. (2016). A method for preliminary seismic design and assessment of low-rise structures protected with buckling restrained braces. *Engineering Structures*, Vol. 123, pp. 141–154.
9. Hosseinzadeh, S., Mohebi, B. (2016). Finite element analysis seismic evaluation of all-steel buckling restrained braces. *Journal of Constructional Steel Research*, Vol. 119, pp. 76–84.
10. Bai, J., Ou, J. (2016). Earthquake-resistant design of buckling-restrained braced RC moment frames utilising performance-based plastic design method. *Engineering Structures*, Vol. 107, pp. 66–79.
11. Patil, H. R. M., Jangid, R. S. (2015). Numerical study of seismic performance of steel moment-resisting frame with buckling-restrained brace and viscous fluid damper. *The IES Journal Part A: Civil and Structural Engineering*, Vol. 8(3), pp. 165–174, doi: 10.1080/19373260.2015.1038862.
12. Atlayan, O., Charney, F. A. (2014). Hybrid buckling-restrained braced frames. *Journal of Constructional Steel Research*, Vol. 96, pp. 95–105.
13. Gua, Q., Zona, A., Penga, Y., Dall'Asta, A. (2014). Effect of buckling restrained brace model parameters on seismic structural response. *Journal of Constructional Steel Research*, Vol. 98(1), pp. 100–113.



MANUFACTURING 2022

7th International Scientific-Technical Conference

MANUFACTURING 2022

May 16-19, 2022 | Poznan, Poland

Special Session SS_11

Mechatronics in mechanical engineering – perspective and new solutions

- Mechatronics devices
- Control systems in mechanical engineering
- Machine learning
- Vision system
- Mechatronic systems supervision



ORGANIZERS SS_11

Dominik Rybarczyk
Poznan University of Technology, Poland
dominik.rybarczyk@put.poznan.pl

Marcin Biątek
Poznan University of Technology, Poland
marcin.biatek@put.poznan.pl

Vitalii Ivanov
Sumy State University, Ukraine
ivanov@tmvi.sumdu.edu.ua

Khrystyna Berladir
Sumy State University, Ukraine
kr.berladir@pmtkm.sumdu.edu.ua

<https://manufacturing.put.poznan.pl/>



Nogueira E. (2020). Applying the concepts of efficiency and effectiveness to analyze the influence of the number of passes in the shell and tubes condenser thermal performance. *Journal of Engineering Sciences*, Vol. 8(1), pp. F1–F10, doi: 10.21272/jes.2021.8(1).f1

Applying the Concepts of Efficiency and Effectiveness to Analyze the Influence of the Number of Passes in the Shell and Tubes Condenser Thermal Performance

Nogueira E.

Department of Mechanics and Energy, State University of Rio de Janeiro,
R. São Francisco Xavier, 524 Maracanã, Rio de Janeiro, 20550-013 Brazil

Article info:

Received:
The final version received:
Accepted for publication:

December 9, 2020
April 24, 2021
May 1, 2021

*Corresponding email:

elcionogueira@hotmail.com

Abstract. The work analyzes the influence of the number of passes in a shell and tubes condenser heat exchanger, with an inlet pressure of R134a refrigerant in the shell equal to 1.2 MPa. The fluid that circulates in the tubes is water or water-based nanofluid with a fraction of aluminum oxide nanoparticles (Al_2O_3), and the methodology used subdivides the heat exchanger into three distinct regions: the overheated region, the saturated region, and the subcooled region. The main parameters used to analyze the thermal performance of the heat exchanger were efficiency and effectiveness. Efficiency in the superheated steam region is close to 1.0. There is scope for increasing thermal effectiveness, which can be improved with more significant passes in the tube. The saturated steam region process is efficient for lower mass flow rates of the fluid in the tube, but it is ineffective. However, it is highly effective for high mass flow rates. There is ample scope for increasing effectiveness in the subcooled region. Still, the fluid inlet temperature in the pipe and the work refrigerant pressure are the limiting factors for greater heat exchange in the subcooled region.

Keywords: heat exchange, refrigerant, tube condenser, thermal performance.

1 Introduction

The article aims to analyze the influence of the number of passes on the tube in a shell and tubes condenser heat exchanger using the concepts of efficiency and effectiveness.

The heat exchanger used as a base consists of a shell and 36 tubes, with three regions of 12 tubes each. The refrigerant is R134a, and the nanofluid in the tubes is based on water and a fraction of aluminum oxide nanoparticles (Al_2O_3). The refrigerant's working pressure is equal to 1.2 MPa, and the inlet temperature is equal to 70.5 °C. The fluid flowing in the tubes has an inlet temperature equal to 25 °C. The shell and tube condenser heat changer in question was analyzed experimentally and theoretically by Lee and Mai [1], and theoretically by Nogueira [2].

2 Literature Review

One of the essential components in a heat pump is the condenser, which transfers energy from the refrigerant to water or another fluid at a lower temperature. Shell and tube condensers are the most commonly used for heating water for their adaptability and easy construction. Heat

pumps are considered moderately high temperatures when the fluid's outlet temperature to be heated varies from 60 °C to 95 °C. In these operating conditions, the temperature difference between inlet and outlet may be above 40 °C, and that the condensation temperature increases, resulting in a decrease in thermal efficiency. The factors that can influence the thermal performance in the shell and tube condenser are many and deserve in-depth investigation in all aspects [1].

The methodology [2] uses the concepts of efficiency and effectiveness to analyze the thermal performance of a shell and tube condenser, with Freon 134a as a refrigerant flowing in the shell at relatively low saturation pressure. Water or water-based aluminum oxide nanoparticles flow in the tubes. The condenser is divided into three regions to facilitate analysis, with four pipes and three passes: 12 tubes. The refrigerant mass flow rate is fixed equal to 0.20 kg/s. As a basis for obtaining theoretical results, the experimental result obtained from reference [1] was used, with a vapor pressure value equal to 1.2 MPa and a water flow equal to 0.41 kg/s.

Bejan [3] presented a procedure to minimize entropy generation at a physical system's components. The work's fundamental idea is to demonstrate that the system's

entropy generation rate is the sum of the contributions of all components. If the irreversibility of a component is minimized, the reduction occurs at the system's general level.

Fakheri [4] presented a solution for defining thermal efficiency in heat exchangers applying thermodynamics' second law. It demonstrates that there is an ideal heat exchanger for each real heat exchanger that has the same thermal resistance, the average temperature difference, and the same temperature ratio of cold to the hot fluid inlet. The ideal heat exchanger transfers maximum energy and generates a minimum amount of entropy, making it more efficient and less irreversible. The article provides a new way to analyze heat exchangers and heat exchanger networks.

Tiwari and Maheshwari [5] demonstrated that a heat exchanger's better thermal performance results from efficient energy use and allows for weight reduction. They claim that a heat exchanger's performance is generally measured by its effectiveness, which does not provide any information about its efficiency. The concept of thermal efficiency must be based on the second law of thermodynamics. Through this procedure, the relationship between effectiveness and efficiency can be explained mathematically.

Hermes [6] presented an approach for the optimum design of condensers and evaporators. He put forward an explicit formulation that expresses the dimensionless rate of entropy generation and an expression for the optimum heat exchanger effectiveness, based on the working conditions, heat exchanger geometry, and fluid. It was found that a heat exchanger design with a high aspect ratio is preferable to a low aspect ratio, and the heat exchanger design that presents the best component-level also leads to the best global system performance.

Nogueira [7, 8] presented an analytical solution for obtaining the outlet temperatures in a shell and tube heat exchanger. He uses the concepts of efficiency, effectiveness (ϵ -NTU), and irreversibility. The nanoparticles' volume fractions ranging from 0.1 to 0.5, and the results for efficiency, effectiveness, and irreversibility were obtained graphically. The flow laminarization effect for nanofluid particles had significant relevance in the results.

The chemical characteristics of refrigerants alternative to CFCs have been proposed and implemented by the refrigeration industries. HFC-134a is one of the options found to replace CFC-12 due to similar physical properties. The change in refrigerant in refrigeration equipment has led to a detailed investigation of the properties of HFC-134a [9].

The refrigerant R134a is considered a suitable alternative for reducing the effect of refrigerants on the ozone layer. The work presented by Roy and Mandal [10] uses liquid density, saturation vapor pressure, state equation, and specific heat at constant volume to obtain mathematical expressions, equations to determine different thermodynamic properties of the refrigerant R-134a. These equations and Maxwell's relations make it possible to calculate enthalpy and entropy for the vapor state.

The condensation process of R134a refrigerant in the circular and flat tubes was investigated numerically by Wen et al. [11]. Two correlations were developed and compared with existing correlations that underestimate both the heat transfer coefficients and pressure gradients.

A circular tube and three-flat copper tubes were used to determine the aspects associated with the condensation enthalpy of R134a. The experimental results demonstrated that the existing correlations are not appropriately applied for the flattened pipes. A new correlation was developed by Kaew-On et al. [12], based on the experimental data.

Albadr et al. [13] reported an experimental study on heat transfer and nanofluid flow with different concentrations in a volume of aluminum oxide – Al_2O_3 (0.3–2.0 %) in a shell and tube heat exchanger under turbulent conditions. The convective heat transfer coefficient results demonstrate that the nanofluid has a thermal performance slightly superior to that of water at the same mass flow and inlet temperature. However, the increase in the concentration of nanoparticles causes an increase in the friction factor.

Heat exchangers are used in many applications, such as air conditioning and domestic water heating. The work developed by Almurtaji et al. [14] provides a systematic review of the use of nanofluids to improve the thermo-hydraulic of such equipment. The objective is to emphasize the importance of nanofluids and how their use significantly increases heat exchangers' thermal efficiency.

3 Research Methodology

3.1 General formulation

Figure 1 shows a diagram for the condenser under analysis. The condenser was divided into three regions. The regions consist of 12 pipes each: 4 tubes in line and three passages in each region. The steam enters the overheated region at a temperature equal to 70.5 °C. The fluid enters at a temperature equal to 25 °C in the subcooled region. There are three horizontal baffles in the supersaturated steam region to increase the efficiency of heat exchange. The steam flow is equal to 0.20 kg/s. The flow rate of the fluid in the tube varies from 0.05 kg/s to 0.40 kg/s. The properties of fluids are shown in Table 1.

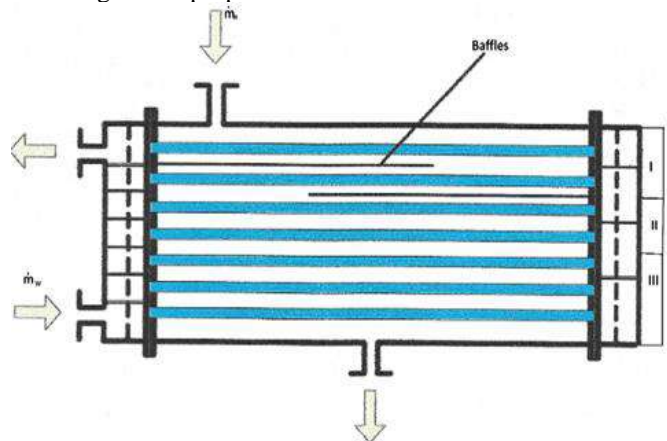


Figure 1 – Scheme for the shell and tubes condenser

Table 1 – Properties of the fluids and nanoparticle

Properties	Freon R134a		Water	Al ₂ O ₃
	I	III		
k , W/(m K)	15.4	74.71	0.60	31.9
C_p , J/(kg K)	1,144	1,498	4180	837
μ , 10^{-6} kg/(m s)	12.3	161.45	75.8	4.65
ρ , kg/m ³	50	1,146	997	3950
ν , 10^{-7} N·m ² /s	2.47	1.40	0.80	0.118
α , 10^{-6} m ² /s	269.0	43.5	0.143	9.65
Pr	1,091	310.7	5.68	818

The initial input data, three passes, for each of the regions are: TRE_{entr} = 70.5 °C; TWE_{entr} = 25.0 °C; Tsat = 46.02 °C;

$$NTube = 4; \quad (1)$$

$$Npass = 3; \quad (2)$$

$$D_W = 0.0127 \text{ m}; \quad (3)$$

$$L = 0.762 \text{ m}; \quad (4)$$

$$B = 0.0145 \text{ m}; \quad (5)$$

$$CL = 1.0; \quad (6)$$

$$CTP = 0.85. \quad (7)$$

So, we have:

$$Pt = 1.25D_W; \quad (8)$$

$$De = \frac{1.27}{D_W} (Pt^2 - 0.785D_W^2); \quad (9)$$

$$Dc = 3.0D_W; \quad (10)$$

$$PR = \frac{Pt}{D_W}; \quad (11)$$

$$A_W = \pi D_W L Ntube Npass; \quad (12)$$

$$Ds = 0.637 \sqrt{CL/CTP} \sqrt{ATPR^2 Dc/L}; \quad (13)$$

$$As = DsB \left(1.0 - \frac{D_W}{Pt}\right); \quad (14)$$

Pt is the tube pitch, DW is the tube diameter, De is the equivalent hydraulic diameter, B is the baffles spacing, Ds is the shell diameter associated with each Region, AW is the heat exchange area, As is the shell-side pass area.

$$Re_R = \frac{\dot{m}_R De}{As \mu_R}; \quad (15)$$

$$Nu_R = 0.36 Re_R^{0.55} Pr_R^{1/3}. \quad (16)$$

At where, \dot{m}_R is the mass flow, μ_R is the dynamic viscosity of the refrigerant, Re_R is the Reynolds number, Pr_R is the Prandtl number and Nu_R is the Nusselt number.

$$h_R = \frac{Nu_R k_R}{De}, \quad (17)$$

where k_R is the thermal conductivity and h_R is the convection heat transfer coefficient;

$$\rho_W = \phi \rho_{Al} + (1 - \phi) \rho_W; \quad (18)$$

$$\mu_W = (1 + 2.5\phi) \mu_W; \quad (19)$$

$$\nu_W = \frac{\mu_W}{\rho_W}; \quad (20)$$

$$Cp_W = [\phi \rho_{Al} Cp_{Al} + (1 - \phi) \rho_W Cp_W] / \rho_W; \quad (21)$$

$$k_W = \frac{K_{Al} + 2k_W + 2(k_{Al} - k_W)(1 + 0.1)^3 \phi}{(K_{Al} + 2k_W - (k_{Al} - k_W)(1 + 0.1)^2 \phi)} k_W; \quad (22)$$

$$\alpha_W = \frac{k_W}{\rho_W Cp_W}; \quad (23)$$

$$Pr_W = \frac{\alpha_W}{\nu_W}, \quad (24)$$

where ρ_W is the density of the fluid, μ_W is the dynamic viscosity of the fluid, ν_W is the kinematic viscosity of the fluid, Cp_W is the specific heat of the fluid, k_W is the thermal conductivity and Pr_W is Prandtl number.

$$\dot{m}_{WT} = \dot{m}_W / Ntube; \quad (25)$$

$$Re_W = \frac{4\dot{m}_{WT}}{\pi D_W \mu_W}, \quad (26)$$

where \dot{m}_W is the flow inlet of the fluid, \dot{m}_{WT} is the flow in each tube and Re_W is the Reynolds number;

$$Nu_W = 4.364 + \frac{0.0722 Re_W Pr_W D_W}{L} \quad \text{for } Re_W \leq 2,100; \quad (27)$$

$$Nu_W = \frac{\left[\left(\frac{ft}{8}\right)(Re_W - 10^3) Pr_W\right] \left(1 + \frac{D_W}{L}\right)^{0.67}}{1 + 1.27 \sqrt{\frac{ft}{8}} (Pr_W^{0.67} - 1)} \quad \text{for } 2,100 < Re_W \leq 10^4; \quad (28)$$

$$ft = [1.82 \text{Log}(Re_W) - 1.64]^{-2}; \quad (29)$$

$$Nu_w = 0.027 Re_w^{0.8} Pr_w^{1/3} \quad \text{for } Re_w > 10^4; \quad (30)$$

ft is the friction factor and Nu_W is the Nusselt number.

$$h_W = (Nu_W K_W) / D_W; \quad (31)$$

$$U_o = \frac{1}{\frac{1}{h_R} + \frac{1}{h_W}}, \quad (32)$$

where U_o is the global heat transfer coefficient;

$$C_R = \dot{m}_R Cp_R; \quad (33)$$

$$C_W = \dot{m}_W Cp_W; \quad (34)$$

$$NTU = \frac{A_W U_o}{C_{min}}; \quad (35)$$

$$Fa = (NTU/2)(1 - C_*); \quad (36)$$

$$C_* = C_{min}/C_{max}; \quad (37)$$

C_R is the thermal capacity of the refrigerant, C_W is the thermal capacity, NTU is called the Number of Thermal Units, Cmin is the smallest of the specific heats;

$$\sigma_T = \tanh(Fa)/Fa; \quad (38)$$

$$\eta_T = \frac{1}{\frac{1}{\sigma_T NTU} + \frac{1 + C_*}{2}}; \quad (39)$$

σ_T is thermal efficiency and η_T is the thermal effectiveness.

3.2 Solution procedure for the region I

$$TW_i = T_{sat} - \Delta T_1, \quad (40)$$

where ΔT_1 – the actual temperature of the fluid inlet in Region I for a given flow in the tube. The experimental data from reference [1] (Table 1) were used: inlet temperature equal to 70.5 °C, and mass flow for the tube fluid equal to 0.41 kg/s. Then, we define:

$$\Delta T_1 = 0.0 \text{ for theoretical results}; \quad (41)$$

$$\Delta T_1 = 2.0 \text{ for experimental results}; \quad (42)$$

$$TR_i = TRE_{ntr}; \quad (43)$$

$$Q_{Actual} = \frac{(TR_i - TW_i)C_{min}}{\frac{1}{\sigma_T NTU} + \frac{1 + C_*}{2}}; \quad (44)$$

$$TW = (Q_{Actual}/C_W) + TW_i; \quad (45)$$

$$TR = TR_i - (Q_{Actual}/C_R), \quad (46)$$

where Q_{Actual} – the heat exchange between fluids, TW_i is the fluid inlet temperature, TR_i is the fluid inlet temperature.

Then,

$$TR_i = TR_i - \epsilon_1. \quad (47)$$

Return to equation (44) and recalculate Q_{Actual} , TW , and TR .

ϵ_1 It is a value that allows precision in determining TR and TW .

The procedure at Region I ends when:

$$TR_i \leq T_{sat}. \quad (48)$$

3.3 Solution procedure for the region II

$$X = 1; \quad (49)$$

$$h_{lv} = hv - hl; \quad (50)$$

$$\mu_R = \mu_{Rl}X + \mu_{Rv}(1 - X); \quad (51)$$

$$\rho_R = \rho_{Rl}X + \rho_{Rv}(1 - X); \quad (52)$$

$$k_R = k_{Rl}X + k_{Rv}(1 - X); \quad (53)$$

$$Cp_R = Cp_{Rl}X + Cp_{Rv}(1 - X); \quad (54)$$

$$Pr_R = Pr_{Rl}X + Pr_{Rv}(1 - X), \quad (55)$$

where X – the steam fraction in Region II;

$$Re_R = (\dot{m}_R De)/(As \mu_R); \quad (56)$$

$$\Delta f = T_{sat} - T_{REF}; \quad (57)$$

$$h_R = 0.943 [k_R \rho_R g h_{lv} / (\mu_R D_s \Delta f)]^{0.25}, \quad (58)$$

where Re_R – the number of Reynolds in Region II; Δf – a reference temperature difference; h_R is the convection heat transfer coefficient, and $T_{REF} = 0$.

h_R varies with properties. The heat exchange between fluids in Region II is achieved by:

$$\sigma_T = \frac{\tanh(Fa)}{Fa}; \quad (59)$$

$$\eta_T = \left(\frac{1}{\sigma_T NTU} + \frac{1 + C_*}{2} \right)^{-1}; \quad (60)$$

$$Q_{Actual} = \frac{(T_{sat} - TW_i)C_{min}}{\frac{1}{\sigma_T NTU} + \frac{1 + C_*}{2}}; \quad (61)$$

$$TW = TW_i - (Q_R/C_*); \quad (62)$$

Therefore:

$$TW_i = TW_i - \epsilon_2 \quad (63)$$

Return to Equation 60 and recalculate Q_{Actual} , TW .

ϵ_2 It is a value that allows precision in determining TW .

The procedure at Region II ends when:

$$X < 0. \quad (64)$$

3.4 Solution procedure for the region III

$$TW_i = 25 \text{ }^\circ\text{C}; \quad (65)$$

$$TR_i = T_{sat}. \quad (66)$$

The initial calculations use the properties as shown in Table 1, Region III. Then equations 15 to 17, 33 to 39 must be recalculated.

$$Q_{Actual} = \frac{(TR_i - TW_i)C_{min}}{\frac{1}{\sigma_T NTU} + \frac{1 + C_*}{2}}; \quad (67)$$

$$TW_o = TW - (Q_{Actual}/C_W); \quad (68)$$

$$TR_o = TR - (Q_{Actual}/C_R); \quad (69)$$

$$TW = TW_o; \quad (70)$$

$$TR = TR - \Delta T_2. \quad (71)$$

Therefore,

$$TW_i = TW_i - \epsilon_2. \quad (72)$$

Return to equation (67) and recalculate Q_{Actual} , TW_o , and TR_o .

ϵ_2 It is a value that allows precision in determining TR_o and TW_o .

The procedure at Region III ends when:

$$TW_i \leq TW_{Entr}. \quad (73)$$

In this case, we have the outlet temperature of the refrigerant.

ΔT_2 allows determining the real temperature of the fluid inlet in Region I. The experimental data of Table 1 of the reference [1] is used as reference: Inlet temperature equal to 70.5 °C, refrigerant pressure equal to 1.2 MPa, and mass flow equal to 0.41 kg/s. Then, we define:

$$\Delta T_2 = 0 \text{ for theoretical results}; \quad (74)$$

$$\Delta T_2 = 0.085 \text{ for the experimental results}. \quad (75)$$

4 Results and Discussion

4.1 Region I – superheated steam

In the region of superheated steam of the heat exchanger in question, Region I, already described and represented by Figure 1, there are three well-defined temperatures: fluid inlet temperature in the tubes, refrigerant inlet temperature R134a, and pressure saturation temperature equal to 1.2 MPa, that is, 46.02 °C. The energy available for heat exchange depends on the temperatures of the refrigerant. With an inlet temperature equal to the outlet temperature of Region II, the fluid entering the tubes of saturated steam absorbs all the energy, and its outlet temperature depends on its mass flow rate. Less mass flow rate, higher outlet temperature, due to its lower thermal

capacity; that is, there is a more significant temperature variation per unit mass. As the nanofluid has thermal diffusivity higher than that of water, its outlet temperature is slightly higher.

Figure 2 presents results for temperature profiles for nanofluid in Region I, superheated steam, for two lengths of the heat exchanger, $L_1 = 0.762$ m and $L_2 = 1.016$ m, and three different flow rates for the flow of the fluid in the tube, 0.05 kg/s, 0.20 kg/s, and 0.40 kg/s. There is a proportional increase of 33.33% in the heat exchanger's length, which provided a maximum increase in the fluid's outlet temperature in the tube equal to 4.3 %, for the lowest flow rate, equal to 0.05 kg/s. The increase in the outlet temperature is insignificant for higher flow rates due to the greater thermal capacity. Increasing the heat exchange area through a longer heat exchanger length is not advantageous when higher outlet temperatures are desired for the tubes' fluid since this procedure is economically more expensive.

Figure 3 presents results for temperature profiles in Region I for water and nanofluid (Al_2O_3). The flow of the fluid in the tube is equal to 0.050 kg/s, that is, the flow that allows the highest outlet temperature in the analysis in question. The number of passes in the tube varies from 3 to 6 passes; that is, the heat exchange area is doubled. The outlet temperature observed between these extremes increases by 6.85 % for the nanofluid and 6.22 % for water. Since it is undoubtedly a less costly procedure than doubling the heat exchanger's length, Auspicious results affect not only Region I but also other regions.

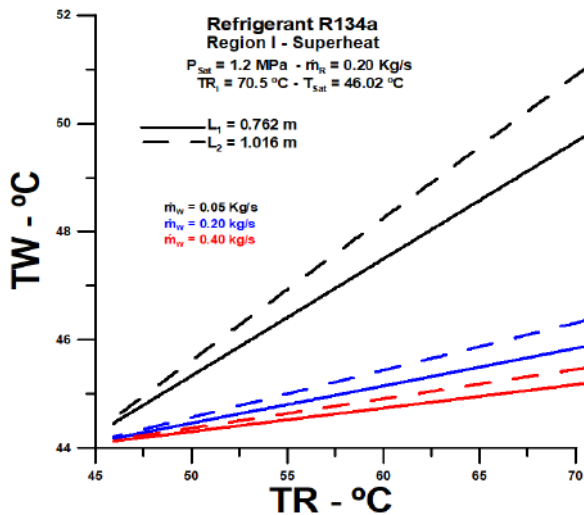


Figure 2 – Influence of heat exchanger length and fluid flow in the tube

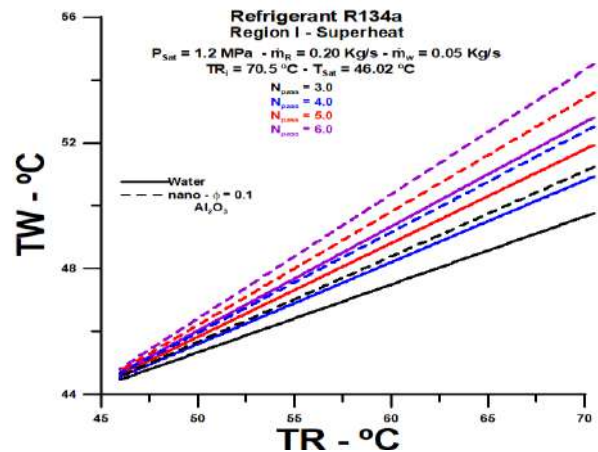


Figure 3 – Influence of the number of passes on the tube on the temperature profile in Region I

The fluid outlet temperature in the tubes in Region I, as a function of the mass flow rate, is represented by Figure 4, for water and nanofluid. As previously noted, the highest outlet temperature corresponds to the lowest flow in the analysis. However, as the tubes' flow increases, the difference between the outlet temperatures, when the number of passes in the tube is doubled, decreases progressively as the flow rate varies from laminar to turbulent regime. It is not advantageous to increase the number of passes for flow rates above 0.3 kg/s, for Reynolds number above 10^4 , within the range of flow rates analyzed, when what is desired is the highest possible outlet temperature for the fluid in the tubes.

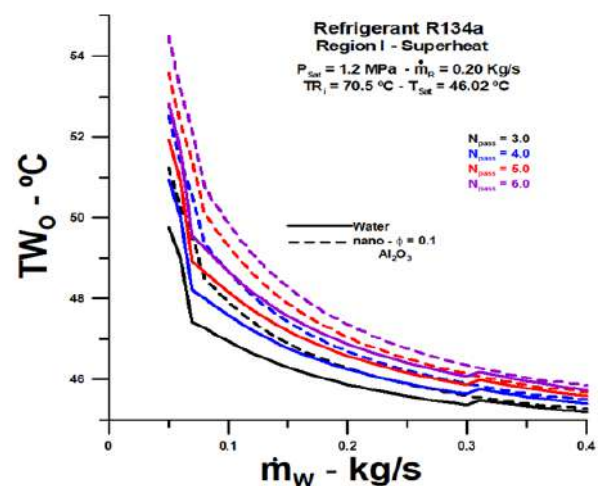


Figure 4 – Influence of the number of passes in the tube on the outlet temperature in Region I

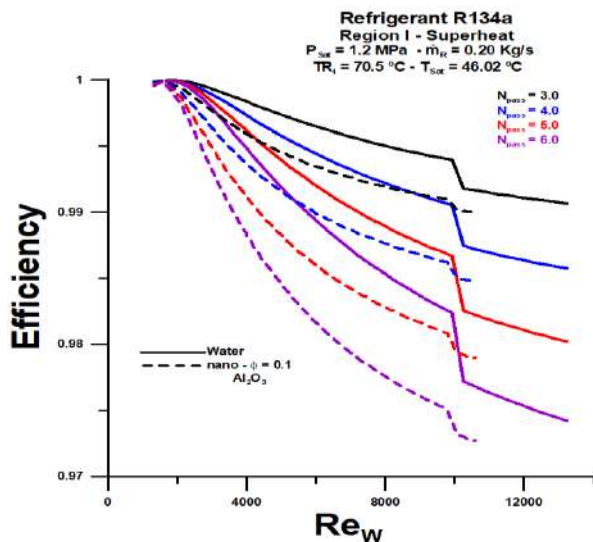


Figure 5 - Influence of the number of passes on the tube on thermal efficiency in Region I

Thermal efficiency in Region I is represented by Figure 5, using the number of passes in the tube as a parameter. Efficiency is exceptionally high in all situations analyzed. However, there is a slight decrease when the number of passes increases and when the flow regime varies from laminar to turbulent. For lower flow, equal to 0.05 kg/s, the efficiency is equal to 1 regardless of the number of passes. This result reflects the fact that there is a more significant temperature variation between inlet and outlet in this flow rate.

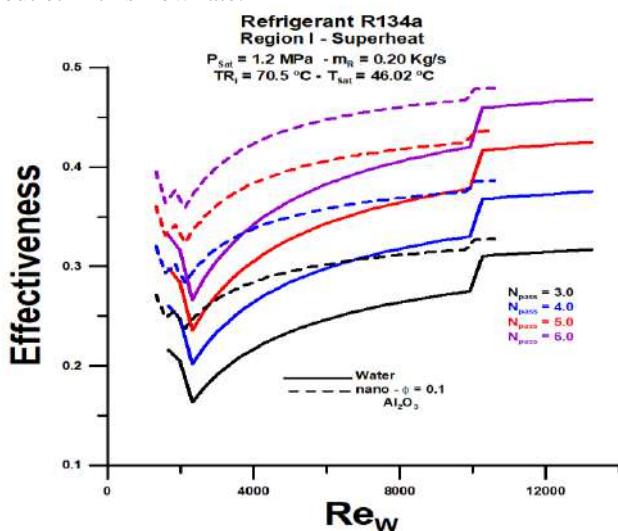


Figure 6 – Influence of the number of passes on the tube on the thermal effectiveness in Region I

Thermal effectiveness in Region I is represented by Figure 6, using the number of passes in the tube as a parameter. The effectiveness is doubled practically when the number of passages in the pipe is doubled for the entire flow range analyzed, varying from 0.2 to 0.4 for flow equal to 0.05 kg/s. Despite this, effectiveness is relatively low, demonstrating that not all of the potential for heat exchange is tapped; that is, the heat exchange is below the

maximum possible for the number of passes under analysis.

As a summary for Region I:

- 1) we can say that the mass flow rate that allows the highest outlet temperature is the lowest possible, equal to 0.05 kg/s;
- 2) the outlet temperature increases as the number of passes through the tube increases;
- 3) there is scope for increasing thermal effectiveness, although efficiency is very close to 1 in all cases;
- 4) the effectiveness can be improved with a more significant number of passes in the tube;
- 5) the heat exchange process in Region I is efficient, it works, but it can become more effective when it comes to obtaining the highest possible outlet temperature for the fluid in the tube.

4.2 Region II – saturated steam

In the region of saturated steam of the heat exchanger in question, Region II, already described and represented through Figure 1, there are two well-defined temperatures: fluid outlet temperature in the tubes and the saturation temperature in the pressure equal to 1.2 MPa, that is, 46.0 °C. However, the quantity of relevant importance is the enthalpy available for each steam fraction X , which varies between dry saturated steam, $X = 1$, and subcooled liquid, $X = 0$. The available energy, therefore, depends on the enthalpy available between these two extremes. As the refrigerant's mass flow rate is constant, equal to 0.20 kg/s, the available energy is the same for all liquid flows in the tubes.

The fluid that passes through the tubes enters Region II with an unknown temperature, to be determined using the methodology described above.

The fluid temperature in the tubes entering Region I and leaving Region II depends on the number of passes in the tube, as shown in Figure 7 below. Although close, there is a slight difference between the number of passes, and a smaller number of passes has a lower outlet temperature in Region II, as shown in Figure 3. As the mass flow rate of the fluid in the tubes is the same, equal to 0.05 kg/s, a more extensive exchange area, that is, a more significant number of passes in the tube absorbs a greater amount of energy, which reflects a more substantial difference in temperature between the entrance and the exit of Region II.

Figure 8 shows the inlet temperatures in Region II to function the number of passes in the tube and the fluid's mass flow rate. As discussed in the paragraph above, in Figure 7, the highest inlet temperature in Region II corresponds to the lowest number of passes in the tube, equal to three passes.

Thermal efficiency in Region II is represented by Figure 9, using as a parameter the number of passes in the tube. Efficiency is equal to 1.0 for lower flow rate, equal to 0.05 kg/s, regardless of the number of passes, and falls progressively as the flow rate increases, with significant dependence on the number of passes. The efficiency is 0.6 for water and 0.5 for nanofluid when the number of passes is equal to 6, and the tubes' flow corresponds to 0.40 kg/s.

The thermal effectiveness in Region II is represented by Figure 10, using the number of passages in the tube, and varying the pipes' flow. The effectiveness increases progressively with the mass flow rate variation, varying between 0.4, for mass flow rate equal to 0.05 kg/s, to 0.8, for mass flow rate equal to 0.40 kg/s, when the number of passes is equal to 3.

When the number of passes in the tube is 6, the effectiveness approaches 1.0 for the highest mass flow rate in the pipes: 0.40 kg/s. Therefore, in this situation, the heat exchange comes at the maximum possible in Region II.

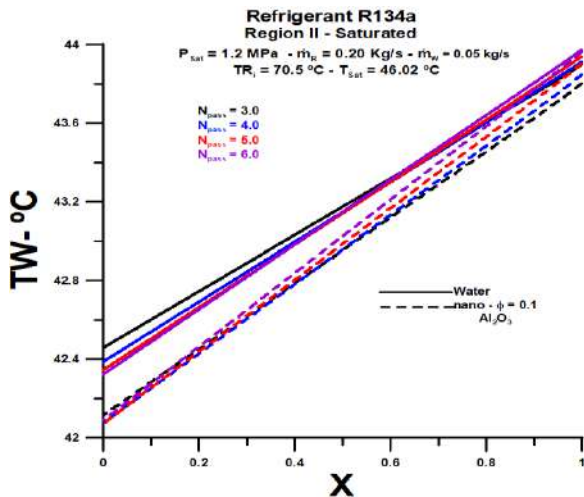


Figure 7 – Influence of the number of passes on the tube on the temperature profile in Region II

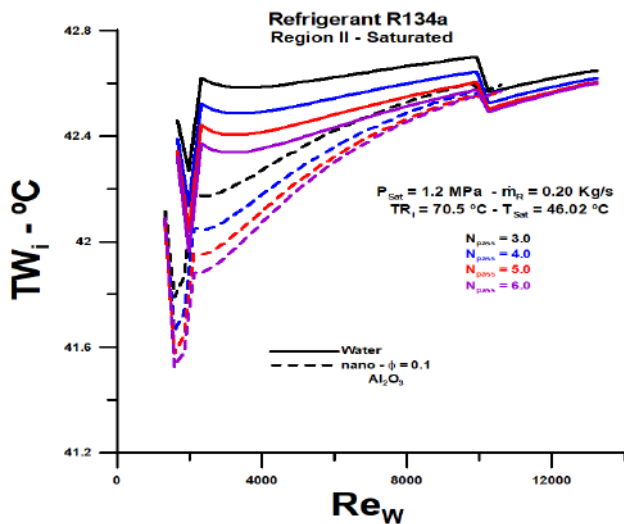


Figure 8 – Influence of the number of passes on the tube on the temperature of entry in Region II

In summary, for Region II:

- 1) the highest inlet temperature is obtained for the lowest flow in the pipe and the lowest number of passes;
- 2) efficiency is high, close to 1.0, regardless of the number of passes in the tube;
- 3) the effectiveness is low for lower flows, and the number of passes equal to 3;
- 4) the effectiveness is rising to values close to 0.8 for a higher flow rate: 0.40 kg/s.

Region II's heat exchange process is efficient, works for lower mass flow rates of the fluid in the tube and fewer passes in the pipe. However, it is not effective; that is, it does not absorb all the available energy.

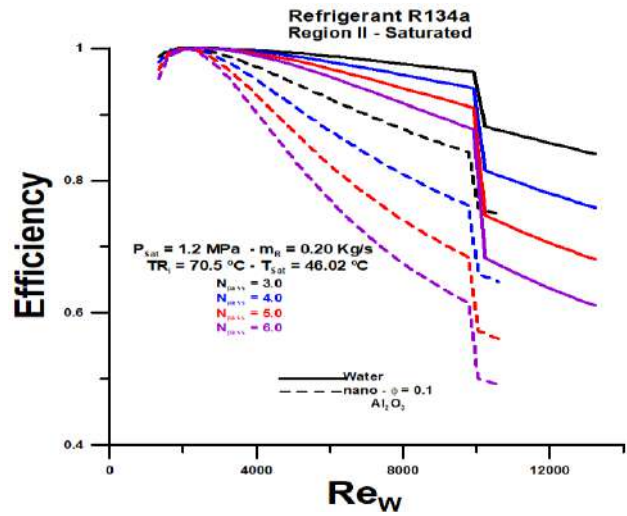


Figure 9 – Influence of the number of passes on the tube on thermal efficiency in Region II

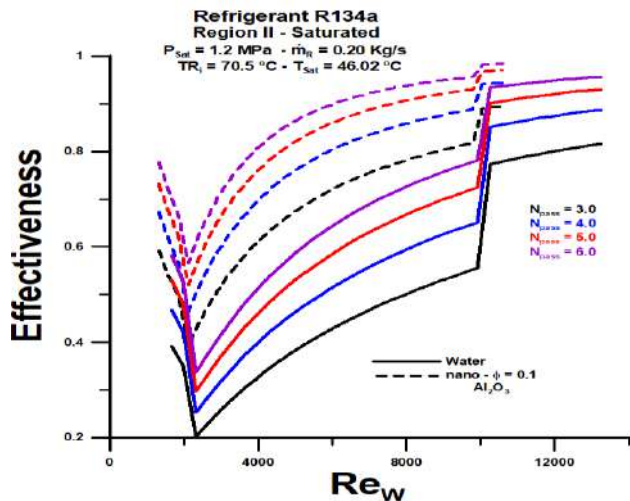


Figure 10 – Influence of the number of passes on the tube on the thermal effectiveness in Region II

4.3 Region III – subcooled liquid

In the region of subcooled liquid of the heat exchanger in question, Region III, already described and represented through Figure 1, three well-defined temperatures are outlet and inlet temperatures in the pipes and inlet temperature refrigerant. The inlet temperature in the pipes is equal to 25.0 °C, and the inlet temperature of the refrigerant is equal to 46.0 °C.

The refrigerant's outlet temperature in Region III is unknown, determined using the methodology described above.

The refrigerant's outlet temperature in Region III, depending on the fluid flow in the tubes, depends on the number of passes in the tube, as represented by Figure 11,

for refrigerant flow equal to 0.20 kg/s. The refrigerant outlet temperature is lower, close to 37 °C, for water flow equal to 0.40 kg/s and the number of passes in the tubes equal to 3. The refrigerant outlet temperature is slightly higher for nanofluids' mass flow rate in the tubes, in all flow rates analyzed. Note that the flow laminarization process, as a function of the fraction of aluminum oxide nanoparticles (Al_2O_3), is observable.

The energy to be absorbed by the refrigerant is defined by the inlet and outlet temperatures and the mass flow rate of the fluid in the tubes. The temperature difference in the refrigerant between the inlet and the outlet is a function of the fluid's thermal capacity in the tubes and the heat exchange area. The fluid with the most significant thermal capacity donates the greatest amount of energy, which allows for a more significant temperature difference for the refrigerant, as represented by Figure 12.

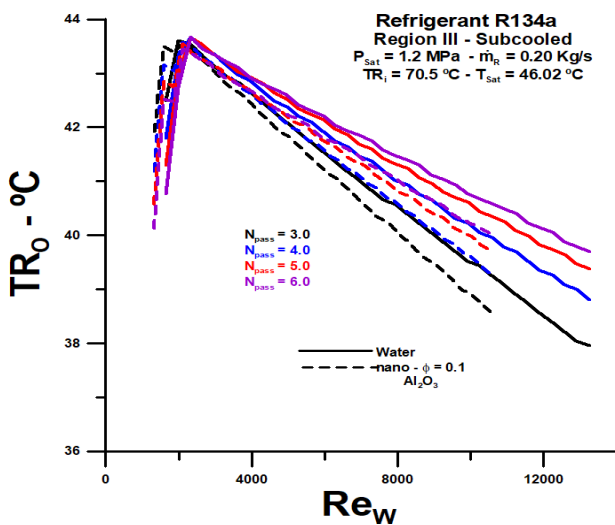


Figure 11 - Influence of the number of passes through the tube on the refrigerant outlet temperature in Region III

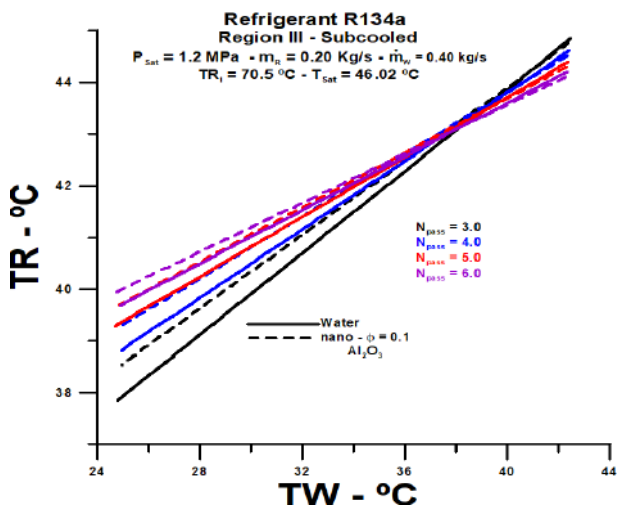


Figure 12 – Influence of the number of passes in the pipe on the temperature of the refrigerant in Region III

When analyzing the heat exchange as a function of the exchange area, depending on the number of passes in the tube, in Region III, it becomes necessary also to consider the overall heat transfer coefficient.

The global heat transfer coefficient is greater for fewer passes in the tube, as shown in Figure 13. It is evident that the smaller number of passes, that is, the smaller heat exchange area, has a greater influence on the global coefficient heat exchange than the most significant temperature difference between inlet and outlet for the refrigerant. Remembering that the available energy is practically the same (Figure 7), depending on the fluid's temperature entering and leaving the tubes.

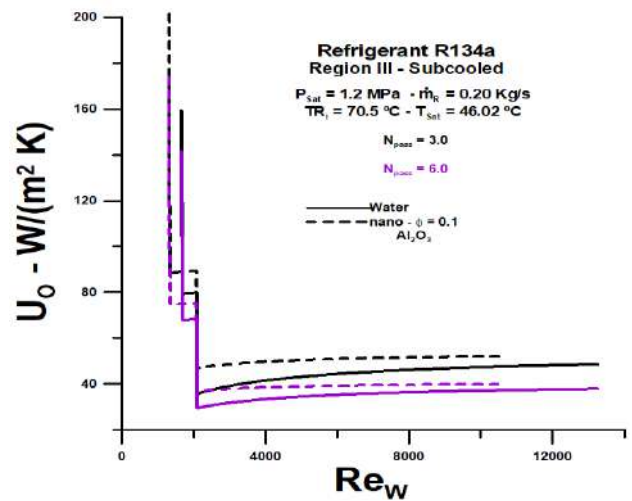


Figure 13 - Global heat transfer coefficient in Region III as a function of the number of passes in the pipe

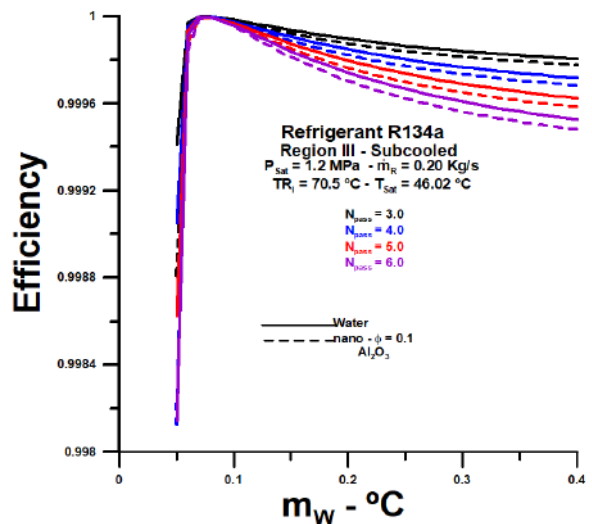


Figure 14 - Influence of the number of passes on the tube on thermal efficiency in Region III

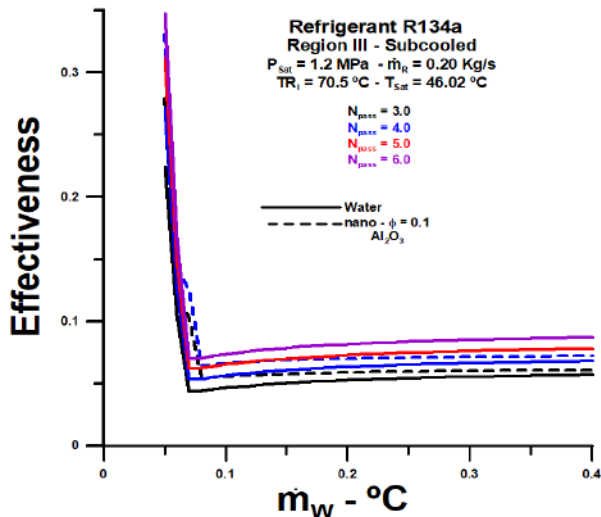


Figure 15 – Influence of the number of passes on the tube on thermal effectiveness in Region III

The thermal efficiency in Region III is exceptionally high, as shown in Figure 14, for the entire range of mass flow and the number of passes in the tube.

The effectiveness is extremely low in Region III, as shown in Figure 15, for the entire range of mass flow in the tube and the number of passes in the tube. It can be observed, in this case, that the effectiveness is slightly higher for a more significant number of passes in the tube and, also, for greater mass flow rates of the fluid in the tube. The heat exchange is shallow, and there is ample scope for increasing effectiveness. However, the fluid inlet temperature in the tube is fixed, equal to 25 °C, and is the limiting factor for greater heat exchange. There are two possibilities to increase the effectiveness in Region III: 1 - decrease the fluid's temperature entering the tube; 2 - increase the refrigerant inlet pressure, increasing the saturation temperature of the refrigerant, thus increasing the temperature difference between fluid outlet and inlet in the tubes.

References

1. Lee, T.-S., and Mai, J.-W. (2011). Modeling and Simulation of the Heat Transfer Behavior of a Shell-and-Tube Condenser for a Moderately High-Temperature Heat Pump. In: Ahsan, A., Ed., *Two-Phase Flow, Phase Change and Numerical Modeling*, InTech, Department of Energy and Refrigerating Air-Conditioning Engineering, National Taipei University of Technology, Chinese Taipei.
2. Nogueira, E. (2020). Theoretical Analysis of a Shell and Tubes Condenser with R134a Working Refrigerant and Water-Based Oxide of Aluminum Nanofluid (Al_2O_3). *Journal of Materials Science and Chemical Engineering*, Vol. 8, pp. 1–22, <https://doi.org/10.4236/msce.2020.811001>.
3. Bejan, A. (1987). The Thermodynamic Design of Heat and Mass Transfer Processes and Devices. *Heat and Fluid Flow*, Vol. 8, pp. 258–276, [https://doi.org/10.1016/0142-727X\(87\)90062-2](https://doi.org/10.1016/0142-727X(87)90062-2).
4. Fakheri, A. (2007). Heat Exchanger Efficiency. *Transactions of the ASME*, Vol. 129, pp. 1268–1276. <https://doi.org/10.1115/1.2739620>.
5. Tiwari, R., Maheshwari, G. (2017). Effectiveness and Efficiency Analysis of Parallel Flow and Counter Flow Heat Exchangers. *IJAIEEM*, Vol. 6, pp. 314–319.
6. Hermes, C.J. L. (2012). Thermodynamic Design of Condensers and Evaporators: Formulation and Applications. *International Refrigeration and Air Conditioning Conference at Purdue*, July 16–19, pp. 1–9.
7. Nogueira, E. (2020) Thermal Performance in Heat Exchangers by the Irreversibility, Effectiveness, and Efficiency Concepts Using Nanofluids. *Journal of Engineering Sciences*, 7, F1-F7.

5 Conclusions

The mass flow rate allows the highest outlet temperature in superheated steam is the lowest possible, equal to 0.05 kg/s.

There is scope for increasing thermal effectiveness in superheated steam. It can be improved with a more significant number of passes in the tube or a change in the inlet temperature of the refrigerant.

The highest inlet temperature for the fluid in the pipe, in the saturated region, is obtained for the lowest flow and the lowest number of passes.

Efficiency in the saturated steam region is 1.0 for a lower flow rate, regardless of the number of passes in the pipe.

The saturated steam region's effectiveness is low for lower flows, rising to values close to 0.8 for a higher flow rate.

The saturated steam region process is efficient for lower mass flow rates of the fluid in the tube but is not effective. However, is highly effective for high mass flow rates.

The thermal efficiency in the subcooled region is exceptionally high for the entire mass flow rate range and passes in the pipe.

The effectiveness is extremely low in the subcooled region for the entire range of mass flow in the tube and the number of passes in the tube.

The subcooled region's effectiveness is slightly higher for a more significant number of passes in the tube and, also, for greater mass flow rates of the fluid in the tube. The heat exchange is shallow, and there is ample scope for increasing effectiveness. The fluid inlet temperature in the pipe equal to 25 °C is one of the limiting factors for greater heat exchange.

Thus, to increase the subcooled region's effectiveness, it is necessary to decrease the fluid's temperature entering the pipe or increase the refrigerant inlet pressure.

8. Nogueira, E. (2020). Efficiency and Effectiveness Concepts Applied in Shell and Tube Heat Exchanger Using Ethylene Glycol-Water Based Fluid in the Shell with Nanoparticles of Copper Oxide (CuO). *Journal of Materials Science and Chemical Engineering*, Vol. 8, pp. 1–12, <https://doi.org/10.4236/msce.2020.88001>.
9. Dalkilic, A. S., Wongwises, S. (2011). *Two-Phase Heat Transfer Coefficients of R134a Condensation in Vertical Downward Flow at High Mass Flux, Heat Transfer - Theoretical Analysis, Experimental Investigations, and Industrial Systems*. In: Prof. Aziz Belmiloudi (Ed.), ISBN: 978-953-307-226-5, InTech, Available from: <http://www.intechopen.com/books/heat-transfer-theoretical-analysis-experimental-investigations-and-industrial-systems/two-phase-heat-transfer-coefficients-of-r134a-condensation-in-vertical-downward-flow-at-high-mass-fl>.
10. Roy, R., and Mandal, B.K. (2014). Computer-Based Thermodynamic Properties of Alternative Refrigerant R-134a. *Engineering Sciences International Research Journal*, Vol. 2, pp. 163–169.
11. Wen, J., Gu, X., Wang, S., Li, Y., Tu, J. (2017). Numerical investigation on condensation heat transfer and pressure drop characteristics of R134a in horizontal flattened tubes. *International Journal of Refrigeration*, <https://doi.org/doi:10.1016/j.ijrefrig.2017.10.024>.
12. Kaew-On, J., Naphattharanun, N., Binmud, R., Wongwises, S. (2016). Condensation heat transfer characteristics of R134a flowing inside mini circular and flattened tubes. *International Journal of Heat and Mass Transfer*, Vol. 102, pp. 86–97, <http://dx.doi.org/10.1016/j.ijheatmasstransfer.2016.05.095>.
13. Albadr, J., Tayal, S., Alasadi, M. (2013). Heat transfer through heat exchanger using Al₂O₃ nanofluid at different concentrations. *Case Studies in Thermal Engineering*, Vol. 1(1), pp. 38–44, <http://dx.doi.org/10.1016/j.csite.2013.08.004>.
14. Almurtaji, S., Ali, N., Teixeira, J. A., Addali, A. (2020). On the Role of Nanofluids in Thermal-Hydraulic Performance of Heat Exchangers – A Review. *Nanomaterials*, Vol. 10, pp. 2–43, <https://doi.org/10.3390/nano10040734>.



Vaneev S. M., Martsinkovskiy V. S., Kulikov A., Miroshnichenko D. V., Bilyk Ya. I., Smolenko D. V., Lazarenko A. D. (2021). Investigation of a turbogenerator based on the vortex expansion machine with a peripheral side channel. *Journal of Engineering Sciences*, Vol. 8(1), pp. F11–F18, doi: 10.21272/jes.2021.8(1).f2

Investigation of a Turbogenerator Based on the Vortex Expansion Machine with a Peripheral Side Channel

Vaneev S. M.^{1*}, Martsynkovskyy V. S.², Kulikov A.³, Miroshnichenko D. V.⁴, Bilyk Ya. I.², Smolenko D. V.¹, Lazarenko A. D.¹

¹ Sumy State University, 2 Rymkogo-Korsakova St., 40007 Sumy, Ukraine;

² TRIZ Ltd., 1, Mashynobudivnykiv St., 40020 Sumy, Ukraine;

³ Technical University of Košice, 31, Šturova St., 080 01 Prešov, Slovakia;

⁴ TOV “NVP “ARMA-T” Ltd., 1, Rymkogo-Korsakova St., 40007 Sumy, Ukraine

Article info:

Received:

February 17, 2021

The final version received:

May 16, 2021

Accepted for publication:

May 21, 2021

*Corresponding email:

s.vaneev@kttf.sumdu.edu.ua

Abstract. The creation of energy-saving turbogenerators is an essential component of the development of small energy systems. The gradual growth of interest in distributed electricity generation necessitates the constant improvement of these units. Moreover, they implement a more environmentally friendly generation method than when using microturbine units that use fuel to carry out the work process. Nowadays, turbogenerators are created based on different types of expansion machines, which have their advantages and disadvantages, given in this article. Compared to competitors, vortex expansion machines have good prospects and the necessary potential to expand their research and produce turbogenerators. An experimental vortex expansion machine with a peripheral-lateral channel and ability to change the geometric parameters of its flowing part was created to meet these needs. Experimental studies of the machine were performed on a special stand with air as a working fluid. As a result of the tests, the data were successfully obtained and processed. They are presented in the form of tables and graphical dependencies. The nature of the influence of thermodynamic parameters and geometric parameters of the flow part on the efficiency of the vortex expansion machine and turbogenerator based on it to further improve and create new turbogenerators is clarified.

Keywords: energy saving turbogenerator, vortex turbine, change of geometrical parameters, utilization, the energy of excess gas pressure.

1 Introduction

The load on energy systems in the modern world only increases with the increasing capacity and number of consumers. It is necessary to generate more and more electricity, which increasingly busy networks must endure. The development of small energy systems can reduce the load on them or even solve this problem.

The efficiency of mini-power plants is relatively high, and there are many types of installations, e.g., mini-CHPs, mini-hydropower plants, geothermal, wind and solar, and heat pump installations.

Such stations are closest to consumers, which minimizes losses on energy transportation, which is why they are considered the future of energy.

2 Literature Review

The electricity needs of large consumers can be met by conventional gas turbines, while micro-turbine plants are increasingly meeting the needs of small and medium-sized consumers. These machines have their power up to 500 kW but can provide power up to 2–3 MW when combined. Microturbine units usually include a compressor, radial turbine, inverter, and recuperator. The efficiency of such plants in the production of electricity is low, but the efficiency is increased significantly in the case of using the cogeneration process and other related systems. The main disadvantage of these plants is the need for fuels such as natural gas, associated petroleum gas, biogas, and alike. There are many schemes for their improvement, but the use of additional resources is costly and not always possible, and in the process of work, in any

case, combustion products are formed, harmful to the environment [1].

A more environmentally friendly way is using turboexpander units in places of gas throttling at gas distribution stations and points in various industrial processes [2–4]. The generation is economically profitable for the development of enterprises and the energy system as a whole, so the topic is essential and relevant [5–7].

There are known examples of the construction of such plants using different types of turbines and related systems. Reciprocating machines are relatively inexpensive but rather bulky, have many moving parts, create significant vibrations, the oil in them comes into contact with the working fluid and needs regular replacement, frequent stops are needed for repairs. Expanders with a rolling piston due to the specific design and internal friction require frequent replacement of parts [8]. At power up to 500 kW, application of vortex expanding machines is possible. As centripetal, axial, and jet-reactive [9], they have a single moving part – the rotor, but lower speeds, which allows gearless execution (for example, with the location of the impeller directly on the generator shaft), providing greater compactness and reliability at lower levels noise. The work [10] is devoted to a turbogenerator based on a screw installation. Compared to it, vortex machines are easier to manufacture and maintain because they use an oil-free working cavity, which significantly simplifies the design, and there are no technologically complex parts such as screws. Prospects for using these energy-saving installations are gradually expanding with the improvement of electronics – increasing the operating time of equipment without human intervention.

Vortex machines have a large variety of flowing parts due to the complex spiral motion of the gas along the length of the flowing part, so they are studied to varying degrees by scientists. For example, turbines with an external peripheral channel are the most studied, and those with a side and peripheral side channel are less studied,

which provides a wide field for further study and improvement.

3 Research Methodology

Employees of TRIZ Ltd. and Sumy State University calculated according to the existing method of calculating vortex expansion machines and then designed and manufactured a turbine with a peripheral side channel (Figure 1). Its design is made two-channel four-stream and involves changing the geometric parameters of the machine. In addition, experimental tests were performed on an air stand (Figure 2) and involved changing the geometric parameters of the flow part of the turbine (Figure 3).

The schematic diagram of the stand is shown in Figure 4.

The studied turbogenerator consists of a vortex expansion machine and an electric generator connected to each other fearlessly through a coupling. An electric motor with a capacity of 10 kW is used as an electric generator. The purpose of the vortex expansion machine is to convert the energy of excess gas pressure by expanding it in the flowing part of the turbine to obtain mechanical work on the machine's shaft.

The working fluid is fed to the vortex turbine via a pipeline from the compressor. Once in the turbine, the flow of gas through the nozzle moves to the flow part, which is formed by the channel of the housing and the interscapular channels of the impeller. The movement of gas particles in these channels is accompanied by a change in the direction and magnitude of the speed, the moment of movement, as a result of which forces appear on the blades, which ensure the rotation of the impeller. Finally, the gas is discharged from the flowing part through the housing and the pipe into the atmosphere. Between the nozzle and the outlet, a cutter is used.

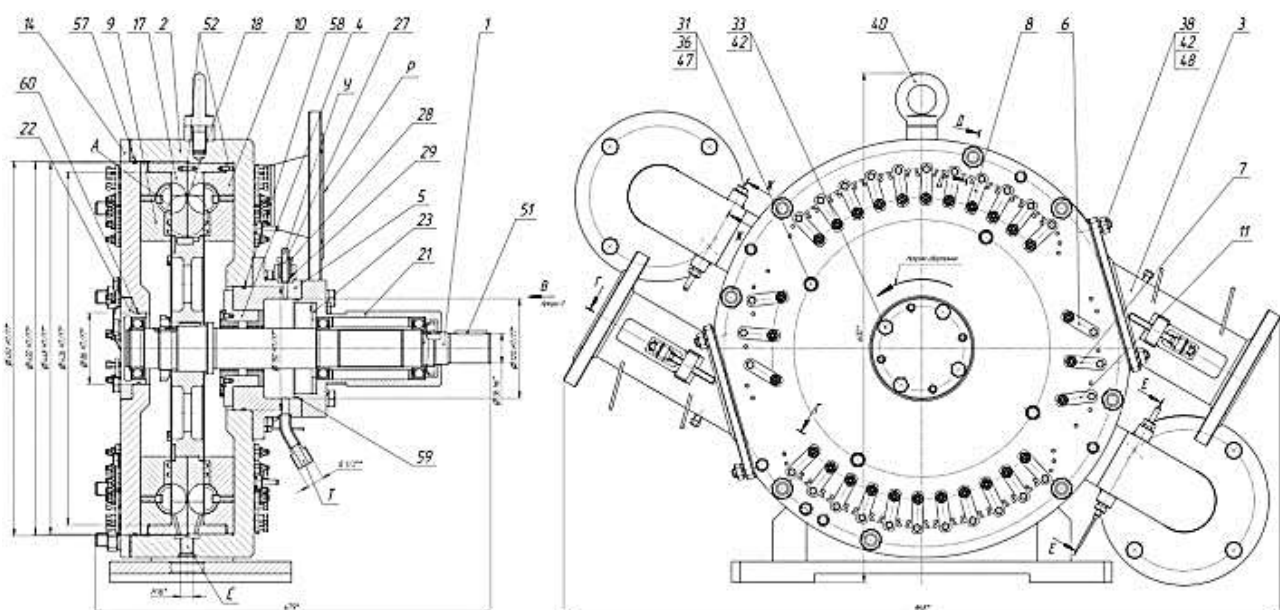


Figure 1 – Turbine drawing



Figure 2 – General view of the turbogenerator on the experimental stand

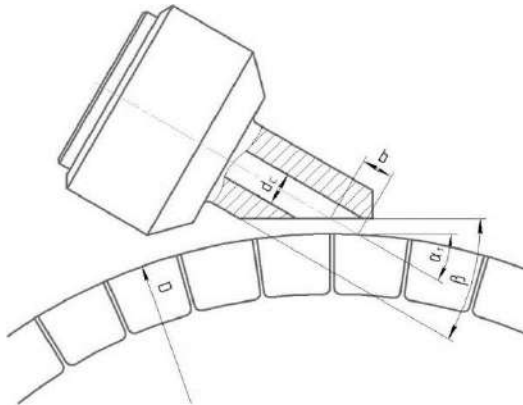


Figure 3 – Main geometric parameters of the flowing part of the machine

During the tests, the pressure at the inlet and outlet of the turbine and the rotor speed changed. Excess pressure at the inlet to the turbine varied from 1 to 5 kg/cm², the pressure at the outlet of the turbine was equal to atmospheric pressure, and, for some modes, was set equal to 1.85 kg/cm², the turbine rotor speed was up to 3000 rpm.

Different geometrical parameters significantly impact the efficiency of energy transfer from the gas flow to the impeller blades. During the research of this turbine, the angle of inclination of the nozzles α_1 , the angle of cut of the nozzles β , and the distance from the nozzles to the blades of the impeller b changed (Figure 3). The primary geometric parameters of the turbine flow are shown in Figure 3, and the change of parameters during testing of the machine is shown in Table 1. Radial gas supply to the impeller is used with an outer diameter $D = 370$ mm with a solid separator and flowing part without guide vanes.

A total of 147 tests were performed: with excess pressure at the inlet $p_{in} = 1; 2; 3; 4; 5$ kg/cm² and at the outlet $- p_{out} = 0; 1.85$ kg/cm² at rotor speeds n from 0 to 3000 rpm in increments of 500 rpm.

Table 1 – Change of the geometric parameters of the flow part of the vortex turbine

Nozzle angle $\alpha_1, ^\circ$	Nozzle cut angle $\beta, ^\circ$	Distance from nozzles to impeller b, mm
30	30	1
30	30	5
30	30	10
30	30	15
45	45	1
45	45	5
45	45	10
45	45	15
60	60	1

During the tests on the stand, the control of necessary parameters is provided: gas pressure before the diaphragm, pressure at the inlet to the turbine and in its case, pressure at the turbine outlet, gas temperatures behind the diaphragm and at the turbine inlet, diaphragm pressure drop, rotor speed and torque on the dynamometer shaft. An electric generator is used as a dynamometer. The stator is embedded in the bearing racks, considering the possibility of rocking. Its movement is transmitted to the dial of the scales through a lever balanced by a counterweight. A complete list of measured parameters and devices is given in Table 2.

4 Results and Discussion

The test results are shown graphically in Figures 5-12. The efficiency of the vortex machine is determined by considering the mechanical losses in the generator, including losses on the fan, i.e., in practice - this is the efficiency of the turbogenerator. When estimating the efficiency of the vortex turbine, these losses are not considered, so the resulting efficiency of the turbine will be higher.

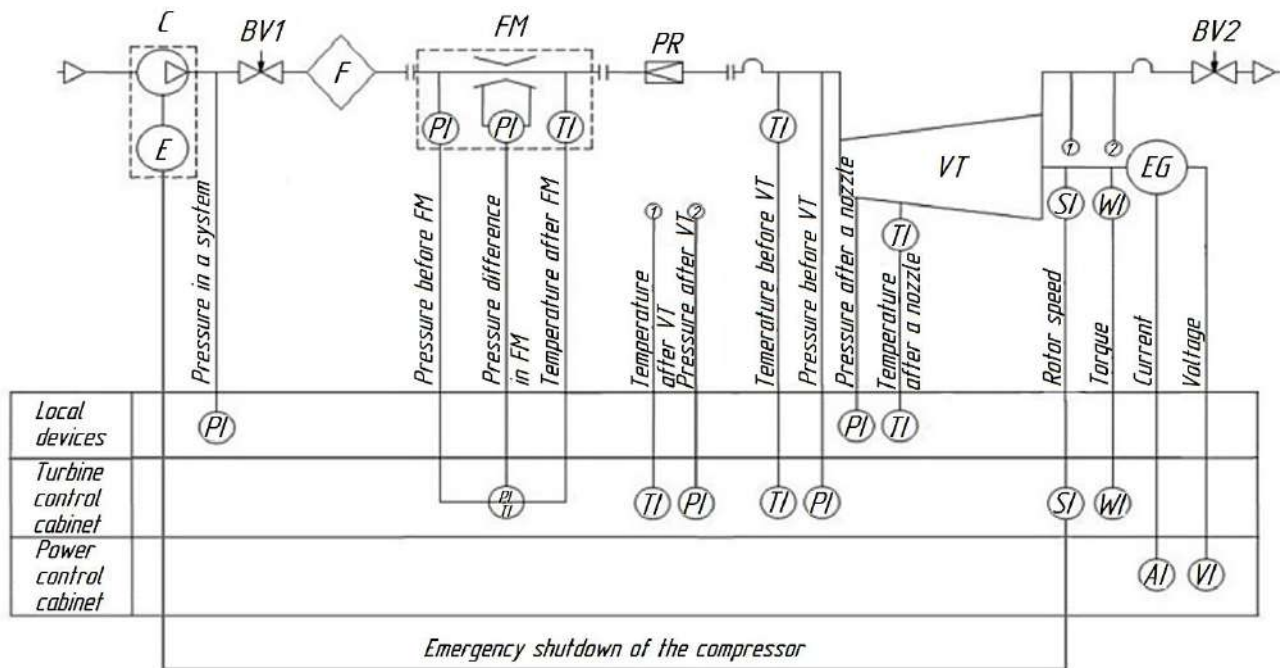


Figure 4 – Schematic diagram of the stand: E – engine; C – compressor; VT – vortex turbine; EG – electric generator; PR – pressure regulator; BV1, BV2 – ball valves; FM – flow meter; F – filter; FI – flow meter display unit; PI – manometer unit; TI – thermometer; SI – tachometer unit; WI – torque display unit; AI – amperemeter; VI – voltmeter

Table 2 – The list of measured parameters and control-measuring devices used for their measurement

Marking on the diagram	Functional purpose	Device name	Device type(s)	Measure range	Accuracy class	Quality class
PI-01	Network pressure	Manometer	MTI	0 – 10 kgf/cm ²	0.6	10
PI-03	Outlet pressure					
PI-10	Inlet pressure					
PI-11	After-nozzle pressure					
PI-14–PI-19	Pressure distribution on the flow part					
FI-06	Air consumption	Flow-meter	PM1	0 – 30 nm ³ /min	4.0	1
TE-08, TI-02	Inlet temperature	Electronic thermometer (temperature sensor and display unit)	TCM-101; II-TC	–40 – +180 °C	0.5	3
TE-12, TI-09	After-nozzle temperature					
TE-22, TI-13	Outlet temperature					
WE-23, WI-24	Torque	Scales	CAS AP-15M	0–15 kgf	0.1	1

Figure 5 shows the dependence of power on the turbogenerator shaft from the shaft speed and the pressure at the inlet to the turbine (nozzle angle $\alpha_1 = 30^\circ$, nozzle cut angle $\beta = 30^\circ$, distance from nozzles to the impeller $b = 1$ mm).

For the pressure at the inlet to the turbine of 6 kg/cm², (absolute) graphical dependencies are given at the degrees of pressure reduction in the turbine $\Pi = 2$, and $\Pi = 6$. It is seen that up to 2000 rpm power increases almost directly in proportion to the shaft speed.

Figure 6 shows the dependences of the turbogenerator efficiency on the shaft speed and angle α_1 (Figure 3) at different values of the degree of pressure drop in the turbine. It is seen that when the speed of the turbogenerator shaft is more than 2000 rpm in all cases, the efficiency at $\beta = 30^\circ$ is greater than in variants with other angles. As the shaft speed increases, the efficiency increases.

Figure 7 presents the dependences of the efficiency of the turbogenerator on the angle α_1 at different values of the shaft speed and the degree of pressure drop in the turbine. Increasing the angle α_1 in the study range and decreasing the shaft speed causes a decrease in efficiency.

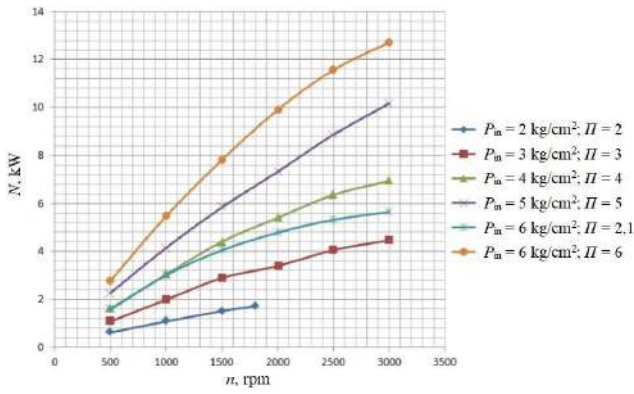


Figure 5 – Dependence of turbogenerator power on rotor speed

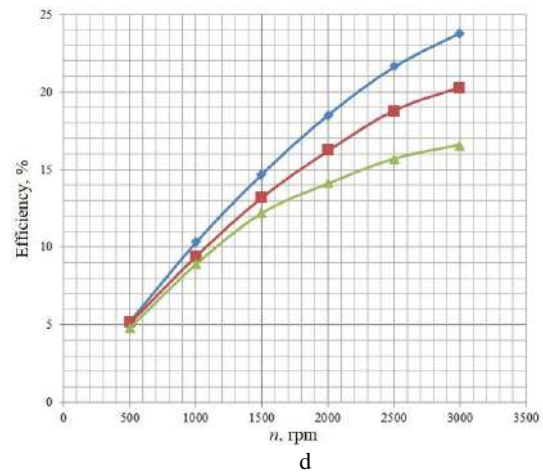
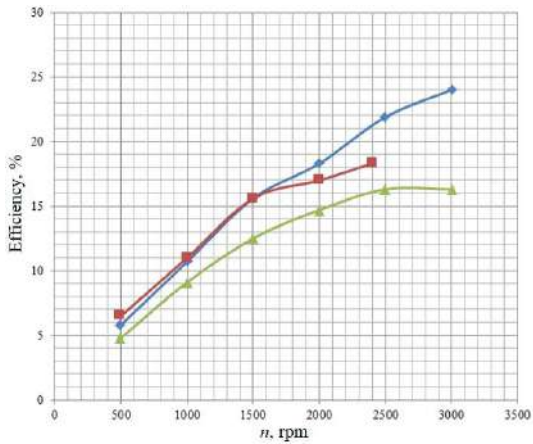
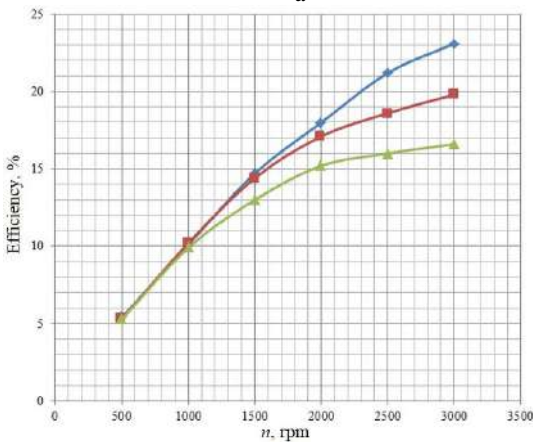


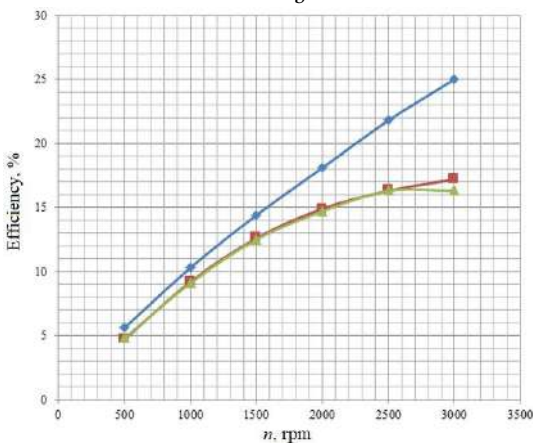
Figure 6 – Dependence of turbogenerator efficiency on rotor speed at different values of the degree of pressure drop in the turbine: a) $\Pi = 3$; b) $\Pi = 4$; c) $\Pi = 5$; d) $\Pi = 6$



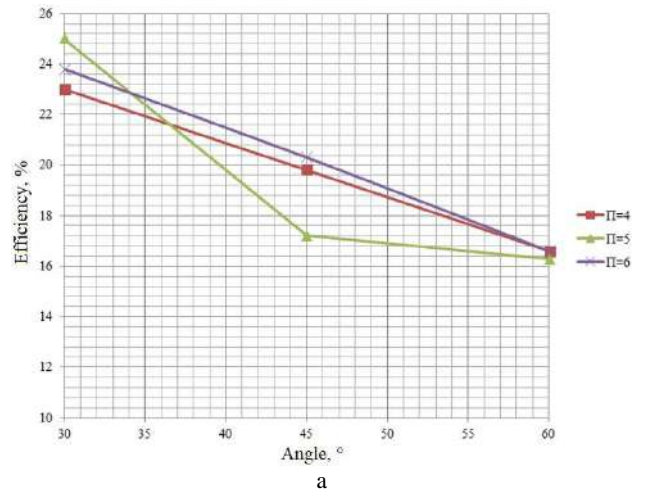
a



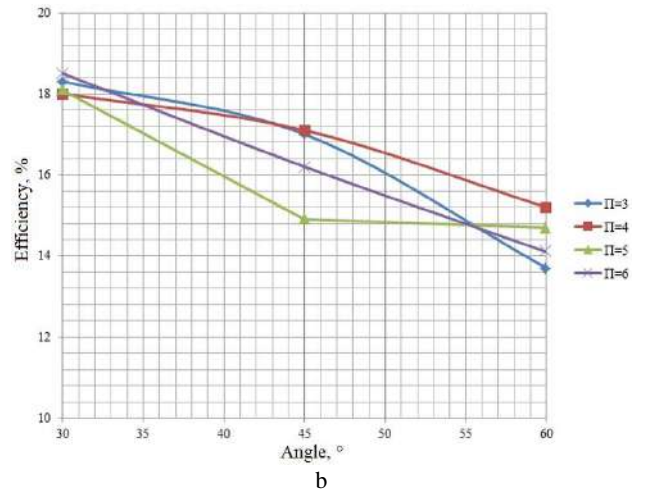
b



c



a



b

Figure 7 – Dependence of efficiency on the angle of the nozzles α_1 at different values of the speed of the turbogenerator shaft: a) 3000 rpm; b) 2000 rpm

Figure 8 shows the dependences of the efficiency of the turbogenerator on the shaft speed, the gas pressure at the inlet to the turbine, and the degree of pressure drop in it at different values of the angle α_1 . It is seen that at the gas pressure at the inlet to the turbine in the range of

3–6 kg / cm² (2–5 kg/cm² excess pressure) for specific values of the speed of the turbogenerator shaft efficiency differs by no more than 3 % and increases with increasing shaft speed.

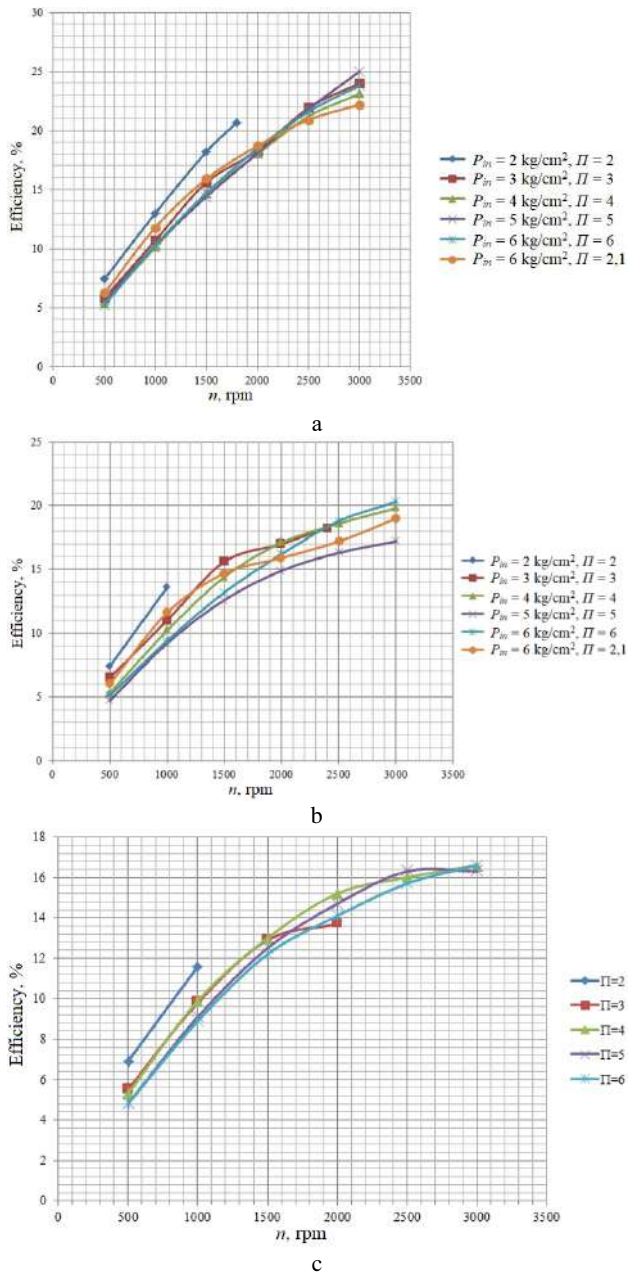


Figure 8 – Dependence of efficiency on rotor speed at different values of angle α_1 : a) $\alpha_1 = 30^\circ$; b) $\alpha_1 = 45^\circ$; c) $\alpha_1 = 60^\circ$

In the theory and practice of turbomachines, the dimensionless complex of the specific circumferential speed of the impeller is essential and widely used, as well as the dependence of the efficiency of the turbomachine on this complex. Moreover, it characterizes the load of the turbine, linking together the parameters that reflect the physical properties of the working fluid and the state of gas flow at the inlet and outlet of the turbine, with the design values and speed of the turbine shaft:

$$\bar{U} = \frac{U}{C_s} = \frac{\pi \cdot D \cdot n}{60 \cdot C_s} \quad (1)$$

where D – outer diameter of the impeller, m; n – impeller speed, rpm; C_s – isentropic gas velocity, that characterizes the available specific work of the expansion machine, m/s:

$$C_s = \sqrt{2h_s} = \sqrt{\frac{2k}{k-1} T_{in}^* R \left(1 - \Pi^{\frac{1-k}{k}}\right)}, \quad (2)$$

where h_s – specific isentropic difference of enthalpies (available specific work of the expansion machine), J/kg; k – an indicator of the isentropy of the working fluid; R – specific gas constant, J/(kg·K); T_{in}^* – gas flow total temperature at the inlet of the machine, K; Π – degree of pressure drop in the expansion machine.

Figure 9 shows the dependences of the efficiency of the turbogenerator on the specific circumferential speed of the impeller and the degree of pressure drop in the turbine (angle of the nozzles $\alpha_1 = 30^\circ$; the angle of the nozzles $\beta = 30^\circ$; the distance from the nozzles to the impeller $b = 1$ mm).

The most significant values of the efficiency of the vortex turbine with a peripheral side channel during the tests correspond to the values of the specific circumferential speed from 0.080 to 0.142. The maximum value of efficiency = 0,25 is received at the specific circumferential speed of 0.12. It is seen that in the whole studied range of the degree of pressure reduction in the turbine for specific values of the specific circumferential speed of the impeller, the efficiency differs by no more than 3 %. Given the upward nature of the graphical dependence of efficiency, it is expected to obtain higher values in the area not included in this study.

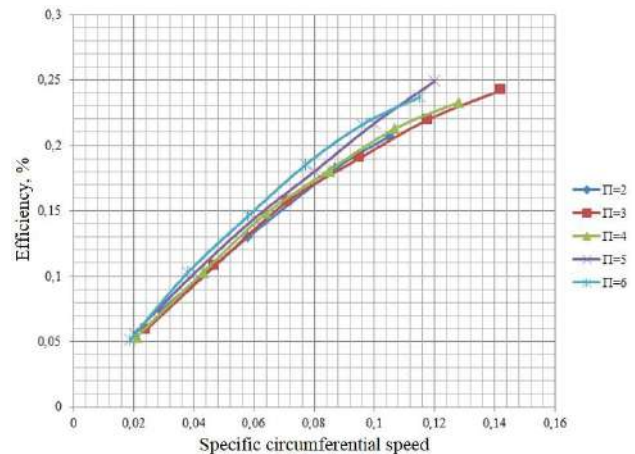


Figure 9 – Dependence of turbogenerator efficiency on the specific circumferential speed of the impeller

The influence of the distance from the nozzles to the impeller b on the power on the turbogenerator shaft for excess pressure at the turbine inlet 5.0 kg/cm² and 1.85 kg/cm² at the outlet (for a pressure ratio of 2.1) is shown in Figures 10–11 (nozzle angle $\alpha_1 = 30^\circ$; nozzle cut angle $\beta = 30^\circ$). Analysis of graphical dependences shows that the distance from the nozzle cut to the impeller blades has little effect on the power of the turbogenerator, especially in the range $b = 1$ –5 mm.

Since the gas flow rate does not depend on the distance of the nozzle cut to the impeller blades, the dependences of the efficiency on the shaft speed and the distance b are identical to the dependences for power (Figure 12).

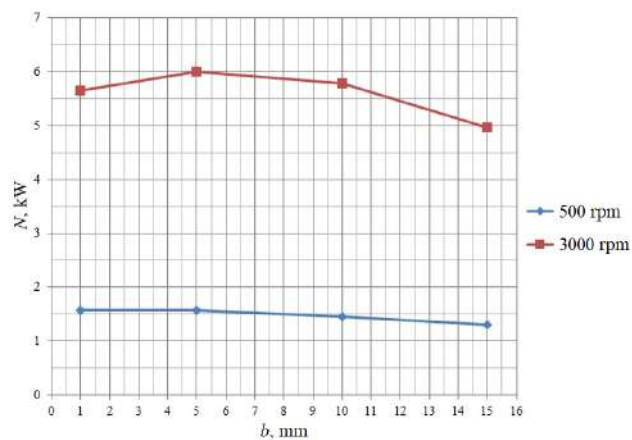


Figure 10 – Dependence of turbogenerator power on the distance from the nozzles to the impeller

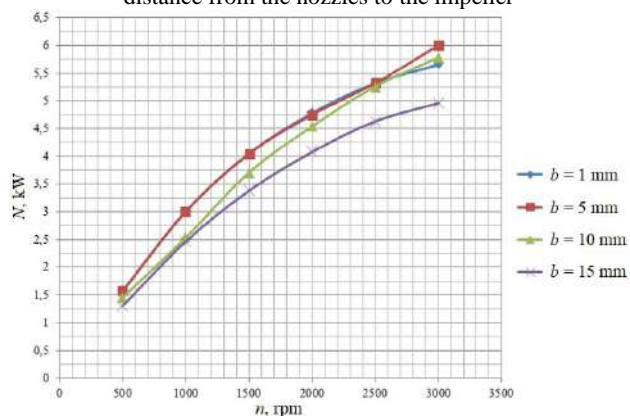


Figure 11 – Dependence of turbogenerator power on the speed at a variable distance from nozzles to the impeller

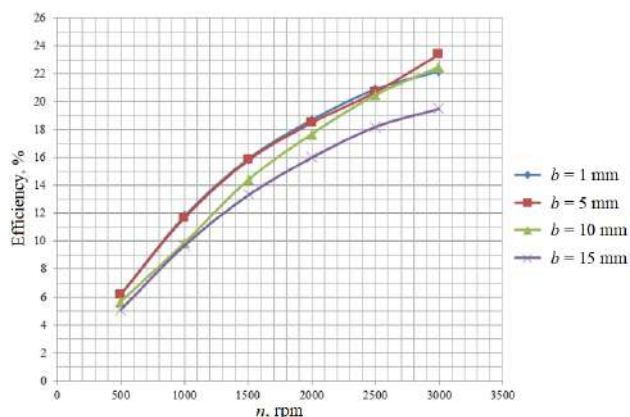


Figure 12 – Dependence of efficiency of the turbogenerator on the frequency of rotation at a variable distance from nozzles to an impeller

5 Conclusions

Experimental tests of a vortex expansion machine with a peripheral side channel and a turbogenerator based on it were carried out on a research stand. The information-measuring system allowed to record of the parameters during the tests with sufficient accuracy. The obtained experimental data are processed and presented in the form of tables and figures.

The experiment showed that the power of the turbine increases almost in direct proportion to the speed of its rotor. Consequently, the efficiency of the turbine also increases with increasing rotor speed.

The highest values of the efficiency of the turbogenerator based on a vortex turbine with a peripheral side channel during the tests correspond to the values of the specific circular speed from 0.080 to 0.142 and increase throughout the interval. Thus, the maximum value of efficiency (25 %) is obtained at the value of the specific circumferential speed of 0.12. Given the ascending nature of this dependence, it is expected to obtain its higher values in the area not covered by this experiment.

It has been found that the angle of the nozzles significantly affects the efficiency of the vortex machine. At the angle $\alpha_1 = 30^\circ$ and speeds greater than 2000 rpm in all cases, the highest efficiency is obtained. An increase in the angle α_1 in the studied range causes a decrease in efficiency.

The nature of the influence of the distance from the nozzle cut to the turbine impeller has been studied. Experimental studies have shown that this distance has little effect on the power and efficiency of the turbogenerator, especially in the range $b = 1-5$ mm.

The obtained research results can be used to design vortex expansion machines with a peripheral side channel and turbogenerators based on them, to continue their improvement and comparison with machines of other types.

References

1. James, J. A., Thomas, V. M., Pandit, A., Li D., Crittenden, J. C. (2016). Water, Air Emissions, and Cost Impacts of Air-Cooled Microturbines for Combined Cooling, Heating, and Power Systems: A Case Study in the Atlanta Region. *Engineering*, Vol. 2(4), pp. 470–480, doi: 10.1016/J.ENG.2016.04.008.
2. Kim, H., You, H., Choi, K-S. Han S (2020). A Study on Interconnecting to the Power Grid of New Energy Using the Natural Gas Pressure. *Journal of Electrical Engineering and Technology*, Vol. 15, pp. 307–314, doi: 10.1007/s42835-019-00324-5.
3. Arabkoohsar, A., Farzaneh-Gord, M., Deymi-Dashtebayaz, M., Machado, L., Koury, R. N. N. (2015). A new design for natural gas pressure reduction points by employing a turbo expander and a solar heating set. *Renewable Energy*, Vol. 81, pp. 239–250, doi: 10.1016/j.renene.2015.03.043.
4. Pajączek, K., Kostowski, W., Stanek, W., (2020). Natural gas liquefaction using the high-pressure potential in the gas transmission system. *Energy*, Vol. 202, 117726, doi: 10.1016/j.energy.2020.117726.
5. Kuczyński, S., Łaciak, M., Olijnyk, A., Szurlej, A., Wlodek, T. (2019). Techno-Economic Assessment of Turboexpander Application at Natural Gas Regulation Stations. *Energies*, Vol. 12(4), 755, doi: 10.3390/en12040755.
6. Seresht, R. T., Ja, H. K. (2010). Retrofit of Tehran City Gate Station (C.G.S. No. 2) by Using Turboexpander. *ASME 2010 Power Conference*. Chicago, Illinois, USA. pp. 207–212, doi: 10.1115/POWER2010-27087.
7. Ardali, E. K., Heybatian, E. (2009). Energy regeneration in natural gas pressure reduction stations by use of gas turbo expander; Evaluation of available potential in Iran. *Proceedings 24th World Gas Conference*, pp. 5–9.
8. Kolański, P., Pomorski, M., Błasiak, P., Rak, J. (2017). Use of Rolling Piston Expanders for Energy Regeneration in Natural Gas Pressure Reduction Stations – Selected Thermodynamic Issues. *Applied Sciences*, Vol 7(6), pp. 1–17, doi: 10.3390/app70605354.
9. Vaneev, S., Rodymchenko, T., Melechuk, S., Baga, V., Bolotnikova, O. (2021). Influence of the degree of off-design of the traction nozzle of a jet reaction turbine on its efficiency. *Journal of Physics: Conference Series*, Vol. 1741, 012004, doi: 10.1088/1742-6596/1741/1/012004.
10. Li, G., Wu, Y., Zhang, Y., Zhi, R., Wang, J., Ma, C. (2016). Performance Study on a Single-Screw Expander for a Small-Scale Pressure Recovery System. *Energies*, Vol 10(1), 6, doi: 10.3390/en10010006.



Hu W. J., Tan K., Markovych S., Liu X. L. (2021). Study of a cold spray nozzle throat on acceleration characteristics via CFD. *Journal of Engineering Sciences*, Vol. 8(1), pp. F19–F24, doi: 10.21272/jes.2021.8(1).f3

Study of a Cold Spray Nozzle Throat on Acceleration Characteristics via CFD

Hu W. J.^{1,2}, Tan K.¹, Markovych S.¹, Liu X. L.²

¹National Aerospace University “Kharkiv Aviation Institute”, 17, Chkalova St., 61000 Kharkiv, Ukraine;

²School of Aeronautics and Astronautics, Nanchang Institute of Technology, Nanchang, China

Article info:

Received:

February 13, 2021

The final version received:

May 26, 2021

Accepted for publication:

May 29, 2021

*Corresponding email:

837406613@qq.com

Abstract. Cold spray technology can obtain coatings in a solid state, suitable for deposition protection, repair, and additive manufacturing. In order to further expand the application areas of cold spraying nozzles, especially the inner surface of the components or areas where a Straight-line conical nozzle cannot be applied, because the study of the throat of the nozzle with the angle will directly reduce the total length of the nozzle (the horizontal direction), hence, the spray with the angle will show its advantage. This study discusses the influence of the throat structure of the conical cold spray nozzle on the acceleration characteristics, including the throat’s size, length, and angle. The results show the following. Firstly, under the premise of keeping the shrinkage ratio and divergence ratio unchanged at normal temperature, the throat diameter is between 2–6 mm in size, and the maximum growth rate exceeds 20 m/s. When the throat exceeds 6mm, the growth rate of the outlet slows down, and the growth rate is only 8 m/s. Secondly, the length of the throat has little effect on the acceleration characteristics, the total range fluctuated from 533 to 550 m/s, and 11 mm length of the throat is the closest to 0mm. Additionally, the 90° throat angle has the least effect on the acceleration characteristics. Finally, the particle trajectory is affected by inlet pressure, injection pressure, particle size, and other factors.

Keywords: cold spray technology, nozzle, acceleration characteristics, particle trajectory.

1 Introduction

Cold spraying technology [1] is an emerging technology. Based on the theory of aerodynamics and fluid mechanics, it produces a process of high-speed collision with substrate and formation of a coating, which is mainly applied for surface repair and protection of coating, or additive manufacturing applications [2, 3]. The cold spray nozzle has essential significance for particle acceleration, and throat structure is the key link in the whole nozzle structure.

In the current study, cold spray nozzle structures are linear conical nozzles or straight pipe ladder nozzles, for example, in order to facilitate the spraying of the inner surface of the part, Li [4] studied a nozzle with a total length of less than 70 mm, but many components require a smaller size on the inside surface to be sprayed. Wu [5] added a straight pipe with the same diameter as the outlet at the nozzle outlet to prevent the powder from dispersing, but this nozzle is more suitable for external surface spraying. In order to facilitate the processing and manufacturing, some nozzles processed the expansion section into a straight pipe ladder type. It can effectively

spray aluminum, and zinc powder [6], the expansion section of this nozzle is generally longer, so it is more used for external surface spraying. If it is necessary to spray the inner surface of the component or areas where a linear nozzle cannot be applied, spray with the angle will show its advantage. Thus the application of the nozzle is further expanded. However, the throat structure with an angle has rarely been studied.

Hence, this present study aimed to research the nozzle with angles and facilitate spraying in a specific space, e.g., the inner surface repair of components or the straight-line nozzle can not reach the place to spray.

2 Research Methodology

The following formula determines the initial model (Figure 1), then three-dimensional modeling, boundary condition setting, and numerical simulation are carried out to study the influence of nozzle throat on the acceleration characteristics.

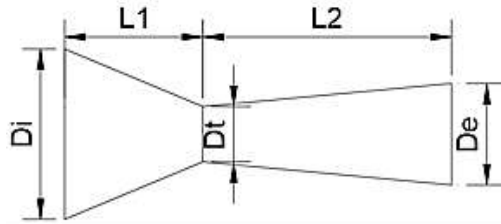


Figure 1 – Initial model

The typical calculation technics is based on the following equations:

$$C = \sqrt{\gamma RT} ; \quad (1)$$

$$Ma = \frac{V}{C} ; \quad (2)$$

$$Ma = \sqrt{\frac{2}{\gamma-1} \left[\left(\frac{P_i}{P_e} \right)^{\frac{\gamma-1}{\gamma}} - 1 \right]} ; \quad (3)$$

$$\frac{A_e}{A_i} = \left(\frac{1}{Ma} \right) \left[\left(\frac{2}{\gamma+1} \right) \left(1 + \frac{\gamma-1}{2} Ma^2 \right) \right]^{(\gamma+1)/(2(\gamma-1))} ; \quad (4)$$

$$C_p = \frac{\gamma R}{\gamma-1} ; \quad (5)$$

$$T_T = T_i + \frac{V_i^2}{2C_p} ; \quad (6)$$

$$p_T = P_i \left(\frac{T_T}{T_i} \right)^{\frac{\gamma}{\gamma-1}} ; \quad (7)$$

$$\rho_T = \frac{P_T}{RT_T} ; \quad (8)$$

$$q_{mcr} = A_i \left(\frac{2}{\gamma+1} \right)^{\frac{\gamma+1}{2(\gamma-1)}} (r p_T \rho_T)^{\frac{1}{2}} ; \quad (9)$$

$$A_i = \frac{q_{mcr}}{\rho_i V_i} \quad (10)$$

$$L_1 = \left(\frac{D_i - D_t}{2} \right) \cot \left(\frac{\alpha}{2} \right) ; \quad (11)$$

$$L_2 = \left(\frac{D_e - D_t}{2} \right) \cot \left(\frac{\beta}{2} \right) ; \quad (12)$$

where C – the ideal speed of sound; γ – is the specific heat ratio of gas; R – the gas constant; T – the ambient temperature; Ma – the Mach number; P_i – the inlet pressure; P_t – the throat pressure; $P_e = 1.01 \cdot 10^5$ Pa – the outlet pressure; q_{mcr} – the mass flow rate, P_T – the stopping pressure; $V_i = 30$ m/s – velocity; ρ_T – the stopping density, T_T – the stopping temperature; C_p – the specific heat capacity of constant pressure.

According to the calculation, the contraction ratio is about 3.0; the divergence ratio is about 1.84; $D_i = 12.3$ mm. According to the empirical value [7, 8], the angle of the contraction section $\alpha = 30$ – 60° , and the angle of the diffusion section $\beta = 0$ – 12° . According to formulas (11) and (12), $L_1 = 7.2$ – 15.5 mm, and $L_2 \geq 17.8$ mm can be obtained for the length of the conical cold spray nozzle's diffusion section. Literature shows that the longer the diffusion section is, the faster the acceleration effect is [7]. Hence, $L_1 = 10$ mm, and $L_2 = 60$ mm are taken. Similarly, all parameters are shown in Table 1.

Table 1 – Cold spray nozzle parameters

Parameter	Values, mm							
D_i	6	9	12	15	18	21	24	27
D_t	2	3	4	5	6	7	8	9
D_e	3.7	5.5	7.4	9.2	11.0	12.9	14.7	16.6
L_1	10							
L_2	60							

3 Results and Discussion

3.1 The influence of throat structures

The one-dimensional isentropic analytical model is a convenient tool for roughly estimating the flow characteristics inside a cold spraying nozzle, but the accuracy of predicting the flow and particle velocity outside the nozzle cannot be guaranteed. With the rapid development of computer technology, the computational fluid dynamics (CFD) model has attracted more and more attention due to its high prediction accuracy and feasibility of simulating different situations [9].

The numerical simulation results are presented in Figure 2.

As shown in Figure 2, the maximum growth rate is more than 20m/s between 2–6 mm. When the throat exceeds

6mm, the growth rate of the outlet slows down, and the growth rate is only 8–10 m/s. Therefore, the throat diameter was determined to be 6 mm.

Further study the throat length factor, the effect of throat length on acceleration characteristics was studied with the throat length is 1–15 mm (odd), respectively. Numerical results show that the throat length has little influence on the acceleration characteristic (Figure 3 a). The overall range fluctuates from 533 to 550 m/s. Simultaneously, the temperature has a positive influence on the acceleration characteristic (Figure 3 b).

Finally, in order to facilitate the analysis of nozzle throat angle, the throat length size of 11 mm was selected. The effects of throat angles of 90° , 60° , and 45° on the acceleration characteristics were studied. The results show that the angle of 90° has an advantage on acceleration characteristics (Figure 3 c).

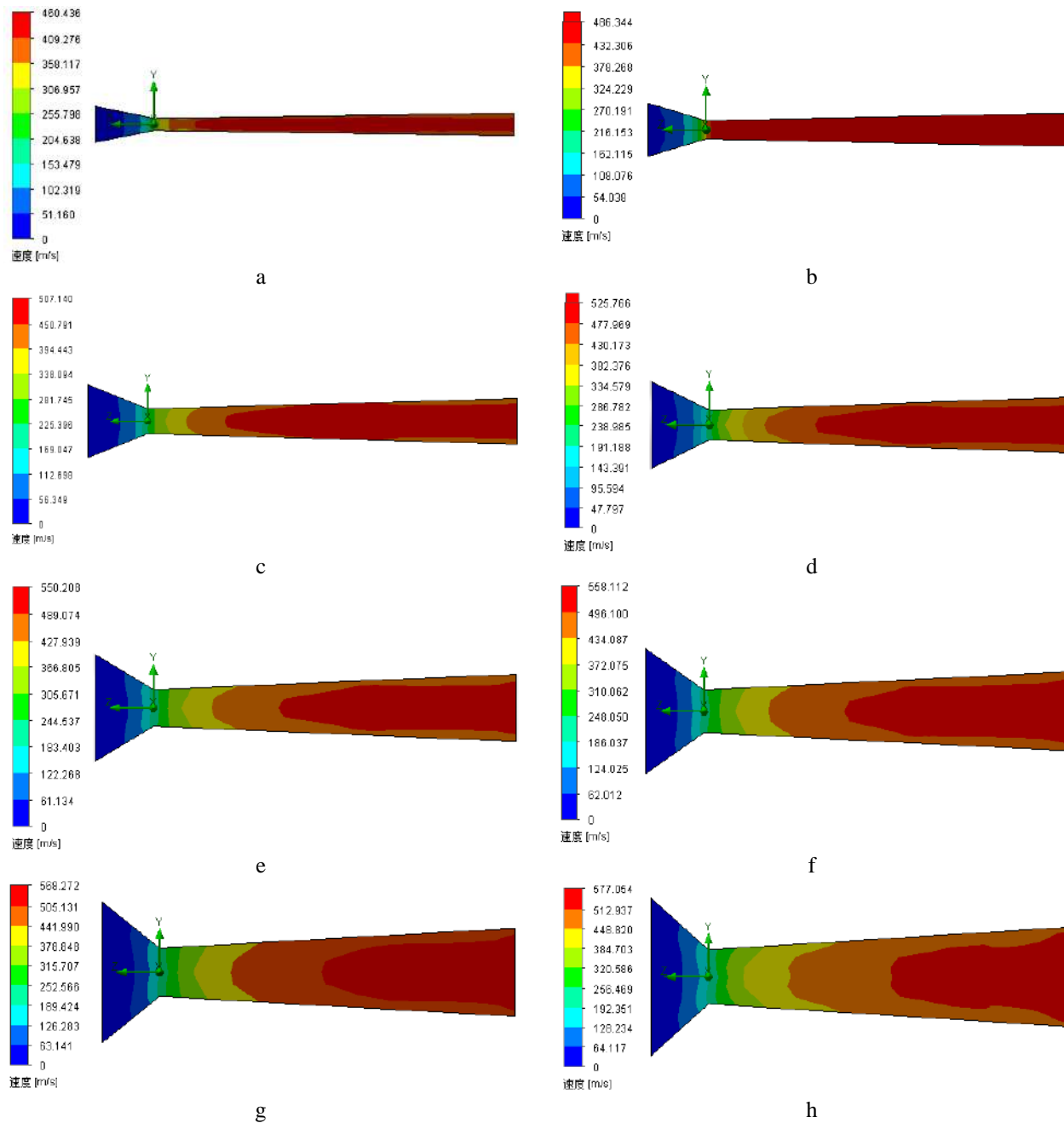
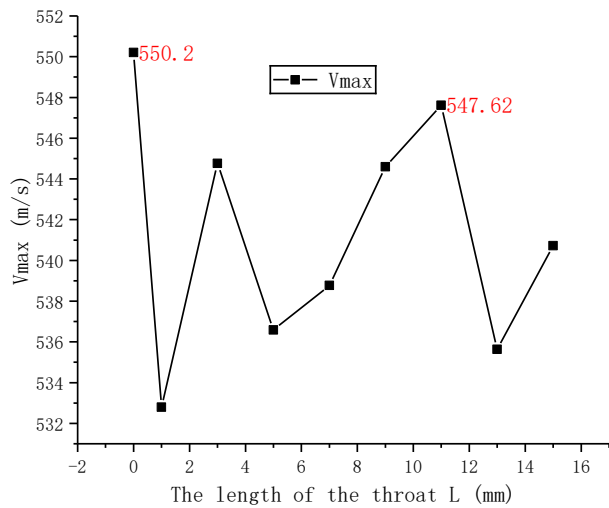


Figure 2 – Nozzles with different diameters of throat: a) 2 mm, $V_{max} = 460$ m/s; b) 3 mm, $V_{max} = 486$ m/s; c) 4 mm, $V_{max} = 507$ m/s; d) 5 mm, $V_{max} = 526$ m/s; e) 6 mm, $V_{max} = 550$ m/s; f) 7 mm, $V_{max} = 558$ m/s ; g) 8 mm, $V_{max} = 568$ m/s; h) 9 mm, $V_{max} = 577$ m/s

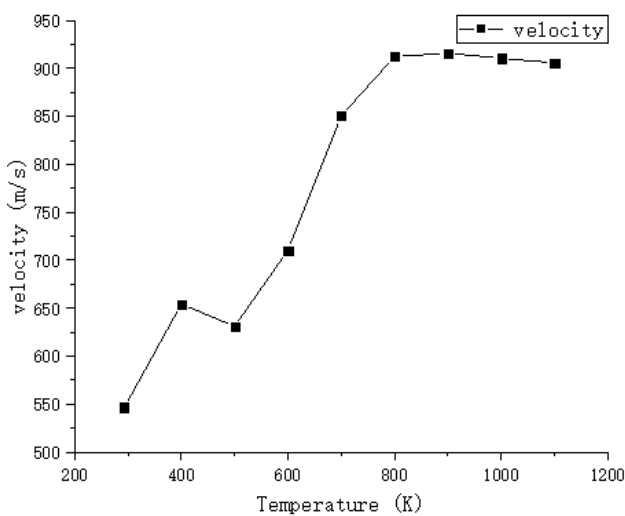
In this study, the 60 mm length of L_2 is selected. If it is necessary to spray in a specific small area, L_2 can be shortened to the required size. Based on this, the structure can be further optimized according to the actual application situation. Although the main factors affecting the impact velocity of powder include propelling gas, particle characteristics, spraying distance, and length of expansion section [10], the throat structure directly affects the acceleration characteristics of the fluid. Sequentially, it affects the deposition characteristics of powder, and the Computational Fluid Dynamics (CFD) method can give researchers a good reference.

3.2 Particle trajectories

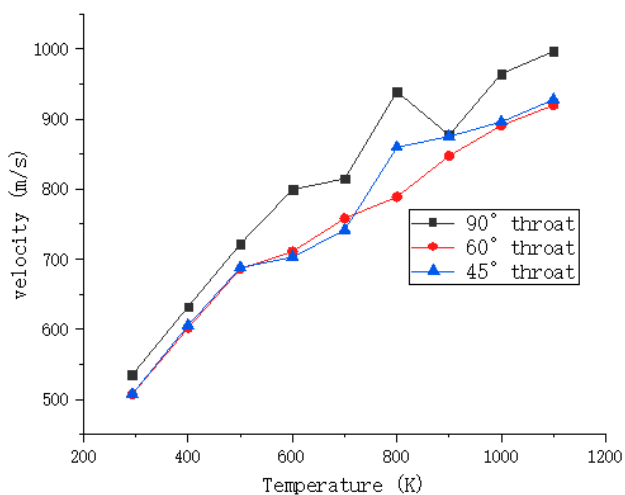
There are many factors influencing the acceleration characteristics of particles, including propulsion gas, temperature, pressure, other factors, and the material properties of particles themselves (i.e., size and shape). Nozzle materials, such as low thermal conductivity, the small heat loss of airflow and particles, are conducive to improving the velocity of particles. However, too high a temperature will cause throat blockage [11].



a



b



c

Figure 3 – Different factors influence the summary of outlet velocity: a – different nozzle throat lengths; b – different temperatures; c – different angles of throat

Therefore, the injector was set at the boundary between the throat and the expansion section in this study. Studies show that [12], when the particle flow diameter is greater than 15 μm , the wall attachment effect disappears, the particle flow is mainly affected by inertia, and the influence of the airflow field on the final trajectory of the particle flow is small. However, the particle diameter is too large, particle collisions with inner nozzle surface basically affect the acceleration characteristics. This chapter utilizes the titanium particles 20 μm in diameter, aluminum particle 30 μm , copper 15 μm , for no angle of nozzle, injection particles nozzle should not be too great pressure, will lead to particle collision on the wall directly, cause energy loss, pressure is too small can't injection, hence, the injection pressure is 1.1 MPa. The other 90° angle throat structure is 1.6 MPa. The results show in Figure 4.

As a result, the trajectory of the particles by the inlet pressure, powder injection pressure, and the combination of factors such as particle size. In addition, the low particle velocity in Figure 5, the main reason is that the initial velocity value and temperature are low.

As Figure 5 b shows, aluminum particles can obtain effective deposition under the collision condition of 400 °C, but the deposition speed of copper particles cannot meet the requirements of deposition. In this case, the parameter of increasing temperature can be considered (Figure 3 b) because the more initial temperature rise, the higher the speed of fluid and particle, and when the temperature of the particles increases (within the melting temperature), the critical velocity will decrease (Table 2), and the effective deposition will be finally achieved. The same can be done with titanium particles or Ti6Al4V material particles [13–15].

4 Conclusions

The Solidworks/Flow numerical simulation can well predict the acceleration characteristics of the nozzle. Some reference values were obtained by numerical analysis of the cold spray nozzle.

By analyzing the throat with 2–9 mm diameter, the fluid acceleration effect is better within 6 mm. For every 1mm increase in the throat, the velocity increases by about 20 m/s. However, beyond 6 mm, the acceleration becomes slow, and the speed increase is no more than 10 m/s. Throat length has little effect on acceleration characteristics, the total range fluctuated from 533 m/s to 550 m/s, and the 11 mm length of the throat is the closest to zero. The temperature has a promoting effect on the acceleration of the nozzle. In a particular range, the outlet velocity has a linear relationship with the temperature. When the temperature reaches 800 K, the exit speed exceeds 900 m/s.

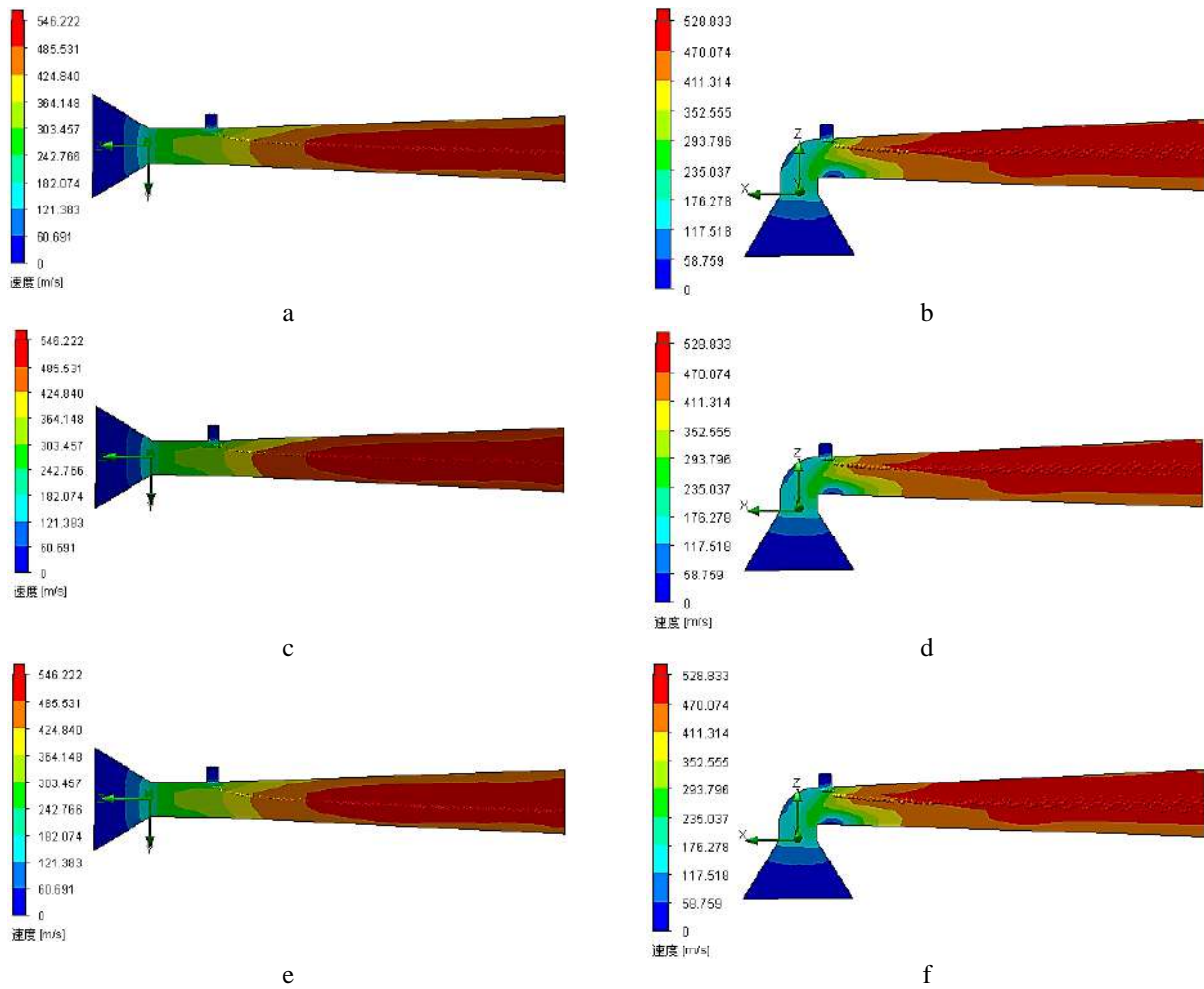


Figure 4 – Optimal conditions for particle trajectories with different throat structures: a, b – 20 μm titanium powders; c, d – 30 μm aluminum powders; e, f – 15 μm copper powders

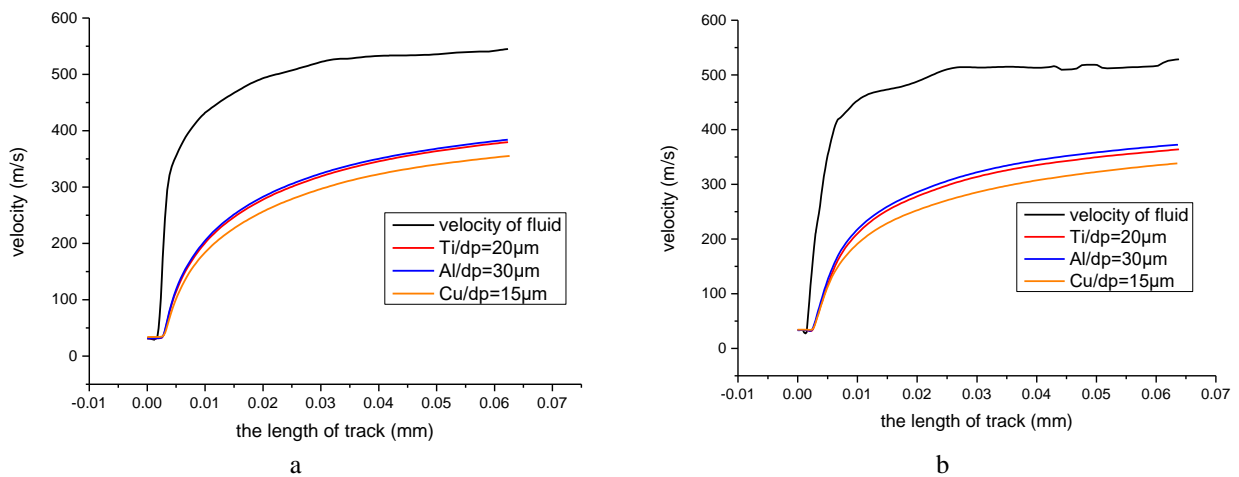


Figure 5 – Different powders and flow velocities: a - without angle; b - 90° nozzle

Table 2 – Critical velocities at different material impact temperatures, m/s

Material	25°C	200°C	300°C	400°C	500°C	600°C	700°C	800°C	900°C
Titanium	719	662	627	590	546	507	460	408	348
Aluminum	630	488	384	239	–	–	–	–	–
Copper	532	465	421	372	316	248	151	–	–

Through the numerical simulation without angle, 90°, 60°, and 45°, it is found that the 90° throat has advantages over 60° and 45°. Compare to no angle nozzle, the 90° throat only reduces the speed of the outlet by 17.4 m/s, which only affects 3 %. Thus, it can be considered that the 90° throat has little influence on the acceleration characteristics. Considering the factors of different material densities, the selected 20 μm titanium powder, 30 μm aluminum powder, and 15 μm copper powder have roughly the same path in the 90° nozzle. If considering the powder of equal diameter, there is a difference in the particle trajectory.

Considering that 90° throat has little influence on acceleration characteristics, it is suggested that in further research, size optimization can be carried out according to the application situations of actual components, and the length of single direction can be optimized, which will expand the application area of cold spraying nozzle.

5 Acknowledgments

The authors would like to thank the China Scholarship Council for the support (Grant No. 202008100011).

References

1. Assadi, H., Gartner, F., Stoltenhoff, T., Kreye, H. (2003). Bonding mechanism in cold gas spraying. *Acta Materialia*, Vol. 51, pp. 4379–4394, doi: 10.1016/S1359-6454(03)00274-X.
2. Hu, W. J., Sergii, M., Tan, K., Shorinov, O., Cao, T. T. (2020). Surface repair of aircraft titanium alloy parts by cold spraying technology. *Aerospace technic and technology*. Vol. 163, pp. 30–42, doi: 10.32620/aktt.2020.3.04.
3. MacDonald, D., Fernandez, R., Delloro, F., Jodoin, B. (2017). Cold spraying of Armstrong process titanium powder for additive manufacturing. *Thermal Spray Technol*, Vol. 26, pp. 598–609, doi: 10.1007/s11666-016-0489-2.
4. Li, W. Y., Li, C. J. (2005). Optimal design of a novel cold spray gun nozzle at a limit space. *Thermal Spray Technology*. Vol. 14, pp. 391–396, doi: 10.1361/105996305X59404.
5. Wu, Z. L. (2011). *Numerical Simulation Research of the Internal Flow Field Cold of the Spray Gun Nozzle and Structural Optimization*. Henan Polytechnic University.
6. Canales, H., Litvinov, A., Markovych, S., Dolmatov, A. (2014). Calculation of the critical velocity of low pressure cold sprayed materials. *Aircraft Design and Manufacturing Issues*, Vol. 3, pp. 86–91. Available online: http://nbuv.gov.ua/UJRN/Pptvk_2014_3_11.
7. Li, Q. (2008). *Structure Design and Optimization of Cold Spray Gun*. The Shenyang University of Technology. Available online: <http://cdmd.cnki.com.cn/article/cdmd-10142-2008203950.htm>.
8. Wenya, L., Changjiu, L. (2005). Optimal design of a novel cold spray gun nozzle at a limited space. *Journal of Thermal Spray Technology*, Vol. 14, pp. 391–396. doi: 10.1361/105996305X59404.
9. Shuo, Y., Meyer, M., Wenya, L., Hanlin, L., Lupoi, R. (2016). Gas flow, particle acceleration, and heat transfer in cold spray: A review. *Journal of Thermal Spray Technology*, doi: 10.1007/s11666-016-0406-8.
10. Alhulaifi, A. S., Buck, G. A. (2014). A simplified approach for the determination of critical velocity for cold spray processes. *Journal of Thermal Spray Technology*, Vol. 23, pp. 1259–1269, doi: 10.1007/s11666-014-0128-8.
11. Congcong, C., Wenya, L., Tianpeng, H., et al. (2019). Simulation study on effect of cold spray nozzle material on particle. *Journal of Netshape Forming Engineering*, Vol. 6, pp. 149–53.
12. Zhang, Y. J., Liang, Y. L., Zhang J. B. (2011). Numerical simulation of particle tracks in the cold gas dynamic spraying process. *Baosteel Technology*, Vol. 5, pp. 12–16, doi: 10.3969/j.issn.1008-0716.2011.05.003.
13. Sunday, T. O., Jen, T. C. (2019). A comparative review on cold gas dynamic spraying processes and technologies. *Manufacturing Rev*, Vol. 25, pp. 1–20, doi: 10.1051/mfreview/2019023.
14. Pelletier, J. L. (2013). *Development of Ti-6Al-4V Coating onto Ti-6Al-4V Substrate Using Low Pressure Cold Spray and Pulse Gas Dynamic Spray*. The University of Ottawa. Available online: <http://dx.doi.org/10.20381/ruor-4265>.
15. Jin, L., Cui, X. Z., Ding, Y. F., Zhang, L., and Su, X. D. (2017). Critical deposition velocity calculations and properties investigations of TC4 cold spray coatings. *Surface Technology*, Vol. 46, pp. 96–101, doi: 10.16490/j.cnki.issn.1001-3660.2017.08.016.



Babalola F. U., Akanji I. O., Oyegoke T. (2021). Comparative analysis of the performance of mixing rules for density prediction of simple chemical mixtures. *Journal of Engineering Sciences*, Vol. 8(1), pp. F25–F31, doi: 10.21272/jes.2021.8(1).f4

Comparative Analysis of the Performance of Mixing Rules for Density Prediction of Simple Chemical Mixtures

Babalola F. U.¹[0000-0001-7812-5311], Akanji I. O.^{2,3}, Oyegoke T.³[0000-0002-2026-6864]

¹ Department of Chemical and Petroleum Engineering, University of Lagos, Nigeria;

² National Oil Spill Detection and Response Agency, Lagos Zonal Office Surulere, Lagos, Nigeria;

³ Department of Chemical Engineering, Ahmadu Bello University Zaria, Nigeria

Article info:

Received: March 4, 2021
The final version received: May 31, 2021
Accepted for publication: June 5, 2021

*Corresponding email:

OyegokeToyese@gmail.com

Abstract. Four different mixing rules (MRs) in three equations of state (EOSs) have been used to account for the intermolecular forces of attraction between dissimilar molecules of different substances that form simple mixtures. The combined effects of the co-volumes of all constituent species of the mixtures were also considered, and the densities of these simple mixtures were predicted. Thereafter, the density results obtained were compared with accurately simulated experimental density values, and the effectiveness of these MRs was determined and compared. The four MRs compared are geometric mean average (GMA), whole square root average (SRA), Expanded geometric average (EGA), and simple average (SA) of attractive force parameter. They were all used in Van der Waals, Redlich Kwong, and Peng Robinson EOSs for two simple mixtures: a binary system (Ammonia – Water system) and a ternary mixture (methyl acetate – water – toluene system). It was found that GMA and EGA gave reasonably accurate estimates of the mixture attractive force parameter (a_m) and hence good density prediction for both Ammonia – Water and Methyl acetate – Water – Toluene systems. SRA gave unrealistic values of mixture densities for both systems and was discarded. SA gave a somewhat good result with Peng Robinson EOS for the ammonia-water system, but not that good in Redlich Kwong EOS and very poor in Van der Waals EOS. SA does not give reasonable estimates of the mixture densities with the three EOSs considered for the methyl acetate – water – toluene system.

Keywords: equation of state, mixing rule, density predictions, chemical mixtures, thermodynamics, models.

1 Introduction

Many industrial processes involve multicomponent systems consisting of more than one liquid mixture. One of the fundamental properties of aqueous solutions commonly used in process industries is density; other properties are solubility, viscosity, vapor pressure, thermal conductivity, and many others. The physical and transport properties of liquid mixtures are essential in understanding the nature of molecular interactions between molecules of liquid mixtures and various transport and process equipment designs. In conjunction with other thermodynamic properties, volumetric properties of aqueous solutions provide helpful information about molecular interactions between liquid mixtures.

Cubic equations of state (EOS) were developed to describe property relationships in pure systems. Usually explicit in pressure (P), an equation of state (EOS) relates other measurable properties such as volume (V) and

temperature (T) of a pure system to its pressure. The attractive forces between the molecules of a pure system, which contribute significantly to these measurable properties, are accounted for by an attractive force parameter called parameter “a.” The volume of the system molecules at infinite pressure is accounted for by the inclusion of a constant called parameter “b” and known as the co-volume. Mixing rules (MR) are employed when an equation of state is applied to mixtures. EOS parameters represent the attractive and repulsive forces between the molecules; hence, mixing rules are used to describe the dominant forces between dissimilar molecules of different substances forming a mixture. Applications of EOSs are of great importance in predicting the pressure-volume-temperature (PVT) relationship and other thermodynamic properties of hydrocarbon fluids and equilibrium calculations.

Researchers have used various mixing rules to employ EOS in predicting various thermodynamic properties of

chemical mixtures (Al-Manthari et al., 2019). The prediction accuracy of EOS varies with the properties being predicted and the system conditions. Two-parameter EOS has been widely applied in the petroleum industry; although accuracy has sometimes been improved by employing EOS with three or more parameters, this is not always the case (Nasrifar and Bolland, 2005, Babalola and Oduwole, 2014). Therefore, a good compromise between the complexity of the EOS model and its prediction accuracy is often required. (Nasrifar and Bolland, 2006). Still, in pursuit of higher accuracy, coupling of two or more EOS using coupling rules has come into focus in recent times (Al-Manthari et al., 2019). For all these applications of EOS, the performance of the mixing rule (MR) used is crucial.

Apparently, for equilibrium calculations and mixture properties prediction, mixing rules (MRs) are used in EOSs. However, the accuracy of EOSs has been found to be non-identical and not particularly adequate for predicting liquid densities of multicomponent hydrocarbon mixtures (Al-Manthari et al., 2019). Performance of some mixing rules for multicomponent systems properties prediction has been found to be poor but quite encouraging for some simple binary or ternary mixtures (Babalola, 2005). Modifications for improving mixing rules have been focused mainly on the attractive force parameter (a), which seems to play a significant role in mixing dissimilar molecules. Over the years, the Van der Waals Mixing Rule (with Geometric Mean Average of the attractive parameter) has been exploited in extending the use of EOSs to multicomponent mixtures. However, they are valid only when molecular size differences of components in a mixture are not too significant (Jian et al., 2000) yet, other mixing rules have not been adequately utilized. Al-Manthari et al. (2019) alluded that Waldman-Hagler (WH) combining rules, used in Van der Waal mixing rules, lacked predictability in most EOSs; consequently, researchers are in continuous search for the best pair of EOS and mixing rule among available ones.

This work presents a study of four different Mixing Rules (MRs) employed in three different equations of State (EOSs) to account for the intermolecular forces of attraction between dissimilar molecules of different substances that form simple mixtures. First, the combined effects of the co-volumes of all constituent species of the mixtures were considered, and the densities of the mixtures were predicted. After which, the density results obtained by using these MRs in the selected EOSs were compared with simulated experimental data and the effectiveness of the MRs were determined and compared.

2 Research Methodology

2.1 Equation of states (EOSs)

The four mixing rules treated here have been proposed in the literature, and some have been in use for some decades. They are termed here as Geometric Mean Average (GMA), Whole Square Root Average (SRA), Expanded Geometric Average (EGA), and Simple

Average (SA) for the attractive force parameter were used in three Equations of State (EOS) for the intermolecular forces of attraction between dissimilar molecules of Ammonia–Water and Methyl acetate—water—toluene thermodynamic systems. Densities of these mixtures were predicted using three EOS and compared, with laboratory simulated data and the effectiveness of the MRs determined.

An equation of state (EOS) is an analytical expression that relates pressure (P) to temperature (T) and volume (V). The Simplest and most widely known EOS is the ideal gas EOS (Ahmed, 2001). Three two-parameters EOS are selected for this study, namely: Van der Waals (1873), Redlich-Kwong (1949), and Peng-Robinson (1976) EOS abbreviated respectively as VW, RK, and PR. Van der Waals EOS is quite simple. PR and RK EOS require less pure component constants and binary interaction parameters than many recently developed EOS and have gained wider acceptance (Estela-Vrube et al., 2004). Nasrifar and Bolland, 2006 found that RK and PR EOSs, are simple, accurate, and more reliable in predicting thermodynamic properties of natural gas mixtures compared to other EOS models. The EOS used in this work is given in PVT and compressibility factor (Z) terms in Table 1.

Table 1 – PVT and Z relations for the selected EOSs

Equation of State (EOS)	Mathematical Expressions
Van der Waals (VW)	$P = \frac{RT}{v-b} - \frac{a}{v^2}$ $Z^3 - (1+B)Z^2 + AZ - AB = 0$
Redlich-Kwong (RK)	$P = \frac{RT}{v-b} - \frac{a}{T^{0.5}v(v+b)}$ $Z^3 - Z^2 + (A-B-B^2)Z - AB = 0$
Peng-Robinson (PR)	$P = \frac{RT}{(v-b)} - \frac{a_c\alpha}{v(v+b)+b(v-b)}$ $Z^3 - (1-B)Z^2 + (A-3B^2-2B)Z - (AB-B^2-B^3) = 0$

2.2 Mixing rules

Mixing rules are used to describe prevailing forces between dissimilar molecules of different substances forming mixtures. Generalized Mixing Rule expressions for the attractive force term (a_m) and repulsive force term (b_m) are given in following equations:

$$a_m = \sum_{i=1}^m \sum_{j=1}^m x_i x_j a_{ij}; \quad (1)$$

$$b_m = \sum_{i=1}^m x_i b_i, \quad (2)$$

where x , a , and b – the mole fraction, the attractive force parameter, and the co-volume or repulsive force parameter, respectively.

Several relationships for attractive forces between two molecules (a_{ij}) have been defined, and these definitions have resulted in various mixing rules (MRs). Attractive force terms for mixtures (a_m) are obtained by different modifications of a_{ij} in equation (1) but the same repulsive force term (b_m) as expressed in equation (2), which has

hardly undergone any significant modification over the years, is employed for all four MRs. This repulsive force term is the volume of a molecule of a constituent species at infinite pressure. It accounts for the force of repulsion between dissimilar molecules in a mixture and is called the co-volume. The four MRs employed in this work for the attractive force term (a_m) are as follows:

1) geometric mean average (GMA) of the attractive force parameter (van der Waals et al., 1873) given as follows:

$$a_{ij} = \sqrt{a_i a_j}, \quad (3)$$

which, when substituted in equation (1), give rise to Van der Waal mixing rules as expressed in equations:

$$a_m = \sum_{i=1}^m \sum_{j=1}^m x_i x_j \sqrt{a_i a_j}; \quad (4)$$

2) the whole square root average (SRA) of the attractive force parameter was proposed by Babalola, 2005 as expressed in equation:

$$a_{ij} = \sqrt{\frac{a_i + a_j}{2} + (a_i a_j)^{1/2}}. \quad (5)$$

Using equation (5) in (1) gives rise to another mixing rule expressed as follows:

$$a_m = \sum_{i=1}^m \sum_{j=1}^m x_i x_j \sqrt{\frac{a_i + a_j}{2} + (a_i a_j)^{1/2}}; \quad (6)$$

3) expanded geometric average (EGA) of the attractive force parameter was also proposed by Babalola (2005) as follows:

$$a_{ij} = \frac{2\sqrt{a_i a_j} + a_i + a_j}{4}. \quad (7)$$

When equation (7) is substituted into equation (1), another Mixing Rule is obtained and expressed as follows:

$$a_m = \sum_{i=1}^m \sum_{j=1}^m x_i x_j \frac{2\sqrt{a_i a_j} + a_i + a_j}{4}; \quad (8)$$

4) the simple average (SA) of the attractive force parameter (Jian et al., 2001) expressed as follows:

$$a_{ij} = \frac{a_i + a_j}{2}. \quad (9)$$

Equation (9) in combination with (1) yields yet another Mixing Rule given as follows:

$$a_m = \sum_{i=1}^m \sum_{j=1}^m x_i x_j \frac{a_i + a_j}{2}. \quad (10)$$

Binary interaction parameters, PIBs, (K_{ij}) are sometimes used to correct attractive parameters. However, BIPs are temperature and EOS-dependent; therefore, to have a fair comparison of results, they are deliberately set at zero (0) for all EOS employed in this work.

2.3 Thermodynamic systems

Densities of an industrial refrigerant (Ammonia – Water system) and an esterification mixture (Methyl acetate – Water – Toluene system) were here predicted at their respective system operating conditions. Ammonia-water system has been known to be environmentally

friendly, cheaply available, energy-efficient, has no global warming potentials, and has therefore been used in industrial refrigeration plants for over 130 years. From chemistry, two products of esterification of methanol and acetic acid are Methyl acetate and water, although both have been known to form binary azeotropes, making their separation difficult. In the industry, toluene is mainly added as an entrainer to make their separation easy. In continuous esterification plants, a mixture of these three components (in the vapor phase) forms the overhead product of the first distillation column. This stream is later separated into organic and aqueous phases. The organic phase contains toluene and methyl acetate, which are separated in the second distillation column. The density of the ternary system, Methyl acetate – water – toluene, is an important physical property in the design of the first distillation column and that of Methyl acetate - Water is helpful in the design of the second column. Methyl Acetate is a crucial chemical substance in perfumery (Bertram, 1982). The physical properties of the mixture constituents are given in Table 2, while Table 3 shows the operating conditions of the binary and ternary thermodynamic systems used in this work.

Table 2 – Physical properties of each component of the mixtures

Component	Critical temperature T_c , °C	Critical pressure P_c , Pa	Acentric factor ω
Ammonia	132.40	111.50	0.253
Water	374.15	218.40	0.343
Methyl acetate	233.70	46.30	0.326
Toluene	320.60	41.60	0.262

Table 3 – Operating conditions of two thermodynamic systems

System	Operating parameter	
	Temperature T , °C	Pressure P , atm
Ammonia – water	-54	0.316
Methyl acetate – water – toluene	60	1

2.4 Computer lab simulation

Four mixing rules, namely, Geometric Mean Average (GMA), Whole Square Root Average (SRA), Expanded Geometric Average (EGA), and Simple Average (SA) for the attractive force parameter, together with a repulsive force term, were used in Van der Waals, Redlich- Kwong and Peng Robinson Equations of State, to predict the densities of two simple mixtures; a binary mixture (Ammonia – Water system) and a ternary mixture (Methyl acetate – Water – Toluene system).

For the Van der Waals EOS and the three MRs, these are the essential steps in predicting the density of these mixtures. The EOS parameters, a_i and b_i For each of Ammonia and Water, were computed, at their critical conditions. Mixture parameters a_m and b_m were then evaluated using Van der Waals Mixing Rule denoted as GMA – equations (4). These parameters were then

computed using other MRs, at various percentage compositions of each mixture component. Thereafter, the EOS A and B coefficients were evaluated at operating conditions (temperature and pressure) of the system. A third-degree polynomial of the Van der Waals EOS was then solved for compressibility factor (Z). Three roots were obtained, the highest being the Compressibility Factor of the vapor phase (Z^V) and the lowest being the Compressibility Factor of the liquid phase (Z^L). The apparent molecular weight of the binary mixture (M_a) was then determined by finding the summation of the product of mole fraction and molecular mass for each component. Liquid and the vapor densities (ρ^L and ρ^V) of the mixture were then obtained, at various compositions of the components, using the density model proposed by Ahmed (2000):

$$\rho = \frac{n(\sum_{i=1}^n x_i M_i)P}{ZRT}, \quad (11)$$

where ρ – the mixture density; n – the mole fraction; x_i – composition of each component of the mixture; M_i – the relative molecular mass of each component of the

mixture; P – system operating pressure; Z – the gas constant; T – the system's operating temperature.

Similar procedures were repeated for density prediction of the ternary system, Methyl acetate – Water – Toluene. Predicted densities with different mixing rules were compared with density data obtained from ASPEN HYSIS at varying compositions of each component and system operating conditions.

2.5 Validation of HYSIS data

HYSIS data were validated and were found reliable and could serve as experimental values (lab data). For validation of Aspen HYSYS data, a 50 ml Pyrex Borosilicate Glass density bottle was used on a Hanchen electronic analytical weighing balance (JJ224BC) with 0.1mg precision to accurately measure the densities of Ethanol – Water mixture at various compositions of ethanol and water (Table 4) at room temperature and atmospheric pressure. Results of the validation step are presented in Figure 1.

Table 4 – Mixture densities by experiment and by ASPEN HYSIS for ethanol – water system

Composition x, % (mole)		Density by experimental measurement, kg/m ³				Density by Aspen HYSIS (kg/m ³)	% AAD
Ethanol	Water	Run1	Run2	Run3	Average		
90	10	796.6	798.2	797.80	797.53	799.0	0.2
75	25	838.6	838.4	838.30	838.43	817.8	2.5
50	50	848.6	850.7	852.10	850.47	847.3	0.4
25	75	893.9	892.0	894.30	893.40	897.8	0.5
10	90	950.6	952.1	951.80	951.50	950.0	0.2

3 Results and Discussion

3.1 Results of HYSIS

As evident from the plots in Figure 1, simulated density results from ASPEN HYSIS are highly accurate and closely match those obtained by experimental laboratory measurements. The simulated results showed an overall accuracy level of 0.1843 and a percentage absolute average deviation of 3.5 % as calculated using the expression given in the following equation:

$$\%AAD = \sum_{i=1}^N \left\| \frac{\|Experimental - Predicted\|}{Experimental} \right\| x \frac{100\%}{N}. \quad (12)$$

3.2 Densities of ammonia – water system

For Ammonia -Water System, when the four MRs; GMA, SRA, EGA, SA, are separately used in Van der Waals, Redlich Kwong, and Peng Robinson EOS, density data are predicted. The predicted densities are then compared to the laboratory data. The percentage absolute average deviation between the experimental and predicted data for each MRs was evaluated using equation (12). The lower the % AAD value, the closer the predicted density value by the MR to the value obtained from laboratory experiments. Table 5 displays the percentage absolute average deviation (% AAD) of predicted density results with GMA, EGA, and SA from the experimental value.

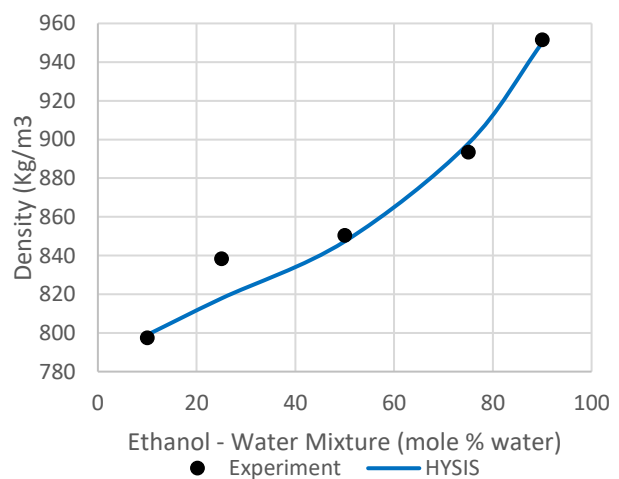


Figure 1 – Variation of density with composition for ethanol-water mixture

The results show that GMA and EGA used in Peng Robinson EOS gave density results reasonably close to the experimental results and relatively good results with Redlich-Kwong EOS, but not with Van der Waals EOS.

Table 5 – Absolute average deviation for GMA, EGA, and SA for ammonia – water binary system

Equation of state (EOS)	Mixing rule (MR)	% AAD
Van der Waals	GMA	46.8
	EGA	46.7
	SA	59.7
Redlich-Kwong	GMA	20.6
	EGA	20.5
	SA	29.9
Peng-Robinson	GMA	9.9
	EGA	9.9
	SA	18.9

On the other hand, SA gave somewhat close results with Peng-Robinson EOS, but not that good with Redlich-Kwong EOS and very poor results with Van der Waals EOS. For this system, GMA and EGA with Peng Robinson EOS gave the least % AAD of 9.9, followed by SA with Peng Robinson EOS with % ADD of 18.9. Thus, GMA, EGA, and SA in the other two EOS gave results that are too far from the experimental values.

Density obtained using the four MRs in the Van der Waals EOS are shown in Figure 2 and plotted on the same axes against compositions. As evident in Figure 2, SRA overestimates densities of the mixture with an Absolute Average Deviation of over 168 %, so it was dropped. Similar trends are observed with SRA in Redlich-Kwong and Peng-Robinson EOSs.

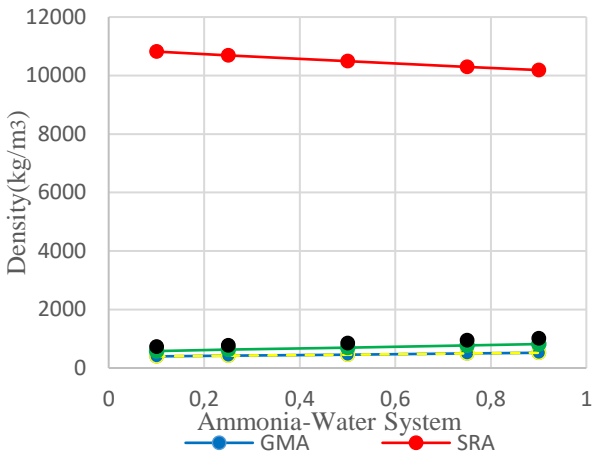


Figure 2 – Comparing predicted densities with four MRs in Van der Waal EOS with Laboratory Data

The whole Square root Average of EOS parameter (SRA) in the three EOS considered for the binary system consistently gave unrealistic density values, with an Absolute Average Deviation of over 168 %, so it was dropped. Consequently, Figures 3–5 are expanded plots of densities against compositions with GMA, EGA, and SA in Van der Waals, Redlich Kwong, and Peng-Robinson EoS for ammonia-water binary system.

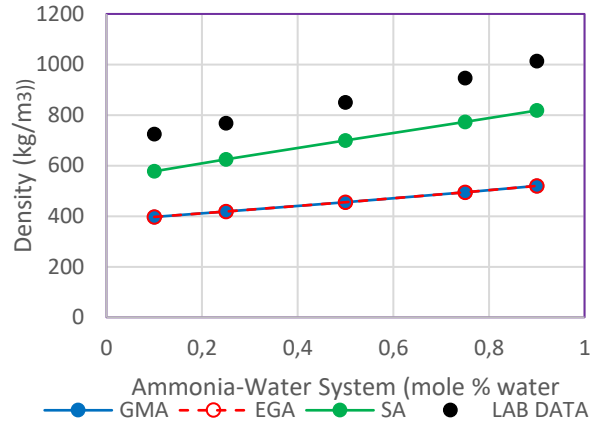


Figure 3 – Predicted densities with GMA, EGA and SA in Van der Waal EOS alongside lab data

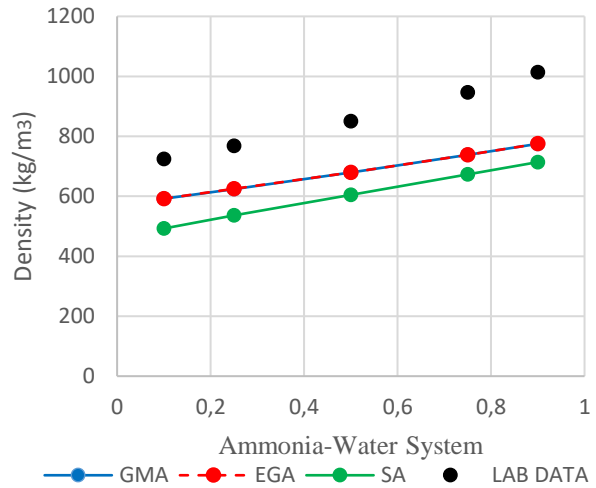


Figure 4 – Predicted densities with GMA, EGA, and SA in Redlich-Kwong EOS against composition

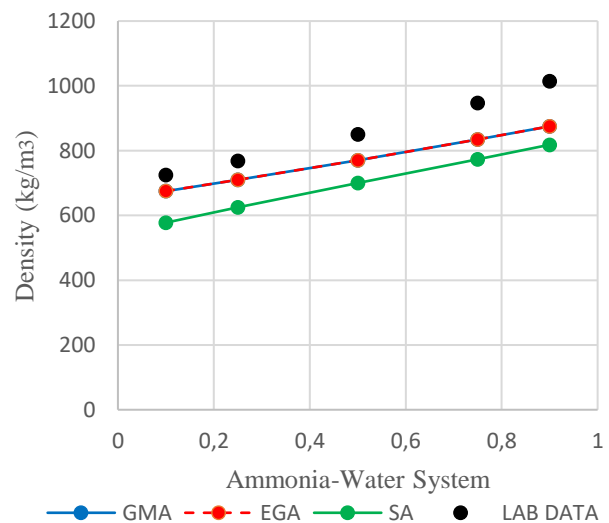


Figure 5 – Predicted density with GMA, EGA, and SA in Peng Robinson EOS against composition

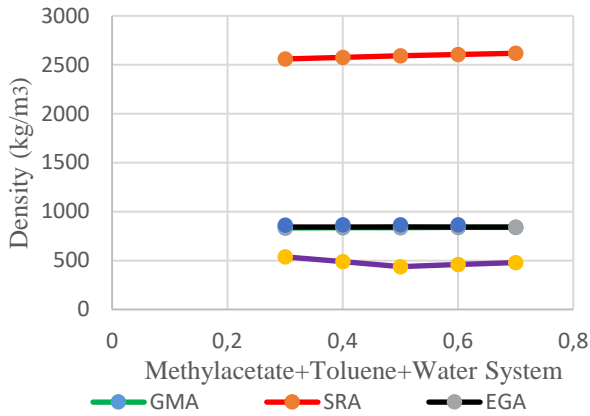


Figure 6 – Density data with four MRs in Peng-Robinson EOS against the composition of mixture components

3.3 Densities of the methyl acetate – toluene – water system

Experimental density data of Methyl Acetate – Toluene – Water ternary System, at varying compositions, and predicted density results with four mixing rules and each EOS are compared. Table 6 displays the deviation of predicted densities with GMA, EGA, and SA from the experimental value, in terms of percentage absolute average deviation (% AAD).

Table 6 – Absolute average deviation for GMA, EGA, and SA for methyl acetate – toluene – water

Equation of state (EOS)	Mixing rule (MR)	% AAD
Van der Waals	GMA	45.3
	EGA	44.2
	SA	46.7
Redlich-Kwong	GMA	18.2
	EGA	17.1
	SA	49.6
Peng-Robinson	GMA	3.4
	EGA	2.5
	SA	44.4

MA and EGA with Peng Robinson EOS gave excellent results with % AAD values of 3.4 and 2.5. Similarly, GMA and EGA are relatively good in Redlich Kwong EOS with % AAD values of 18.2 and 17.1, respectively. Van der Waals EOS does not give a good density prediction with GMA, EGA, and SA because their % AAD are 45.3, 44.2, and 46.7, respectively. SA does not give reasonable estimates of the mixture densities with the three EOSs considered, and SRA deviates too largely from experiment values, so it was discarded.

Experimental and predicted density data of Methyl acetate – Toluene – Water with the four MRs in Peng-Robinson EOSs are plotted against the composition of mixture components in Figures 6. As evident from the plot, the Whole Square Root Average of attractive force parameter (SRA) used in the PR EOS for the ternary Methyl acetate – Toluene – Water system is found to overestimates density data, with an unrealistic Absolute Average Deviation. Similar trends were observed with SRA in Van der Waals and Redlich-Kwong EOSs; hence SRA was knocked off.

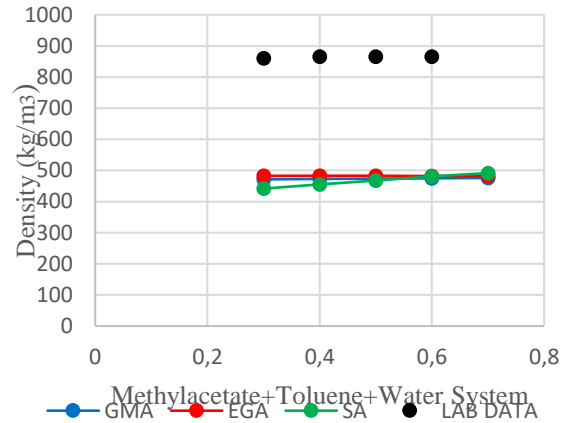


Figure 7 – Predicted density data with four mixing rules in Van der Waal EOS against compositions of mixture components

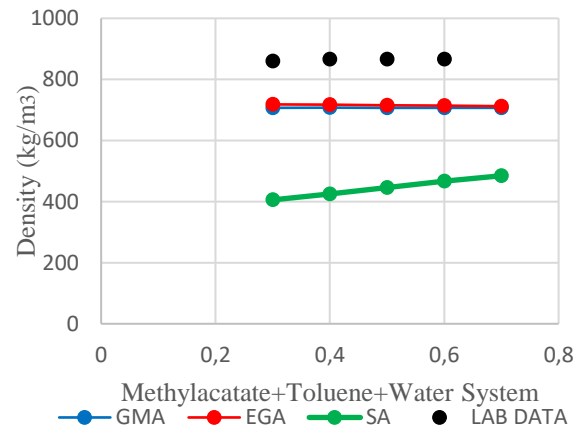


Figure 8 – Density data with GMA, EGA, and SA in Redlich Kwong EOS against compositions of mixture components

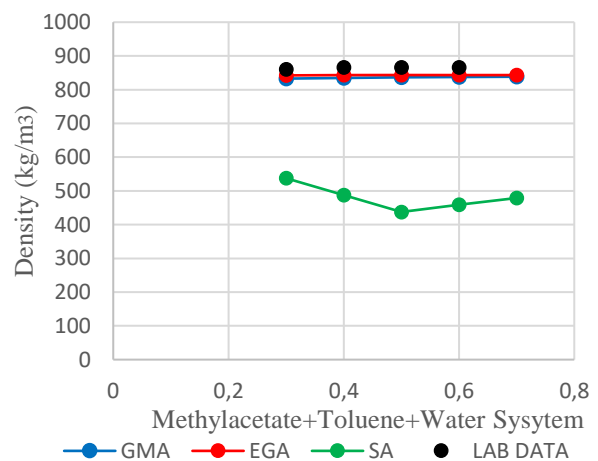


Figure 9 – Density data with GMA, EGA, and SA in Peng Robinson EOS against compositions of mixture components

Consequently, expanded density plots against the compositions with GMA, EGA, and SA in Van der Waals, Redlich Kwong, and Peng-Robinson EOS were made for the ternary system, and the plots are displayed in Figures 7–9.

4 Conclusions

Four Mixing Rules expressions have been accurately used to account for the intermolecular forces of attraction between dissimilar molecules of different substances that formed simple mixtures. The combined effects of co-volumes of all constituent species of the mixtures were also considered. The four MRs compared are; Geometric mean average (GMA), Whole Square Root Average (SRA), Expanded Geometric Average (EGA), and Simple Average (SA) of attractive force parameter. For the four MRs, it is assumed that all components of mixtures are similar; hence they are known as random mixing rules. We established that it is possible to adapt EOS to accurately predict densities values of simple mixtures by using Mixing Rules. GMA and EGA gave a reasonable estimation of the mixture attractive force parameter (a_m) and hence good density prediction results for Ammonia – Water and Methyl acetate – Toluene – Water systems. Their predicted density results are approximately equal. SRA underestimate the mixture attractive force parameter (a_m); consequently, it overestimated the mixture densities for the two thermodynamic systems. The accuracy of the predicted mixture density with different EOS, separately combined with different MRs, depends on the versatility of the EOS. When GMA and EGA are used in Peng Robinson EOS, the best density prediction is obtained. Redlich Kwong EOS also gives relatively good results.

5 Abbreviations

% AAD	absolute average deviation in percentage;
a, b, c	parameters in the EOS;
A, B, C	parameters in the EOS;
A	reduced temp. function in the EOS;
EOS	equations of state;
MR	mixing rule;
a_i	attractive parameter of component i ;
a_j	attractive parameter of component j ;
b_i	co-volume parameter of component i ;
a_{ij}	attractive parameter of components i and j combined;
a_m	mixture attractive force term;
b_m	mixture repulsive force term;
K_{ij}	the binary interaction parameter;
N	number of molecules;
P	pressure;
R	ideal gas constant;
T	temperature;
V	volume;
ω	acentric factor;
Z	compressibility factor;
Z_l	compressibility factor of mixture in the liquid phase;
Z_v	compressibility factor of mixture in the vapor phase;
ρ^L	liquid density of the mixture;
ρ^V	vapour density of the mixture;
x_i	mole fraction of component i in the liquid phase;
x_j	mole fraction of component j in the liquid phase;
c	critical condition;
r	reduced condition;
m	molar value.

References

1. Ahmed, T. H. (2000). *Reservoir Engineering Handbook*. Gulf Professional Publishing, Houston, Texas.
2. Ahmed, T. H. (2001). Comparative Study of Eight Equations of State for Predicting Hydrocarbon Volumetric Phase Behavior. *SPE Reservoir Engineering Journal*, Vol. 3(1), pp. 337–348, doi: 10.2118/15673-PA.
3. Al-Manthari, M. S., Al-Wadhahi, M. A., Reza, V. G., Nasrifar, K. (2019). A Systematic Study of Cubic Equations of State with van der Waals Mixing Rules and Different Combining Rules in Predicting the Densities of LNG and Natural Gas Model Systems. *International Journal of Thermodynamics*, Vol. 22(2), pp. 107–116, doi: 10.5541/ijot.528164.
4. Babalola, F. U. (2005). *Equilibrium and Stability of Multicomponent Multiphase Systems of Chemical Mixtures*. PhD Thesis, School of Postgraduate Studies, University of Lagos, Akoka, Chemical Engineering Department. Lagos.
5. Babalola, F. U., Oduwole, D. O. (2014). A comparative analysis of the performance of various equations of state in thermodynamic property prediction of reservoir fluid systems. *Trends in Chemical Engineering*, Vol. 15, pp. 47–58.
6. Estela-Uribe, J. F., De Mondoza, A. T., Trusler, J. P. (2004). Extended corresponding states model for fluids and fluid mixture II application to mixtures and natural gas system. *Journal of Fluid Phase Equilibrium*, Vol. 183-184, pp. 21–29, doi: 10.1016/S0378-3812(01)00417-4.
7. Jian, C., Jian-Guo, M., Kwong-Yu, C. (2001). Comparison of different mixing rules for prediction of density and residual internal energy of binary and ternary Lennard–Jones mixtures. *Journal of Fluid Phase Equilibria*, Vol. 178, pp. 87–95.
8. Nasrifar, K., Bolland, O. (2005). Predicting Natural Gas Dew Points from 15 Equations of State. *Journal of Energy and Fuel*, Vol. 19, pp. 561–572, doi: 10.1021/ef0498465.
9. Nasrifar, K., Bolland, O. (2006). Prediction of thermodynamic properties of natural gas mixtures using 10 equations of state including a new cubic two-constant equation of state. *Journal of Petroleum Science and Engineering*, Vol. 51, pp. 253–266, doi: 10.1016/j.petrol.2006.01.004.
10. Peng, D. Y., Robinson, D. B. (1976). A New Two-Constant Equation of State. *Ind. Eng. Chem. Fundamental*, Vol. 5, pp. 59–64, doi: 10.1021/i160057a011.
11. Redlich, O., Kwong, J. N. S. (1949). On the Thermodynamics of Solutions. V. An Equation of State. Fugacities of Gaseous Solutions. *Chem. Rev.*, Vol. 44, pp. 233-244 (doi: 10.1021/cr60137a013).
12. Van der Waals, J. D. (1873). *Over de Continuïteit van den Gas-en Vloeistoftoestand*. Doctoral Thesis, University of Leiden, Leiden.
13. Yeomans, B. (1982). United State of America Patent No. 4342627.



sustainability



an Open Access Journal by MDPI

Industry 4.0 Technologies for Sustainable Asset Life Cycle Management

Guest Editors:

Dr. Malgorzata Jasiulewicz-Kaczmarek

malgorzata.jasiulewicz-kaczmarek@put.poznan.pl

Prof. Dr. Katarzyna Antosz

katarzyna.antosz@prz.edu.pl

Dr. Chao Zhang

cz@buaa.edu.cn

Prof. Dr. Vitalii Ivanov

ivanov@tmvi.sumdu.edu.ua

Deadline for manuscript submissions:

15 March 2022

Message from the Guest Editors

Dear Colleagues,

Asset life cycle management is not a new concept for industries. Life cycle thinking means that people have a life cycle model in mind that affects the scope of their activities. A life cycle perspective for manufacturing assets is often mentioned in the literature regarding sustainability. This approach aims to understand and analyze individual stages of the asset life cycle, identify potential economic, social, and environmental risk factors and opportunities at each stage, and create possibilities to take advantage of these opportunities and reduce potential risks. In the Industry 4.0 era, manufacturers can monitor assets and make smart decisions in each phase of their life cycle through real-time communication and cooperation with humans, machines, sensors, etc. These technologies can support all stages of ALC through various emergent communication, information, and intelligence technologies.



mdpi.com/sj/93508

Special Issue



Gundu M., Abhaysinha S. (2021). *Experimental study on the performance of concrete mix with paper waste, waste plastic, quarry dust, and fly ash*. *Journal of Engineering Sciences*, Vol. 8(1), pp. H1–H7, doi: 10.21272/jes.2021.8(1).h1

Experimental Study on the Performance of Concrete Mix with Paper Waste, Waste Plastic, Quarry Dust, and Fly Ash

Gundu M.^{1*}, Abhaysinha S.²

¹Dr. Vishwanath Karad MIT World Peace University, Kothrud, Pune, India-411058;

²School of Civil Engineering, Dr. Vishwanath Karad MIT World Peace University, Kothrud, Pune, India-411058

Article info:

Received:

January 17, 2021

The final version received:

April 27, 2021

Accepted for publication:

May 2, 2021

*Corresponding email:

mukeshgundu007@gmail.com

Abstract. In recent years, concrete in the construction industry has rapidly increased worldwide, including developing countries like India. The raw materials required to produce such a quantity require huge depletion of natural resources. On the other hand, disposal of paper waste, fly ash, and plastic waste is one of the biggest problems faced by many countries, including India, the amount of waste collected and recycled is less compared to disposal quantity. The use of these wastes in concrete reduces the disposal of waste in nature. In this experiment work, the use of these wastes in the concrete has been studied. Preliminary tests like specific gravity, fineness modulus, and water absorption have been carried out on the materials. Various mix designs are prepared by partial replacement of cement with fly ash and paper pulp, and sand is completely replaced with the quarry dust, and coarse aggregate is replaced with shredded plastic waste to create sustainable concrete. A comparative study on the properties like slump cone, the weight of the cubes, compressive strength and split tensile strength, and feasibility of such concrete has been carried out. Results indicated that the weight of cubes started to decrease with the addition of waste. Compressive strength and split tensile strength show that the strength started to fall with the addition of plastic. The cost of concrete decreased with the addition of waste. 5 % of plastic waste in concrete and 3 % of paper pulp, and 5 % of fly ash is considered the optimal replacement percentage.

Keywords: slump cone, split tensile, compressive strength, fly ash, quarry dust, plastic waste, paper waste.

1 Introduction

Concrete is one of the major and widely used materials in the construction industry all over the world. From a study, developing countries have been consuming around 400 million concrete, and the quantity of consumption is expected to increase in the coming decades. The raw materials used for concrete like sand, coarse aggregate, and cement are taken from the Earth's core, depleting each year. Many countries face another fundamental problem with solid waste disposal, which causes a significant threat to the environment and human health.

Plastic waste is one of the solid wastes which causing a great threat to the environment and ecology. A study report on India from CPCB (Central Pollution Control Board) of 2018–2019 shows around 3,360,043 metric tonnes per annum (Roughly around 9200 metric tonnes per day), and among the total collected, only 60 % is recycled, and the remaining are disposed or incineration which ultimately causing pollution to the environment. To reduce this

disposal or incineration we can use these materials in the construction.

Another major solid waste is paper waste, and it is the 3rd biggest polluter of the environment. To meet the demand of industry million trees are cut down, which resulting in global warming. According to a study to meet the demand of India 3 million tonnes of paper waste is collected, which is only 20 % of the total production the remaining end's up as landfill or incinerated.

Fly ash is the waste residue of the thermal power plant which ends up as a landfill. Quarry dust is generated during the crushing process of aggregate in the quarry. Many researchers have tried to study the properties of this waste in concrete as a replacement for cement and the results are quite acceptable. In this study, the use of these materials in the concrete and study of their properties and feasibility of the concrete has been discussed.

2 Literature Review

Shyam and Drishya [1] studied concrete properties by replacing fine aggregate with plastic waste. High-density polyethylene (HDPE) is replaced with M Sand at 5, 10, 15, and 20 %, and results show 5 % replacement as the optimum percentage of replacement. Pooja et al. [2] has carried out a study on concrete behavior by replacing fine aggregate with plastic waste. Mixes are prepared by replacing plastic waste at 15, 20, and 30 % in fine aggregate. The results show that the concrete strength has increased up to 15 %, and further strength has decreased. Kalapad et al. [3] had carried a study to reduce paper waste. To obtain a proper mix design, tests like specific gravity, initial and final setting time, sieve analysis, and bulking of sand on materials. Tests like slump cone on fresh concrete and compressive strength on hardened concrete. The test results found that the paper waste replacement with cement at 10 % shows maximum strength and by addition of the wastepaper sludge, there is a slight reduction in the workability. Ilakkiya et al. [4] had carried out a study to use paper waste in concrete. Various properties of the concrete had been studied. The test results had concluded that 10 % of paper waste shown an acceptable strength property. Ahmad et al. [5] had done an experimental study by replacing cement with paper sludge ash as 5, 10, 15, and 20 %. Different tests had performed, and test results show 5 % of replacement as the optimum mix for the M25 grade of concrete. Bhargavi et al. [6] had studied the use of wastepaper sludge in the concrete. Wastepaper sludge is partially replaced with cement, 4 mixes are prepared for M30.

Moreover, the test results shows suggest that 4 % of replaced concrete can be used as a structural element. Balwaik et al. [7] prepared samples by replacing cement with paper pulp at 0, 5, 10, 15, and 20 %, and a comparative study with the conventional concrete was done. The percentage of water absorption of the concrete has increased. This is due to the increased percentage of the paper pulp that had been noticed. Khandelwal [8] had suggested that 4 % of replacement of the shredded plastic with sand shown better results of the compressive strength and flexural strength. Dhaarani et al. [9] studied the concrete properties by replacing coarse aggregate with plastic, and the test results show 10 % as the optimum mix for modified concrete. Khajuria and Sharma [10] had carried an investigation on the properties of the concrete by replacing natural coarse aggregate with plastic at 0, 2.5, 5.0, 7.5, and 10 %. The test results show 2.5 % of replacement as the suitable replacement for the concrete. Minhas and Jain [11] had carried a review paper on the use of plastic waste in concrete and observed a significant increase in the strength properties with plastic waste like PET in concrete.

This literature review aims to study the various research work carried out on paper and plastic waste. The literature review concludes that both paper and plastic waste can be used in concrete, but the combined effect of these materials needs to be studied. This experimental work is to study the combined effect of these materials in concrete.

3 Research Methodology

3.1 Research objectives

The research objectives are as follows:

- to prepare various mix designs for partial replacement of paper waste, plastic waste, fly ash, crush sand;
- to investigate the properties of the concrete by replacing the cement with fly ash (5 %), paper waste (3 %), sand with quarry waste, and plastic waste (0, 5, 10, and 15 %) in the coarse aggregate;
- to carry out a comparative analysis of test results with the conventional concrete;
- to carry out the techno feasibility study on the plastic paper concrete;
- to recommend the optimum percentage of the replacements in the concrete.

3.2 Methodology

The following flow of methodology is followed in the present experimental work (Figure 1).

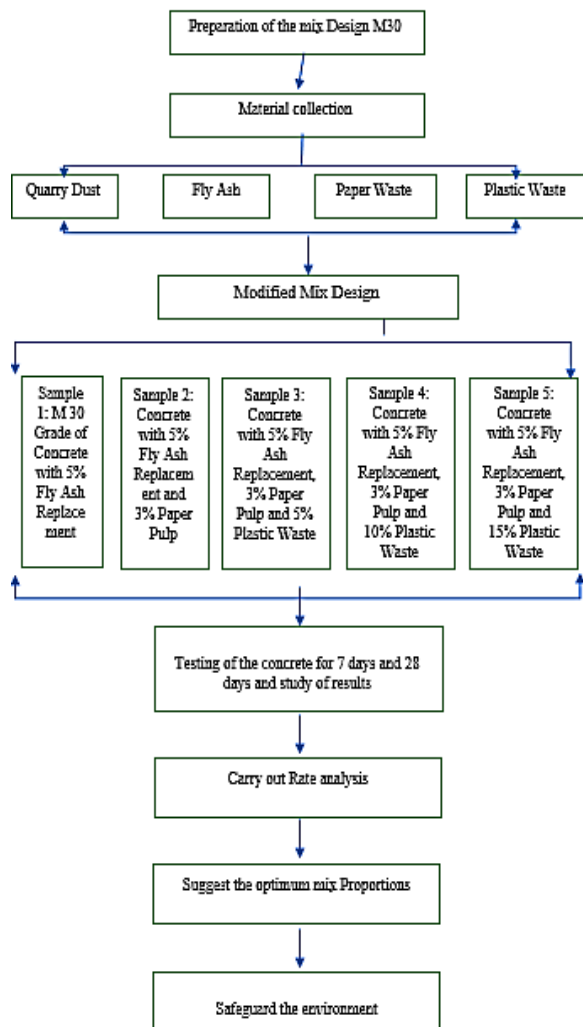


Figure 1 – Flow chart of the methodology

3.3 Materials and methods

The plastic waste (polypropylene plastic waste), paper waste, fly ash, quarry dust was collected from the plastic waste shredding site, local book manufacturer and printing press, stone crusher site in Dist. Warangal, Telangana. Fly ash from the nearby thermal power plant. The basic tests on the materials are conducted as per IS Codes.

Physical properties of the quarry dust are presented in Table 1, other components of the mix – Table 2.

Table 1 – Physical properties of the quarry dust

Sr. No	Property	Obtained Value
1	Specific gravity	2.57
2	Surface texture	Rough
3	Water absorption	0.30
4	Fineness modulus	2.80

Table 2 – Physical properties of other components of mix

Sr. No	Property	Obtained Value
1	Specific gravity of cement	3.15
2	Fineness of cement %	4
3	Specific gravity of 20 mm aggregate	2.68
4	Specific gravity of plastic	0.905
5	Admixture	Kuna plast PC 30

3.4 Mix design of the concrete mix

The mix design for concrete preparation is selecting the right proportion of each material to obtain the required properties like strength, workability, and economical. M30 grade of concrete is selected as this concrete can be used in different structure components (Table 3).

Mix design was prepared for specimen by replacing cement with 5 % fly ash, 3 % paper pulp, coarse aggregate with plastic waste by 5, 10, and 15 %. The combination of the mix design is as follows.

Sample 1 – cement is replaced with 5 % fly ash. Sand is replaced with quarry dust.

Sample 2 – cement is replaced with 5 % fly ash and 3 % paper pulp. Sand is replaced with quarry dust.

Sample 3 – cement is replaced with 5 % fly ash and 3 % paper pulp. Sand is replaced with quarry dust. Coarse aggregate is replaced with 5 % shredded plastic.

Sample 4 – cement is replaced with 5 % fly ash and 3 % paper pulp. Sand is replaced with quarry dust. Coarse aggregate is replaced with 10 % shredded plastic.

Sample 5 – cement is replaced with 5 % fly ash and 3 % paper pulp. Sand is replaced with quarry dust. Coarse aggregate is replaced with 15 % shredded plastic.

Table 3 – Mix design of M30

Sample 1		
Material	Quantity, kg	Ratio
Cement	399	1
Fly ash	21	0.053
Paper pulp	0	0
Quarry dust	675	1.692
Coarse aggregate	1137	2.850
Shredded plastic	0	0
Water	201	0.504
Admixture	2.1	0.005
Sample 2		
Material	Quantity	Ratio
Cement	386.4	0.968
Fly ash	21	0.053
Paper pulp	12.6	0.032
Quarry dust	675	1.692
Coarse aggregate	1137	2.850
Shredded plastic	0	0
Water	201	0.504
Admixture	2.1	0.005
Sample 3		
Material	Quantity	Ratio
Cement	386.4	0.968
Fly ash	21	0.053
Paper pulp	12.6	0.032
Quarry dust	675	1.692
Coarse aggregate	1137	2.850
Shredded plastic	19	0.048
Water	200	0.501
Admixture	2.1	0.005
Sample 4		
Material	Quantity	Ratio
Cement	399	1
Fly ash	21	0.053
Paper pulp	12.6	0.032
Quarry dust	675	1.692
Coarse aggregate	1137	2.850
Shredded plastic	39	0.098
Water	200	0.501
Admixture	2.1	0.005
Sample 5		
Material	Quantity	Ratio
Cement	399	1
Fly ash	21	0.053
Paper pulp	12.6	0.032
Quarry dust	675	1.692
Coarse aggregate	1137	2.850
Shredded plastic	58	0.145
Water	199	0.499
Admixture	2.1	0.005

4 Results

4.1 Test conducted on specimens

4.1.1 Slump cone test

A slump cone test was performed for each sample to know the workability of the modified concrete. Initially, the slump value started increasing till sampling 3, and further, the slump started decreasing (Figures 2–3, Table 4).



Figure 2 – cylinders testing

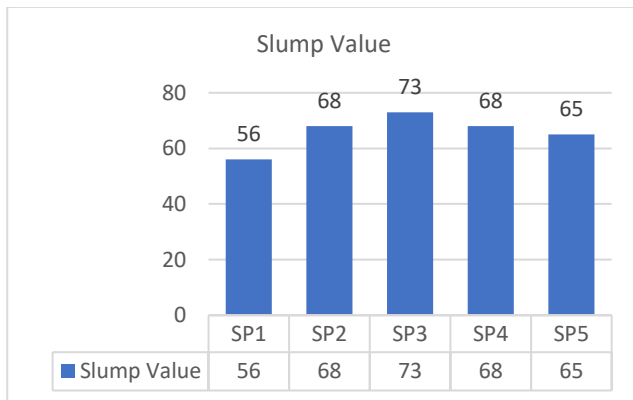


Figure 3 – Slump cone test values

Table 4 – Slump values and placing conditions

Degree of workability	Slump, mm	Placing conditions
Very low	< 25	Blinding concrete; shallow concrete sections; pavement using pavers
Low	25–75	Mass concrete; lightly reinforced sections slabs; columns, beams, walls, floors; hand placed pavements; canal lining; strip footings
Medium	50–100	Heavily reinforced sections in slabs, beams, walls columns slip formwork; pumped concrete
High	75–100	Trench fill; in-situ piling tremie
Very high	100–150	concrete

Slump values from the test results fall under the medium workability range, which concludes that this modified concrete can be used for manually compacted flat slabs and beams.

Specimens were prepared with proper precaution and quantity as mentioned in the above mix design. Cubes of sizes 150 mm x 150 mm x 150 mm, and cylinder of size height 300 mm and diameter 150 mm were prepared by mixing the materials according to the given proportions for replacement of 5 % fly ash and 3 % paper pulp to cement, and sand is completely replaced with the quarry dust, coarse aggregate is replaced with 5, 10, and 15 % of the shredded plastic. A total of 300 cubes and 10 cylinders were cast, including 6 cubes and 2 cylinders for each percent replacement of every 3 cubes for 7 days and 28 days of testing and 2 cylinders for 28 days of each replacement.

4.1.2 Cube weight

After 24 hours of the specimen cast, the specimens were unmolded, and weights of 3 cubes were noted. It was observed that the weight of the samples started decreasing with the increase in the plastic content in the concrete (Figure 5).

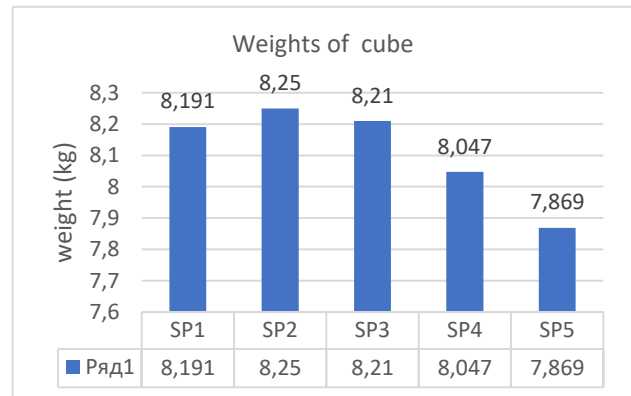


Figure 4 – Weights of the cubes

4.1.3 Compressive strength test

After the curing periods of 7 days and 28 days, the samples were taken out of the curing tank allowed for the drying process. Then the samples were placed in the automatic compression testing machine. The load was applied according to the is code. The peak load at which the specimen fails has been noted to interpret the results (Figure 5).

4.1.4 Tensile strength test

The specimens were taken for testing after 28 days of curing and the specimen is allowed for the drying process. Then the specimen was placed in the automatic compression testing machine and the load is applied till the specimen fails and the results were noted for the interpretation (Figures 5–6).

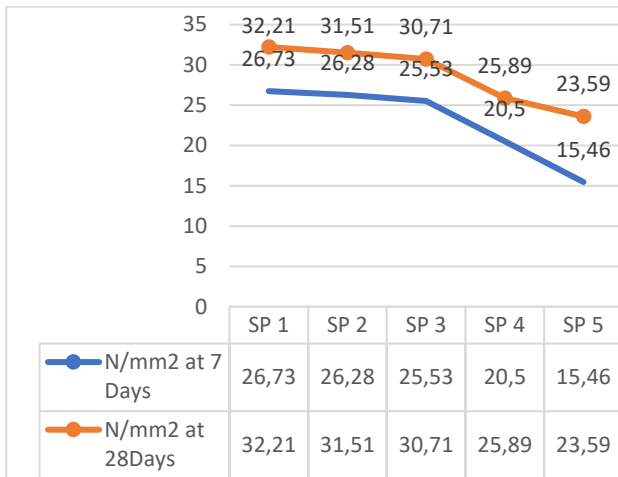


Figure 5 – Compressive strength test results

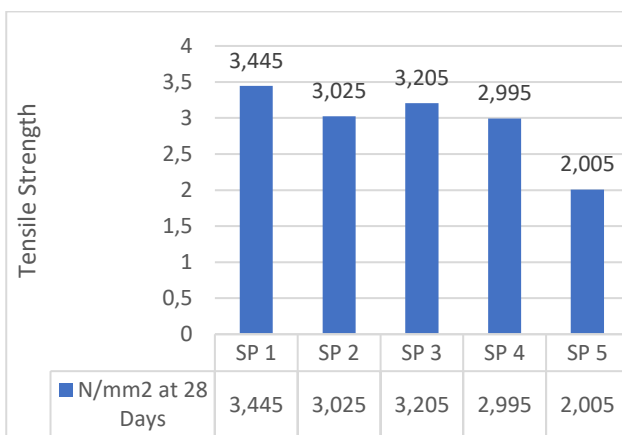


Figure 6 – Split tensile strength results

4.2 Rate analysis

The rate of the materials is collected from the suppliers from Pune, Maharashtra, to carry out the rate analysis for the M30 grade of concrete (Table 5). A comparative analysis is done with the conventional concrete and the modified concrete to replace fly ash, paper pulp, quarry dust, and paper waste.

Table 5 – Normal concrete rate analysis

Material	Unit	Quantity	Price	Total cost
Cement	kg	420	6	2520.00
Sand	–	0.687	2826.8	1942.01
20 mm aggregate	–	1.137	777.38	883.88
water	lit	201	0.5	100.50
Admixture	lit	2.1	110	231.00
Total Cost				5677.39

Rate analysis is carried out on the samples with the addition of plastic waste, fly ash, paper waste, and quarry dust in various proportions (Figures 7–11).

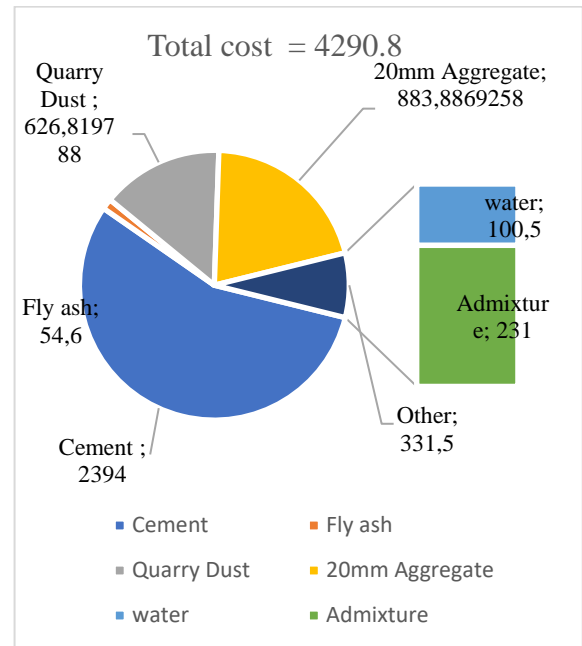


Figure 7 – cost graph of sample 1

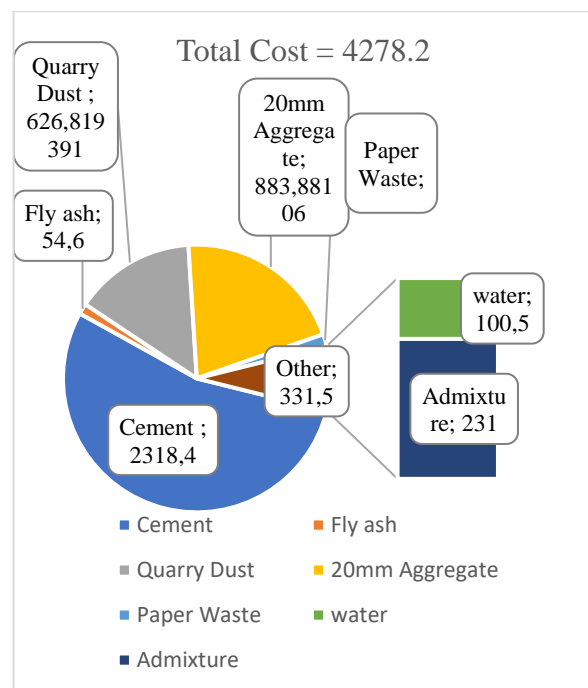


Figure 8 – Cost graph of sample 2

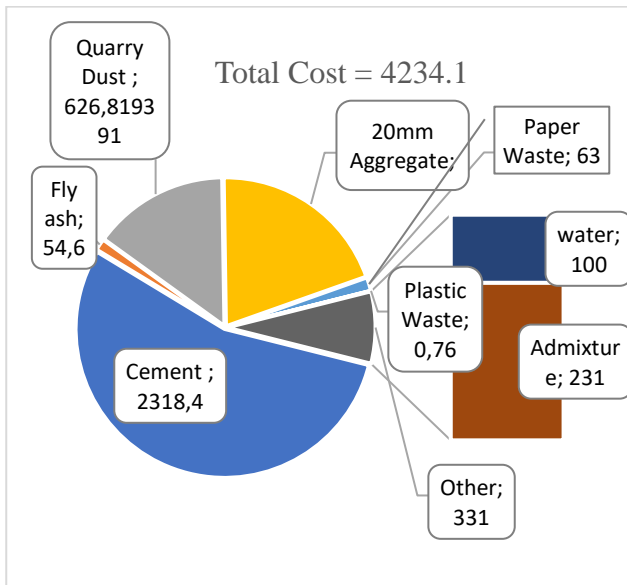


Figure 9 – Cost graph of sample 3

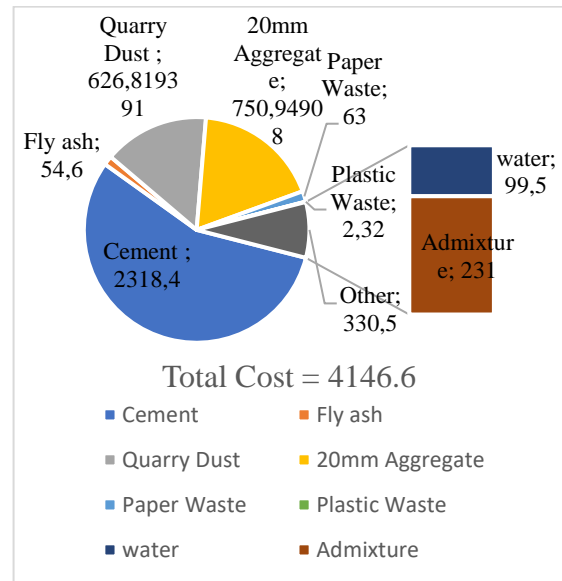


Figure 11 – Cost graph of sample 5

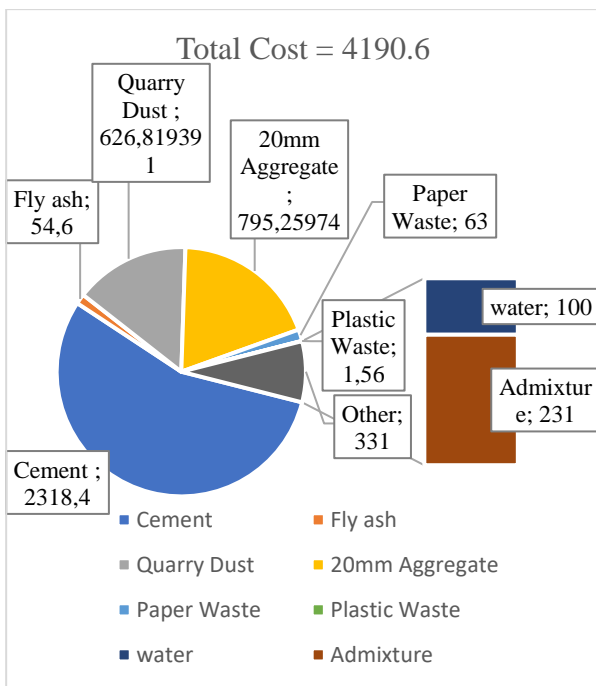


Figure 10 – Cost graph of sample 4

5 Discussion

The test results on the modified concrete are as follows. Initially, the weight of the cube for sample 1 with fly ash is 8.191. With the addition of paper pulp, the weight has increased to 8.25. With the addition of the plastic in the concrete, the weight of the cubes decreased to 8.210, 8.047, and 7.869.

Compressive strength test results after 28 days are as follows: 32.21, 31.51, 30.71, 25.89, and 23.59, indicates that with the addition of plastic, the strength of concrete decreases as mentioned by Shyam and Drishya [1].

The split strength indicates that with the addition of paper pulp, the strength drops initially, and with the addition of plastic waste, the strength of concrete increases till 5 % addition and a further increase in plastic, strength started to drop. The cost of the normal concrete is 5677.4, and with the addition of plastic waste, paper waste, quarry dust, and fly ash, the cost of concrete 4290.8, 4278.2, 4234.1, 4190.6, and 4146.5, which indicates a decrease in the cost of the concrete.

6 Conclusions

From the tests and results on plastic waste, paper waste, fly ash, and quarry dust in concrete, the following conclusion is drawn.

The compressive strength of concrete started to decrease with the addition of plastic waste. This may be due to the flaky and elongated shape of plastic. The weight of the concrete decreases with the addition of paper and plastic waste. The cost of concrete reduces with the use of the wastes. The split tensile strength initially decreases, and with the addition of plastic, the strength increases.

Based on the study results, fly ash of 5 %, paper pulp of 3 %, and plastic waste of 5 % can be used in producing concrete. These wastes can be used to reduce natural resources.

Since the presence of paper waste in concrete, we cannot use this concrete in the water logging area. It can be used by providing a waterproofing coating.

References

1. Shyam, S., Drishya, P. (2018). Reuse of plastic waste as replacement of M sand in concrete. *IOSR Journal of Engineering*, Vol. 8(6), pp. 2278–8719.
2. Pooja, P., Vaitla, M., Sravan, G., Reddy, M. P., Bhagyawati, M. (2019). Study on behavior of concrete with partial replacement of fine aggregate with waste plastics. *Materials Today: Proceedings*, Vol. 8, pp. 182–187, 01084, doi: 10.1051/e3sconf/202018401084.
3. Kalapad, J. D., Mansute, M., Swami, V., Sulbhewar, V., Khandale, T. M. (2019). A study on partial replacement of cement by waste paper pulp in concrete. *International Journal of Innovations in Engineering and Science*, Vol. 4(4), pp. 80–85.
4. Ilakkiya, R., Dhanalakshmi, G. (2018). Experimental investigation on concrete using waste paper. *International Research Journal of Engineering and Technology*, Vol. 5(2), pp. 1995–1999.
5. Ahmad, S. (2013). Study of concrete involving use of waste paper sludge ash as partial replacement of cement. *IOSR Journal of Engineering*, Vol. 3(11), pp. 6–15, doi: 10.9790/3021-031130615.
6. Bhargavi, P., Karthikeyan, S. K., Sneha, G., Vinothini, A. (2016). Experimental investigation on usage of waste paper sludge (WPS) in concrete making. *International Journal of Latest Technology in Engineering, Management and Applied Science*, Vol. V(III), pp. 69–72.
7. Balwaik, S. A., Raut, S. P. (2011). Utilization of waste paper pulp by partial replacement of cement in concrete. *International Journal of Engineering Research and Applications*, Vol. 1(2), pp. 300–309.
8. Vikas Khandewal. (2019). Replacement of sand with shredded plastic in cement concrete. *International Journal of Engineering Research and Technology*, Vol. 8(6), pp. 946–949.
9. Dhaarani, D., Shanmuganathan, N., Gokila, M., Akalya, A., Abirami, D., Dhilshath, B. J. (2018). Crushed plastic waste in concrete. *International Research Journal of Engineering and Technology*, Vol. 5(3), pp. 3638–3640.
10. Khajuria, A., Sharma, P. (2019). Use of plastic aggregates in concrete. *International Journal of Innovative Technology and Exploring Engineering*, Vol. 9(1), pp. 4406–4412, doi: 10.35940/ijitee.A5088.119119.
11. Minhas, S., Jain, R. (2020). Review on use of plastic in concrete. *International Journal of innovation in Engineering and Technology*, Vol. 15(4), pp. 26–28, doi: 10.21172/ijiet.154.05.



Shtepa V. N., Chernysh Ye. Yu., Danilov D. V. (2021). Preventive improvement of wastewater treatment efficiency. *Journal of Engineering Sciences*, Vol. 8(1), pp. H8–H15, doi: 10.21272/jes.2021.8(1).h2

Preventive Improvement of Wastewater Treatment Efficiency

Shtepa V. N.^{1,3}[0000-0002-2796-3144], Chernysh Ye. Yu.^{2,3*}[0000-0003-4103-4306], Danilov D. V.²[0000-0002-1883-0964]

¹ Polissya State University, 23, Dneprovskoy Flotilii St., 225710, Pinsk, Belarus;

² Sumy State University, 2, Rymkogo-Korsakova St., 40007, Sumy, Ukraine;

³ International Innovation and Applied Center “Aquatic Artery”, 2, Rymkogo-Korsakova St., 40007, Sumy, Ukraine

Article info:

Received:

December 12, 2020

The final version received:

May 15, 2021

Accepted for publication:

May 20, 2021

*Corresponding email:

e.chernish@ssu.edu.ua

Abstract. This paper focuses on studying the effect of electrolytic water on wastewater decontamination processes, using model solutions and wastewater from the food-processing plant. The aqueous solutions under study were obtained by changing the redox potential (ORP), and pH of ordinary tap water using a pH corrector, which is a flow-through electrolyzer with a membrane separating the cathode and anode zones, and the solutions were obtained by adding to tap water a solution containing products of electrokinetic synthesis. Parameters that changed as a result of the study: ORP, TDS, pH. Solutions capable of almost complete inhibition of the vital activity and growth of microorganisms were obtained. Also, solutions were obtained that promoted their development, and when seeding them on a dense nutrient medium, there was continuous growth. Further research is advisable to detail the technical and economic indicators of municipal and industrial facilities' water supply and sewerage schemes with preventive water treatment processes.

Keywords: wastewater, meat, methods of pretreatment, pH corrector, biostimulation, bioinhibition.

1 Introduction

Food products are a good breeding ground for microorganisms. Therefore, to preserve food quality, i.e., meat products, they are subjected to salting, refrigerated storage, and other types of preservation [1]. At the same time, during slaughtering, animal carcasses are constantly washed with water, which is subsequently discharged as effluent and sent to sewage treatment plants. Accordingly, the wastewater enterprises of the meat industry have a high degree of bacterial contamination. Particularly dangerous are pathogenic microorganisms in them by E. Coli, worm eggs, anthrax. In this connection, before discharging into water bodies or on the ground areas of sewage of enterprises of the meat industry, they should be subjected to effective cleaning and disinfection [2].

At the same time, it is essential to solving the problem of the contamination of the effluents from meat industry enterprises based on washing the carcasses of slaughtered animals with an aqueous solution with predetermined parameters.

2 Literature Review

Methods of wastewater treatment in the meat processing industry from pathogens and various pollutants can be divided into the following basic methods [3–5]: mechanical (physical), chemical, physicochemical, biological, and combined.

Examining the scientific periodicals indexed by the Scopus metric database, it was found that this topic was first covered in 1978. Since then we can see a sharp decrease in the study of this topic until 2006, with a further decrease in publication activity, with variable values over the years: 2009, 2019–2020. (Fig. 1). This trend is very popular in the countries with a high indicator of consumption of meat and milk products. Therefore, according to the results of the study of this topic, the first place for the number of publications is occupied by the United States of America - more than 100 scientific works, followed by Brazil – 61 papers, China and Canada – about 50 papers.

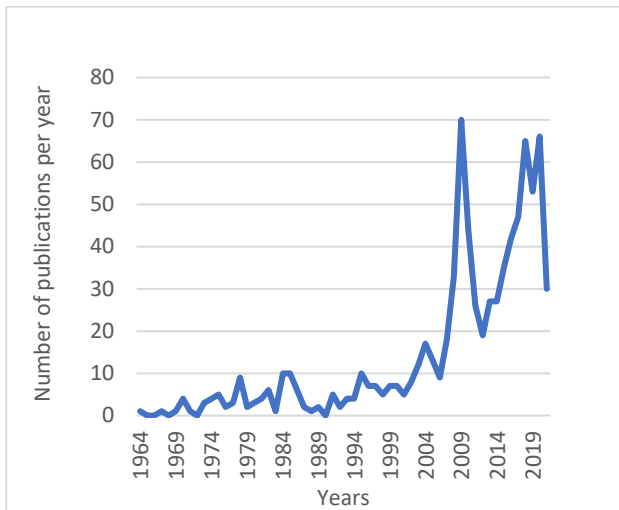


Figure 1 – Analysis of search results by years

The most significant number of scientific works is focused on improving ecological situation in regions and engineering sector, biofuel production, and chemical machine-building with the production of different kinds of chemical additives (Fig. 2). The most critical areas of research are actual for Ukraine.

Looking at the 2019–2021 years, we can see that the primary position of the majority of works reveals the solution of environmental problems of food enterprises. Such works can include the following topics [6–8]: assessment of toxicity of wastewater of the meat-processing industry, optimization of processing technology of liquid wastes from food processing plants, and processes of anaerobic pickling for purification of high-quality wastewater.

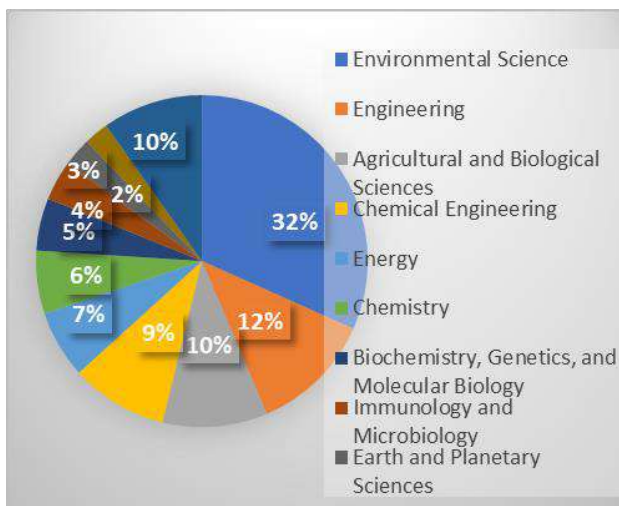


Figure 2 – Search results in the use of bioenergy technology

Ivanchenko et al. (2020) developed a quick analysis for an unbiased and accurate assessment of wastewater properties and its sediments. Biotests allow quick identification of integral toxicity and can be used for screening investigations. The optimal method for determining the overall toxicity of complex sums is to

evaluate the properties of the hydrogenous fraction since it is a real threat if it enters the human body. Biotests on the representatives of different trophic levels allowed one to assess the safety of the investigated wastewater in a short time. That is why they were recommended as test systems to control the environmental safety of wastewater to identify several specific chemical spores, integral toxic potential, and long-term consequences for natural and piece ecosystems [9].

In the process of research by Kulikova et al. (2019) special attention was paid to the study of the new combined unit - aerobic treatment reactor (FLOTEX - AERO) and anaerobic treatment reactor (FLOTEX - ARO). They were designed taking into account the main advantages and disadvantages of the used tanks for fat removal, brine collectors, floating and aerobic treatment plants intended for non-cleaning biologically, as well as the special features of wastewater from meat and dairy plants [10].

Harris and McCabe (2020) investigated improvements in anaerobic wastewater recycling in the Australian black-bean industry. Anaerobic lagoons are an economically efficient method of waste management when land availability is not an issue; however, high-fat loadings in wastewater can negatively impact the anaerobic lagoon system and fail anaerobic digestion characteristics. This work will discuss the importance of primary pretreatment and consider a low level of research aimed at optimizing the operation of the cooking apparatus and improving the biological composition of the fat. These studies include the following: influence of temperature and mixing; the influence of microelement composition and additives; potential benefits from the previous treatments such as chemical, thermobaric, thermochemical, and bi-PAR. Recommendations are given for the optimal operation of the cooking apparatus and future possibilities in adopting alternative variants of anaerobic digestion technology [11].

For disinfection, you can use the approaches described in paragraph 9.2.11.1 of SP 32.13330.2012 “Sewage. Outdoor networks and facilities” domestic wastewater and their mixtures with industrial wastewater discharged into water bodies or used for technical purposes should be subjected to disinfection. This is aimed at maintaining the environmental safety of the environment [12].

SanPiN 2.1.5.980-00 “Hygienic requirements for the protection of surface waters”, which regulates the disinfection of sewage, establishes the following requirement: “Wastewater hazardous by epidemiological criteria may be discharged into water bodies only after appropriate treatment and disinfection to the number of thermotolerant coliform bacteria CFU/100 ml \leq 100, the number of total coliform bacteria CFU/100 ml \leq 500 and the number of coliforms CFU/100 ml \leq 100”.

In this case, a sequential scheme of water treatment is classically used (Fig. 3).

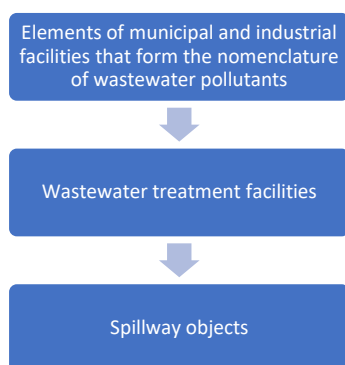


Figure 3 – Classical scheme of wastewater treatment by municipal and industrial facilities

This study aims to investigate the effect of electrolytic water on wastewater decontamination processes, using the example of model solutions and wastewater from meat-processing production.

3 Research Methodology

3.1 Methodology for the study of model aqueous solutions obtained from meat processing

The aqueous solutions under study were obtained by changing the redox potential (ORP), and pH of ordinary tap water using a pH corrector, which is a flow-through electrolyzer with a membrane separating the cathode and anode zones, and solutions were obtained by adding a solution containing electrokinetic synthesis products (ECO) to tap water (Table 1).

Table 1 – Composition of the solution

Component	Quantity, g/l
Pancreatic hydrolysate of fish meal dry (PGRM dry)	7.5
Peptone dry fermentative for bacteriological purposes	7.5
Pancreatic casein hydrolysate dry (PHC dry)	10.0
Yeast extract	2.0
Sodium chloride	3.5
D-Glucose	1.0

The anolyte was obtained by sampling the solution from the anodic zone of the pH corrector; the catholyte was sampled from the cathodic zone. The sampled solutions were used both separately and mixed to obtain a neutral solution.

For obtaining ECO-1 solutions, 15 ml of activated solution was added to 150 ml of tap water. For obtaining ECO-2 solutions, 30 ml of activated solution were added to 150 ml of tap water. After obtaining each of the solutions, fresh pig meat was soaked in them for 30 seconds to simulate the process of washing animal carcasses at meat processing plants. Six different solutions were obtained, the values of which are shown in Table 2.

Table 2 – Indicators of obtained aqueous solutions for meat treatment

Solution/indicators	ORP, mV	TDS	pH	t, °C
Tap water	-7.7	207	7.13	17
Anolyte	92.5	278	5.42	22.6
Catholyte	-129	220	9.18	22
Anolyte + catholyte (in equal proportions)	21	270	6.64	22.7
ECO-1 (ele-based solution)	-2	280	7.03	19.6
ECO-2	-1.6	380	7.03	20.5

Then, after soaking, all indicators of the solutions were measured again. We also measured the concentration of nitrogen compounds (ammonia/ammonium, nitrites, nitrates) in the solution. All measurements were repeated after 5 hours as well as one day after receiving solutions. Also, these solutions were plated on a dense agarized nutrient medium to determine the total microbial count and then compare the insemination of these solutions. It was also concluded that changes in the values of aqueous solutions for washing meat affect their subsequent infestation and the ability of microorganisms to live and multiply in these solutions.

A specific nutrient-dense medium for determining the number of mesophilic aerobic and facultative anaerobic microorganisms (CMAFANM) was used to assess the total insemination of various meat flushes.

Prepared nutrient medium, which is a hygroscopic fine-dispersed powder of beige color, was used for cultivation. The combination of components in the medium provides the nutrient requirements for visual growth detection and determination of mesophilic aerobic and facultative anaerobic microorganisms.

Preparation of the medium: (50±5) g of dry medium is introduced into (1±0.05) dm³ of cold water (both distilled and tap water, previously prepared, can be used). The mixture is thoroughly mixed, brought to a boil, and boiled for 3-5 minutes without allowing it to burn. If there is a precipitate, filter it through a cotton-gauze filter. The medium is heated to boiling again, poured into flasks or tubes, sealed with cotton plugs, and sterilized at (121 ± 2) °C for (15 ± 1) minutes. The prepared medium is transparent and has a yellowish-brown color. Immediately before use, the medium is melted by placing the container with the medium in a water bath. The molten medium is carefully cooled to a temperature of 40–45 °C without foaming. Nutrient medium is introduced into sterile Petri dishes in the amount necessary to create a layer of a medium of at least 2 mm (usually 12–15 cm³ of agar medium is required) growth is judged by the appearance of visible colonies of microorganisms on the nutrient medium.

A universal nutrient medium, meat-peptone agar, a natural nutrient medium, was used to determine the PMF. Composition of the nutrient medium: 1 l of meat broth, 10 g of peptone, 5 g of NaCl, 20 g of agar-agar.

Preparation: Mix meat broth with peptone and table salt, boil for 10 minutes, filter through a paper filter. Then the necessary amount of agar-agar is added. The pH is

adjusted to 7.2–7.4. Feeding tubes are sterilized by autoclaving at 121°C and 1 atm for 20 minutes.

GRM-agar nutrient medium is designed for the cultivation of a wide range of microorganisms. It can be used in sanitary research of water, sewage, and other materials. If necessary, it can be enriched with carbohydrates, blood, serum. It is a hygroscopic fine-dispersed powder of light yellow color.

Composition of the nutrient medium (in grams per liter of distilled water): pancreatic hydrolysate of fish meal – 24.0; sodium chloride – 4.0; agar-agar – 12.0 (± 2.0).

Preparation: a suspension of 39.0 g of the drug in the amount indicated on the label is stirred in 1 liter of distilled water and boiled for 1–2 min until the agar is completely melted, filtered through a cotton-gauze filter. The medium was poured into bottles and sterilized by autoclaving at 121 °C for 15 min. Sterile medium cooled to 45–50°C is poured into sterile Petri dishes with a 4–6 mm layer.

After preparation and sterilization, the prepared nutrient medium was poured into Petri dishes and waited for solidification. Then, all aqueous samples were diluted ten times in sterile tap water under a laminar flow box. The obtained solutions in the volume of 1 ml were placed on a solid nutrient medium and distributed on the nutrient medium using circular movements of the Petri dish and spatula. We placed the seeded microorganisms in a thermostat with a temperature of 37 °C.

3.2 Research methodology for wastewater from a meat processing plant

To assess the degree of contamination of wastewater, mineralization, TDS, and pH (Table 3).

Table 3 – Indicators of the main indicators in the composition of wastewater JSC “Pinsk meat processing plant”

Indicators	pH	TDS	ORP, mV	t, °C
Wastewater sample	6.44	1116	32.8	19.6
Anolyte	2.38	1600	270.0	22.2
Catholyte	11.46	1200	-237.0	21.3
ECO-2	6.48	1100	32.3	38.8

Different wastewater treatment methods from various organic and microbiological pollutants were also carried out by adding anolyte and catholyte solutions, treatment with hydrogen peroxide; exposure to ultraviolet radiation; dosing biocidal product (BP) (with a mass fraction of 5 % – 4 ml/l).

During the experiments, 5 containers with a volume of 5 liters were taken, adding 1 liter of wastewater to each. For treatment with anolyte, catholyte, and ECO-2, 1 liter of wastewater was taken into the tank. When BP was exposed, its concentrated solutions and liquid glass were diluted to obtain solutions with a mass fraction of the substance of 5 %. In the first tank, 2 ml of diluted liquid glass solution was introduced to alkalize the wastewater, and after 2 minutes, 4 ml of BP solution was introduced. Flakes began to form in 20 seconds after introducing the flocculant: flakes were formed quite large, in the form of a coarse curd mass, capturing all large particles in the

solution, indicating that BP, as a flocculant, not only catalyzes the process of coagulation but also enhances it by order.

100 ml each of the anolyte and catholyte solutions were added to the following two containers. After mixing thoroughly, let stand for the effective passage of all processes. We added 0.4 ml of hydrogen peroxide to 1 liter of wastewater, stirred thoroughly, and poured the solution into a unit containing two ultraviolet lamps. It was treated with ultraviolet radiation for 5 minutes.

4 Results and Discussion

4.1 Study of biostimulation and bioinhibition of model aqueous solutions

After treating the meat with ordinary tap water (control experiment) and bacteriological seeding of this water sample on the nutrient medium KMAFANM, the total insemination was no more than $4 \cdot 10^{10}$ CFU/ml (Fig. 4).



Figure 4 – The contamination of tap water 2 days after washing fresh pork meat with this water

There is also a colony of fungi on the medium. This colony-forming unit may have gotten into the solution during the preparation of dilutions.

As a result of washing meat with water sampled from the anodic zone (anolyte), no total insemination of the sample was planted on the nutrient medium KMAFANM. It can be concluded that high ORP values have a deleterious effect on the vital activity of microorganisms, and solutions having such ORP values can be used as disinfectants in the process of washing meat carcasses at meat processing plants without being toxic substances (Fig. 5).



Figure 5 – The contamination of water sampled from the anode zone 2 days after washing fresh pork meat with this water

After washing the meat with water sampled from the cathodic zone (catholyte), there was a solid overgrowth of the KMAFANM medium, counting colonies, in this case, is impossible in both replications, which indicates the positive effect of negative ORP values on the vital activity

of microorganisms, indicating that these solutions are not suitable for meat treatment to obtain an antibacterial effect (Fig. 6).



Figure 6 – The contamination of water sampled from the cathodic zone 2 days after washing fresh pork meat with this water

After treating the meat with a mixed solution consisting of equal proportions of catholyte and anolyte, there was uniform growth of microorganisms in both cups and amounted to about $9 \cdot 10^{11}$ COE/ml, which indicates that this solution is also not suitable for washing the meat to disinfect it and obtain an antibacterial effect (Fig. 7).



Figure 7 – The contamination of a mixed water sample from the cathodic and anodic zones, 2 days after washing fresh pork meat with this water

After introducing a certain amount of ECO-2 products into normal water, and as a result of subsequent soaking in this solution of meat, the sowing of this solution did not occur, and only on one of the cups can be seen a colony of fungus, presumably caught in the solution during the preparation of dilutions. This result may indicate that using these reagents in the process of washing animal carcasses at meat processing plants can serve as a good measure to prevent the contamination of wastewater with microorganisms (Fig. 8).



Figure 8 – The contamination of the solution containing ECO-2 products in the amount of 30 ml/150 ml of tap water 2 days after treatment of fresh pork meat with this solution

The results obtained after introducing a smaller amount of ECO-1 products are similar to those described above - there is no contamination of this solution, indicating an apparent bactericidal effect of electrokinetic oxidation products in lower concentrations as well (Fig. 9).



Figure 9 – The contamination of a solution containing IVF products in the amount of 15 ml/150 ml of tap water 2 days after treatment with this solution of fresh pork meat

4.2 Studies of the number of nitrogen compounds formed in the treated model solutions

In parallel with the infestation, we also measured the number of nitrogenous compounds formed in the solution, which allowed us to judge the preventive effect on microorganisms and various kinds of protein molecules, which also contaminate the wastewater. Initial values were measured immediately after soaking the meat in each of the solutions. Further measurements were made 8, 16, and 24 hours after soaking the meat, the values of nitrogen compounds in the solutions are shown in Fig. 10–12.

In all solutions, after some time, the values of acidity began to tend to neutral values, so the values of alkaline solutions shifted closer to 7, and acidic solutions - closer to 6, initially neutral solutions remained as such over time.

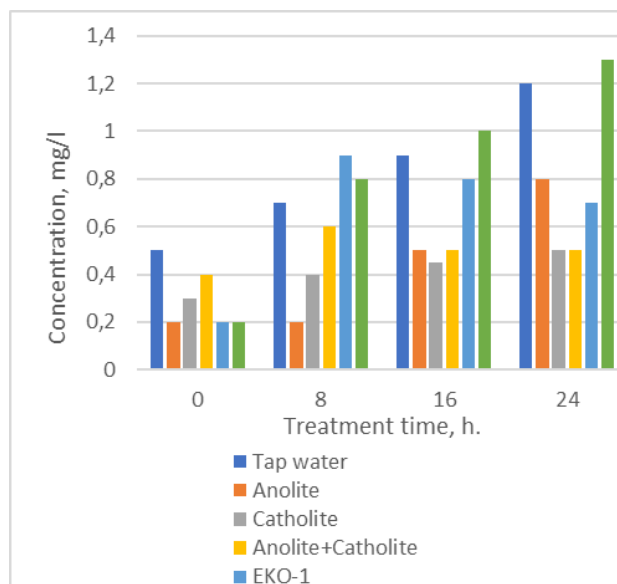


Figure 10 – Changes over time of NH_4^+ concentration, mg/L in the model solution at different treatment methods

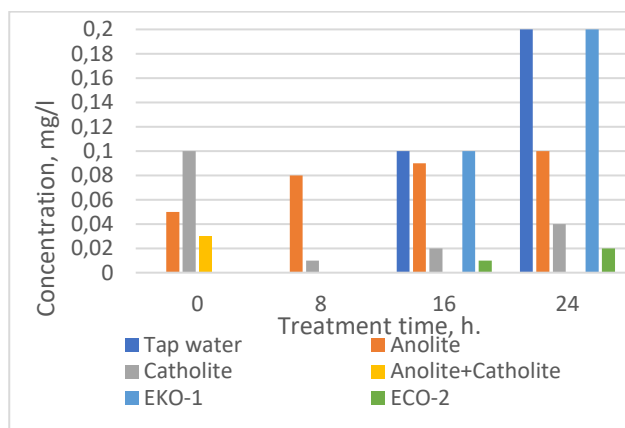


Figure 11 - Changes over time of NO₂⁻, mg/L concentration in the model solution at different treatment methods

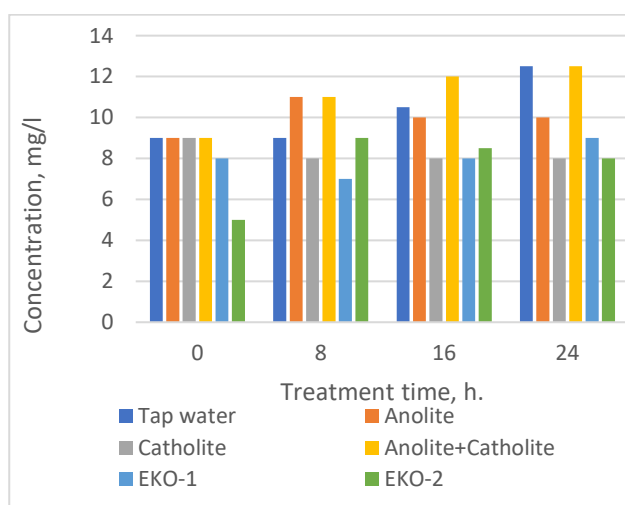


Figure 12 – Changes over time of NO₃⁻, mg/L concentration in the model solution at different treatment methods

Indicators of nitrogenous changes also underwent some changes, so the values of ammonium ion in almost all solutions increased, respectively. This led to a slight increase in other nitrogenous compounds, namely nitrites and nitrates, to which the ammonia/ammonium in the solution decomposes. This fact suggests that after 8 hours in the solutions began to decompose protein molecules into simpler mineral compounds, which indicates the effectiveness of the solutions shown not only as antibacterial agents but also as agents suitable for cleaning water from some organic pollutants. Solutions containing products of electrokinetic oxidation proved to be the most effective solutions at this time interval. Ammonia/ammonium values in each of these solutions increased 4-fold.

One day later, various changes also continued to occur in the solution. As for nitrogen compounds, active growth of ammonia/ammonium was observed in the solution, which contained more ECO-1 and ECO-2 products, and the amount of this ion in the anolyte solution increased 4-fold completely suppressed the development of microorganisms. Other indicators of nitrogenous compounds also began to increase. The amount of both

nitrite ion and nitrate ion increased, indicating that the toxic ammonia/ammonium ion is undergoing decomposition in these solutions.

4.3 Determining the effectiveness of wastewater treatment methods from microorganisms

After wastewater treatment, using the 5 different methods described above, all the indicators of the solutions were measured again. The measurements were repeated after 5 hours and one day after the wastewater treatment. Solutions were filtered, and 2 samples were taken for analysis to determine the effectiveness of wastewater treatment methods from microorganisms.

Six samples of previously prepared water were taken. Then, the first dilution was prepared with distilled water (10⁻¹). After that, a series of dilutions was prepared: 1 ml of the sample was taken from the first and diluted 1:10 with a physiological solution (second dilution (10⁻²)). The following dilutions were prepared in the same way up to the 10th dilution (10⁻¹⁰).

In all 6 samples, 0.5 ml of the last dilutions were inoculated on KMAFNM medium. The cultures were incubated in an incubator at 37°C for 2 days. A control was performed on the second day.

TDS, ORP, and pH values were taken one hour after purification, after 5 hours, and after 24 hours. The results are shown in Table 4.

Table 4 - Changes in the leading indicators of wastewater

Value	Catholyte	Anolyte	ECO	UV+H ₂ O ₂	BP
OVP1h	18.80	30.30	18.90	-23.80	-140.20
OVP5h	20.00	28.10	16.30	-23.00	-138.50
OVP24h	24.00	30.20	18.60	-17.20	-140.00
TDS1h	1080.00	1060.00	1090.00	1130.00	1250.00
TDS5h	1000.00	1020.00	1020.00	1077.00	1175.00
TDS24h	960.00	985.00	963.00	980.00	1120.00
pH1h	6.68	6.49	6.68	7.40	9.39
pH5h	6.65	6.52	6.72	7.39	9.39
pH24h	6.61	6.48	6.68	7.31	9.38

Before the experiment, conducted a control as a reference in all scientific laboratory experiments. The control cup did not germinate, indicating the experiment's validity and compliance with all rules of sterilization of laboratory utensils and media throughout the experiment.

In the cup in which the initial (waste) water was sown, solid growth was detected, indicating a high content of microorganisms (Fig. 13).

The number of colony-forming units exceeded 30 on plates on which water treated with anolyte and ultraviolet radiation with the addition of hydrogen peroxide was sown.

On the surface of the medium where the catholyte-treated sample was planted, 11 colony-forming units were counted, which is equal to 5.6 · 10¹¹ when converted to ml of water. This proves that the decomposition of chlorides in the pH-corrector (in wastewater, the chloride concentration is 1100 mg/l) with the formation of sodium hypochlorite.

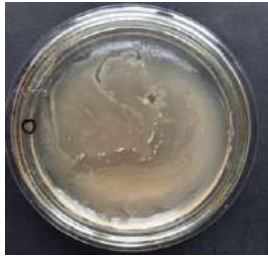


Figure 13 – Source wastewater discharged on KMAFANM medium

In a cup with a water sample treated with ECO-2, the number of colony-forming units was equal to 8, which in terms of 1 ml of water is $4 \cdot 10^{10}$. Since ECO-2 has pronounced coagulating properties, most of the microorganisms settled down together with large particles floating in the water column.

No colonies were found on a cup with a water sample treated with flocculant BP. This can be explained by the fact that the flocculant is not only a catalyst for coagulation but also enhances it many times (Fig. 14). In addition, it also has a high disinfecting effect.



Figure 14 – Sample treated with BP

The final results of wastewater treatment using 5 different treatment methods are shown in Table 5.

Table 5 – Number of CFU/ml when using different methods of meat-processing wastewater treatment

Cleaning methods	Total infestation, CFU/mL
Source water	Solid growth
Catholite	$5.6 \cdot 10^{11}$
Anolite	Less than $6 \cdot 10^{11}$
ECO-2	$4 \cdot 10^{10}$
UV+H ₂ O ₂	Less than $1.0 \cdot 10^{11}$
BP	0

Based on the results obtained, we can recommend a water supply and sewerage scheme with a preliminary impact on water solutions in places of formation of pollutants (Fig. 15) to preventively improve the effectiveness of wastewater treatment of municipal and industrial facilities.

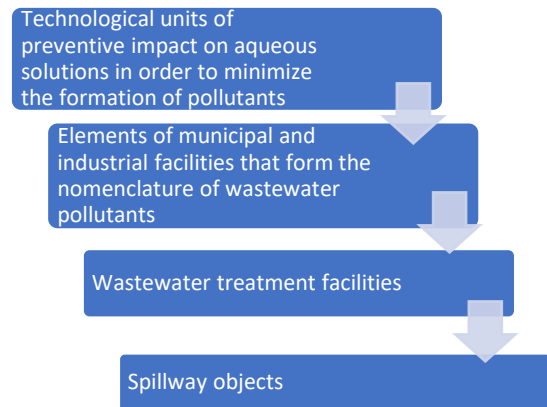


Figure 15 – Modernized scheme of water supply and sewerage of municipal and industrial facilities

The results of chemical and microbiological analysis of wastewater treated by 5 different methods show that flocculant BP is the most effective in wastewater treatment because it disinfects and catalyzes effect. Due to the complex action of different methods, it is possible to make a multistage treatment of wastewater, which will be much more effective than using each method separately.

The practical implementation of such a scheme (Fig. 15) will allow one to reduce the cost of creating (modernizing) sewage treatment plants, to reduce operating costs for wastewater treatment, and to increase the ability of water circulation systems to more flexibly counteract abnormal situations in the “spillway” channel: salvo emissions of pollutants, and breakdowns of individual components of such systems.

5 Conclusions

As a result of the studies, it was found that the change in the parameters of aqueous solutions during the treatment of the meat with these solutions directly affects the population of these solutions with microorganisms. Parameters that were changed as a result of the study: ORP, TDS, and pH.

Solutions capable of almost entirely inhibiting the activity and growth of microorganisms have been obtained, and solutions have also been obtained that, on the contrary, promoted their development and in which solid growth occurred when sown on a dense nutrient medium.

Based on the above, it can be concluded that to prevent pollution and contamination of wastewater at meat industry enterprises, instead of treating meat carcasses with ordinary tap water can be used solutions with modified parameters TDS, pH, and ORP, namely with a slight (acceptable) increase in total mineralization. Solutions containing biocidal products are also effective for this purpose since they also have antimicrobial properties and can decompose organic pollutants quickly.

Further research is advisable to focus on detailing the technical and economic indicators of water supply and sewerage schemes of municipal and industrial facilities with preventive improvement of water treatment processes.

References

1. Khamnaeva, N. I. (2006). Features of sanitary-microbiological control of raw materials and food of animal origin: Textbook. VSGTU, Ulan-Ude, pp. 136.
2. Natynchik, T. M., Levshuk, O. N., Zasimovich, T. I. (2016). Significance and levels of wastewater treatment at meat processing plants. *Innovative Approaches in Veterinary and Zootechnical Science and Practice*, pp. 519–526.
3. Valley, L. F. (2011). Wastewater treatment from nutrients. Continent. Dnipro, Ukraine, pp. 198.
4. Burenin, V. V. (2009). New methods and devices for wastewater treatment and disposal of industrial enterprises. *EKiP: Ecology and Industry of Russia*, Vol. 9, pp. 12–15.
5. Michukov, M. (2008). Chlorine-free method of wastewater disinfection. *Ecology and Life*, Vol. 8, pp. 35–39.
6. Uzcategui, L. U. M., Vergara, K., Bordes, G. M. (2021). Sustainable alternatives for by-products derived from industrial mussel processing: A critical review. *Waste Management and Research*, doi: 10.1177/0734242X21996808.
7. Abirama V., Mohamed R. M. S. R., Al-Gheethi A., Malek, M. A., Kassim, A. H. M. (2021). Meat processing wastewater Phycoremediation by *Botryococcus* sp.: a biokinetic study and a techno-economic analysis. *Separation Science and Technology*, Vol. 56(3), pp. 577–591, doi: 01496395.2020.1718708.
8. Leng, L., Zhang, J., Xu, S., Xiong, Q., Xu, X., Li, J., Huang, H. (2019) Meat & bone meal (MBM) incineration ash for phosphate removal from wastewater and afterward phosphorus recovery. *Journal of Cleaner Production*, doi: 10.1016/j.jclepro.2019.117960.
9. Ivanchenko, O., Khabibullin, R., Le Huong, T., Balanov, P., Smotraeva, I. (2020). Toxicity assessment of meat-processing wastewater. *E3S Web of Conferences (ICEPP-2020)*, Vol. 161, 01044, doi: 10.1051/e3sconf/202016101044.
10. Kulikova, M. A., Kolesnikova, T. A., Gribut, E. A., Okovitaya, K. O., Surzhko, O. A., Zemchenko, G. N. (2019). Optimization of technology for processing liquid waste from meat processing plants. *IOP Conference Series: Earth and Environmental Science*, Vol. 10, 022067, doi: 10.1088/1755-1315/421/2/022067.
11. Harris, P. W., McCabe, B. K. (2020). Process optimisation of anaerobic digestion treating high-strength wastewater in the Australian red meat processing industry. *Applied Sciences (Switzerland)*, Vol. 10(21), 7947, doi: 10.3390/app10217947.
12. SP 32.13330.2012. Code of rules. Sewerage. External networks and structures. SNiP 2.04.03-85. Available online: <https://docs.cntd.ru/document/5200017>.



Kiran A. V. N. S., Ramanjaneyulu B., Lokanath M., Nagendra S., Balachander G. E. (2021). Control of exhaust emissions using piston coating on two-stroke SI engines with gasoline blends. *Journal of Engineering Sciences*, Vol. 8(1), pp. H16–H20, doi: 10.21272/jes.2021.8(1).h3

Control of Exhaust Emissions Using Piston Coating on Two-Stroke SI Engines with Gasoline Blends

Kiran A. V. N. S.^{1*}, Ramanjaneyulu B.¹, Lokanath M.², Nagendra S.², Balachander G. E.²

¹Department of Mechanical Engineering, SVU College of Engineering, SV University, Chittoor Dist., Tirupati, India;

¹Department of Mechanical Engineering, JNTUA Anantapur, India;

²Department of Mechanical Engineering, Annamacharya Institute of Technology and Sciences, Kadapa Dist., Rajampet, India

Article info:

Received: March 10, 2021
The final version received: June 16, 2021
Accepted for publication: June 21, 2021

*Corresponding email:

kiran.avns321@gmail.com

Abstract. An increase in fuel utilization to internal combustion engines, variation in gasoline price, reduction of the fossil fuels and natural resources, needs less carbon content in fuel to find an alternative fuel. This paper presents a comparative study of various gasoline blends in a single-cylinder two-stroke SI engine. The present experimental investigation with gasoline blends of butanol and propanol and magnesium partially stabilized zirconium (Mg-PSZ) as thermal barrier coating on piston crown of 100 μm . The samples of gasoline blends were blended with petrol in 1:4 ratios: 20 % of butanol and 80 % of gasoline; 20 % of propanol and 80 % of gasoline. In this work, the following engine characteristics of brake thermal efficiency (BTH), specific fuel consumption (SFC), HC, and CO emissions were measured for both coated and non-coated pistons. Experiments have shown that the thermal efficiency is increased by 2.2 % at P20. The specific fuel consumption is minimized by 2.2 % at P20. Exhaust emissions are minimized by 2.0 % of HC and 2.4 % of CO at B20. The results strongly indicate that the combination of thermal barrier coatings and gasoline blends can improve engine performance and reduce exhaust emissions.

Keywords: brake thermal efficiency, Mg-PSZ, exhaust emissions, gasoline blends, specific fuel consumption.

1 Introduction

Research in biofuels aims to achieve two essential goals. The first goal is to improve the engine performance and efficiency of the engine. And the second goal is the minimizing of exhaust emission gases from the engine. Several researchers have done their experimental investigations on alternative fuels in the last few decades to achieve the above goals and reduce fossil fuel dependency and harmful engine emissions. Among those, bio-alcohols such as butanol and propanol are considered very promising alternative fuels.

The available surface modification technologies will be the most crucial method to expand piston use, especially the aluminum alloy piston, for automotive. However, since the coating is primarily helpful for corrosion resistance, it should be reconsidered against high temperatures. Therefore, the application of thermal barrier coating, which was widely investigated in the 1980s, can increase thermal efficiency and reduce emissions. Most of the researchers have analyzed the thermal barrier coatings on piston crowns for internal combustion engines.

2 Literature Review

In the article [1], the authors investigated thermal barrier coatings as magnesium partially stabilized zirconium with ethanol and butanol as gasoline blends. From the experimentation, the author concluded that the engine performance parameters of SFC are 1.8 % minimized at B20 for Mg-PSZ, brake thermal efficiencies is 4.5 % maximized at B20 for Mg-PSZ, emission characteristics of HC are minimized by 2.4 % at E20, and CO is minimized by 3.7 % at E20 for Mg-PSZ coated piston is compared with the normal piston of gasoline, and gasoline blends at different concentrations.

In the article [2], the authors carried out their experimental investigations on two-stroke SI engines using a novel piston and gasoline blends as ethanol and methanol to observe the exhaust emissions and engine performance. From the experimentation results, the exhaust emissions are HC and CO is minimized by 10–15 %, and 7–12 % for ethanol-gasoline blend, the brake thermal efficiency is maximized by 1.0 %, and SFC is

minimized by 10–12 % for methanol gasoline blend for a novel piston.

Kumar et al. [3] performed experimentation on SI engines with thermal barrier coatings and gasoline blends to reduce exhaust emissions. The experimentation results have shown that the brake thermal efficiency is increased by 9.0 %, the SFC is minimized by 4.5 %, and exhaust emissions of HC and CO are minimized by 6.0 % and 5.6 %.

Nagini et al. [4] realized their investigations on four-stroke SI engines with copper as thermal barrier coat with different gasoline blends along with catalytic converters at exhaust manifold to monitor the exhaust emissions. From the investigations, the authors concluded that exhaust emissions are minimized.

Dhomne et al. [5] discussed the thermal barrier coatings for two-stroke SI engines. The author discussed different thermal barrier coating materials and their properties that affect SI engine performance, combustion, and emission characteristics. From the reviews, the authors concluded that the proper selection of material should be made. It gives a positive result.

Dudareva et al. analyzed thermal barrier coatings on aluminium alloy piston coatings is micro-arc oxidation on piston crown by using ANSYS. The MAO coating thickness of 76 and 106 μm was applied to the piston crown. The author concluded that the thickness does not significantly affect the thermal state of pistons from the analysis.

Masum et al. [7] conducted experiments on SI engines to determine the effect of ethanol on NO_x emissions. The author discussed the prospect of fuel ethanol as a gasoline substitute and comparative physicochemical properties of ethanol and gasoline. Finally, the author discussed the engine parameters and their effect on NO_x. Finally, the author concluded that the ethanol showed the effect, i.e., a lower amount of NO_x emissions were formed and improved engine performance.

Mittal et al. [8] investigated SI engines with partially coated LHR as Zirconium Dioxide by 8.0 %, by weight of Yttrium Oxide to a thickness of 0.3 mm by plasma spray method on piston crown with gasoline blend as n-butanol 10.0 % and 15.0 % by volume. The author concluded that the SFC is minimized by 1.5–0.9 %, the brake thermal efficiency is maximized by 3.2–7.4 %, and exhaust emissions are decreased due to LHR coated on the piston crown.

Krishna et al. [9] comparatively studied the performance evaluation of two-stroke copper-coated 300 μm thickness on spark-ignition engines with alcohols and catalytic converters. The authors have done investigations to find the effect of engine performance parameters and exhaust emissions. From the results, the authors concluded that the brake thermal efficiency is increased by 4 % on CCE with gasoline blends, the emissions are reduced by 20–40 %.

Parlak et al. [10] found the effect of the M15 blend on SI engine for engine performance and exhaust emissions with thermal barrier coatings. The author concluded that reducing HC and CO emissions is 32.2 % of 6.2 % and

SFC is reduced to 3.4 %, and brake thermal efficiency is increased by 8.2 %, respectively.

Kumar et al. [11] conducted experimental investigations to find the performance and emission characteristics of low heat rejection spark-ignited engines fuelled with E20. Al₂O₃ of 0.3 mm thickness applied on piston crown and cylinder head. From the results, the brake thermal efficiency is increased by 13.5 %. HC emissions are reduced to 2.3 to 17.6 %, and 3 to 16.0 % of emissions are reduced.

Magadam et al. [12] investigated the performance and emission testing of modified pistons in 2-stroke engines using refractive index material coating to improve engine efficiency and reduce emissions. The author inferred from the findings that the actual fuel consumption is reduced by 3.0 % and that thermal efficiency – by 0.9 %.

Sharma et al. [13] conducted experimentation on SI engine with thermal barrier coating by adding argon as inert gas to find the performance and emission characteristics. The author concluded that by adding inert argon gas as an intake mixture, exhaust emissions are reduced, and engine performance increases.

Most researchers have analyzed the effect of thermal barrier coatings on piston crowns for single-cylinder petrol engines with gasoline blends from the above literature review. The present experimental investigations were done on the Magnesium Partially Stabilized Zirconium (Mg-PSZ) coating on piston crown of 100 μm with gasoline blends butanol and propanol of ratio 1:4 where less experimentation will be done.

3 Research Methodology

The schematic experimental setup is shown in Figure 1.



Figure 1 – Experimental setup

The experiments were conducted at five load levels at no load condition, 25 %, 50 %, 75 %, and at full load condition at a constant speed of 3000 rpm. The tests were conducted on two pistons: basic piston and Mg-PSZ coated piston shown in Figure 2 and run with gasoline blends of B20 and P20.

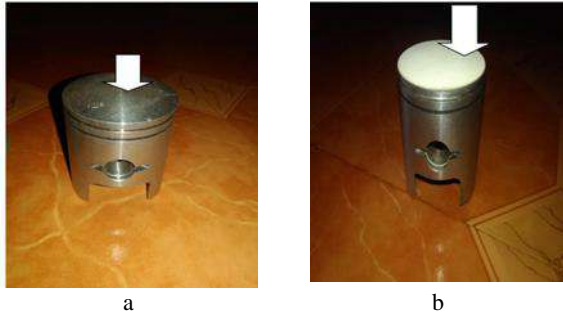


Figure 2 – Normal (a) and coated (b) pistons

The Mg-PSZ coating on piston crown of 100 μm is applied by the plasma spray method. In early attempts, used MgO to stabilize zirconia in its cubic state by adding 25 wt. % MgO. Zirconia can be fully stabilized to its cubic phase by adding 20 % yttria by weight. However, such fully stabilized zirconia coatings perform very poorly in thermal cycling tests.

Typically 7–9 wt. % yttria is used to stabilize zirconia partially, although other stabilizers have been used as well. The primary criteria for selecting a suitable stabilizer include a suitable cation radius similar to that of zirconium and a cubic crystal structure. In spite of the addition of a stabilizer to ensure the top coat's phase stability, phase changes in the topcoat might still be induced during service. The gasoline blends of butane and propane will be supplied to the engine to reduce exhaust emissions.

The above explanation shows the experimental setup, and the procedure should be as follows. When the engine starts with the standard piston and pure petrol, butanol, and propanol at no load condition, check the time taken for fuel consumption, and the current and voltage will be observed on the panel board, with gas analyzer notice the exhaust emissions. Then by applying the different loads, the same procedure will be followed. Replacing the new piston, i.e., piston coated with Mg-PSZ, and the test procedure will be repeated. A comparative result analysis will be made between the normal piston and piston coatings along with gasoline blends by noticing all the parameters.

A two-stroke air-cooled single-cylinder spark-ignition engine with an electrically loaded eddy current dynamometer is used for the investigation.

Tables 1–2 give a specification of the engine and dynamometer. Tables 3–4 present properties of Mg-PSZ and fuel, respectively.

Table 1 – Engine specification

Item	Specifications
BHP	3HP
Speed	3000 RPM
No of Cylinders	1
Bore	57mm
Stroke	57mm
Compression Ratio	7.4:1

Table 2 – Dynamo mater specification

Item	Specifications
Power	3 kW
Speed	3000 rpm
Type	Compound wound

Table 3 – Properties of Mg-PSZ

Property	Value in metric unit
Density, kg/m^3	5600
Modulus of elasticity, GPa	350
Flexural strength, MPa	545
Compressive strength, MPa	1700
Fracture toughness, $\text{MPa}\cdot\text{m}^{0.5}$	6
Hardness, HV	1100
Thermal expansion (20 °C), 1/K	$1\cdot 10^{-5}$
Thermal conductivity, $\text{W}/(\text{m}\cdot\text{K})$	2.5
Specific heat capacity, $\text{J}/(\text{kg}\cdot\text{K})$	400
Max. working temperature, °C	1000
Dielectric strength (AC), kV/mm	6

Table 4 – Properties of fuel

Parameters	Petrol	Propanol (P20)	Butanol (B20)
Density, kg/m^3	745	0.754	0.810
Flashpoint, °C	N/A	29.2	33.3
Fire point, °C	25	30.0	36.5
Calorific value, MJ/kg	43	32.4	33.3
Octane number	90	100	96

4 Results and Discussion

4.1 Specific fuel consumption

The results which are obtained from the experimental setup are discussed below. From the results, a comparative study will be taken for both pure petrol and gasoline blends with changing of the regular piston and Mg-PSZ coated piston. The comparative statements will be discussed on brake thermal efficiency, specific fuel consumption, HC, and CO. Load vs SFC is presented in Figure 3.

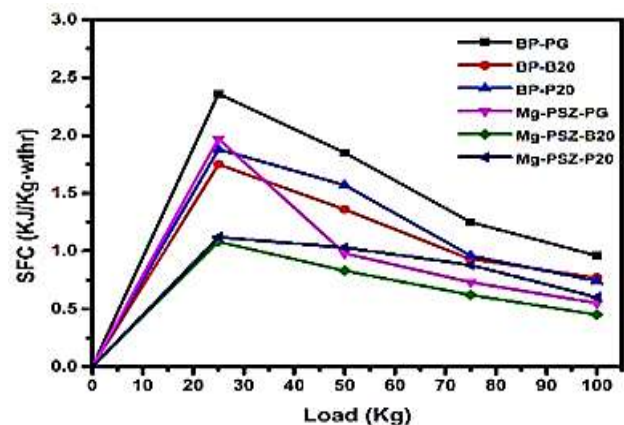


Figure 3 – Load vs SFC

Comparison of load vs SFC of both the base and the coated pistons runs at maximum speed when fuelled with gasoline blends of P20 and B20 is shown above in Figure 3. It can be observed from the results that the gasoline blends B20 and P20 with Mg-PSZ coated on piston crown reduces the SFC when compared with the uncoated piston. This may be due to the increased temperature of the piston crown, which increases the temperature of the cylinder, which causes high temperature, which contributed to higher vaporization rates of gasoline blends extracting the minimum energy out of combustion from gasoline fuels in the combustion chamber. The graph shows that for the base piston and coated piston, the SFC, for pure gasoline, is minimized by 2.74 %, minimized by 2.71 % at B20, and minimized by 2.23 % at P20.

The overall specific fuel consumption is enhanced by 2.23 % on Mg-PSZ coated piston at P20 when compared to the base piston with the blends of butanol and propanol.

4.2 Brake thermal efficiency

Load vs brake thermal efficiency (BTH) is presented in Figure 4.

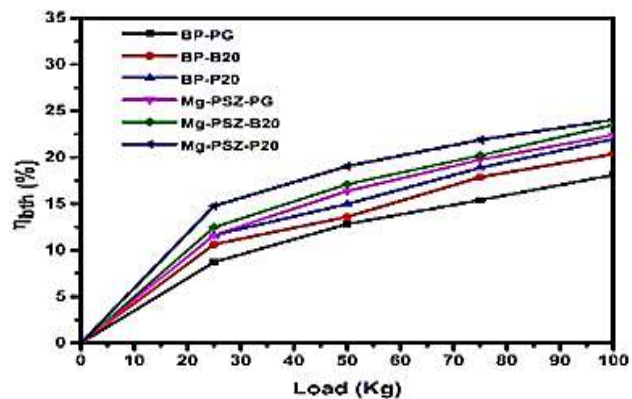


Figure 4 – Load vs BTH

Comparison of brake thermal efficiency vs a load of both the base piston and coated piston runs at maximum speed with gasoline and gasoline blends as shown in Figure 4. This may be attributed to the lower amount of energy consumption required to generate some energy with thermal barrier coatings and gasoline blends, making use of higher gas temperatures and the characteristic advantage of more oxygen in gasoline blends to improve brake thermal efficiency. The graph shows that on pure gasoline for base piston and coated piston, the efficiency is increased by 2.09 %, at B20 2.15 % of efficiency is increased, and for P20 2.23 % of efficiency is increased.

Therefore, the overall brake thermal efficiency is enhanced by 2.23 % on Mg-PSZ coated piston at P20 compared to the base piston with blends of butanol and propanol.

4.3 Hydrocarbons

Load vs hydrocarbons (HC) is presented in Figure 5.

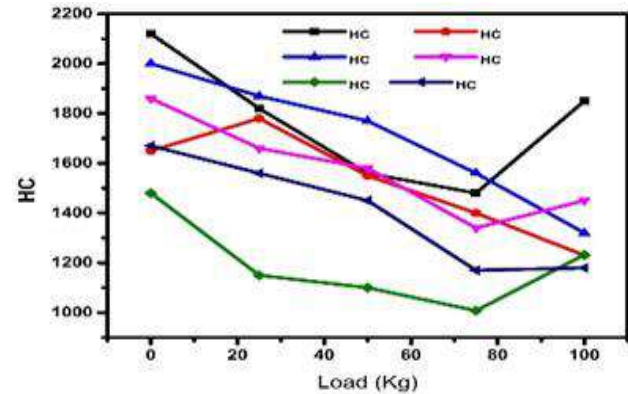


Figure 5 – Load vs HC

Comparison of HC emissions from engine exhaust concerning pure and gasoline blends for both base and coated piston runs at maximum speed as shown in Figure 5. The amount of HC emissions depends upon the engine operating conditions and fuel properties. The engine operated with B20 and P20 gasoline blends and Mg-PSZ piston coating lead to reducing HC emissions due to the sufficient temperature and oxygen presence in the combustion leading to proper combustion. From the graph at pure gasoline at base and Mg-PSZ coated piston, the HC emissions are minimized by 2.27 %, at B20 2.0 %, at P20 2.11 % of emissions are minimized.

Therefore, overall HC emissions are minimized by 2.0 % at B20 for Mg-PSZ coated piston compared with the base piston at B20 and P20.

4.4 Carbon mono oxide (CO) emissions

Comparison of CO emission from engine exhaust concerning pure gasoline and gasoline blends for both base and coated piston runs at maximum speed as shown in Figure 6.

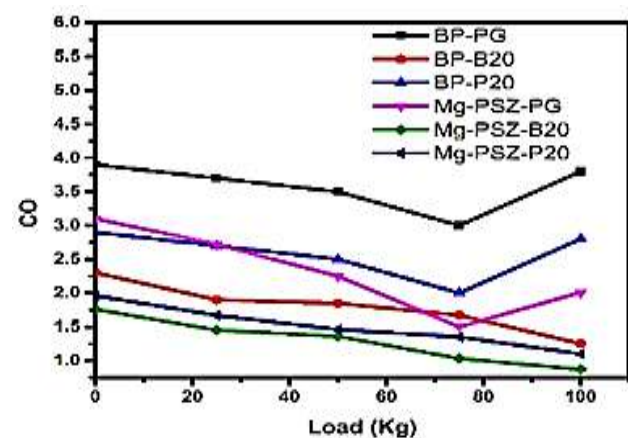


Figure 6 – Load vs CO

It can be observed from the results that the coated piston with gasoline blends reduces the CO due to the presence of oxygen in combustion plays a significant factor in CO emissions for SI engines. The addition of piston coatings and gasoline blends leads to proper combustion explained by supplying sufficient oxygen and increasing combustion temperature during the expansion stroke. From the graph, at pure gasoline for base and Mg-PSZ coated piston, the CO emissions are minimized by 3.54 %, at B20 2.4 %, and at P20 2.8 % of emissions are minimized.

Therefore, overall CO emissions are minimized by 2.4 % at B20 for Mg-PSZ coated piston compared with the base piston at B20 and P20.

5 Conclusions

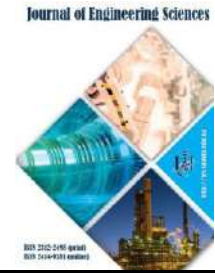
The experimental setup of the work was to characterize the effect of Magnesium Partially Stabilized Zirconium (Mg-PSZ) piston coatings for different gasoline blends of propanol and butanol on engine behavior is compared with the regular piston. The Mg-PSZ piston coating shows the most effective engine performance and emission characteristics with the gasoline blends of B20 and P20.

The effect of Mg-PSZ piston coating at P20 by noticing that the minimizing of the fuel consumption is 2.23 %. The brake thermal efficiency is maximized by 2.23 % at P20 for Mg-PSZ coated piston. The emissions are minimized by 2.0 % of HC at B20 for Mg-PSZ coated piston. The 2.4 % of CO with the Mg-PSZ piston coating at B20.

These results are compared to the base piston and Mg-PSZ coated piston with P20 and B20. The emissions were minimized at B20 for Mg-PSZ coated piston. The performance characteristics are maximized at P20 for the Mg-PSZ coated piston.

References

1. Kiran, A. V. N. S., Nagendra, S., Lokanath, M., Saleemuddin, S. M., Ramanjaneyulu, B. (2020). Experimental investigations on two stroke SI engine with piston coatings and gasoline blends. *I-Manager's Journal on Mechanical Engineering*, Vol. 10(4), pp. 1–7, doi: 10.26634/jme.10.4.17392.
2. Kiran, A. V. N. S., Kumar, B. S., Loknath, M., Saleemuddin, S. M., Nagendra, S. (2019). Experimental studies on two stroke SI engine by using novel piston and gasoline blends. *Journal European Des Systemes Automatises*, Vol. 52(1), pp. 11–15, doi: 10.18280/jesa.520102.
3. Kumar, G. G., Rajeswaran, S., Panneerselvam, K. (2019). Emission reduction in SI engine by using thermal barrier ceramic coated piston. *Journal of Engineering Research and Application*, Vol. 5(2), pp. 16–19, doi: 10.9790/9622-0905021619.
4. Nagini, Y., Krishna, M. V. S. M., Priyadarsini, Ch. I., Sharada, S. N., Sri, P. U., Kumar, K. R. (2016). Experimental investigations on exhaust emissions of four stroke copper coated spark ignition engine with gasohol with catalytic. *Special Section on Current Research Topics in Power, Nuclear and Fuel Energy, SP-CRTPNFE 2016, from the International Conference on Recent Trends in Engineering, Science and Technology 2016, 1 June 2016, Hyderabad, India, Energy Procedia, Elsevier*, pp. 1–8.
5. Dhomne, S., Mahalle, A. M. (2019). Thermal barrier coating materials for SI engine. *Journal of Materials Research and Technology*, Vol. 8(1), pp. 1532–1537, doi: 10.1016/j.jmrt.2018.08.002.
6. Dudareva, N. Y., Enikeev, R. D., Ivanov, V. Y. (2017). Thermal protection of internal combustion engines pistons. *Procedia Engineering*, Vol. 206, pp. 1382–1387, doi: 10.1016/j.proeng.2017.10.649.
7. Masum, B. M., Masjuki, H. H., Kalam, M. A., Fattah, I. M. R., Palash, S. M., Abedin, M. J. (2013). Effect of ethanol-gasoline blend on NO_x emission in SI engine. *Renewable and Sustainable Energy Reviews*, Vol. 24, pp. 209–222, doi: 10.1016/j.rser.2013.03.046.
8. Mittal, N., Athony, R. L., Bansal, R., Ramesh Kumar, C. (2013). Study of performance and emission characteristics of a partially coated LHR SI engine blended with n-butanol and gasoline. *Alexandria Engineering Journal*, Vol. 52(3), pp. 285–293, doi: 10.1016/j.aej.2013.06.005.
9. Krishna, M. V. S. M., Kishor, K., Murthy, P. V. K., Gupta, A. V. S. S. K. S., Kumar, S. N. (2012). Comparative studies on performance evaluation of a two stroke copper coated spark ignition engine with alcohols with catalytic converter. *Renewable and Sustainable Energy Reviews*, Vol. 16(8), pp. 6333–6339, doi: 10.1016/j.rser.2012.07.008.
10. Parlak, A., Ayhan, V., Deniz, C., Kolip, A., Köksal, S. (2008). Effects of M15 blend on performance and exhaust emissions of spark ignition engine with thermal barrier layer coated piston. *Journal of the Energy Institute*, Vol. 81(2), pp. 97–101, doi: 10.1179/174602208X300223.
11. Kumar, C. R., Nagarajan, G. (2012). Performance and emission characteristics of a low heat rejection spark ignited engine fuelled with E20. *Journal of Mechanical Science and Technology*, Vol. 26(4), pp. 1241–1250, doi: 10.1007/s12206-012-0206-0.
12. Magadam, A., Sridhara, S. N. (2017). The performance and emission test for modified piston of 2 stroke petrol engine. *International Journal of Scientific and Research Publications*, Vol. 7(9), pp. 350–354.
13. Sharma, T. K. (2014). Performance and emission characteristics of the thermal barrier coated SI engine by adding argon inert gas to intake mixture. *Journal of Advanced Research*, Vol. 6(6), pp. 819–826, doi: 10.1016/j.jare.2014.06.005.



Copyright Agreement

We, the Authors of the Article publishing in the Journal of Engineering Sciences, in the case of acceptance for publication, transfer to Founders and Editorial Board the underlined rights:

- publishing this article in English and distribution of the printed version;
- English translation of the article and distribution of the hard copy of the translation;
- distribution of the electronic version of the article through any electronic means (by hosted on the official website of the Journal, in electronic databases, repositories, etc.).

We reserve the rights without the consent of the Editorial Board or Founders:

- to use the article materials partially or in whole for educational purposes;
- to use the article materials partially or in whole to write own dissertations;
- to use the article materials for thesis preparing, conference materials, as well as for presentations;
- to post electronic copies (including the final electronic version downloaded from the official website of the Journal):
 - on the personal web-sources of all the co-authors (websites, webpages, blogs, etc.);
 - on the web-sources of authors working organizations (including electronic institutional repository);
 - on the International scientometric databases;
 - on non-commercial open-access sources.

In all cases, the presence of citations to the article or hyper-link to the electronic copy of the journal's official website is obligatory.

By this agreement, we also certify that the submitted article:

- does not violate the copyrights of other persons or organizations;
- has not been published previously in other publishing houses and submitted for publication in other Journals.



Dear Authors of the Journal of Engineering Sciences!

The Editorial Board of the Journal of Engineering Sciences pays special attention to the structure of the articles according to the [List of Scientific Professional Editions of Ukraine](#) (Category “B”, Minutes No. 1208 of 07.11.2018, Appendix No. 8). Only original articles by the authorship of up to 5 authors are accepted for publication according to the [Template](#) with the following elements:

- general statement of the problem and its relationship with the essential scientific or practical problems;
- analysis of the recent investigations and publications in the same research field;
- statement of the significance of the general problem that was not solved before;
- statement of the purpose of the research article;
- description of the initial data of the research with the justification of the achieved scientific results;
- conclusions and ways for further development of the research.

All the articles are reviewed by the independent double-blind procedure.

All the authors should send via e-mail jes@teset.sumdu.edu.ua the electronic version of the following materials:

- article **in English** according to the [Template](#);
- information about authors and their affiliation with the related address.

ATTENTION!

If one of the mentioned components is not sent or there are many stylistic, orthographic, and grammatical errors, the article will not be considered by the Editorial Board and will not be reviewed.

The minimum size of the materials:

1. Scientific – theoretical articles (up to 25,000 symbols; about 14 pages) that deal with the theoretical research and descriptions of physical laws concerning the investigated phenomena; theoretical generalizations and fundamental principles proved by the experimental research data.
2. Scientific-practical articles (up to 10,000 symbols; about 6 pages) that deal with scientific experiments and recent experience. They include the proposed methods for the experimental research or means to observe the studied phenomena. An essential part of these articles is the description of the achieved results and their explanation acquired in immediate interaction with the object of investigations, its significance, and practical implementations.
3. Scientific-methodological articles (up to 15,000 symbols; about 8 pages) that deal with the review of processes, methods, instruments for solving scientific and applied problems; the statement of the new methodology, results of which allow creating more precise methodology based on an up-to-date methodology for the implementation of discovered laws.